Transition Metal Oxide Composite Nanomaterials as Anodes in Lithium-Ion Energy Storage Devices

Yiana Scott Shakespeare MRes, MChem

A Thesis submitted to UCL for the degree of *Doctor of Engineering,* (EngD)

Department of Chemistry

University College London

April 2022

Signed Declaration

I, Yiana Scott Shakespeare confirm that the work presented in this thesis is my own. Where information has been derived from other sources, I confirm that this has been indicated in the thesis.

April 2022

Abstract

The work in this thesis explores the use of a Continuous Hydrothermal Flow Synthesis (CHFS) method to create nano-sized transition metal oxides and carbon-metal oxide composites for use as anodic active materials in lithium-ion batteries (LIBs) and hybrid ion capacitors (HICs).

In the first study, the novel use of a CHFS method to create the target nanomaterial $TiNb_2O_7$, (TNO) was investigated. The electrochemical properties in LIBs were explored. The CHFS TNO exhibited high capacity at low and high currents, good long term cycling stability and prominent levels of pseudocapacitive charge storage. The formation of a composite carbon/TNO material was also explored. This composite material was found to have improved capacity at all currents tested.

The second investigation was a materials discovery study centering around tertiary mixed metal oxides. A library of V/Nb/Mo oxides were synthesised and characterised physically and electrochemically in LIBs. The relationships between composition, physical properties and electrochemical behaviour were studied. The novel material, $V_{0.3}Nb_{0.1}Mo_{0.6}$ oxide (VNM316) was discovered, which showed high capacity at low and high currents.

The third study built on the second and investigated the formation of carbon/metal oxide composite materials of the promising VNM composition. Nanoparticles of carbon-VNM316 were successfully synthesised by an assisted CHFS method. These materials showed a large improvement in capacity at high current and performed well as LIB and HIC anodes.

Lastly, lessons learnt from previous studies were applied to a library of mixed metal oxides containing Fe, Mn, and Zn. Electrochemical and physical characterisation highlighted the composition $Fe_{0.2}Mn_{0.75}Zn_{0.05}$. Carbon composite materials based on mixed Fe/Mn/Zn were then formed. The materials $C(Fe_{0.66}Mn_{0.21}Zn_{0.11})$-4HT and $C(Fe_{0.72}Mn_{0.17}Zn_{0.09})$-5HT displayed high capacities of 932 and 715 mAh g^{-1} at low current and 271 and 202 mAh g^{-1} at high current respectively. CV and EIS analysis indicated degradation over long-term cycling causing a drop in capacity retention.

Impact Statement

In order to reduce the impact of human activity on climate change, the world is increasingly looking to electrified vehicles to replace the internal combustion engine and cut down one of the biggest sources of greenhouse gas emissions. Lithium-ion batteries are at the forefront of energy storage technology for electric vehicles. Forecasts suggest that both electric car production and subsequent demand for lithium-ion energy storage devices will increase dramatically over the next decade. At present, the lithium-ion technology found in electric cars does have several limitations that are hindering the widespread take-up of electrified transport. These include: low energy densities; low power densities; issues with safety; and expensive low abundance elements. The development of anodic and cathodic materials for lithium-ion storage devices that are higher performing, cheaper and use sustainable methods of production is critical for electrified transport to meet the demands of tackling greenhouse gas emissions.

The work herein reports Continuous Hydrothermal Flow Synthesis (CHFS) to create nanosized compositions and materials for use as anodes in lithium-ion energy storage devices. Libraries of previously unreported elemental compositions and composite carbon-metal oxides were successfully synthesised, investigated electrochemically as anode materials, and then physically characterised to elucidate composition-structure-performance relationships. This research has led to certain compositions and materials being submitted for patenting (GB, Patent Application No.: 2018556.7). This work could have direct commercial value as well as help to direct and inform future academic research projects in both this research field of energy storage materials, and other related research fields that utilise mixed element nanomaterials and green synthesis methods.

Sections of the research discussed in this thesis were presented nationally to the JUICED Energy Hub (EP/R023662/1), as well as to the Henry Royce Student Summit in 2021. Parts of the research were also presented internationally at the Advanced Inorganic Materials conference in 2018 in Padova, Italy. Several elements of this research are due to be published in peer-reviewed journals.

Acknowledgments

First, I would like to thank my supervisor Professor Jawwad Darr for all his guidance and advice over the past four years, and for providing me with the opportunity to come to UCL. To Professor Rob Palgrave for being my second supervisor and always being happy to help with the many XPS questions I had. I would also like to thank all the members of the CMTG who I have had the good fortune to work with over my time in the group. It has been a joy to work with so many great people. Thank you for everything you've taught me and for all the laughs we have had – Alex, Carlos, Charles, Dan, Dustin, Ian, Liam, Min, Shutao, Tom, Rob, Yijie and Zuharia. To Tony for being the most helpful person on campus, to Martin and Jeremy for all your help with diffraction, pattern fitting and always having a cup of coffee at the ready, and to Steve for your endless patience and help with the TEM, SEMs, and Raman. I would also like to thank Martyn, Katherine, and Helena for all your help in organising and running the battery module. I learnt a lot from that experience, and it was a pleasure to work with you all.

A large amount of thanks goes to the many squad members, coaches, and alumni of ULBC. It was an honour to be a part of a boat club filled with such highly driven people, which taught me how to manage time effectively, how to really push myself and that the total sum is always greater than the value of the individual parts. Thank you for not only showing me that sport and research are compatible, but also giving me the opportunity to achieve both. I am forever grateful to you all. Thank you to Kevin and Max for making the last year in the flat brilliant fun. To Stuart for being both a mentor and a friend. To Fergus for everything since we started this chemistry journey eons ago. To my parents, Simon and Marijke thank you supporting me on this journey, thank you for all your love and being a constant source of inspiration and motivation. Thank you to my brother, Samora for all the games of ping pong and for pushing me to always go for more, and to my extended family, you are all wonderful, inspiring people, thank you and hartelijk bedankt. To Phil and Catherine, thank you for looking after me since I came to London and for everything you have done.

Lastly, to Megan, none of this would have would have been possible without your love and support, thank you for everything.

Table of Contents

1.0 Introduction to Electrochemical Energy Storage and Synthesis of Nanomaterials

'*So is life: the very problems you must overcome also support you and make you stronger in overcoming them*' – George Pocock

Introduction

As humanity strives to reduce the effects of global warming on earth, the ability to store and use green electrical energy has never been more in demand. In order to meet climate change targets, the development of renewable energy technologies and energy storage techniques must be accelerated.[1] In the fight against the rising CO_2 levels and the global increases in temperature that have been observed over the past 150 years (Figure 1.1a), the use of renewable energy sources such as wind and solar have been heavily pursued and have seen a large rise in the consumption of energy generated from these methods in the last decade.[2] However, due to the inherent intermittency of these sources, the need for energy storage methods to smooth out the collection and distribution of energy to match the needs of the grid is essential. Alongside heavy industry and aviation, one of the other main producers of CO_2 in society is personal transport. In order to counter this, the number of electric vehicles (EVs) on the road has seen vast growth over the past few years and is forecast to continue in a steep upward trajectory with the majority of this growth being driven by China.[3]

a) b)

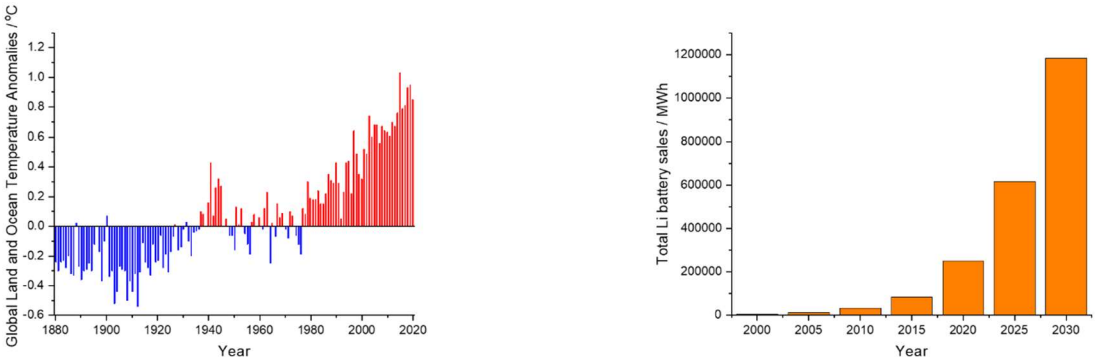

Figure 1.1: a) Graph showing the increase in global land and ocean temperature anomalies for the past 150 years, data compiled from the NOAA [2], b) graph showing the current and forecasted global sales of lithium-ion batteries in MWh, data compiled from source [3].

The forecast for worldwide sales of lithium-ion batteries, the main power source in electric cars, predicts a vast increase by a factor of four, over the next decade (Figure 1.1b). Electrochemical energy storage has a long history of use at the forefront of technological advances. For example, NASA have been using energy storage devices such as rechargeable batteries, electrochemical capacitors and fuel cells since the launch of Explorer in the 1950's.[4] The lithium ion battery is currently the first choice of device for both EVs and un-manned spacecraft as the primary power supply in a vehicle, a source of power during eclipse periods and as a method of load leveling for radioisotope powered space missions.[5] Electrochemical capacitors or supercapacitors have already found many commercial uses as current smoothing devices for intermittent renewable energy sources, emergency back-up power systems for critical infrastructure such as hospitals and as energy storage devices in energy recovery systems such as the regenerative braking system found in Formula 1 cars.[6]

At present, two of the most important properties of electric vehicles that need improving are the driving range achievable on a single charge, and the time it takes to charge the battery. Addressing these two metrics will give electric vehicles the ability to compete far better with the internal combustion engine (ICE) and to give EVs the access to more rural areas and thereby become applicable to those living outside developed urban areas.[7] In the next decade NASA has intentions to explore the outer planets of the solar systems and their respective moons in search of potential ocean worlds such as Titan, Europa and Callisto. For such missions, the specific characteristics of the rechargeable energy storage devices will differ depending on the location. For instance, the proposed mission to Titan will require the battery/capacitor to meet all the power and load leveling demands, whilst being able to operate in the extremely low temperatures found on Titan's surface, long durability and reliability to be able to last the journey and then perform the tasks, high heat and radiation resistivity for the journey and surface landings, and high energy density so that greater amounts of physical space on the craft can be utilized for scientific equipment.[8] The 2017 report by the Jet Propulsion Laboratory and NASA outlines the energy storage device requirements for different proposed missions, Table 1 summarises the specific energy storage device needs for future Mars missions.[4]

Type of Mission	Energy Storage Device Type	Energy Storage Device Needs
Orbital Missions	Rechargeable batteries/Capacitors	- High specific energy (>250 Wh kg^{-1}) - Long cycle life (>50,000 cycles at 30% depth of discharge) - Long lifetime (>15 years) - Low-medium specific power
Aerial Missions (Drones)	Rechargeable batteries/Capacitors	- High specific energy (>250 Wh kg^{-1}) - Long cycle life (>1000 cycles at 70% of depth of discharge) - Long lifetime (>5 years) - Low temperature operation (<−40℃) - High specific power (3000 W kg^{-1})
Surface Missions (Robotic landers and rovers)	Rechargeable batteries/Capacitors	- High specific energy (>250 Wh kg^{-1}) - Long cycle life (>1000 cycles at 70% of depth of discharge) - Long lifetime (>5 years) - Low temperature operation (<−40℃) - Low-medium specific power - Heat and radiation resistant
Landers and Rovers in preparation for Human Missions	Regenerative Fuel Cells	- High specific energy (>500 Wh kg^{-1}) - Long cycle life (>1000 cycles) - Long lifetime (>5 years) - Low temperature operation (<−40℃) - High specific power (500 W kg^{-1}) - Heat and radiation resistant

Table 1: Different proposed Mars missions and their respective energy storage device needs. Compiled from source [4].

In addition to the creation and design of rechargeable energy storage devices on Earth for use in outer space, as the prospect of a human outpost on Mars looks set to quickly follow the upcoming Artemis missions in the mid-2030's, the issue of creating energy storage systems off-world using only the elements and materials that are found there becomes apparent. Previous Rover missions have identified what are the main components of the surface of Mars, and now the next generation of missions are beginning to investigate what may lie beneath the surface. This knowledge is driving research into rechargeable energy storage devices that are centered around the materials that future explorers will find there.[9]

In the pursuit of electrochemical energy storage devices that are able to store larger amounts of energy and deliver greater amounts of power while reducing the mass, volume and cost, a lot of research has been directed at investigating different materials and alternative devices to the standard lithium-ion battery and electrochemical capacitor.

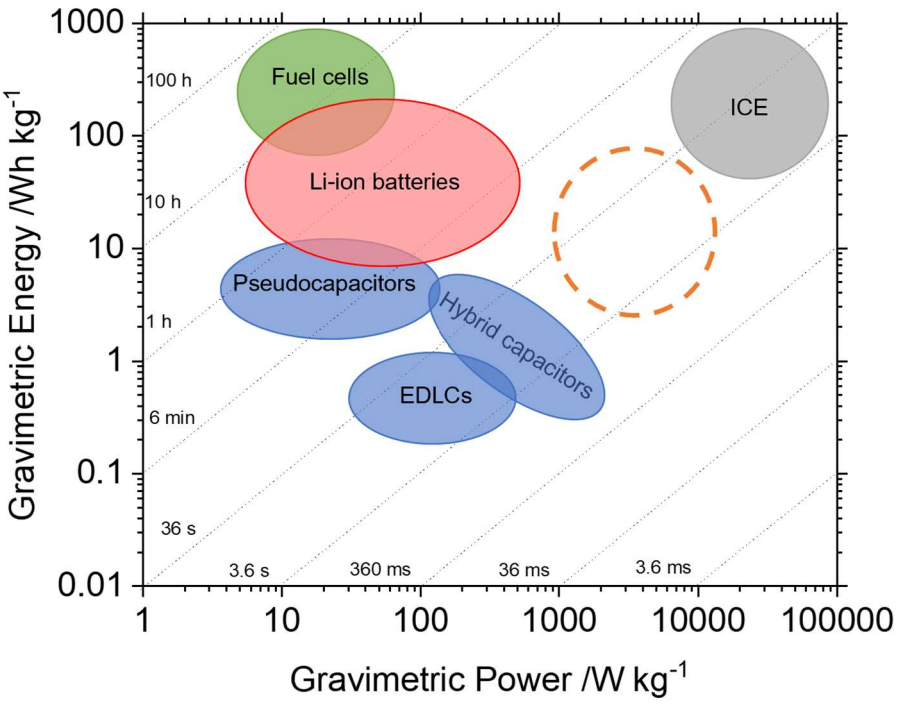

Figure 1.2: Simplified Ragone plot of different electrochemical energy storage technologies (EDLCs – electric double layer capacitors, ICE – internal combustion engines). The desired performance of batteries and capacitors is denoted by a dashed circle. Data compiled from sources 9 and 10. The diagonal dotted lines represent the operation timescales as labelled and are calculated by dividing energy by power.

One such type of alternative electrochemical energy storage device is the hybrid capacitor.[10] These energy storage devices represent a center ground between a lithium-ion battery and an electrochemical supercapacitor, both in construction and performance. By replacing one half of the two activated carbon electrodes in a supercapacitor for a metal oxide electrode, analogous to those found in LIBs, a device can be created which retains high specific power and improved specific energy. A Ragone plot is a plot of logarithmic gravimetric energy vs logarithmic gravimetric power and is used to compare the performance of different energy storage methods. The general positions of current lithium-ion batteries, electrochemical supercapacitors, hybrid capacitors, (and the performance metrics that are the target for many research institutions as the minimum needed for widespread replacement of fossil fuels and combustion engine vehicles) are shown below in Figure 1.2.[6,11] To push the performance of these devices into the areas needed to fulfil the criteria of both EVs and spacecraft, research is needed to both develop existing electrode chemistries and discover new candidates which have high capacity, high intrinsic conductivity, high durability, low cost and high safety.[7,12–15]

Aims, Objectives and Overview of Thesis

The work described in this thesis was aimed to utilise a controllable (hydrothermal flow) bottom-up synthesis method to develop previously unreported new heterometallic oxide anode materials and composites for use in lithium-ion batteries and hybrid capacitors and investigate structure-property relationships. This research has been evaluated for structures containing key elements or structural families that have shown some promise compared to the most recent literature. The role of composition on structure, physical properties and electrochemical behaviour was investigated with a wide range of complementary techniques to probe the atomic and electronic interactions and the understand the effect of these on electrochemical charging and discharging.

Chapter 1: Describes the theory of energy storage and the mechanisms associated with electrochemical charge storage and explains the techniques used to evaluate materials and devices. It also discusses the theory and practice of synthesising nanoparticulate metal oxides using traditional literature methods, as well as the development, benefits, and costs of CHFS.

Chapter 2: Illuminates the underlying theory and use of advanced physical characterisation analysis and techniques utilised in this thesis. The experimental information including reactor schematics, experimental conditions, precursor solutions and post CHFS processing are also outlined here.

Chapter 3: Investigates the use of CHFS to synthesise $TiNb_2O_7$, a highly regarded anode material for commercial lithium-ion materials. The CHFS nanoparticles were investigated further for their lithium diffusion kinetics through complementary electrochemical techniques. The synthesis of mixed titanium niobium oxide nanomaterials with graphitic carbon coatings for increased electrochemical performance in lithium-ion batteries was also explored.

Chapter 4: Delves into a combinatorial study of mixed vanadium, niobium, and molybdenum oxides. High performing compositions are discovered. The relationships between composition and charge storage capabilities in both lithium-ion batteries and hybrid capacitors were also explored.

Chapter 5: Builds on the previous study and investigates how the best performing mixed vanadium-niobium-molybdenum oxide can be improved through the synthesis of a variety of different composite carbon-metal oxide materials for use in lithium-ion batteries and hybrid capacitors.

Chapter 6: Coalesces the knowledge gathered from previous work and centres around a materials discovery study of mixed metal iron, zinc, and manganese oxides. The physical and electrochemical characterisation, and the relationships between composition and properties were explored. The higher performing materials were then subjected to the use of carbon coating techniques, in order to improve their performance as anodes in both lithium-ion batteries and hybrid capacitors.

1.1 Fundamentals of Electrochemical Energy Storage

The storing of energy can occur through many different processes. The work in this thesis will focus solely on different electrochemical methods such as redox reactions, capacitive charge storage and pseudocapacitive charge storage.

The design of the battery is such that the electrons are driven by a potential difference through a load, whilst ions travel in the opposite direction through the electrically insulating electrolyte. One of the simplest examples of this is the galvanic cell, which consists of a zinc anode in a solution of $ZnSO_4$, a copper cathode in a solution of $CuSO_4$, a wire connecting the two electrodes and a salt bridge allowing the flow of ions between the two solutions (Figure 1.3)[16].

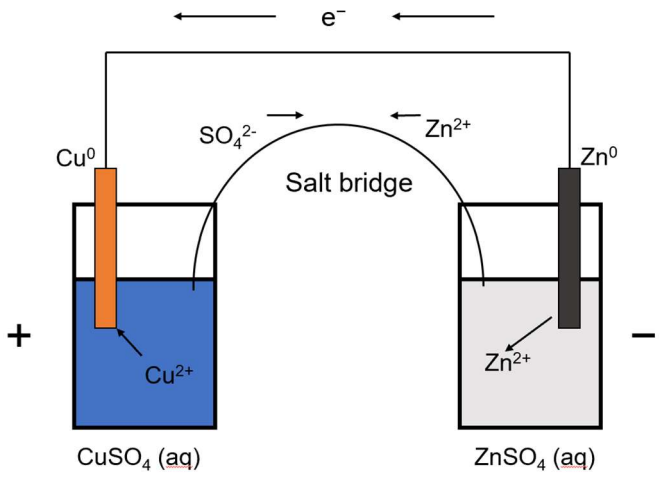

Figure 1.3: Diagram of a simple galvanic cell.

For facile comparison of the different chemical redox reactions occurring in a galvanic cell, the half-cell reactions are written for each electrode and are referenced against the Standard Hydrogen Electrode (SHE) to give the standard potentials, E^0, (shown in equations 1.1 – 1.3). The convention used in science states that the SHE is set as having a potential of zero as this allows for the sign of the electrode potential to be dependent on the direction of the reaction.

Anode: $Zn^{2+}(aq) + 2\ e^- \rightarrow Zn^0(s)$ ($E^0 = -0.76$ V vs SHE) (1.1)

Cathode: $Cu^0(s) \rightarrow Cu^{2+}(aq) + 2\ e^-$ ($E^0 = -0.34$ V vs SHE) (1.2)

Total cell reaction: $Zn^{2+}(aq) + Cu^0(s) \rightarrow Zn^0(s) + Cu^{2+}(aq)$ (1.3)

The two half-cell reactions can be added together to give the total standard potential of the Daniel cell of −1.10 V. The Gibbs free energy of the total cell reaction can be calculated with equation 1.4:

$$\Delta G^0_{total} = (\Delta G^0_{products} - \Delta G^0_{reactants}) = \Delta G^0_{cathode} - \Delta G^0_{anode} = -nFE^0_{cell} \quad (1.4)$$

In which F is Faraday's constant (96485 C mol^{-1}), n is the number of electrons transferred during the reaction and E^0_{cell} is the total cell standard potential. Therefore, the more positive the cell potential, the more thermodynamically favourable the reaction will be in that direction. The Gibbs free energy is related to the standard Gibbs free energy under non-standard conditions by the equation 1.5:

$$\Delta G = \Delta G^0 + RTlnQ \quad (1.5)$$

In which R is the ideal gas constant and T is the temperature in kelvin. Q is the reaction quotient, which is calculated by equation 1.6:

$$Q = \frac{[C]^c[D]^d}{[A]^a[B]^b} = \frac{a_{ox}}{a_{red}} \quad (1.6)$$

Using this, the original expression for Gibbs free energy can be written as equation 1.7, which is then simplified into the Nernst equation (1.8).

$$-nFE = -nFE^0 + RTlnQ \quad (1.7)$$

$$E = E^0 - \frac{RT}{nF} ln \frac{a_{ox}}{a_{red}} \quad (1.8)$$

Where E^o is the standard reduction potential, n is the number of electrons transferred, F is Faraday's constant, R is the ideal gas constant, T is the temperature and a is the activity of either the oxidised or reduced species:

For the comparison of materials and their use in lithium cells, the SHE is replaced by the reduction potential of Li/Li$^+$ (given as −3.04 V vs SHE) for more relevant calculations.[17] One of the key metrics for a battery material is the theoretical gravimetric capacity (Q / C g^{-1}), calculated using equation 1.9 in which M is the specific mass (g mol^{-1}). This is then converted into the more commonly used term of mAh g^{-1} by using the relationship of 1 mAh = 3.6 C.

$$Q = \frac{F \cdot n}{M} \quad (1.9)$$

Another two key metrics of battery materials are the gravimetric energy (*E*) and gravimetric power (*P*). These are related to the discharge time (*t*) using the equations 1.10 and 1.11:

$$E = Q \cdot V = \int_0^t I \cdot V \, dt \qquad (1.10)$$

$$P = \frac{\delta E}{\delta t} = \frac{\delta Q}{\delta t} \cdot V = I \cdot V \qquad (1.11)$$

In which, *I* is the current and *V* is the potential. The other central parameters reported in literature and used for comparison of battery materials are coulombic efficiency and cycle life. Both these metrics, together with the specific capacity, are reported for certain C-rates or specific currents. A C-rate of 1 (denoted as 1C) represents one full charge or discharge in 1 hour (e.g., C/2 represents a full charge or discharge cycle in 2 hours).

1.2 Construction of Energy Storage Devices

1.2.1 The Lithium-ion Battery Design

The standard lithium ion battery has retained its core design since its first inception by the Nobel prize winners J. Goodenough, S. Whittingham and A. Yoshino.[18–22] The standard lithium ion battery consists of a metal oxide cathode

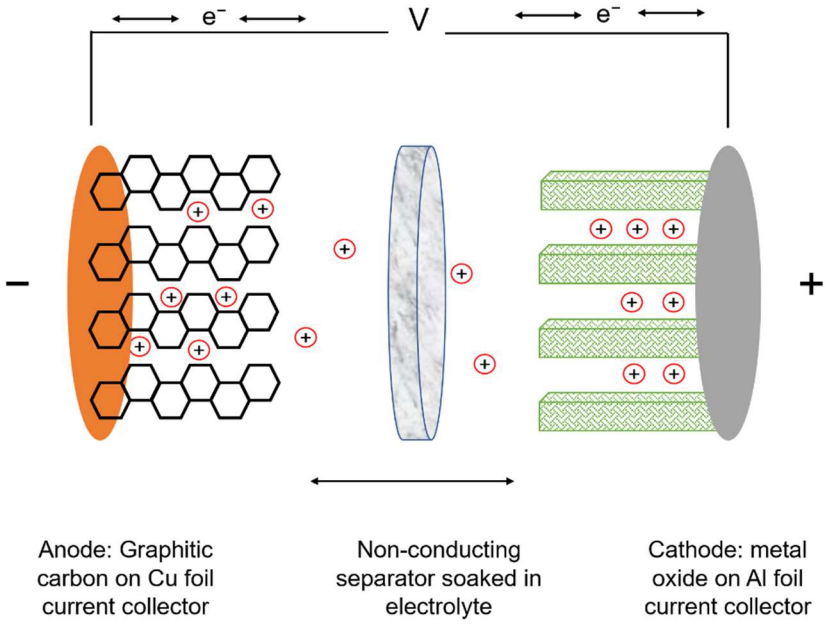

Figure 1.4: Diagram showing the internal components of a standard commercial lithium-ion battery with the positively charged lithium ions shuttling between the graphitic carbon anode and the metal oxide cathode.

(positive electrode), a physical separator that is soaked in liquid or solid phase electrolyte that is ionically conductive, a graphite based anode (negative electrode) and metallic foil current collectors (Figure 1.4). The cathode and anodes are further broken down into the active material, conductive carbonaceous materials and polymeric binder.[23] The anode is defined as the electrode which is oxidised and the cathode is defined as the electrode which is reduced.[14] The anodic and cathodic active materials, together with the electrolyte are the most important components that collectively determine battery performance through the combination of the total lithium ion storage capacity and the potential of the cell. The capacity of active materials to store lithium ions is dependent on several factors such as: the available space within the structure to host Li^+ ions; the ability for the ions to undergo redox reactions; and the reversibility of those reactions.[24] The working voltage of the battery is determined by the potential difference between the anode and cathode.[13] During the charging of a cell, lithium ions are deintercalated from the cathode and intercalated into the anode, increasing the voltage up to a set maximum. During discharge the opposite occurs, with the lithium ions re-intercalating into the cathode from the anode. Therefore, certain considerations with regards to material properties must be taken into account in order to maximise performance. For the cathode, the active material must act as the major source of lithium ions in the cell, due to the current inability for lithium metal to be used as the anode because of as yet unresolved safety issues. It must therefore have a structure that can not only intercalate large quantities of lithium ions, but also remain structurally stable when the Li^+ ions are removed upon charging, as well as providing the highest possible potential within the limits of the electrolyte (discussed below).[25,26] At present, the cathode materials employed in the lithium-ion batteries found in electric vehicles are lithiated transition metal oxides, such as lithium iron phosphate olivines ($LiFePO_4$) and mixed Ni, Mn and Co layered oxides ($Li\ Ni_{0.33}Mn_{0.33}Co_{0.33}O_2$).[27,28] For the anode, there are several considerations that must be taken into account including the working potential, the risk of lithium plating and the type of charge storage mechanism.[29] In attempting to maximise the working potential of the cell, lowering the potential at which the anode material becomes active is the obvious path. However, at low potentials (<1 V vs Li/Li^+) there is a significant risk of lithium ions plating onto the anode as lithium metal in structures, called dendrites, which

can cause a short circuit and potentially fire.[30] This means that in order not to compromise safety, the overall energy and power capabilities are lowered by the smaller potential difference between the electrodes. As previously mentioned, the anode of choice currently in commercial cells is graphite, due to its ability to intercalate lithium ions in between the carbon sheets at low potentials (theoretical capacity of 372 mAh g^{-1}), the ease of synthesis and its abundance.[31] However, graphitic anodes with their low capacity, poor lithium ion diffusion coefficient and safety issues are unable to meet future performance targets (Figure 1.2), therefore a wide range of different anodic materials are the focus of many research institutions.[32–34] The different materials and their lithium storage mechanisms are discussed in depth below.

1.2.2 Intercalation Mechanism Active Materials

The most prevalent type of active materials in commercial lithium-ion batteries are intercalation materials. These are defined as materials which exhibit very little rearrangement of atoms upon insertion and extraction of lithium ions into the host structure.[35] The diffusion of the intercalate (lithium ions) though the electrolyte, the separator, insertion into the host structure and the reverse reaction is defined as the 'rocking-chair' cell by Goodenough,[18,21] and is described by equations 1.12 and 1.12 for the lithium cobalt oxide cathode and graphite anodes respectively:

$$Li_{1-x}CoO_2 + xLi^+ + xe^- \leftrightarrow LiCoO_2 \qquad (1.12)$$

$$C_6 + xLi^+ + xe^- \leftrightarrow Li_xC_6 \qquad (1.13)$$

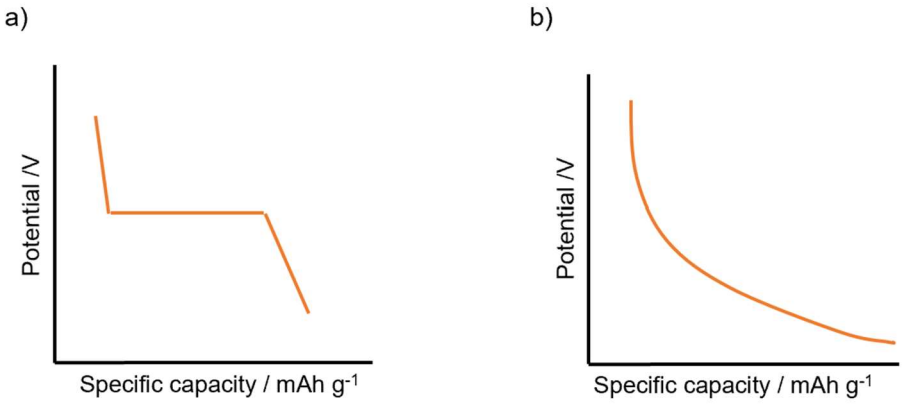

Figure 1.5: (a) diagram showing a flat voltage plateau characteristic of a two-phase transition lithiation/delithiation (b) diagram showing a smooth continuous voltage profile characteristic of a solid-solution phase transition.

The intercalation of lithium ions and the transfer of electrons within the host structure causes the formation of new phases. The behaviour of these new phases can be separated into first- and second-order phase transitions.[36,37] First-order phase transitions describe the formation of two distinct phases that are segregated from each other as lithiation occurs, whereas second-order phase transitions describe the formation of a solid-solution of different phases of lithiated and un-lithiated material. The crucial difference between the two-phase transitions is the stability of the intermediate phases formed. If the intermediate phase created by lithiation is unstable, then phase separation between the lithiated and un-lithiated crystals is observed. Mechanisms of phase separation include the Domino Cascade mechanism and the Bulk Two-Phase mechanism as described by Strobridge *et. al.*[36] The existence of separate phases creates interface interactions that can have implications for further intercalation and extraction of the lithium through electrochemical cycling.[38] The co-existence of different phases within the same particle has been shown to cause structural damage leading to capacity loss and reduced performance at high rate. In contrast, the formation of a solid-solution of partially-lithiated and un-lithiated materials has been observed not to contain energetically unfavourable phase boundaries. This leads to higher rate active materials, as well as improved capacity retention over cycling. Factors that can affect the phase transition order have been shown to include particle size, doping of transition metals, charge/discharge rate and temperature during operation.[39–41] Electrochemically, both phase transitions manifest themselves as different responses to current. Two-phase transitions exhibit a flat plateau at the voltage of lithiation as shown in Figure 1.5a, whereas solid-solution phase transitions give a smooth profile over the voltage range (Figure 1.5b).[37] One of the most investigated and commercially developed alternatives to graphite is the spinel $Li_4Ti_5O_{12}$ (LTO). LTO inherently displays several advantageous properties, such as an intercalation mechanism with a high operating voltage of ~1.55 V vs Li/Li^+ which can avoid lithium plating. It can accommodate up to three Li^+ ions per molecule without any volume increase, thereby giving very good cycle life stability. The natural abundance of titanium in the crust is also very high at 0.63 wt. %.[42] Two of the drawbacks for LTO however, are a low theoretical capacity of 175 mAh g^{-1} and low electrical conductivity of $<10^{-13}$ S cm^{-1}).[43]

In order to overcome these limitations, the incorporation of conductive carbon matrices was reported by Zhang *et al.* in which nanocrystals of LTO were synthesised inside a micrometre-sized porous carbon foam.[44] This composite was found to give a high specific capacity of 73 mAh g^{-1} at a very high rate of 80 C, as well as a capacity loss of only 5.6 % over 1000 cycles at 20 C. There are a wide range of different intercalation metal oxides and related composite materials which are currently being researched as next generation anode materials. These include other titanium oxides,[45] niobium-based oxides,[46] manganese-based oxides[47] and most recently niobium/tungsten-based oxides such as $Nb_{18}W_{16}O_{93}$ and $Nb_{16}W_5O_{55}$.[48,49] These materials are discussed in depth in later chapters.

1.2.3 Conversion and Alloying Mechanisms in Active Materials

Two further mechanisms of energy storage of high interest to researchers are conversion and alloying. Conversion, like intercalation reactions, involves an addition of lithium to the active material and the subsequent conversion to elemental metal and the binary lithium compound (Li_nX) and follows the general reaction as shown in equation 1.14.[50,51] In general this type of reaction occurs for transition metal compounds of M_aX_b,, where M = Mo, Mn, Co, Cu, Ni, Fe, and where X = O, S, Se, F, N and P.[52] The reaction potentials of these compounds are usually within the range of 0.5-1.0 V vs. Li/Li^+, therefore rendering them as possible anode materials. The formation and decomposition reactions of the metallic elements and the Li_nX compounds offer some of the highest theoretical capacities. For metal oxides, capacities can be as high as 1007 mAh g^{-1} for Fe_2O_3,[53] 838 mAh g^{-1} for MoO_2,[54] and 715 mAh g^{-1} for CoO.[55]

$$M_aX_b + (b \cdot n)Li^+ + (b \cdot n)e^- \leftrightarrow bLi_nX + aM \qquad (1.14)$$

The formation of Li_nX in the lithiation process is thermodynamically favourable, however the reverse reaction of the decomposition of Li_nX by elemental M powder is very difficult due to the electrochemical inactivity of the lithium species.[56] Due to this, the reversibility of the conversion mechanism relies on the formation of highly electrochemically active nanoparticles of M within a matrix of Li_nX surrounded by the solid electrolyte interface layer (Figure 1.6).[56,57] One of the major drawbacks of conversion materials is the volume expansion caused by the structural reorganisation within the particles of active material, which can cause pulverisation of the particles and therefore give poor cycling stability.[29]

The large structural rearrangements are also responsible for the voltage hysteresis observed, resulting in low energy efficiency over cycling, as well as the generation of heat.[57] The size of the voltage hysteresis has been observed to be directly related to the anionic species of the conversion material in the order:, fluorides > oxides > sulphides > nitrides > phosphides.[58] Further issues include the possibility of the nanoparticles of M that are formed during cycling causing decomposition of the electrolyte.[59] Finally, because the conversion reactions occur at low potentials, along with the slow kinetics of structural reorganisation, conversion materials do not represent a serious contender for high power applications without these issues first being addressed.

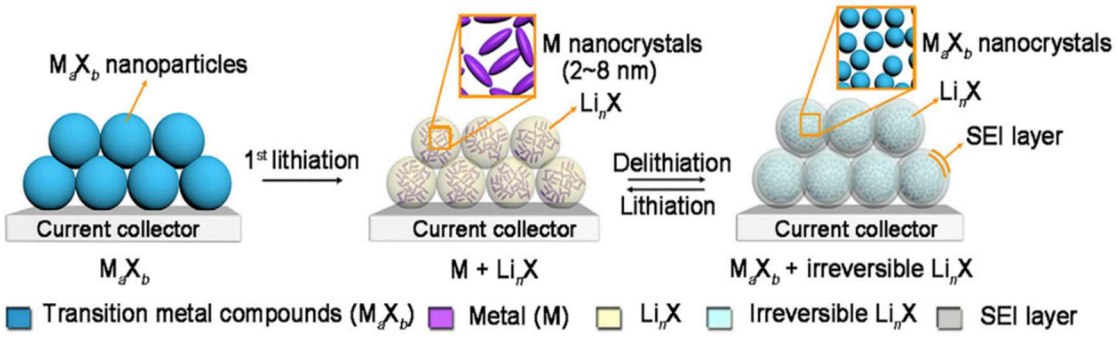

Figure 1.6: Schematic diagram of the chemical reactions and physical transformations that occur during conversion reactions. Reprinted with permission from Y. Lu, L. Yu and X. W. Lou. Copyright 2018 Elsevier Inc.

Alloying mechanisms are also of great interest, offering even higher theoretical capacities compared to intercalation and conversion materials, as they are able to intercalate far higher numbers of lithium ions per molecule. The highest theoretical capacity of those alloying materials is Li metal (3860 mAh g^{-1}). The use of lithium metal as an anode material is one of the ultimate aims for battery materials research, however issues such as dendrite growth, serious safety concerns and poor coulombic efficiency during cycling mean Li metal has a long way to go before being considered a credible candidate.[60] Other alloying materials such as Si (3572 mAh g^{-1}) and Sn (993 mAh g^{-1}) do not suffer from the same safety concerns as lithium and offer the potential performance to meet the future targets. This has meant that silicon in particular is at forefront of alloying battery materials research.[61,62] In contrast to conversion reactions, alloying does not involve the formation of two discreet products, however alloying materials still

suffer from large volume expansion (~300% for $Li_{15}Si_4$). This pulverises the particles of active material causing loss of electrical contact and rapid capacity degradation over cycling and is one of the major hurdles that must be overcome.[63] The current approach taken by industry to attempt to apply silicon to anodes is to effectively dope a graphite electrode with a very small amount of silicon oxide particles (typically 3-5 %). The design rationale is that the graphite can absorb the swelling of the silicon over cycling. This approach can indeed improve the capacity of cells as has been proven in the Panasonic 2170 cells used by Tesla. However in order to go any further, developments at the nanoscale are needed.[64] Many different approaches at the electrode, microstructural and atomic levels are being explored to address the volume expansion issues that inhibit conversion, and thereby prevent alloying materials from being used successfully in electrochemical energy storage devices (Figure 1.7). These include nanosizing of active materials,[47,51,65] the formation of 1D and 2D polymorphs of conversion materials,[59,66] hierarchical 3D configurations,[67,68] and the construction of hollow structures.[69,70] Recent examples of these techniques applied to Si include silicon-core-carbon-shell nanoparticles synthesised by Mangolini *et at.*[71] where a substitution for 10 wt. % graphite in a standard electrode gave a 60 % increase in the storage capacity and a capacity retention of 86 % over 100 cycles. Another example, reported by Chen *et al.* involved silicon/carbon nanotube particles encapsulated by polymethyl methacrylate, which when tested gave a reversible capacity of 1024.8 mAh g^{-1} after 200 cycles.[72]

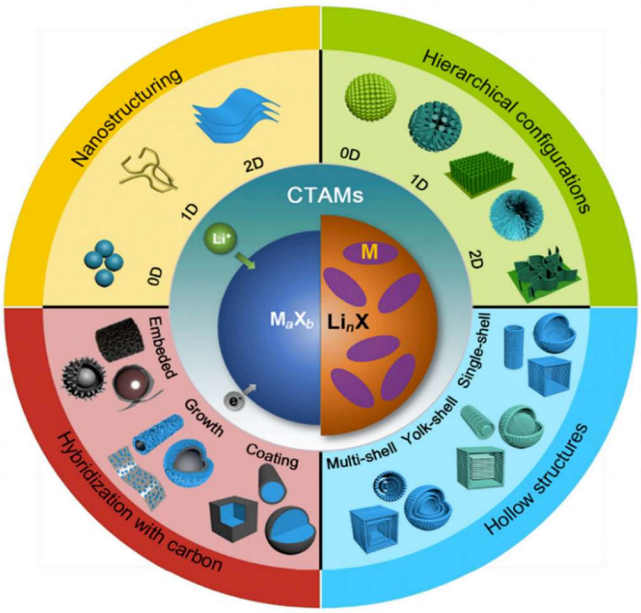

Figure 1.7: Schematic showing the various different nanosized engineering approaches to high performing conversion materials. Reprinted with permission from Y. Lu, L. Yu and X. W. Lou. Copyright 2018 Elsevier Inc.

One further alloying reaction that is of note, is that which can occur between Li and Al at low potentials and has a theoretical capacity of 993 mAh g^{-1}.[73] Aluminium has been investigated as a possible anode material, however in practice the occurrence of this reaction is the reason why anode materials are deposited on copper sheets rather aluminium, so as to avoid unwanted alloying and destruction of the electrode and current collector over cycling.

In order for electrochemical energy devices to reach the high targets required for widespread use in EVs, new materials that satisfy a wealth of considerations must be identified and optimised. Such considerations include the cost, earth abundance and sustainability of the raw materials. As an example, the current state of the art cathode material is lithiated nickel manganese cobalt oxide (LiNMC),[74] however due to the abundance in the Earth's crust of elements such as cobalt and nickel being 0.00116 and 0.00186 wt. % respectively, the cost of currently producing battery materials consisting of these materials is very high.[75,76] This cost is only set to increase with forecasting models predicting a global shortage of cobalt by the year 2025 as demand outstrips supply.[75] Another factor that must be taken into account is the scalability of a material from

laboratory discovery (g/hr) to industrial (kg/hr) scale, as this can render many promising candidates unfeasible if the output of the synthesis method cannot be increased without diminishing either the quality or repeatability.[77] One of the most important criteria for new energy storage materials is safety, in particular for anode materials, a high operating voltage.[48] This is because at low potentials there is a serious risk of formation of lithium dendrites on the surface of the electrode, which can cause short circuits in the cell leading to thermal runaway and fire.[78] Other safety concerns include toxicity to humans and the environment throughout the entire life cycle from the mining of raw materials, the usage in energy storage devices and end of life disposal and recycling.[79,80]

One further consideration is that the behaviour of an active material in a test environment, which allows for easy comparison between different materials, can differ greatly from those conditions found in the final application, such as the large temperature increases experienced by cells undergoing high-rate energy storage and how the different thermodynamic conditions affects the energy storage capabilities of the active materials.[81]

1.2.4 Capacitance

Electrochemical capacitors, also known as supercapacitors, differ from traditional lithium ion battery technology in both fundamental charge storage mechanism and their application.[82] The most basic description of a supercapacitor is of two metal plates separated by a dielectric material and saturated in electrolyte.[83] In contrast to lithium ion batteries, supercapacitors store charge electrostatically, through the formation of a Helmholtz double layer of oppositely charged ions and electrons at the surfaces of each electrode. This results in electric double-layer capacitance (EDLC, shown in Figure 1.8).[84] The amount of charge (q) that can be stored is directly proportional to the voltage applied (V) and is calculated using the capacitance (C), surface area of the metal plate (electrode, A), the distance between the two plates (d) and the permittivity of the dielectric separator (ε) via equation 1.15.

$$q = V \cdot C = V \cdot \frac{(\varepsilon A)}{d} \qquad (1.15)$$

The energy of the corresponding capacitor is defined by equation 1.16:

$$E = \frac{1}{2} C \cdot V^2 \quad (1.16)$$

The power of the capacitor is limited by the cell resistance (R_s) and is described by equation 1.17:

$$P = \frac{V^2}{4 \cdot R_s} \quad (1.17)$$

In commercial EDLC's, the active material of choice is activated carbon printed onto current collectors.[85] The activated carbon has a very high Specific Surface Area (SSA) and consequently has a very large interface which can interact with ions dissolved in the electrolyte (Figure 1.8). The porosity of the activated carbons was found to be a useful method to increase the capacitance of the EDLC, especially when the pore size is matched to the size of the electrolyte ion.[86] Due to the electrostatic nature of the charge storage, the total energy stored is small compared to lithium ion batteries, however power achievable is far greater and the rates of charge and discharge are much faster. Examples of different activated carbons reported in literature include carbon nanotubes, graphitic carbon and coconut derived carbon.[87–89]

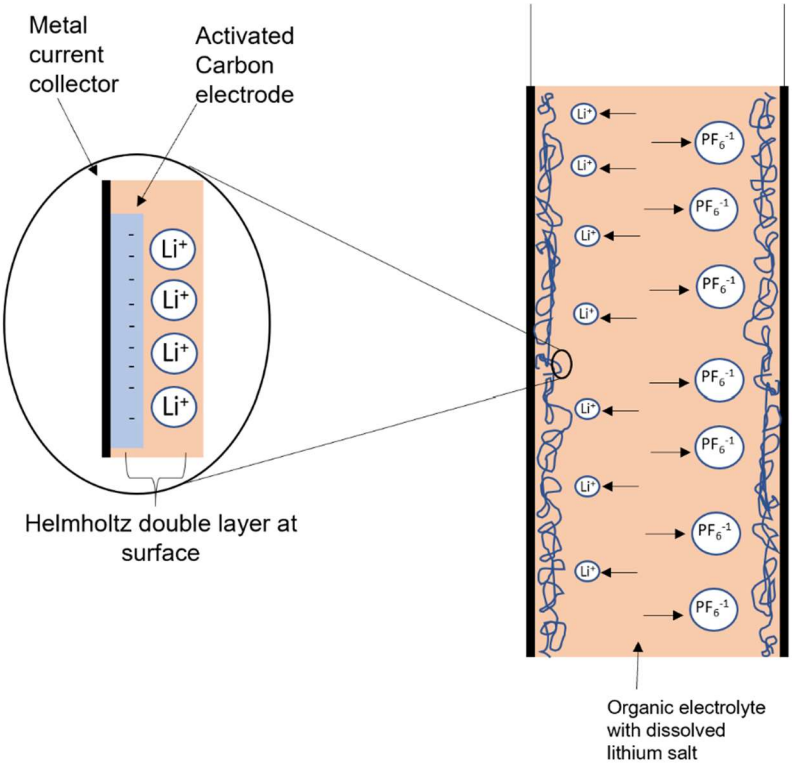

Figure 1.8: Diagram displaying the Helmholtz double layer formed at both electrode interfaces between the electrolyte ions and their opposite electric charge build up in the active material.

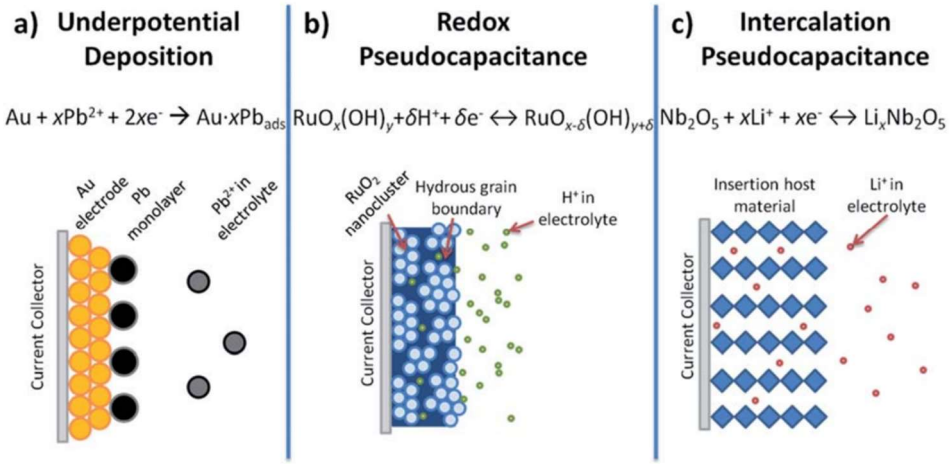

Figure 1.9: Diagram showing the different types of reversible redox mechanisms that come under the umbrella of pseudocapacitance: a) underpotential deposition, b) redox pseudocapacitance, and c) intercalation pseudocapacitance. Reprinted with permission from V. Augustyn, P. Simon and B. Dunn, *Energy Environment Science*, 2014, Royal Society of Chemistry.

1.2.5 Pseudocapacitance

The term pseudocapacitance was coined to describe a type of capacitance which involves faradaic charge transfer reactions.[90] Pseudocapacitive materials have been found to exhibit greater charge storage capabilities than Helmholtz double-layer materials, but also display far faster charge and discharge times compared to battery intercalation materials. It was observed by Conway that three different mechanisms can result in pseudocapacitive behaviour.[85] Adsorption pseudocapacitance is described as the underpotential deposition of electrolyte onto the surface of the electrode such as Pb on Au (Figure 1.9a). Redox pseudocapacitance is the adsorption of ions onto the surface of the active material followed by faradaic charge transfer reaction occurring, as depicted for RuO_2 in Figure 1.9b. Intercalation pseudocapacitance is the intercalation of electrolyte ions into layers or tunnels of the active material followed by a faradaic charge transfer reaction that does not induce a crystallographic change in phase, as described for niobium (V) oxide in Figure 1.9c.[91] The different mechanisms all display similar electrochemical signatures, such as potential response to current stimulus due to the adsorption/desorption of ions at the electrode/electrolyte interface, as is described by the Nernst equation (1.18).

$$E \sim E^0 - \frac{RT}{nF} ln\left(\frac{X}{1-X}\right) \qquad (1.18)$$

In which, E is the potential (V), n is the number of electrons involved in the redox reaction, F is the Faraday constant (96485 C g^{-1}), R is the ideal gas constant (8.314 J mol^{-1} K^{-1}), T is the temperature and X is the extent of fractional coverage of the surface.[92] The typical electrochemical features of purely capacitive, intercalative and pseudocapacitive mechanisms for both cyclic voltammetry and current application are shown in Figure 1.10a, b and c respectively.

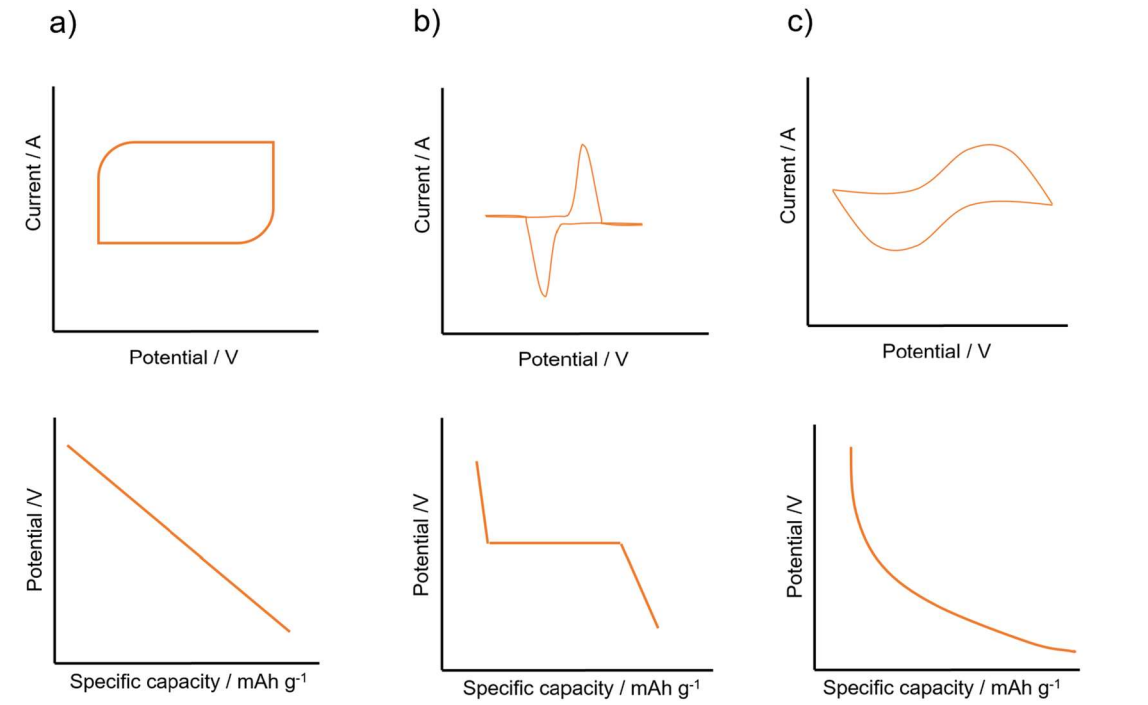

Figure 1.10: Diagram showing the typical electrochemical responses to cyclic voltammetry and galvanostatic charge/discharge cycling for a) capacitive materials, b) intercalative battery materials, and c) pseudocapacitive materials.

The shape of a galvanostatic charge/discharge curve of potential vs specific capacity for a pseudocapacitive material is not entirely linear as for a capacitive material (Figure 1.10a) and neither does it display clearly defined voltage plateaus for the two-phase transitions of battery-like redox reactions (Figure 1.10b). The result is a smooth non-linear response hence the term *pseudo*capacitance (Figure 1.10c).[93] The shape of the cyclic voltammograms further mirrors this behaviour by having very broad redox peaks and a large overall area reminiscent of a capacitor. Due to all pseudocapacitive mechanisms being located at the surface of materials, the kinetics of charge storage are not limited by solid state diffusion and thus allow for fast charge and discharge rates that are comparable to capacitor materials.[12] One further differentiation is that of intrinsic and extrinsic pseudocapacitance. Materials such as MnO_2 and RuO_2 are intrinsically pseudocapacitive, meaning they exhibit pseudocapacitance independent of any other factors.[94,95] In comparison, extrinsically pseudocapacitive materials are ones that only exhibit the requisite behaviour once a critical size of crystallite is obtained. Below this critical size, a large number of redox centres become available at the surface of the particles and can then perform fast faradaic charge transfer reactions, as well as reducing the diffusion

coefficients for electrolyte ions into intercalation materials.[96] Engineering materials to display pseudocapacitance has been well documented for V_2O_5, TiO_2 and $LiCoO_2$.[58,97,98]

Deconvolution of electrochemical behaviour to obtain a quantifiable contribution of pseudocapacitance to total charge storage is important to give insight into the physical properties occurring within active materials. For a pseudocapacitive redox process, the current response to a voltage sweep will vary directly with scan rate (v). In contrast, a diffusion-limited process will exhibit a current response that varies with $v^{1/2}$.[99] Therefore, the current response at a specific potential can be described by an adaptation of the power law to give equation 1.19.

$$i(V) = k_1 v^{1/2} + k_2 v \qquad (1.19)$$

Computing for values of k_1 and k_2 at each potential in the cyclic voltammetry permits the differentiation of diffusion-limited and capacitive current contributions as shown in Figure 1.11.[100]

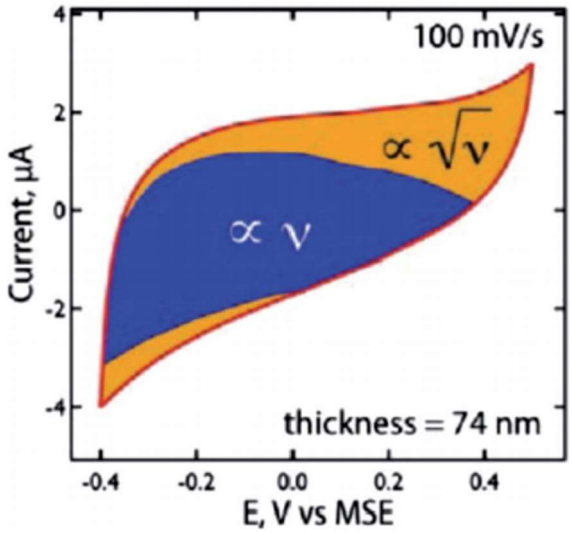

Figure 1.11: Graph of CV at 100 mVs^{-1} of Au/MnO_2 core-shell nanowires separated into capacitive contributions (shaded blue) and diffusion contributions (shaded yellow) determined from eqn. 2.19. Reprinted with permission from W. Yan, J. Y. Kim, W. Xing *et al.*, Copyright 2012 American Chemical Society.

This analysis has been reported extensively in literature to evaluate various nanomaterials. However, by itself this method cannot establish the exact mechanism of charge storage occurring and requires complimentary analytical techniques to corroborate it. A further related procedure described by Trasatti *et al.* uses equation 1.20 to describe the relationship between capacity and scan rate.[101]

$$Q = Q_{v\infty} + A(v^{-0.5}) \qquad (1.20)$$

Where $Q_{v\infty}$ is the capacity contribution of the "outer" surface of the active material at a theoretical infinite scan rate, A is the diffusion-limited capacity and is limited by $v^{-0.5}$. By plotting a graph of Q vs $v^{-0.5}$ and extrapolating the linear fit of the graph to give the y-intercept gives a value for $Q_{v\infty}$ which is reported as a percentage of the total capacity (Figure 1.12).

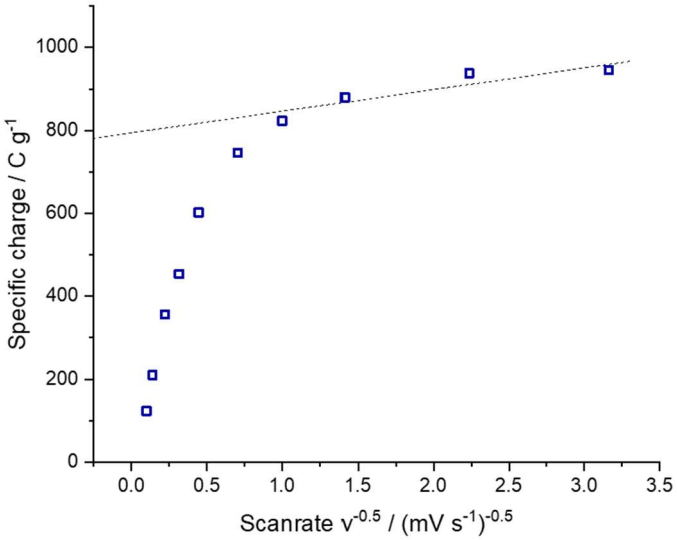

Figure 1.12: Graph of the total specific charge vs. scanrate$^{-0.5}$. with the linear portion extrapolated by a line of best fit to an infinite scan rate to give a value for the pseudocapacitive charge stored, as described in eqn. 2.20.

However, due to physical factors such as resistance at high scan rates, it is impossible to experimentally measure the capacity at scan rates approaching infinity. Further to this, this analysis requires an extrapolation of the linear portion of the data as it is not mathematically possible to fit the entire dataset with a linear function. The selection of where to apply the fit is arbitrary and at the discretion of the analyst and thus can give different values for the same material. One

further technique is based on the Cottrell equation (equation 1.21), in which current is related to charge/discharge time (t).[102]

$$i = at^{-0.5} \quad (1.21)$$

$$i = av^{b} \quad (1.22)$$

Replacing t with the reciprocal of scan rate gives equation 1.22. The premise of the equation is that b = 1 for purely capacitive contributions and b = 0.5 for diffusion-limited contributions. This method has been reported in literature for a range of materials, however it also suffers from oversimplification by separating charge-storage mechanism based on the speed of the processes. In summary, there are several methods for deconvoluting and evaluating the charge storage mechanisms from electrochemical analysis, however these types of analysis do have caveats and require more in-depth techniques to corroborate the findings and give scientifically reliable descriptions of the specific processes occurring.

1.2.6 Hybrid Capacitors

At present lithium ion batteries and electrochemical capacitors are the two principal types of electrochemical storage devices that fulfil the roles required by the consumer electronics, aerospace and automotive markets.[10] Commercial lithium ion cells can deliver specific energies of 200 Wh kg^{-1} and above, however they are only able to achieve a specific power of 350 W kg^{-1}. In comparison

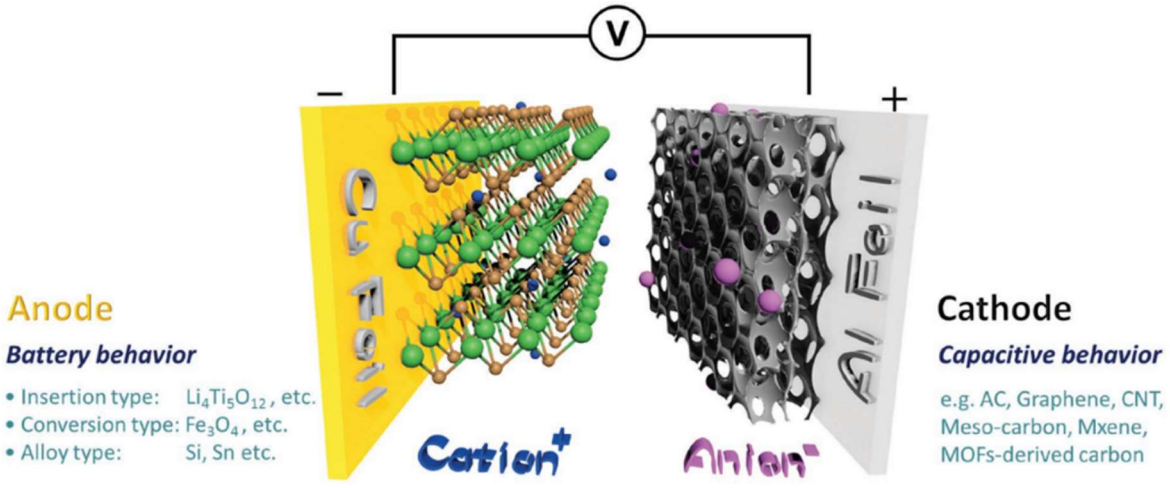

Figure 1.13: Diagram showing the structure of a hybrid capacitor cell. Reprinted with permission from H. Wang, C. Zhu, D. Chao *et al*. Copyright 2017 John Wiley and Sons.

commercially available supercapacitors can display very high specific power (up to 10 kW kg^{-1}), but are only capable of specific energies of ~5 Wh kg^{-1}.[15,103–105]

This difference in device performance has fuelled research into improving the specific power of lithium-ion batteries and increasing the specific energy of supercapacitors. One of the targets for researchers is to build a single device that can encompass both high energy and high power.[106] Hybrid Ion Capacitors (HICs) have emerged as devices that in principle can deliver energy levels in-between that of supercapacitor and a lithium-ion battery, whilst exhibiting the power levels and high cyclability characteristics of supercapacitors. Hybrid capacitors can achieve this performance by consisting of a high energy battery anode, a high power EDLC cathode and a non-aqueous lithium ion electrolyte (Figure 1.13).[107] Mechanistically charge is stored simultaneously at both electrodes asymmetrically through surface adsorption/desorption of ions at the cathode and Li^+ insertion/removal at the anode, both of these mechanisms have different optimal charge/discharge times, this can lend itself to applications which involve slow charging and fast discharging.[107] Because the different processes at each electrode are also performed in different potential ranges, the overall potential window is increased, thus increasing the overall energy density.[108]

One example of an application of HICs as energy storage devices is in the Kinetic Energy Recovery System (KERS) found in Formula One cars.[109] Regenerative braking systems such as those in high performance vehicles can also be found in heavy goods vehicles and trains. These represent a vast untapped market for HICs due to the shortcomings of the current energy storage technology available.[110] A study of the New York City train network and the potential use of energy storage devices for regenerative braking identified that the current energy cost of running a single train for a year is ~2150 GWh, equating to more than $250,000,000 (valid as of prices in 2009).[111] The study identified that despite regenerative braking being a method of dramatically reducing this cost, the current energy storage technology was unable to satisfy the exact requirements (Figure 1.14).[111] Commercial lithium ion batteries are unable to cope with the high power demands and therefore can only harvest a small fraction of the braking energy generated, which requires charge/discharge rates in the region of 18s or 200C (1C = 3600s). In contrast, commercial supercapacitors can achieve the power demands but cannot exhibit the necessary energy density and therefore

are too large by weight and volume to be space efficient or economically viable.[112] The application of lithium ion hybrid capacitors to energy recovery systems in a range of different applications has also been explored.

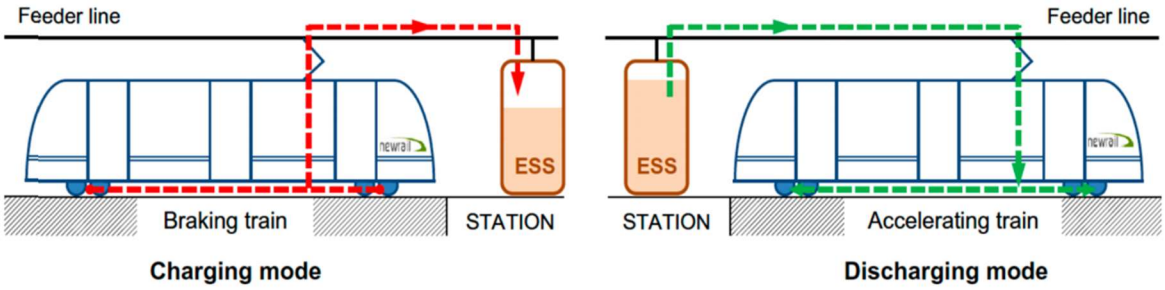

Figure 1.14: Illustration of regenerative braking for energy storage on trains. Reprinted with permission from A. Gonzalez-Gil, R. Palacin, P. Batty. Copyright 2013 Elsevier Ltd.

The typical requirements of an energy storage system for a bus include a voltage range of 700-800 V, power demands of 150 kW (10s charge/discharge) and a cycle life of over 1,000,000 cycles. When comparing a standard EDLC system and a lithium ion hybrid capacitor system for the role it was calculated that the EDLC system would be clearly outperformed on both mass and volume metrics (135 to 340 kg and 317 to 470 dm^3 respectively).[113]

In order to meet the high performance standards required by the specific applications discussed above and make the leap from laboratory to commercial production, the choice and design of a material for the anode is of critical importance.[114] An ideal anode material should have the following properties:

1) High capacity at fast C-rates. This allows for much higher current densities to be achieved by the hybrid cell by bringing the power densities that are achievable by the anode, much closer to/match those of the cathode materials.

2) High specific capacity. The higher the specific capacity of the anode material, the greater the energy density of the hybrid cell that can be achieved.

3) A low voltage plateau. This allows the maximum voltage of the hybrid cell to be higher because the anode can undergo lithiation during the charge step. A wider potential window will lead to higher overall energy density for the hybrid cell.

4) Long cycling lifetime and stability. Carbonaceous materials, such as those used in symmetric supercapacitors and the cathode materials of hybrids, show excellent long term cycling capabilities. Therefore, the anode material must also be able to exhibit good long term cycling behaviour and stability to compete with carbon-carbon supercapacitors.

5) Low cost. Due to the raw cost of carbon-based materials being so low, any alternative material candidates must not contain expensive or raw elements.

6) Simple manufacturing process. Ensuring that any manufacturing process to convert raw materials into the final anode material must be as simple and as few steps as possible. This becomes critically important once the topic of commercial production is considered.

1.2.7 Beyond Lithium-Ion Energy Storage

Other alternatives to lithium ion based energy storage devices include sodium ion batteries (NIBs) and capacitors (NICs).[107,115] The use of sodium as the charge carrier has received wide interest due to the increased abundance and accessibility on Earth, and therefore the resultant reduction in cost. NIB research is still a long way off current LIB technology with many obstacles yet to overcome, the largest being the sluggish reaction kinetics caused by the larger ionic radius of Na^+ compared to Li^+ (1.02 Å and 0.76 Å respectively). This has been cited as the cause for lower capacities, poor rate capabilities and low cycling stabilities.[116] Just like its lithium counterparts, there are the three mechanisms that dictate the ability to store charge using sodium ions. These are the intercalation, conversion, and alloying reactions. Many intercalation materials exhibit sloping voltage plateaus that are desirable for high performance energy storage, with the most researched material being hard carbon.[117,118] Again, one of the major attractions of sodium ion cell electrode materials that exhibit conversion mechanisms are the high capacities that can be observed. However, there is also the big drawback of large volume fluctuations upon sodiation/desodiation. This can lead to the pulverisation of the active material, rapid capacity loss and delamination of the active material from the current collector.[115]

One of the most interesting properties of sodium-ion battery technology is that the sodium ion (when solvated) is smaller than its lithium counterpart. This

therefore gives it faster diffusion through materials and higher ionic conductivity. It therefore gives sodium-ion technology an opportunity to compete with lithium-ion in the field of high power energy storage.[107] Research on NICs is in its infancy but is garnering high levels of interest from the scientific community. One further motivation for the development of NICs is the added safety of the cells. This is due to the fact that non-graphitic materials are used as anodes, primarily due to graphitic carbon having an interlayer spacing that is unsuitable for sodium intercalation. This reduces the risk of sodium metal plating and therefore very little risk of dendrites causing cell failure.[119]

1.2.8 Electrolytes

For lithium ion HICs, the two main electrolyte types explored in literature are aqueous and non-aqueous. Aqueous electrolytes such as $LiNO_3$ and Li_2SO_4 exhibit very low viscosity, high ion mobility and therefore high-rate capabilities. However they have a major limiting factor of low operational voltage due to the evolution of oxygen above 1.6 V.[120] The main electrolyte type is $LiPF_6$ dissolved in a mixture of organic solvents, such as ethylene carbonate (EC) or diethylene carbonate (DEC). The main benefit of organic electrolytes is the large operational voltage window which can be up to 3 V for insertion type materials and up to 4 V for conversion materials.[108]

Due to the lack of an active material containing lithium within HIC devices, the electrolyte acts as the sole source of lithium ions. This can be a cause for loss of performance as electrolyte is consumed by either parasitic side reactions or the formation of the solid electrolyte interface (SEI) in the first charge/discharge cycle.[121] To combat this, prelithiation of the anode material was developed, increasing the number of Li ions present in the device. This is achieved by inserting Li into the anode by electrochemical methods (e.g. cycling) against a Li metal counter electrode.[122] The necessity of this step to reduce capacity loss disadvantages the commercialisation of HICs as it is time consuming and difficult to scale. One approach to this problem is the use of sacrificial material that can release lithium upon the initial cycle. For example, Zhang *et al*. reported the addition of Li_2CuO_2 to the electrode slurry of the activated carbon cathode and constructed a HIC with $Li_4Ti_5O_{12}$ (LTO) anode. When cycling, the lithium copper oxide additive released Li^+ ions, thus countering the first cycle capacity loss, and producing the electronically conductive species CuO.[123]

One of the major drawbacks to the organic carbonate electrolytes is the high flammability. Ionic liquids (ILs) are defined as salts with melting points below 100 °C.[124] The majority of ILs constitute organic cations and anions which allow for flexibility in design and promotion of certain properties. ILs have been recognised as both a solvent and electrolyte as they exhibit desirable characteristics such as high thermal stability, low volatility, high ionic conductivity, and high voltage stability.

In comparison to standard organic electrolytes, ILs can offer far greater energy densities by allowing for higher operating voltages and wider voltage windows. The vast majority of IL electrolyte research has centred around their use in supercapacitors.[125] The most explored ILs are imidazolium or pyrrolidinium cations with tetrafluoroborate (BF_4), bis(trifluoromethanesulfonyl) imide (TFSI) or hexafluorophosphate (PF_6) anions.[126] This is due to both families of cations having an operating potential of >3 V and conductivities of 10 and 2.6-3.8 mS cm^{-1} respectively.[86] There are however drawbacks of using ILs as electrolytes, such as high viscosity which can affect electrode wetting, low ionic conductivity at room temperature meaning most IL devices require operating at high temperature, and high cost due to the complex synthesis process.[127] These disadvantages must be addressed in future research efforts in order to apply ILs as electrolytes in lithium ion energy storage devices.

1.2.9 Solid Electrolyte Interface

The Solid Electrolyte Interface (SEI) is a layer that forms on the surface of the electrode materials (particularly the anode) of LIBs and HICs during initial cycling. It consists of by-products formed by electrolyte decomposition.[128] The reactions that occur consume lithium from both the electrolyte salt and the lithiated cathode material, reducing overall concentration of lithium ions in the cell, causing up to 10% of the original capacity to be lost during the first full charge/discharge cycle.[129] Once the SEI layer has been formed over the entire surface of the active material, the electrode is considered “passivated” as the SEI forms a barrier between the electrolyte and the electrode surface inhibiting any further decomposition reactions.[121] The formation step primarily takes place during the first cycle, however the process continues over proceeding cycles until the layer is completely formed. This has resulted in highly complex cycling protocols for LIBs during construction.[13] The quality of the SEI layer is important because any

imperfections can cause continued decomposition of electrolyte through growth of the layer. This can cause large issues with capacity retention over long cycling lifetimes.[130] An ideal SEI layer has a very low electronic conductivity such that no further electron-transfer reactions can occur between the organic electrolyte compounds and the anode material. The SEI should also exhibit high ionic selectivity and permeability, to allow only charge carrier-ions (lithium/sodium) access through to the active material. It is also desirable for the SEI to have high stability against a range of factors and processes such as high temperatures, dissolution back into the organic electrolyte and against physical fracturing caused volume changes during cycling.[121] SEI formation usually takes a long time as the initial C-rates that form stable layers are very slow (~C/20). After these initial cycles, a range of C-rates and different temperatures are used to complete the formation process.

The extensiveness of this process is one area that could drastically reduce the cost of commercial LIBs if it could be improved.[131] Figure 1.15 shows an energetic diagram of the cathode, electrolyte and anode in a typical LIB. The electrochemical potentials of the cathode and anode materials are labelled as μ_C and μ_A respectively. The potential stability window of the electrolyte is the difference (labelled E_g) between the Highest Occupied Molecular Orbital (HOMO)

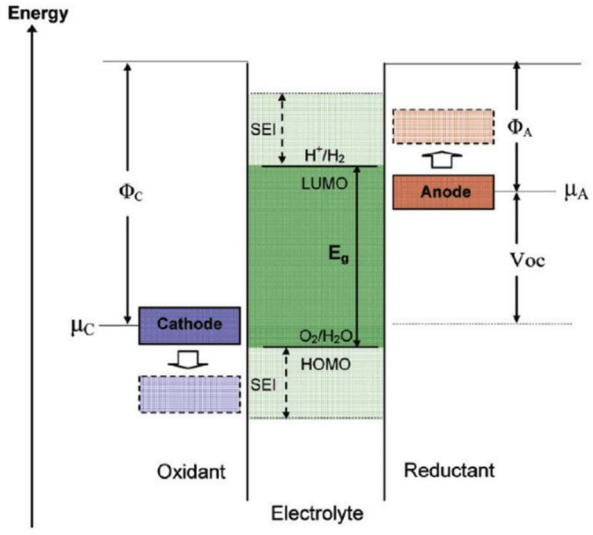

Figure 1.15: Open-circuit energy diagram of an aqueous electrolyte. Φ_A Φ_C are the anode and cathode work function. E_g is the window for thermodynamic stability of the electrolyte. The formation of an SEI layer is needed when μ_A and μ_C are greater than or lower than the LUMO and HOMO respectively. Reprinted with permission from J. B. Goodenough, Y. Kim. Copyright 2010 American Chemical Society.

and the Lowest Unoccupied Molecular Orbital (LUMO). The difference between μ_C and μ_A has to be maximised to give the cell the largest possible energy density, however if μ_C is above the HOMO then the electrolyte will be oxidised at that potential and if μ_A is below the LUMO then consequently the electrolyte will be reduced. For the most common electrolytes used currently, the oxidation potential is at ~4.7 V vs Li/Li^+ and the reduction potential is at ~1.0 V vs Li/Li^+.[121]

The composition of the SEI is critical to ensuring it has the desirable attributes for capacity retention and stability. Recent studies have shown the SEI to have a complex arrangement of insoluble inorganic salts such as Li_2CO_3, LiF and Li_2O, organic compounds such as ROLi, $ROCO_2Li$ (R = low M_w alkyl chain), esters, alkoxides, carbonates, and polymers.[132] High concentrations of insoluble salts can be found at the surface of the electrode, forming the dense layer, and more soluble organic compounds can be generally found at the electrolyte interface. The exact composition, and therefore properties of the SEI, is profoundly affected by the composition and morphology of the active material, as well as by the electrolyte solvent (Figure 1.16).[133] One particular compound that can be formed during electrolyte decomposition is hydrofluoric acid (HF). The formation of HF takes place because the PF_6^- salt can produce PF_5 gas which is a strong Lewis acid. This can then go on to react with any trace amounts of water and the organic carbonate solvent molecules to form a range of fluorinated compounds including more HF.[134] HF can then attack the SEI causing degradation, and can attack the metal oxide which releases more water that can react with more $LiPF_6$ repeating the process.[135] The generation of HF is therefore associated with serious performance loss and cell failure.[136] It has been shown that the larger the surface area of the active material , the greater is the capacity loss due to a thicker SEI layer.[137] This is one of the main issues facing the use of high surface area nanoparticles, as the extra capacity loss must be accounted for during the mass balancing of the active materials. Investigations into to combat this increased degradation and improve the SEI layer have found that electrolyte additives, such as vinylene carbonate (VC) and fluoroethylene carbonate (FEC), can polymerize during cycling and form insoluble polymers which stabilise the SEI.[138] Other methods, including a carbonaceous coating on the surface of conversion materials, can assist in reducing the volume expansion during cycling. This helps to maintain a dense un-fractured SEI layer helping to retain capacity.[52]

In general, the exact composition and nature of the SEI layer is still poorly understood, with only the presence of the major compounds and effects of certain additives or cycling profiles being confirmed by different studies.[134,139] The reasons for the lack of detailed understanding is primarily due to difficulties in analysis of the SEI layer in-situ, the huge variation in electrolyte and electrode composition, and multiple different formation pathways for the SEI.

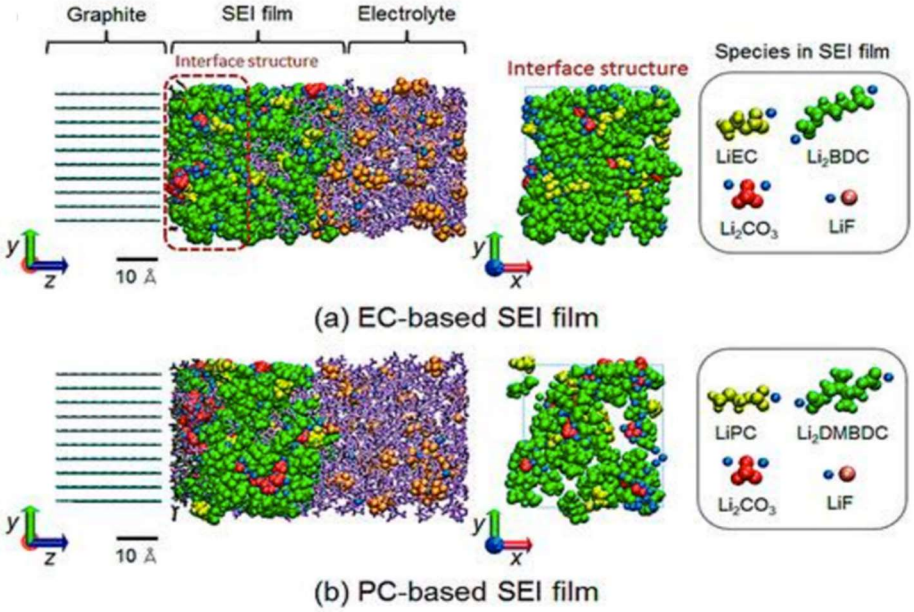

Figure 1.16: Diagram showing the role of the electrolyte solvent (EC vs PC) on the composition and structure of the SEI layer. Reprinted with permission from N. Takenaka, Y. Suzuki, H. Sakai *et al.* Copyright 2014 American Chemical Society.

1.2.10 Nanosizing of Active Materials

In order to build HICs that can fill the performance gap between supercapacitors and LIBs the development of ceramic anode materials that can exhibit very high C-rates is crucial. The nanosizing of intercalative active materials has been found to be a useful method for improving power performance, as it vastly decreases the ion diffusion path lengths and increases the specific surface area of the electrode/electrolyte interface. This causes more redox centres to be available at the surface of the particles which can decrease the time taken for charge storage.[1] Further benefits can include an increase in charge stored via extrinsic pseudocapacitive mechanisms for materials such as $LiCoO_2$,[96] as well as the suppression of two-phase transformations found in bulk materials to give smooth continuous phase transformations like those shown in Figure 1.17.[37,140,141]

The effect of nanosizing has also been shown to induce the ability to perform reversible reactions with lithium in contrast to the bulk material. The often noted example for this is for β-MnO_2.[47]

Nanosizing of anode materials has also been found to be a successful method for navigating the issues facing conversion materials.[52] These benefits include reducing diffusion path lengths which can counter low intrinsic conductivity and improve the rate capabilities. It can also promote the formation of nanosized particles of metal M during lithiation, which are very electrochemically active and

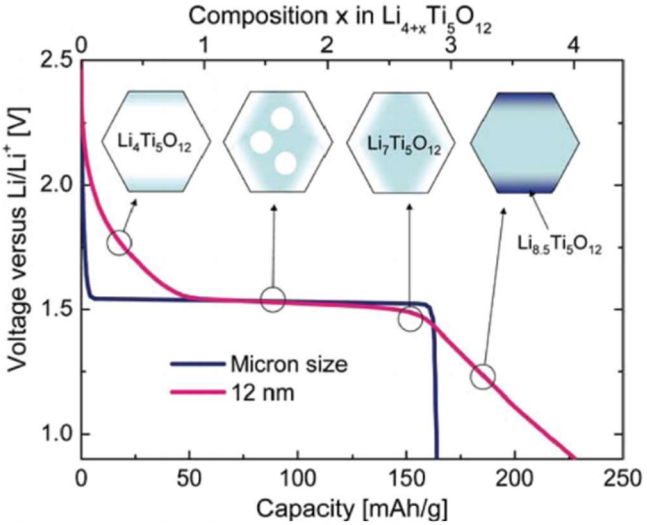

Figure 1.17: Illustration of the possible lithiation states that result in the curved voltage profile seen for nanosized LTO. Reprinted with permission from M. Wagemaker, F. M. Mulder. Copyright 2013 American Chemical Society.

increase the reversible capacity of the active materials.[29,47] Through the nanosizing of conversion materials, a series of additional structural features and modifications become available to provide advantages. One-dimensional (1D) and two-dimensional (2D) nanostructures can expedite the transport of electrons throughout the electrode, leading to improved conductivity.[59,66] The combination of nanoparticles into large 3D structures allows for the creation of very large surface areas and complex configurations of pores giving further performance improvements.[68] The introduction of negative spaces or hollow structures with nanoparticles has also been shown to counter the volume expansion experienced by conversion materials (Figure 1.18).[142] The use of carbonaceous coatings on nanosized conversion materials has been highlighted as an effective method of improving several properties of conversion materials including, the intrinsic conductivity, reducing the impact of volume changes and providing a barrier between the highly electrochemical active nanoparticles of metal M and the electrolyte thereby inhibiting the decomposition of the electrolyte through side reactions.[57,141]

However, the nanosizing of active materials does have several disadvantages. The creation of very high surface areas can have the negative effect of increasing the size of the SEI, therefore increasing the consumption of lithium. Another disadvantage is the inherently low packing density of nanomaterials as this directly impacts the volumetric energy and power densities that can be achieved This is of vital importance in commercial applications.[143] Further disadvantages include the high synthetic cost of achieving the desired level of material complexity as well as ensuring consistency between synthesis batches or over a period of time if the method is continuous.[144] Finally, the environmental toxicity of nanoparticles have also been studied and are of serious concern.[145,146]

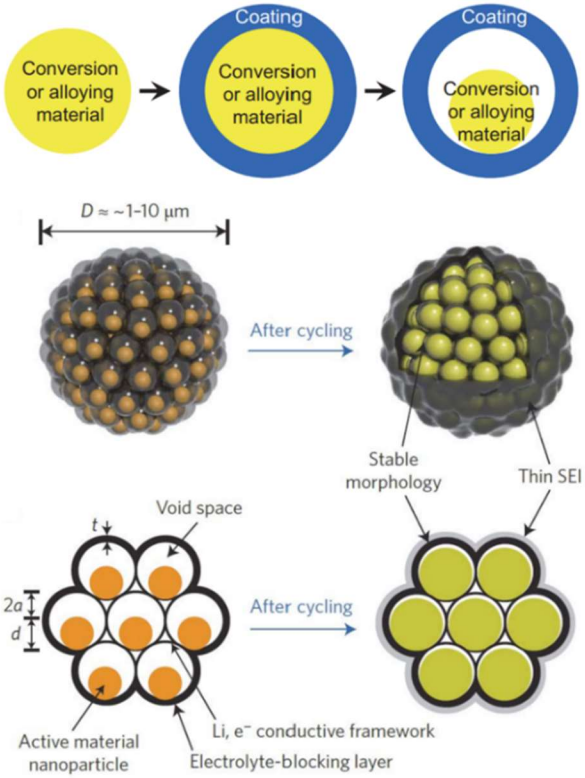

Figure 1.18: Illustrations showing the use of a nanoscale coating on particles of conversion materials to reduce the effects of pulverisation due to volume fluctuations, and surface area loss due to agglomerations. D, diameter of the pomegranate microparticle; t, the thickness of the electrolyte blocking layer; 2a, the dimension of the void; d, the diameter of the active material particles. Reprinted with permission from N. Liu *et al*. Copyright 2014 Nature Publishing Group.

1.3 Synthesis of Nanomaterials

The definition of a nanomaterial as given as a:

"Natural, incidental or manufactured material containing particles, in an unbound state or as an aggregate or as an agglomerate and where, for 50% or more of the particles in the number size distribution, one or more external dimensions is in the size range 1 nm to 100 nm.[147]

Reducing the size of energy storage to the nanoscale can cause desirable properties to be exhibited. This has spurred research interest in applying nanosizing to a wide range of different materials. These enhanced properties include increased levels of electrochemical activity due to higher numbers of active sites being present on the surfaces of the particles, increased cycling stability of particles caused by smaller levels of volume expansion and contraction, and faster reaction kinetics owing to the shorter diffusion path lengths.[29]

There are two pathways to obtaining nanosized materials. The first is the top-down method in which bulk materials are reduced in size to large particles and then to nanomaterials (Figure 1.19a). Top-down methods include mechanical grinding (where abrasive material such as zirconia balls are used in conjunction with mixing machines to break up larger particles) or lithography (where lasers are used to ablate materials to give nano structures either on the surfaces or as a distinct particles).[100,148] At present, many battery materials such as LFP are synthesised commercially using top-down methods such as Mechano-chemical activation, in which mixtures of precursors are ball-milled at high speed and then calcined in an inert or even reducing atmosphere furnace.[149,150] Almost all of the top-down methods found in literature have unsolved issues surrounding them such as high levels of waste generated, high usage of energy, issues with impurities from the milling materials and difficulties with accuracy and repeatability of particle size distribution.[151]

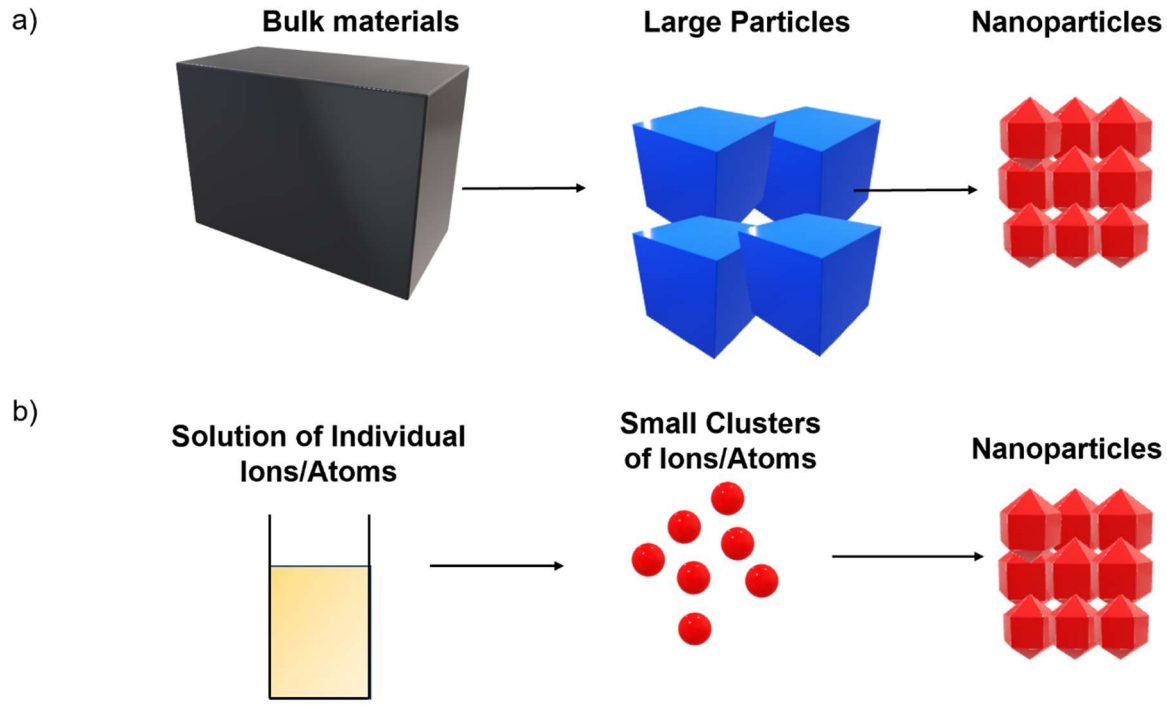

Figure 1.19: Diagram showing the two different synthesis approaches to creating nanoparticles, a) top-down methods such as mechanical milling and lithography, and b) bottom-up methods such as solvothermal synthesis.

The other strategy to the formation of nanoparticles is referred to as bottom-up (Figure 1.19b). Bottom-up techniques include precipitation, sol-gel methods, aerosol synthesis and solvothermal methods.[152–156] These methods have all presented advantages over top-down approaches due to relatively fast synthesis times, ease of scalability, ability to create complex mixed element materials and most importantly they give good control over particle characteristics such as size and morphology through easy to manipulate parameters such as temperature, concentration and pH. This is represented in industry with one of the leading cathode material producers in China using a method of solvated co-precipitation of metal sulphate salts with sodium hydroxide and ammonium hydroxide to form a metal hydroxide precursor, followed by calcination steps with lithium carbonate to synthesise LiNMC111 on an industrial scale.[80]

1.3.1 Supercritical Water and Hydrothermal Synthesis Methods

Of all the solvothermal methods explored as bottom-up techniques, hydrothermal and in particular supercritical (SC) hydrothermal methods, represent a low-cost option that has the added benefit of being far more environmentally friendly than solvothermal methods that utilise harmful organic solvents. It also offers high levels of tunability for synthesis.[157] Supercritical water is defined as a physical state of matter that exists above both the critical temperatures (T_C) and pressure (P_C) values of 374℃ and 22.1 MPa respectively.[158] Above these values, water changes from the distinct liquid and gas phases into the supercritical phase which exhibits specific properties of both a liquid and a gas. Figure (1.20) shows how the properties of water such as the density, viscosity, thermal conductivity, and isobaric heat capacity all vary with temperature at the critical pressure. As the critical temperature is neared, the density of water (ρ) decreases significantly from 1 g m^{-3} to 0.322 g m^{-3}, as does the thermal conductivity of water (*k)* from 0.6 (at 20 ℃) to less than 0.2 W/(m K) (above 400 ℃).[77,159,160]

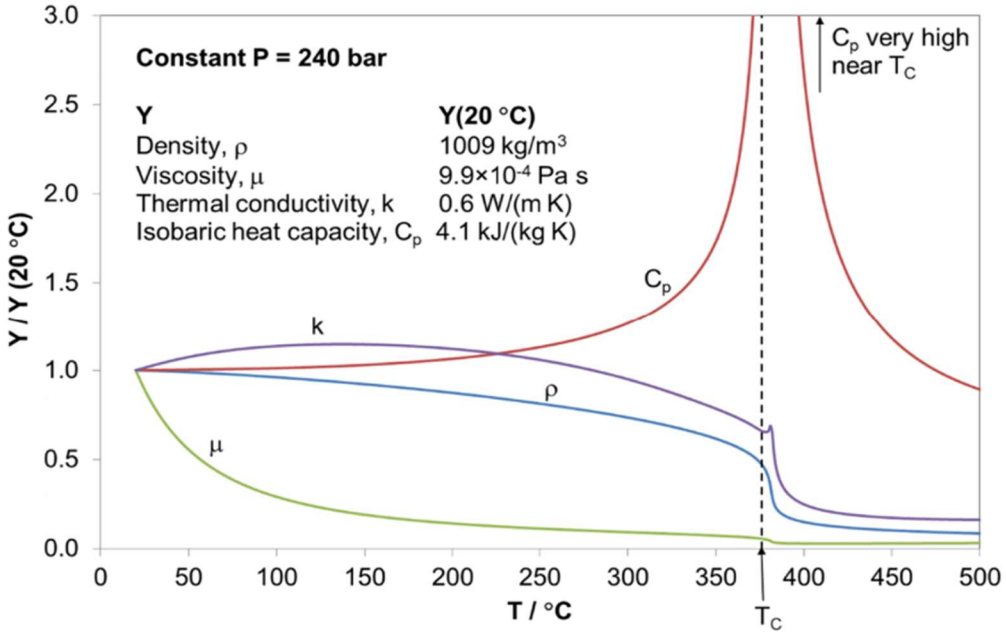

Figure 1.20: Diagram showing how the properties of water, such as isobaric heat capacity, density, viscosity and thermal conductivity, all change with increasing temperature at a set pressure. Reprinted with permission from J. A. Darr, J. Zhang, N. M. Makwana *et al*, Chemical reviews. Copyright 2017 American Chemical Society.

The isobaric heat capacity (C_p) of water is the amount of heat to be supplied to a given mass of water to in order to cause a unit change in its temperature whilst at a constant pressure.[161] The C_p of water increases slowly with temperature and then rises very rapidly to a peak as the T_C is approached. As the temperature increases further this property decreases back down to normal levels (Figure 2.27a). When the temperature reaches and crosses the critical point the normal hydrogen bonds within the water break down causing the dielectric constant decrease from 80 to 5 m^{-1}. These properties render SCH_2O unfavourable for the solvation of aqueous inorganic salts such as nitrates or sulphates. One of the key elements in the production of nanomaterials using hydrothermal processes is supersaturation.[162] Supersaturation is the ratio of the concentration of a solvated species to the saturation concentration. When this is maximised, it can increase the rate of nanoparticle synthesis and also the number of nuclei formed, thereby decreasing the final particle size.[163] A further property of SCH_2O that lends itself very well to nanoparticle synthesis is the variation of the ionic product of water with temperature (K_w described in equation 1.23).

$$K_w = [H^+][OH^-] \quad (1.23)$$

In which, the concentration of protons and hydroxide ions are both equal to 1 X 10^{-7} mol dm^{-3}. This gives a value of 14 for the pK_w at room temperature (equation 1.24).

$$pK_w = -log_{10}K_w \quad (1.24)$$

When water transitions to supercritical, the value of pK_w decreases to 11, which equates to approximately a 30-fold increase in the prevalence of both hydrogen and hydroxide ions in solution, therefore creating a far more hydrolysing environment.[164] The reactions taking place at the interface between metal salts and solvent can be simplified as a series of hydrolysis and dehydration reactions:

$$M(NO_3)_{x(aq)} + xH_2O \rightarrow M(OH)_{x(s)} + xHNO_3 \quad (1.25)$$

$$Dehydration: M(OH)_{x(s)} \rightarrow M(O)_{x/2(s)} + \frac{x}{2}H_2O \quad (1.26)$$

As well as these reactions, there are a multitude of other reactions taking place such as the decomposition of anions, or the partial hydrolysis/dehydration to form metal oxyhydroxides.[157]

The LaMer model, first developed in the 1950s, describes the synthesis of nanoparticles from solution. It separates particle synthesis into nucleation and growth phases through the concept of burst nucleation, in which all the nuclei are generated instantaneously and then grow without the need for any further nucleation to occur.[165]

A graphical representation of the model is shown in Figure 1.21. It can be explained as follows:

- (I) The concentration of ions (monomers) is increasing and after a certain period of time reaches critical supersaturation (C_s), at this concentration level nucleation becomes possible.
- (II) Beyond this point the saturation increases, passing the minimum level at which the activation energy for nucleation is overcome (C_{min}) and reaching the maximum critical limit of supersaturation (C_{max}) at which point nucleation rapidly occurs.
- (III) Due to the nucleation occurring, the supersaturation level decreases immediately below C_{min} thus ending the nucleation period.
- Growth can then occur via multiple different mechanisms such as the remaining ions (monomers) in solution diffusing towards the more thermodynamically stable nuclei. This is known as Ostwald ripening, in which very small nuclei that have the ability to dissolve can be redeposited onto the surface of larger nuclei, or through the coalescence of nuclei to form larger particles.[166]

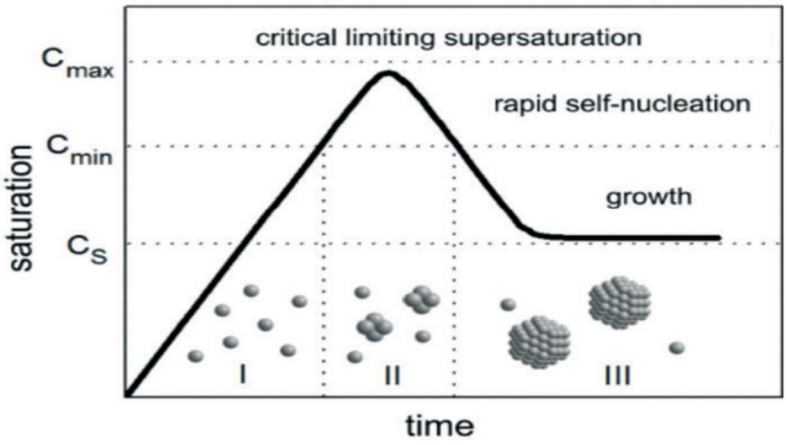

Figure 1.21: Diagram of the LaMer model of nanoparticle nucleation and growth. Reproduced from J. Polte, *CrystEngComm*, 2015, with permission from the Royal Society of Chemistry.

1.3.2 Continuous Hydrothermal Flow Synthesis

Continuous Hydrothermal Flow Synthesis (CHFS) is an environmentally-friendly method that utilizes supercritical water and very short reaction times to synthesise a wide range of different nanomaterials.[157] By varying different parameters such as concentration of reactants, temperature and residence time, CHFS can give good control over the characteristics displayed by the nanomaterials including particle size distribution and morphology.[143] The major benefits to the CHFS process are the ease of synthesising doped or mixed materials, the use of water as a green solvent, the scalability of the synthesis (g/hr to kg/hr) and the high yields that can be achieved (>90 %).[168]

The typical CHFS process involves superheating water under high pressure (240 bar) to above the critical temperature (450 ℃) to create a very hydrolysing environment. This is then fed into a stream of ambient aqueous solvated metal salts. The rapid change in temperature, highly hydrolysing environment, short reaction times and high turbulence are all properties that lend themselves to synthesising nanomaterials.[157] Using these techniques a wide range of different nanomaterials for various applications have been successfully synthesised, such as metal oxides, sulphides, hydroxides, oxyhydroxides and elemental metals.[156,169–172]

Due to the sensitivity of material characteristics on different parameters, the design of the mixing point of a CHFS process is very important to give the desired materials with high reproducibility. Many different types of mixer design have been tried and tested over the years including, T-shaped, Y-shaped, cross shaped, counter current and co-current (Figure 1.22).[157] The mixer design used in this thesis was solely the coaxial or confined jet mixer (patent GB1008721) (Figure 1.23). The advantages of this design include instantaneous mixing of the SCH_2O and room temperature precursor feeds and higher flow rates of the SCH_2O feed are achievable. This can increase the temperature at the mixing point far above the critical temperature (350 ℃). The design also allows for the placing of a second mixer in series. This can be used to add water to quench the temperature of the solution and therefore the reaction or to add capping or coating agents to the feed.[173]

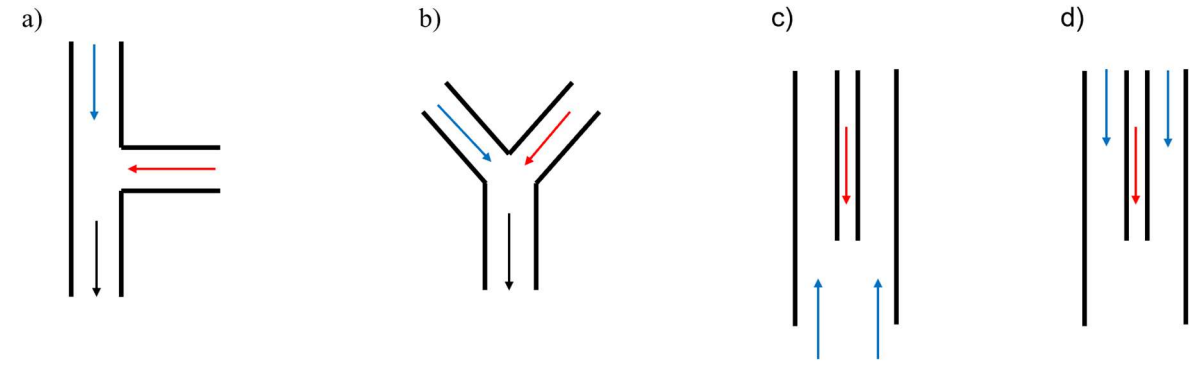

Figure 1.22: Simplified diagrams of mixers used in CHFS with the SCH_2O (red arrows), and metal salt (blue arrows) flows highlighted, a) T-shaped mixer, b) Y-shaped mixer, c) counter-current mixer and d) co-current mixer.

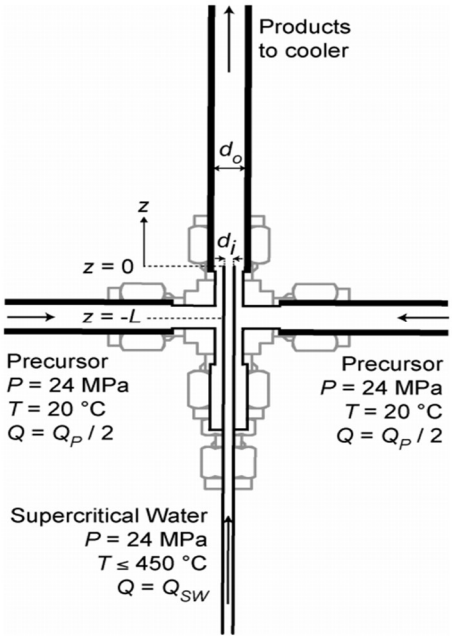

Figure 1.23: Diagram showing the geometry of the confined jet mixer. Reprinted with permission from R. I. Gruar, C. J. Tighe, J. A. Darr, *Industrial & Engineering Chemistry Research*. Copyright 2013 American Chemical Society.

1.3.3 CHFS for Combinatorial Materials Synthesis

In the pursuit of ever greater materials discovery capabilities, the concept of combinatorial synthesis offers a method of casting a wide net over an area of interest, synthesising a wide range of compositionally related materials, and rapidly evaluating them for structure/performance relationships. Due to the use of water-based metal salt precursors, CHFS has been successfully applied to combinatorial studies for the discovery of electrochemically active materials.[174] Several examples of this can be found where a ternary plot of composition is used to synthesise a range of different materials and then electrochemical performance metrics or physical properties can be overlayed to identify areas of compositional space of interest: such as the 66-sample complete ternary diagram for $Ce_xZr_yY_zO_{2-\delta}$ that was synthesised in less than twelve hours using a High-Throughout CHFS reactor.[175] The ceramic materials were then subjected to a heat treatment and analysed using the robotic beamline I11 at the Diamond Light Source for high resolution X-ray diffraction data. From this, the phase information for each material, as well as the variation in unit cell volume with composition and the relative crystallite size, were plotted (Figure 1.24).

Johnson *et al*. showed another example of using phase diagrams with CHFS to investigate composition-structure-performance relationships, where a range of different compositions of carbon coated V- and Fe- doped $LiMnPO_4$ were synthesised via CHFS and tested as high voltage cathode materials (Figure 1.25a).[176] It was shown that the variation in unit cell volume was smooth with respect to composition and decreased as more iron and vanadium were doped into the material. The specific capacity was measured at both low (C/2, Figure 1.25c) and high (5C, Figure 1.25d) charge/discharge rates, and it was shown that a 20 % doping of Fe gave the highest cycling capacities at all C-rates.

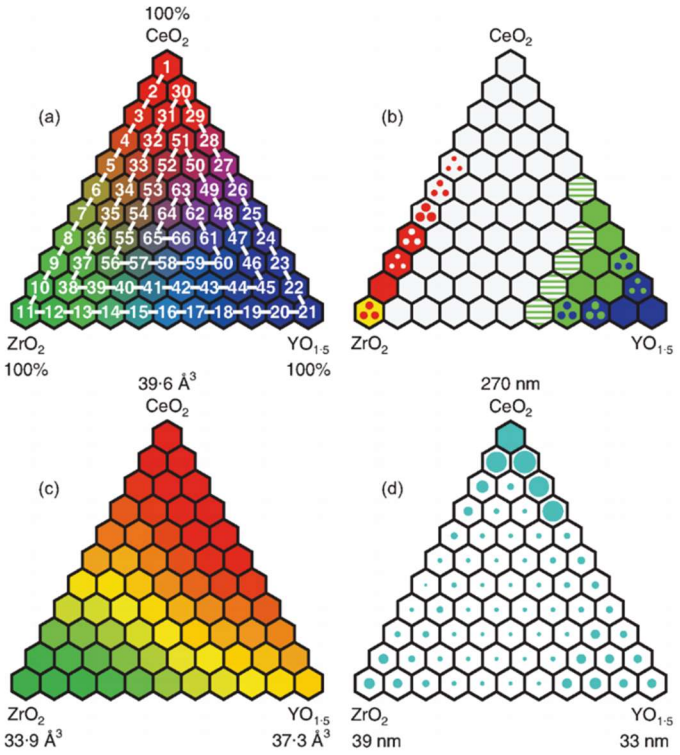

Figure 1.24 (a): The compositional space for the mixed $Ce_xZr_yY_zO_{2-\delta}$ (for $0 \leq x, y, z \leq 1$) materials, with the sample numbers and direction of synthesis indicated. Each hexagon represents a single sample and the relative ratios of Ce, Zr and Y are proportional to the amount of red, green and blue colours respectively. (b) The different crystal phases identified by PXRD, fluorite (grey), monoclinic zirconium oxide (ZrO_2, yellow), tetragonal zirconium oxide (ZrO_2, red), bixbyite (blue) and a 2x2x2 pseudo-Y_2O_3 fluorite superstructure that has oxygen-vacancy ordering (green). Single colour hexagons indicate a single-phase material, three dots indicate two-phase behaviour, and stripes indicate a single-phase region with a smooth transition between the fluorite and the 2x2x2 fluorite superstructure. (c) Lattice parameter information regarding mean volume per unit ($MO_{2-\delta}$) displaying a smooth pseudolinear variation with composition. The volume at each nominal point can be approximated with the linear equation $V = 40.3x + 33.5y + 37.5z$. (d) The relative crystallite sizes calculated from the Scherrer equation and shown proportionally by the size of the blue circles. Reprinted with permission from X. Wang et al. J. Comb. Chem. Copyright 2013 American Chemical Society.

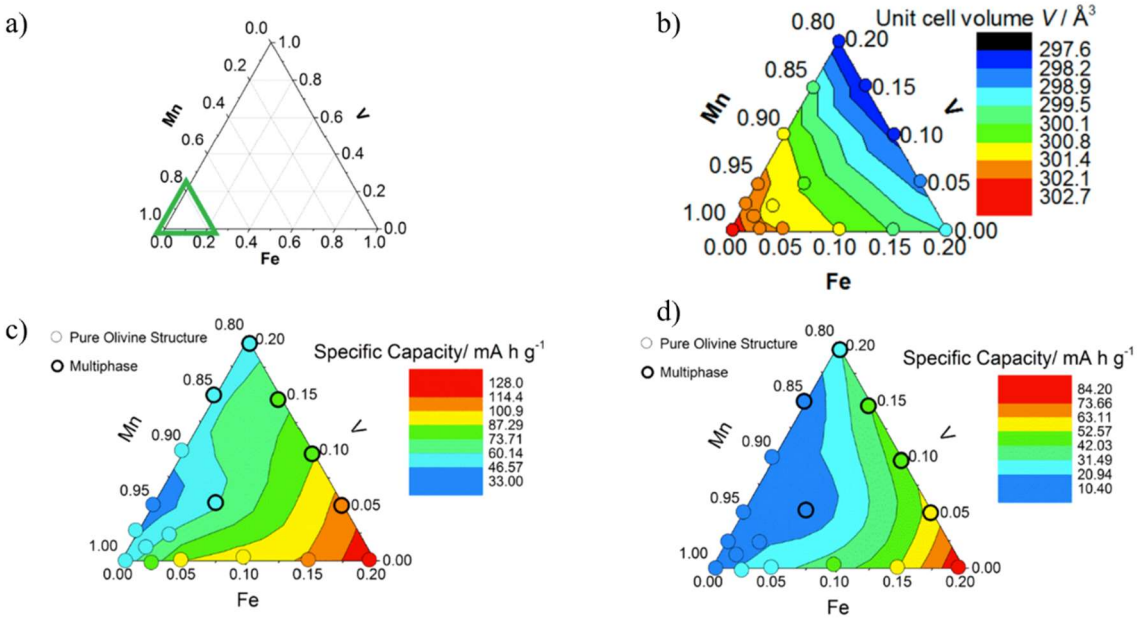

Figure 1.25 (a): Ternary phase diagram of $LiMn_{1-x-y}Fe_xV_yPO_4$ with the compositional area investigated shown with a green triangle. (b) The unit cell volume for each material overlayed as a heat map onto the green triangle area. (c) Specific capacity values at C/2 cycling shown as a heat map. (d) Specific capacity values at 5C cycling shown as a heat map. Adapted and reprinted with permission from I. D. Johnson *et al. ACS Combi Chem*, https://pubs.acs.org/doi/10.1021/acscombsci.6b00035. Copyright 2016 American Chemical Society. Further permission related to this material excerpted should be directed to the ACS.

2.0 Characterisation Methods and Materials

'*If I have seen further, it is by standing on the shoulders of giants*' – Isaac Newton

2.1 Physical Characterisation of Materials

2.1.1 Powder X-ray Diffraction (PXRD)

Powder X-ray diffraction (PXRD) is a technique used to give structural information about the crystal system(s) present in a sample of powdered material. The fundamental basis of PXRD is that an incident beam of electromagnetic radiation is shone at a sample of powdered material, the atoms in that material will cause scattering of the radiation and by interference (constructive or destructive) of the radiation yield information regarding the position of planes of atoms within the partially crystalline powder due to the relationship between the angle of the radiation and the spacing between lattice planes as described by Bragg in the early 20th Century (equation 2.1).[177]

$$2d_{hkl} \cdot sin(\theta) = n \cdot \lambda \quad (2.1)$$

In which, d_{hkl} is the distance between two parallel *hkl* lattice planes, *n* is the number of lattice planes and λ is the wavelength of the incident X-ray radiation. Reflection of the radiation only occurs when the Bragg equation conditions are met. The radiation collected is then converted to give an XRD pattern with intensity vs 2θ angle.[178] These patterns are unique to each different crystal system that exists and are used to identify unknown materials by comparison to databases of known patterns such as the Inorganic Crystal Structure Database (ICSD).

Further information can be extracted from the PXRD patterns such as domain crystallite size using the Scherrer equation:

$$d = \frac{K \cdot \lambda}{\beta \cdot cos\theta} \quad (2.2)$$

Where *d* is the domain crystallite size (nm), *K* is a shape factor that ranges from 0.86 to 0.98 and is most commonly approximated to be equal to 0.9, λ is the wavelength of the incident radiation (MoKα = 0.7097 Å),θ is the Bragg angle and β is the full width at half maximum (FWHM) of the peak in question.[179,180]

Powder x-ray diffraction patterns of all powders synthesised was performed on a STOE StadiP diffractometer (Darmstadt, Germany) utilising MoKα radiation (λ = 0.7107 Å). The patterns were typically collected between 2θ values of 2 – 40°, with a step size of 0.5° and a step time of 10 s. Peak fitting was performed by Fityk software (version 1.3.1).[181] Phase identification was performed on the collected diffraction patterns by Match! Software (Crystal Impact, Germany, version 1.11h) on a PDF-2 database created by the International Centre for Diffraction Data. Structural models of the materials were created by Visualisation for Electronic and Structural Analysis software (VESTA, version 3.4.8, copyright Koichi Momma and Fujio Izumi).[182]

Structure solution and refinement from diffraction patterns is a technique that is used to calculate the atomic or molecular structure from the peak intensities and positions. The method used herein is the Le Bail whole pattern method, performed by Reitica software (version 4.0).[183] In which, an iterative method of least squares is used to fit and refine parameters for the unit cell, peak width and other shape factors.

2.1.2 X-ray Fluorescence Spectroscopy (XRF)

X-ray Fluorescence Spectroscopy (XRF) is a non-destructive technique for quantitatively determining the elemental composition of materials in either the solid, liquid or powder forms and with a sensitivity up to ppm level.[184] In XRF, the sample is irradiated with incident radiation photons which when they reach the atoms present in the material can, if they are of the right energy, expel an electron from one of the innermost electron shells (such as the K-shell) creating a hole. This puts the atom into a higher energy excited state, to fill the hole and restabilise the atom, an electron from a higher energy shell (such as the L-shell) transfers to fill the hole (Figure 2.1). This L-shell electron has a higher energy than the hole that it is filling, and the excess energy is released as an X-ray photon and is picked up by the detector and is seen as a line on a spectrum. Because there are specific differences between the energy levels of the shells of different elements, the energy of the photon is characteristic of the atom from which it came. The combination of the different lines from the different electron transitions occurring in each atom can give a fingerprint for each element which is then combined with

the intensities to give quantitative analysis of the elemental composition of the sample being analysed. The quantitative analysis of the elements present in the materials synthesised in this thesis was performed by a Panalytical Epsilon 4 (Malvern, UK).

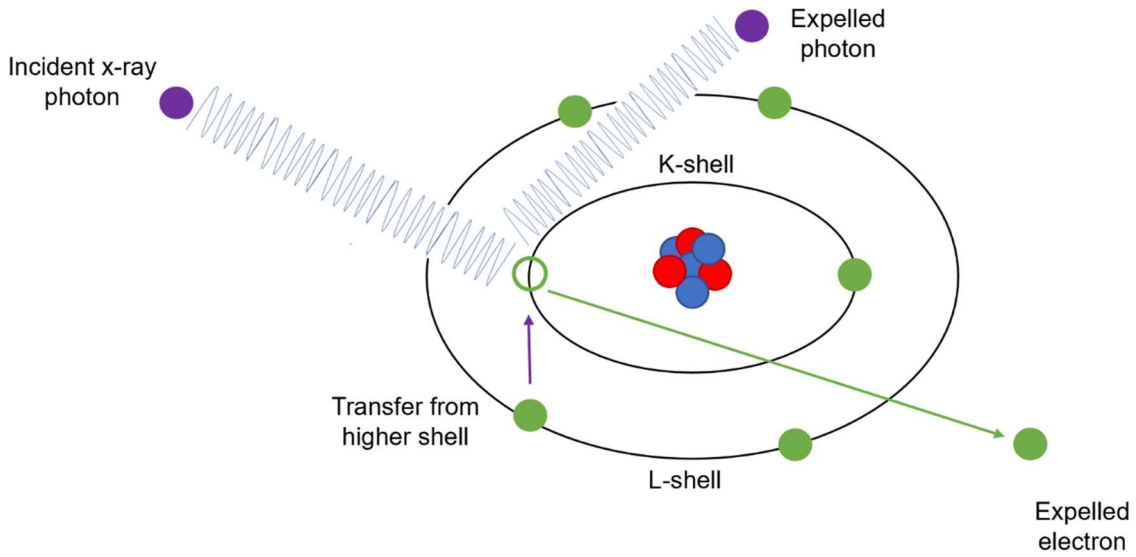

Figure 2.1: Diagram showing the process that enables XRF, including the expulsion of an inner shell electron by an incident x-ray photon, the transfer of a higher shell electron to fill the hole and the resulting photon of excess energy released.

2.1.3 X-ray Photoelectron Spectroscopy (XPS)

X-ray photoelectron spectroscopy (XPS) is a non-destructive, quantitative technique that is used to determine the elemental composition and electronic state of the chemical species of the materials analysed. In XPS, an incident x-ray photon penetrates the material and excites an electron in a low energy shell of an atom, this excited electron is expelled out of the material and into the vacuum where it is detected. From this the binding energy ($E_{binding}$) of the electron can be calculated using equation 2.3. In which, E_{photon} is the energy of the incident x-ray photon, $E_{kinetic}$ is the measured energy of the detected electron and Φ is the minimum energy required to release an electron from a solid into a vacuum that is directly above the surface (also known as the work function).[185]

$$E_{binding} = E_{photon} - E_{kinetic} - \Phi \quad (2.3)$$

Because the specific oxidation state of the element will directly influence the binding energy of the electrons, the electronic state and local environment can be determined. Due to the technique requiring the penetration of the incident x-rays, the excitation of the electrons and the detection of emitted electrons, the probability of a photoelectron being generated as you travel further from the surface of the material decreases. This means XPS can only analyse up to 1-10 nm from the surface of the material. For the materials in this thesis, XPS was performed by a Thermo scientific K-alpha™ Spectrometer using Al-Kα radiation (1486.6 eV). High resolution scans for elements were performed at 50 eV. Analysis and peak fitting were performed by CasaXPS software (version 2.3.16) with the C1s peak calibrated to 284.8 eV. Powder samples were affixed onto double-sided carbon tape and vacuumed down to a chamber pressure below 1 $x10^{-8}$ torr.

2.1.4 Raman Spectroscopy

Raman spectroscopy is a non-destructive technique that is used for the identification of materials by measuring the specific vibrational modes of molecules.[186] In Raman spectroscopy, a monochromatic light source from a laser is shone at the sample, the photons emitted interact with the molecular phonons or vibrational modes of the material and excite them to virtual energy states (Figure 2.2). The relaxation back to the vibrational energy states emits photons which are detected. The vast majority of the vibrational states are excited and then relax back to the same state, emitting a photon of the same energy, this is known as Rayleigh scattering. However if the vibrational energy states are not the same, either higher (known as Stokes Raman scattering) or lower (known as anti-Stokes Raman scattering) than the initial energy state then the wavelength of the photon is subtly shifted.[187] This shift in energy is directly related to the difference in energy states of the molecule and therefore gives information about the specific energy states of the molecule and can be used to create a fingerprint spectrum and to identify materials.

Raman spectroscopy was performed on the materials in this thesis using a Renishaw *inVia*™ Microscope with a 514.5 nm wavelength laser set to full power. Scans were collected over the range 3200 to 100 cm^{-1}.

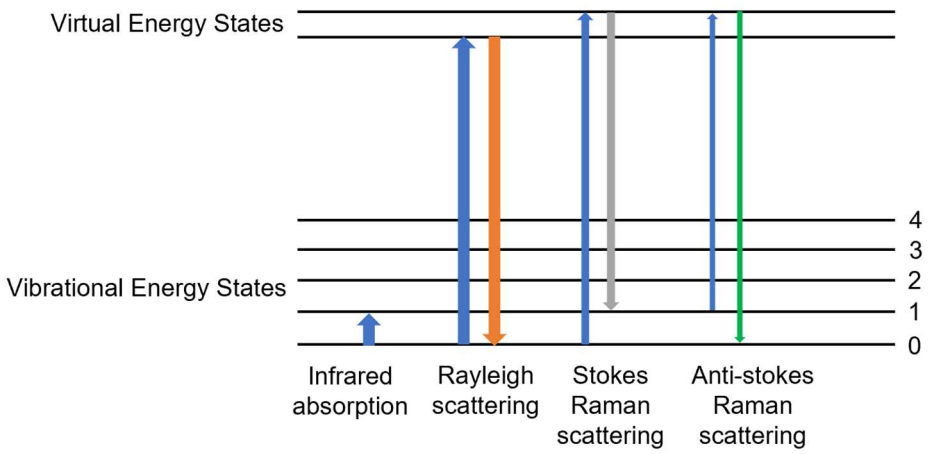

Figure 2.2: Diagram showing the different types of scattering that occur during Raman spectroscopy.

2.1.5 BET Surface Area and BJH Pore Size Distribution

Brunauer-Emmett-Teller Specific Surface Area (BET-SSA) is a technique used to measure the specific surface area of materials using the adsorption and desorption of gas molecules. In a BET measurement, nitrogen gas is adsorbed and desorbed onto/from the surface of a solid material at a range of different pressures at a constant temperature of 77K to create an isotherm. To calculate the SSA, the nitrogen molecules must adsorb onto the surface in discrete layers that do not interact with each other.[188] The BET equation for adsorption is shown below in equation 2.4, in which P is the equilibrium pressure, P_0 is the saturation pressure, n_{ad} is the quantity of adsorbed nitrogen, n_m is the monolayer adsorbed quantity of nitrogen. C is the BET constant which is calculated by equation 2.5, in which E_1 is the heat of adsorption of the first layer and E_L is the heat of vaporisation.[189]

$$\frac{P}{n_{ad}(P_s - P)} = \frac{1}{n_m C} + \frac{C-1}{n_m C} \cdot \frac{P}{P_0} \tag{2.4}$$

$$C = \exp\left(\frac{E_1 - E_L}{RT}\right) \tag{2.5}$$

$$S = \frac{v_m N s}{V \cdot m} \tag{2.6}$$

From the adsorption isotherm plot, the slope and intercept give values for C and n_m respectively. Taking these values and inputting them into equation 3.4, combined with the knowledge that a single molecule of nitrogen has a cross-sectional area of 0.162 nm^2, allows for the calculation of the SSA. In equation 2.6, v_m is the volume of adsorbed nitrogen, N is Avogadro's number (6.02214 x 10^{23} mol^{-1}), m is the mass of the material, V is the molar volume of the adsorbed nitrogen, s is the adsorption cross-section of nitrogen and S is the specific surface area (m^2 g^{-1}). BET measurements were performed by a Micrometrics Tristar II using liquid nitrogen. All materials were degassed at 120 ℃ for 2 hours under a flow of nitrogen.

Barrett-Joyner-Halenda (BJH) pore size distribution is a technique that is used to estimate the pore sizes and their distribution across the material. The BJH theory is built on the isotherms of physisorption equilibrium and has two central assumptions, the first being that the shape of the pores is cylindrical and the second that the quantity of adsorbed nitrogen gas results from the physisorption onto both the pore walls and capillary condensation in mesopores.[190] The Kelvin equation (2.7) is used to calculate the meniscus radius, BJH uses this and the sum of the multilayer thickness to calculate the radius of the pore.[191]

$$\ln\left(\frac{P}{P_0}\right) = \frac{2\gamma V_m}{rRT} \qquad (2.7)$$

In which, P/P_0 is the relative pressure of the meniscus in equilibrium, γ is the surface tension of nitrogen in the liquid phase, V_m is the molar volume of the liquid, r is the radius of the meniscus formed inside the mesopore, R is the universal gas constant and T is temperature. BJH uses the decrease in relative pressure from the desorption isotherm to calculate the change in the thickness of adsorbed film. Each decrease is considered to result from evacuation of adsorbate from the largest pores from the capillary condensate and a reduction in the thickness of the physisorbed layer. All of this theory yields a complex equation that is solved iteratively usually by computation.[190]

Several limitations of the BJH method have been identified, such as the inability to describe the diameter of micropores and narrow mesopores and the effect of pore networks on the calculated values.[192]

All BJH measurements were performed by a Micrometrics Tristar II using liquid nitrogen. All materials were degassed at 120 ℃ for 2 hours under a flow of nitrogen.

2.1.6 Scanning Electron Microscopy (SEM)

Scanning electron microscopy (SEM) is an electron microscopy technique, in which a beam of electrons (primary) replaces the beam of visible light in normal microscopes. The electron beam is focused through a range of aperture and lenses onto a sample where they collide with weakly bonded electrons in the outer shells of atoms causing them to be knocked out and detected as secondary electrons. The angle of detection and the yield of secondary electrons will be dependent on how smooth the surface is, with more electrons being generated from rougher surfaces. The samples are first sputtered with a very low amount of conductive substrate, such as gold, to make them more conductive and to improve the images. This technique is used to observe and measure the surface and topography of large particles through the collection of images.

Field emission gun scanning electron microscopy (FEG-SEM) was used to collect images of the materials in this thesis using a JEOL JSM-6701 microscope.

2.1.7 Transmission Electron Microscopy (TEM)

Transmission electron microscopy (TEM) is another electron microscopy technique used to image materials in high detail. The fundamental difference between TEM and SEM is that in contrast to SEM detecting electrons which have been knocked off, TEM measures the electrons that have been transmitted through the sample to create images.[193] This allows for much higher resolutions and magnifications of images and is used for the measurement of lattice spacings.

High-resolution transmission electron microscopy (HR-TEM) was performed by a JEOL JEM 2100 using a LaB_6 filament. All samples were dissolved in methanol and sonicated before pipetting onto carbon coated copper film grids (300-mesh, Agar Scientific, UK). A Gatan Orius digital camera was used for image capture and Gatan Microscopy Suite software for analysis of the particle sizes and d-spacing of lattice planes. Sample preparation involved dispersion of powder in methanol by ultrasonication for 10 minutes, then pipetted onto 300-mesh copper film grids and air dried.

2.1.8 Energy Dispersive X-ray Spectroscopy (EDS)

Energy dispersive x-ray spectroscopy (EDS) is an analytical technique that is used alongside HR-TEM for elemental identification and quantification. It operates on a similar principle to XRF, in that the incident beam of electrons collides with electrons in the atoms of the crystal lattice causing them to be ejected. To fill this hole, electrons from higher energy shells drop down the lower energy level with the excess energy released as x-rays. Due to the difference between energy shells being specific to the element, the x-rays collected can be used to identify which elements are present in the sample. The number of x-rays that are collected can be used to quantify the relative amounts of each element present in that bit of the material under analysis. By overlaying the EDS results with HR-TEM images, a spatial map of elemental distribution across particles can be created.

EDS was performed on the materials in this thesis using the JEOL JEM 2100 also used for HR-TEM with an Oxford Instruments detector.

2.1.9 CHN Analysis

CHN analysis is a technique that is used to quantify the relative amounts of carbon, hydrogen, and carbon present in a sample. Milligram amounts of each sample are subjected to flash combustion which instantaneously oxidises the sample into simple products. These are then passed through a reduction furnace and into a chromatographic column where they are separated, detected, and quantified by a Thermal Conductivity Detector (TCD). CHN analysis was performed by the Geology department, University of Edinburgh. A Thermo Fisher Scientific Flash SMART instrument was used with a prepacked quartz reaction tube, an oven temperature of 60 ℃, a furnace temperature of 950 ℃, a run time of 600 s and a TCD detector.

2.2 Electrochemical Cells

2.2.1 Electrode Manufacture

The formation of electrodes is as follows: the metal oxide active materials were mixed with conductive carbon powder (Super P™, Sigma Aldrich, UK) and a pre-dissolved 10 wt.% solution of polyvinylidene fluoride (PVDF) in N-methyl-2-pyrrolidone (NMP, Sigma Aldrich, UK) in the mass ratio of 80:10:10 respectively. To the mixture, additional NMP (1.25 ml for every 0.4g of active material) was added to decrease the viscosity, the mixture was then ball-milled with 10 zirconia balls for 1 hour at 1000 rpm (Pulverisette 7, Germany). The resulting slurry was spread onto either copper (9 μm thickness, PI-KEM, UK) or aluminium foil (15 μm thickness, PI-KEM, UK) using a doctor blade (PI-KEM, UK). The foil sheets were then dried on a hotplate at 80℃ until visibly dry inside a fume hood. Discs of either 15 or 12 mm diameter were cut using a dye and press (PI-KEM, UK). The cut discs were dried overnight in a vacuum oven at (40℃) to remove any remaining moisture.

The activated carbon electrodes used as cathodes in HICs and as both electrodes in symmetrical EDLCs were manufactured by WMG (Warwick Manufacturing Group, UK). YP50F activated carbon powder (Kuraray Chemical Co., Japan) was mixed with Super P™ conductive carbon and PVDF in NMP solution in the mass ratio 87:5:8 respectively. The slurry was mixed by a high torque mixing unit to give a smooth slurry. This was coated onto aluminium foil using a Magtec reel-to-reel coater. The electrodes were dried in a three-phase oven which utilised a vacuum and 120℃ to remove any moisture or NMP solvent that remained.[194] The electrode sheets were printed to a thickness of 100 μm, 15 and 12mm discs were cut using a dye and press (PI-KEM, UK) and were found to have a mass loading of ~3.5 mg cm^{-2}.

2.2.2 Cell Construction

The electrode discs were transferred to an argon filled glovebox (MBraun, Germany) in which the oxygen and water levels were kept below 0.1 ppm. Half cells of lithium were made using CR2032 coin cell components (PI-KEM, UK) and glass microfibre separators (Whatman®, Grade D, US). The glass microfibre separators were soaked in electrolyte. Figure 2.3 shows the expanded construction of a coin cell. The Top case was followed by the metal oxide foil electrode, then a glass microfibre separator drenched in electrolyte, with the

lithium chip counter electrode, steel spacer, wave spring and top cap. For the construction of HICs, the cells were built using the same components except for the activated carbon electrodes as the cathode and the metal oxide electrodes as the anode.

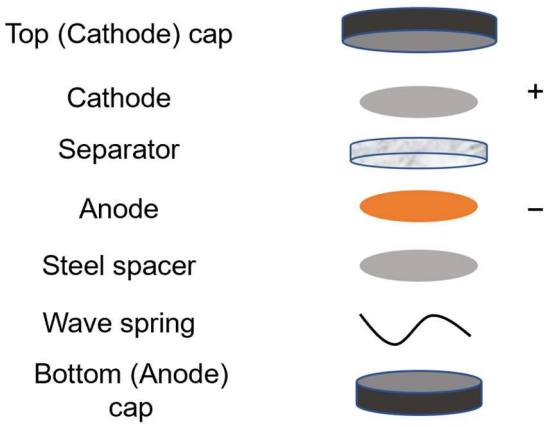

Figure 2.3: Diagram showing the internal components of a coin cell.

2.3 Electrochemical Characterisation Techniques

2.3.1 Cyclic Voltammetry

Cyclic voltammetry (CV) experiments involve cycling the potential of the working electrode in a linear fashion at a constant scan or sweep rate (v), between an upper (V_{max}) and lower (V_{min}) potential limit. The current response is recorded and plotted as a function of potential (Figure 2.4). Analysis of the location of the peaks present can give information regarding the activation potentials of the lithiation and delithiation reactions. Changes in the shape and size of the peaks over multiple cycles can indicate the stability of materials to repeated insertion/removal of lithium. Analysis of the CVs over a range of different scan rates can be used to interpret the different mechanisms providing charge storage as described in section 1.2.4.[92]

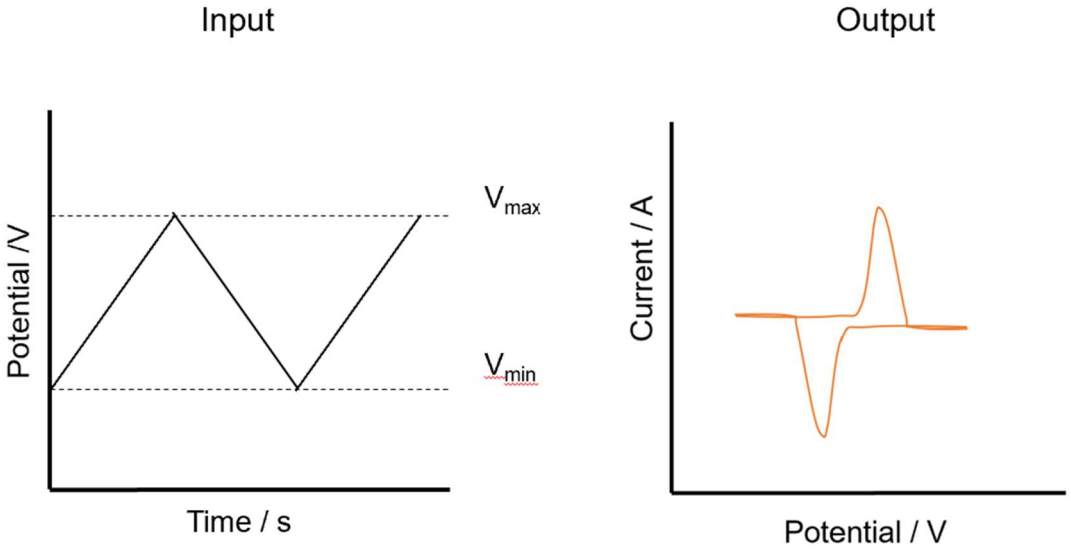

Figure 2.4: diagram showing the input of a CV test, where the voltage is cycled between a maximum and a minimum value and the current response is recorded and plotted as shown on the right.

The diffusion coefficient of lithium ions within the electrochemical cell can be estimated from CVs using the Randles-Sevcik equation (equation 2.10).[195] The peak current (I_p) is directly related to the number of electrons involved in the reaction (n), the surface area of the electrode (A), the diffusion coefficient (D_{Li}), the concentration of lithium ions (C_{Li}) and the scan rate (v). This can be simplified to equation 2.11 at a temperature of 298 K.[196] From a plot of the peak current vs the square root of the scan rate ($v^{0.5}$), the slope is then used to give a value for the diffusion coefficient.

$$I_p = 0.4463 n^{\frac{3}{2}}.F^{\frac{3}{2}}.C_{Li}A.R^{-1}.T^{-1}.D_{Li}^{\frac{1}{2}}.v^{\frac{1}{2}} \quad (2.10)$$

$$I_p = 2.69\ X\ 10^5 n^{\frac{3}{2}}.A.D_{Li}^{\frac{1}{2}}.C_{Li}.\ v^{\frac{1}{2}} \quad (2.11)$$

For the estimation of D_{Li} from Randles-Sevcik there are however several assumptions that are made, which in turn are limitations that must be taken into consideration. The first is the value used for the surface area, traditionally in literature there have been two approaches which are to either use the simpler value for the surface area of the electrode disc, or the more accurate surface area of the active material determined by BET.[197] The next assumption is the concentration of lithium, again several different approaches and values are reported in literature. The first is to use the concentration of lithium found in the

electrolyte solution (typically 1 mol dm^{-3}), as this is the typical approach for cyclic voltammetry calculations of standard cells such as Daniel cells. This assumption gives a value for the diffusion coefficient that applies for the whole cell, not just the active material. The other approach is to calculate the concentration of lithium in the active material, in order to make D_{Li} more representative of just the active material. This is achieved by calculating the concentration of lithium ions within the unit cell. However, the calculation of this is further complicated due to the fact that the concentration of Li^+ is a function of potential and therefore must be estimated for the specific potential at which I_P is taken from. These assumptions thereby render the comparison of exact values of D_{Li} from different sources that may have used different experimental set-ups or made different assumptions in the calculations difficult. However, the comparison of D_{Li} values between materials measured with the exact same conditions, set-ups and assumptions can provide useful information. It can also be useful when investigating the changes in diffusion coefficients of materials as a function of potential, time, or cycle number.

2.4.2 Galvanostatic Techniques

Galvanostatic methods refers to the application of a set current and the observation of the potential response as a function of time. For battery devices, the standard galvanostatic techniques involve the application of positive and negative set currents to induce charging and discharging cycles. The positive current corresponds to an increase the potential difference to an upper potential limit, the negative current corresponds to a decrease in the potential difference to a lower potential limit.

$$Q_{charg\ /discharge} = I \cdot t \cdot m^{-1} \tag{2.12}$$

$$CE = \left(\frac{Q_{discharge}}{Q_{charge}}\right) \cdot 100 \tag{2.13}$$

The charge (or discharge) capacity of a half-cell is calculated from equation 2.12 where *I* is the current in amps (A), *t* is the charge/discharge time in seconds and *m* is the mass of the active material in grams. The coulombic efficiency is used as a measure of the proportion of charge capacity is retained during discharge. This number should typically be greater than 99% in most cases, with large fluctuations away from this suggesting the occurrence of undesired

electrochemical reactions. The coulombic efficiency is calculated using equation 2.13. For the hybrid ion capacitors, the capacitance of the cells (C g^{-1}) was calculated using equation 2.14 in which ΔV is the potential window during discharge and *m* is the active masses of both the anode and cathode.

$$C_{HIC} = (I \cdot t)(\Delta V \cdot m^{-1}) \quad (2.14)$$

The gravimetric power (W kg^{-1}) and energy (Wh kg^{-1}) of the hybrid capacitors was calculated from the galvanostatic charge and discharge plots using equations 2.15 and 2.16 respectively.

$$P = \Delta V \cdot \left(\frac{I}{m}\right) \quad (2.15)$$

$$E = P \cdot \left(\frac{t}{3600}\right) \quad (2.16)$$

In which, ΔV is the average potential during the discharge, *I* is the current (A), *t* is the discharge time in seconds and *m* is the total active mass of both the anode and cathode in kilograms.

2.4.3 Electrochemical Titration Techniques

Galvanostatic or Potentiostatic Intermittent Titration Techniques (GITT or PITT) are methods of determining the thermodynamic and kinetic values for electrochemical processes within different materials.[198] In the work reported here, the GITT experiment was selected as it allows for the ohmic drop to be separated from the total potential response recorded. In a GITT experiment, a current pulse is applied to a cell. This is followed by a relaxation period in which the potential response is recorded as a function of time as the system relaxes from the active state towards the thermodynamic state of equilibrium (Figure 2.5). The relaxation process takes the form of ionic diffusion though the system as the potential induced in the active step equilibrates. During lithiation GITT experiments, the current pulse decreases the potential of the system by an amount that is proportional to the ohmic, or internal resistance (IR) drop due to internal resistance. Immediately after this, the cell potential will slowly decrease following the normal lithiation process as dictated by the concentration gradients of lithium. After the pulse and during the relaxation period, the concentration gradients of lithium in the system will slowly change via ionic diffusion until the change in cell potential is zero at equilibrium. During delithiation GITT experiments, the current

pulse is directed to increase the potential of the cell and the relaxation period to allow for ionic diffusion to equilibrate the cell in the same manner. The diffusion coefficient (*D*) of the mobile lithium ions (*Li*) is determined using equation 2.17 which is based on Fick's second law.[197]

$$D_{Li} = \frac{4}{\pi}\left(\frac{m_B V_M}{M_B A}\right)^2 \cdot \left(\frac{\Delta E_s}{\tau(dE_\tau/d\sqrt{\tau})}\right)^2 \left(\tau \ll \frac{L^2}{D_{Li}}\right) \quad (2.17)$$

In which m_B is the mass of the active materials on the electrode, V_M is the molar volume of the active material, M_B is the molecular weight of the materials, τ is the duration of the current pulse in seconds, A is the area of the electrode, ΔE_τ is the change in cell potential during the pulse, ΔE_s is the change in cell potential during the relaxation period and L is the lithium-ion diffusion distance. When plotting the change in cell potential with duration time versus $\tau^{1/2}$ gives a linear relationship, the equation can be simplified to give 2.18.

$$D_{Li} = \frac{4}{\pi\tau}\left(\frac{m_B V_M}{M_B A}\right)^2 \cdot \left(\frac{\Delta E_s}{\Delta E_\tau}\right)^2 \left(\tau \ll \frac{L^2}{D_{Li}}\right) \quad (2.18)$$

This equation makes the assumption that the molar volume (V_M) of the active material remains constant throughout the insertion and removal of lithium.[197] One area of ambiguity is the definition of the constant L, as this value has been reported in literature as several different distances and can therefore give different diffusion coefficients for the same exact material.[199] In the work reported here, the value of *L* was set as the thickness of the electrode in the cell. The quantification of the diffusion coefficient is an average value of all of the different diffusion kinetics occurring throughout inhomogeneous sites within the active material and the solid/electrolyte interfaces that are all present in the cell.[200]

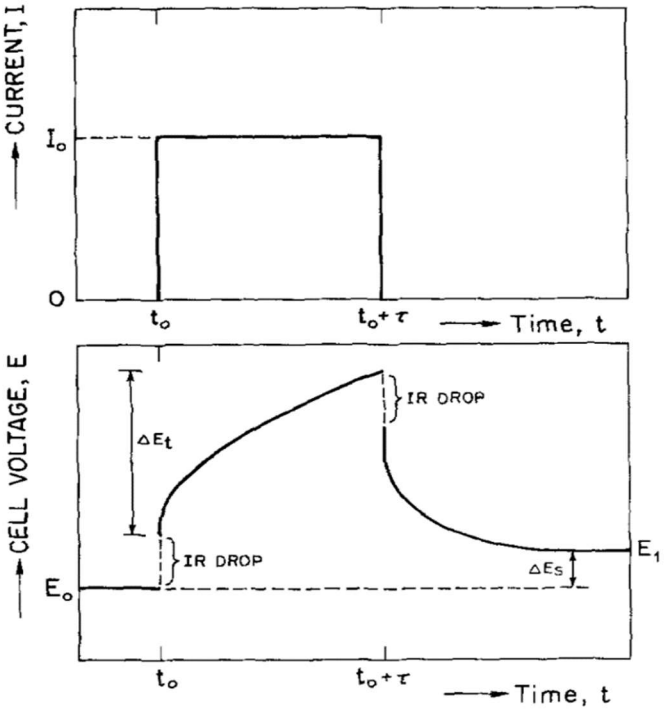

Figure 2.5: Graphs showing the Galvanostatic intermittent titration technique (GITT). The top graph shows the application of a charging current pulse (I_0) for a period of τ. The bottom graph shows the response. Upon the pulse, an initial IR drop is seen followed by a smooth increase in potential (E_t). Once the pulse has finished ($t_0+\tau$), the potential of the cell again experiences an IR drop followed by a relaxation period over which the voltage reaches the new potential E_1. The exact opposite process is seen for a discharge current pulse. Republished with permission of IOP Publishing, from Determination of the Kinetic Parameters of Mixed-Conducting Electrodes and Application to the System Li_3Sb, W. Weppner and R. A. Huggins, **124**, 1977; permission conveyed through Copyright Clearence Center Inc.

2.3.4 Electrochemical Impedance Spectroscopy

Electrochemical Impedance Spectroscopy (EIS) is an analytical technique that is used to probe the kinetic and electrical interactions inside the cell. By definition, impedance contains information regarding the phase and magnitude of resistance and is therefore an extension of the resistance found in AC circuits. This allows for the fitting of impedance data by equivalent circuits, and elucidates useful information about a range of processes occurring within the system.[201] In an EIS experiment, a very small alternating current potential (in the order of ~10 mV ms^{-1}) is applied to the working electrode of a cell at a range decreasing of oscillating frequencies from very high frequency (100 kHz) to very low frequency (10 mHz). The current response is transformed into complex real and imaginary resistive data. Ohm's law states that resistance is the equal to voltage (*U*) divided by current (*I*) as shown in equation 2.19.

$$R = \frac{U(t)}{I(t)} \tag{2.19}$$

This expression of resistance is only valid for the behaviour of an ideal resistor in a single element circuit. Therefore, to account for impedance involving the complex division of voltage by current, the corresponding complex behaviour of a real resistor must be expressed by the dependency of the voltage and current on the frequency.[202] Equation 2.20 describes how angular frequency (ω) is related to the frequency (*f*). Equations 2.21 and 2.22 describe how the complex voltage and complex current responses are derived respectively.

$$\omega = 2\pi f \tag{2.20}$$

$$U(t) = U_0 \sin(\omega t) \tag{2.21}$$

$$I(t) = I_0 \sin(\omega t + \Phi) \tag{2.22}$$

U(t) is an AC excitation at time *t*, U_0 is the amplitude of the excitation signal, *I(t)* is the current equivalent of *U(t)* and I_0 is the amplitude of the current shifted by the phase shift (Φ).

Taking these expressions and Ohm's law, allows for a more useful expression of impedance and the magnitude (Z_0) as shown in equations 2.23 and 2.24. This is then expressed through Euler's formula (2.25) to give the complex impedance (2.26).

$$Z = \frac{U_0 \sin(\omega t)}{I_0 \sin(\omega t + \Phi)} \quad (2.23)$$

$$Z = Z_0 \frac{\sin(\omega t)}{\sin(\omega t + \ )} \quad (2.24)$$

$$e^{(i\phi)} = \cos(\phi) + j\sin(\phi) \quad (2.25)$$

$$Z(\omega) = Z_0 e^{(i\phi)} = Z_0(\cos(\phi) + j\sin(\phi)) \quad (2.26)$$

EIS data of a Li/Na ion cell is typically plotted as either a Nyquist plot of real and imaginary impedance (Figure 2.6) or as a Bode plot. The impedance response can be modelled by the summation of contributions from different elements representing different processes occurring within the cell. The Randles circuit is the most common model utilised for fitting of Nyquist plots of Li and Na ion cells (Figure 2.7). It consists of the resistors R_s and R_{ct}, which represent the resistance of the electrolyte solution and the charge-transfer resistance respectively.[203] The C_{dl} element represents the double layer capacitance of the cell, and W (the Warburg element) represents the impedance related to mass-transfer within the cell. To account for the effects of the formation of the ionically passivating SEI layer and their inherent effect on diffusion kinetics, the Randles circuit was adapted to include elements that allow for the estimation of the dielectric constant, thickness of the SEI layer and its ionic resistance.[204]

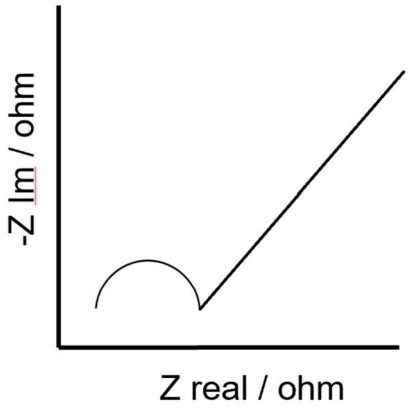

Figure 2.6: Graph showing the typical Nyquist plot of a Li/Na ion cell.

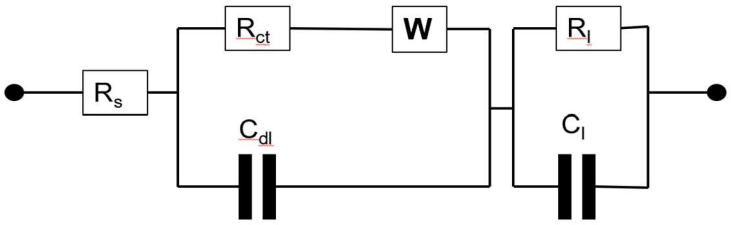

Figure 2.7: Diagram showing of the adapted Randles circuit that is used to model the impedance behaviour of Li/Na ion cells.

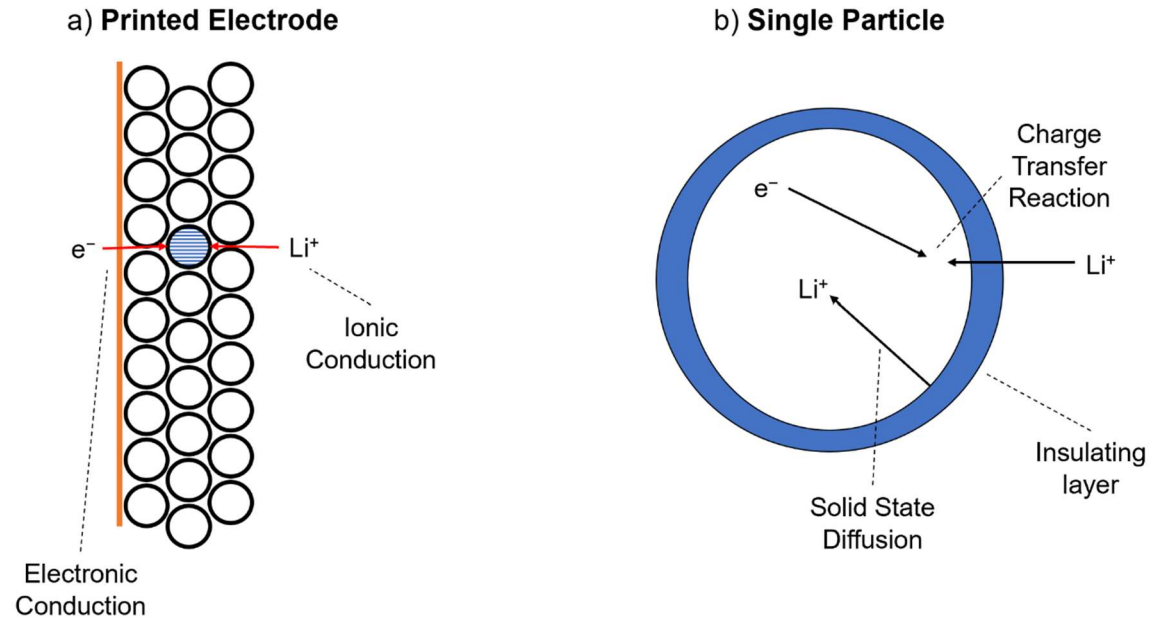

Figure 2.8: Illustration showing a) the electronic and ionic conductivity process occurring in a printed electrode. b) the various kinetic process occurring in a single particle of active material. Figure adapted from source [209].

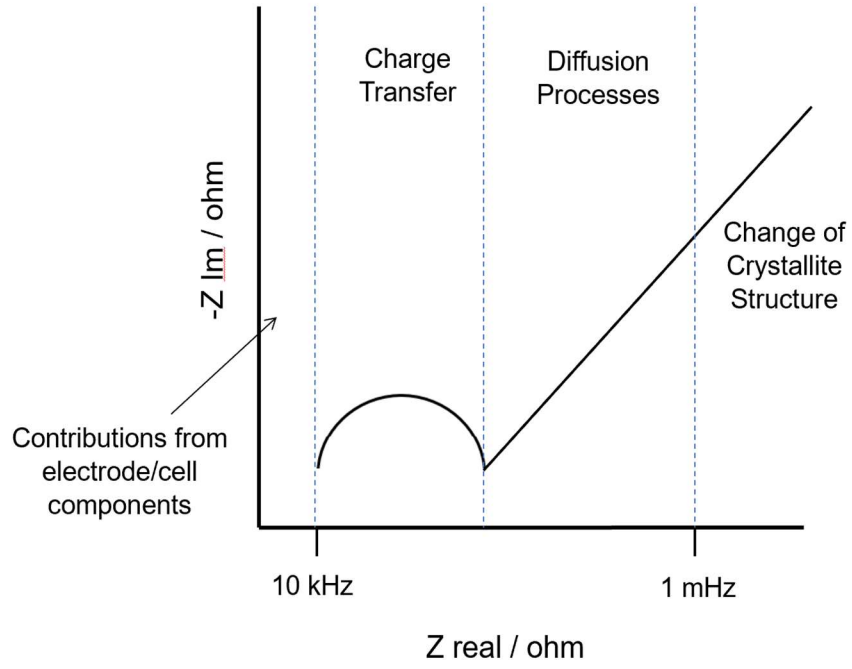

Figure 2.9: Illustration relating the physical process described in figure 2.8 and relating them to the Nyquist response observed. Figure adapted from source [209].

The different kinetic steps that occur during operation of a battery on the active material layers and at the single particle level, respectively in Figure 2.8a and 2.8b. At the surface interface of each individual particle, the Li^+/Na^+ ions must diffuse through the insulating layer and (via solid-state diffusion) enter the bulk material. The charge-transfer reaction involves the resistance of the activated electron transfer at the electronic-ionic boundary and the resistance of the insulating layer. Further processes include the electronic conduction through the electrode layer material, and the ionic conduction of electrolyte through the hollows and spaces between particles. These processes are related to their relevant frequencies and observed behaviour of the Nyquist plot as shown in Figure 2.9.

Due to the majority of the electrochemically active centres of materials residing in the bulk of the particles, solid-state diffusion of charge carriers through open crystalline structures is critical to the suitability of a material to charge storage.[205] The analysis of impedance for finite-length diffusion of different boundary conditions and of different particle geometries such as spherical, cylindrical and planar was defined by Jacobsen and West.[206] Equation 2.27 describes the impedance response for spherical geometry as a function of electrical terms.

Equations 2.28 and 2.29 converts the electrical terms into electrochemical terms.

$$Z(s) = \frac{\tanh\left(\sqrt{3 \cdot C_d \cdot R_d \cdot s}\right)}{\sqrt{\frac{3 \cdot C_d \cdot s}{R_d} - \frac{1}{R} \cdot \tanh\left(\sqrt{3 \cdot C_d \cdot R_d \cdot s}\right)}} \quad (2.27)$$

$$\frac{dE}{dc} = \frac{F \cdot n}{C_d} \cdot \frac{4}{3} \cdot \pi \cdot r^3 \quad (2.28)$$

$$D = \frac{r^2}{3 \cdot C_d \cdot R_d} \quad (2.29)$$

Where r is the radius of the spherical particles, C_d is the capacitance and R_d is the resistivity, s is the surface area, F is Faraday's constant and n is the number of electrons transferred. These equations describe the impedance and diffusion coefficient for a single spherical particle however, a real electrode consists of a vast number of particles either touching each other or connected via carbon particles and polymer binder. To calculate the diffusion coefficient for electrolyte ions through the entire electrode, the low frequency impedance real data (Z *real*) is plotted against $\omega^{-0.5}$ (one over the square root of angular frequency) in a

Randles plot.[207] This gives a linear relationship from which the slope represents the value of the Warburg coefficient (σ). This can be related to the diffusion coefficient of electrolyte ions by equation 2.30, which is rearranged to give equation 2.31:

$$\sigma = \frac{RT}{F^2 A\sqrt{2} D^{\frac{1}{2}} C} \quad (2.30)$$

$$D = \frac{0.5\left(\frac{RT}{\sqrt{2}F^2\sigma C}\right)^2}{A} \quad (2.31)$$

In which, D is the diffusion coefficient ($cm^2\ s^{-1}$), R is the universal gas constant (8.314 J $mol^{-1}\ K^{-1}$), T is the temperature (K), F is Faraday's constant (96485.33 C mol^{-1}), C is the concentration of electrolyte ions (mol cm^{-1}), and A is the surface area of the electrode (cm^2). As with CV methods for determining diffusion coefficients, there are however several assumptions that are made in the calculation of D and therefore limitations in its use for analysis. The first is the surface area which can either be set as the surface are of the electrode or as the surface area of the active material as determined by a method such as BET. One of the other limitations is the concentration of lithium. This is typically taken as the concentration of the electrolyte; however, this is not an accurate representation of the concentration of lithium within the active material which is itself a function of potential. This therefore means that any value for D calculated is an estimate and can be associated to the reasons why a wide range of different values for similar materials are reported in literature and comparison of exact values of diffusion coefficients between different studies is difficult. The investigation of trends between calculated diffusion coefficients and parameters such as different potentials, time, cycle number, changes in material composition or morphology, can be useful provided the same experimental set-ups, conditions and numerical assumptions are used.

Supercapacitors, and by extension hybrid capacitors, have been found to operate at two different states depending on the frequency applied. At very high frequencies (>10 kHz) they behave like a pure resistor, and at lower frequencies they behave like a capacitor which can store charge generated by the voltage oscillations.[208] The frequency at which this behaviour changes is determined by the time taken for the capacitor to react to a voltage stimuli and store charge. It is defined as the dielectric relaxation time (τ_0) and is used as a figure of merit for

supercapacitors.[209] The determination of this value is determined from the normalized imaginary (also known as reactive $|Q|/|S|$) and real (also known as active $|P|/|S|$) parts of the complex power vs. frequency. The imaginary part represents purely capacitive behaviour, and the real part represents purely resistor behaviour. At very high frequency all of the power is dissipated throughout the capacitor giving completely resistive behaviour. As the frequency decreases the plot of imaginary power (capacitive behaviour) increases to a maximum at which point the cell behaves as purely capacitive. The cross over point of these two plots represents the frequency at which the behaviour changes (resonance frequency) and is used to calculate the time relaxation constant (Figure 2.10). The expressions for active and reactive power are described in equations 2.32 and 2.33:

$$P(\omega) = \omega C''(\omega)|\Delta V_{rms}|^2 \quad (2.32)$$

$$Q(\omega) = -\omega C'(\omega)|\Delta V_{rm}\ |^2 \quad (2.33)$$

In which, ω is the angular frequency (ω = 2πf), the real and imaginary complex capacitances are given as C'(ω) and C"(ω) respectively. The value of the $|\Delta V_{rms}|^2$ term is equal to the change in the maximum amplitude of the alternating current excitation (V_{max}) divided by the square root of 2.[210] The relationship of the resonance frequency (f_0) to the time relaxation constant (τ_0) is described by equation 2.34:

$$\tau_o = \frac{1}{2\pi f_o} \quad (2.34)$$

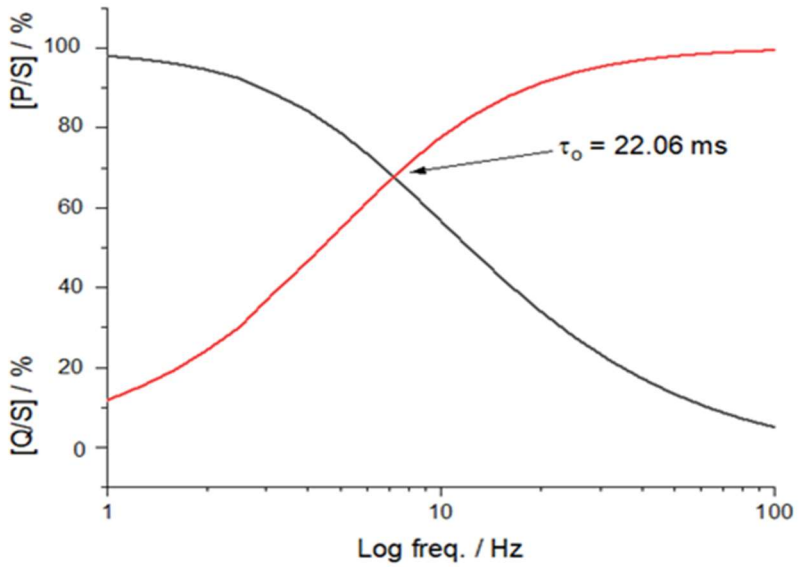

Figure 2.10: Graph showing the plot of normalised active ([P/S]) and reactive ([Q/S]) power against log frequency for an AC//TNO hybrid lithium-ion capacitor. The cross over point gives the resonance frequency which is converted to the relaxation constant via equation 2.47.

2.3.5 Mass Balancing of Electrodes in Full Cells

To obtain the largest possible energy densities of lithium/sodium ion batteries and hybrid capacitors, the accurate balancing of electrode materials is of the utmost importance.[211] Due to inherent differences in the charge storage capabilities of different anode and cathode materials, the amount of each active material in a cell must be carefully controlled to ensure that the total charge that can be charged and discharged is equal. This ensures that there is no material on either electrode that is surplus and unused during operation, and that there isn't a deficiency of material that hinders the performance of the cell.[211] In addition to this, to stop the possibility of lithium plating within the cell, and therefore increase safety and lifetime, the anode is oversized compared to the cathode (1.2:1 of anode to cathode).[211,212] By knowing the capacities of the individual electrode materials at the same specific currents, the theoretical capacitance of a full cell at different ratios of cathode to anode can be calculated using equation 2.35:

$$C_{FC} = \frac{C_- m_- C_+ m_+}{(C_- m_- + C_+ m_+)(m_- + m_+)} \qquad (2.35)$$

Where C_{FC} is the theoretical capacitance of the full cell (F g^{-1}), C_+, C_-, m_+ and m_- are the capacitances and the active masses of the cathode and anode materials respectively. By calculating the value of C_{FC} at a range of different cathode to anode ratios a plot of theoretical capacitance vs mass ratio can be used to identify the highest theoretical full cell performance (Figure 2.11).

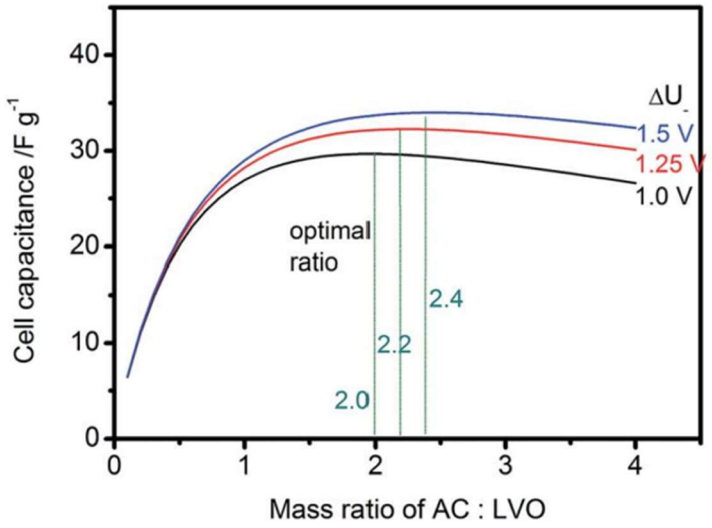

Figure 2.11: Calculated values of the cell capacitance versus the AC:LVO mass ratio. Reprinted with permission from H-Y. Wei, D-S. Tsai and C-L. Hsieh, *RSC Advances*, 2015, Royal Society of Chemistry.

2.4 Synthesis of Materials

2.4.1 Titanium Niobium Oxides and Carbon Titanium Niobium Composite Materials

Precursors for Materials Synthesis: Titanium bis (ammonium lactate) dihydroxide ($[CH_3CH(O-)CO_2NH_4]_2Ti(OH)_2$, TIBALD), potassium hydroxide (KOH), sodium hydroxide (NaOH) and ammonium niobate oxalate hydrate ($C_4H_4NNbO_9{\cdot}4.8H_2O$) were purchased from Sigma Aldrich, Dorset, UK.

Titanium niobium oxides were synthesised on a lab scale CHFS reactor using a balanced single mixer set up. In the first composition optimisation study, the precursors TIBALD, ammonium niobate oxalate and KOH were pre-dissolved in D.I. water in separate solutions before mixing the metals in a range of molar ratios as outlined in appendix table 2.

The molar ratios of the metal precursors to potassium hydroxide investigated in the first base optimisation study are outlined in appendix table 3.

The molar ratios of the metal precursors to sodium hydroxide explored in the second base optimisation study are described in appendix table 4.

The molar ratio of the metal precursors to sodium hydroxide used to synthesise the base material for the flash heat treatment study was [Ti] = 0.1 mol dm^{-3}, [Nb] = 0.2 mol dm^{-3} and [NaOH] = 0.001 mol dm^{-3}.

The total concentration of the metal salts in each pre-cursor solution was 0.3 mol dm^{-3}. The CHFS reactor used three diaphragm pumps (Primeroyal K, Milton Roy, France) to provide feeds into a Confined Jet Mixer (CJM, patent GB1008721) that was constructed out of Swagelok parts (UK). The configuration used in this set up was as follows: pump 1 (P1, flowrate of 80 ml min^{-1}) delivered a feed of supercritical D.I. water (450℃), pump 2 (P2, flowrate of 40 ml min^{-1}) delivered a feed of metal salt precursor and pump 3 (P3, flowrate of 40 ml min^{-1}) delivered a feed of base. The feeds of P2 and P3 were premixed in a T-piece before entering the CJM where they then mixed with the SCH_2O feed from P1 resulting in the formation of nanoparticles. The solution of nanoparticles was then fed through a pipe-in-pipe cooler to reduce the temperature. The solution then passed through a back pressure regulator and collected as a slurry. The post synthesis processing is described in section 2.4.7. The as collected blue/white powders for

the initial KOH study and the NaOH optimisation study were both heat treated in air at 1000 ℃ for 3 hours using an Elite tube furnace (UK). This yielded light brown/white powders as the final materials.

Precursors for Carbon Titanium Niobium Composite Materials Synthesis: Titanium bis (ammonium lactate) dihydroxide ($[CH_3CH(O\text{-})CO_2NH_4]_2Ti(OH)_2$, TIBALD), sodium hydroxide (NaOH), sucrose ($C_{12}H_{22}O_{11}$) and ammonium niobate oxalate hydrate ($C_4H_4NNbO_9{\cdot}4.8H_2O$) were purchased from Sigma Aldrich, Dorset, UK.

Carbon titanium niobium oxide composites (denoted as CTNO) were synthesised on a lab scale CHFS reactor using a balanced single mixer set up. The precursors TIBALD, ammonium niobate oxalate, sodium hydroxide and sucrose were pre-dissolved in D.I. water in separate solutions before mixing the metals and sucrose in a range of molar ratios as outlined in appendix table 5.

The total concentration of the metal salts and sucrose in each pre-cursor solution was 0.3 mol dm^{-3}. The CHFS reactor used three diaphragm pumps (Primeroyal K, Milton Roy, France) to deliver feeds into a Confined Jet Mixer (CJM, patent GB1008721) that was constructed out of Swagelok parts (UK). The configuration used in this set up was as follows: pump 1 (P1, flowrate of 80 ml min^{-1}) delivered a feed of supercritical D.I. water (450℃), pump 2 (P2, flowrate of 40 ml min^{-1}) delivered a feed of metal salt precursor and pump 3 (P3, flowrate of 40 ml min^{-1}) delivered a feed of base. The feeds of P2 and P3 were premixed in a T-piece before entering the CJM where they mixed with the SCH_2O feed from P1 resulting in the formation of nanoparticles. The solution of nanoparticles was then fed through a pipe-in-pipe cooler to reduce the temperature. The solution then passed through a back pressure regulator and collected as a slurry. The post synthesis processing is described in section 2.5.6. The as collected powders were brown in colour and subjected to a heat treatment of 750 ℃ for 3 h under an inert (nitrogen) atmosphere in an Elite furnace (UK). The final products were collected as black powders.

2.4.2 Combinatorial Study of Mixed Vanadium, Niobium, Molybdenum Oxides

Precursors for Synthesis of Mixed Metal Oxide Composite Materials: Ammonium metavanadate (NH_4VO_3), ammonium heptamolybdate tetrahydrate ($(NH_4)_6Mo_7O_{24}.4H_2O$), ascorbic acid ($C_6H_8O_6$), ammonium niobate oxalate hydrate ($C_4H_4NNbO_9.4.8H_2O$) and oxalic acid ($C_2H_2O_4$) were purchased from Sigma Aldrich (UK).

Mixed vanadium, niobium and molybdenum oxide materials were synthesised on a balanced lab scale CHFS reactor using a CJM mixer and quench set up (appendix Figure 1a and 1b). The nominal ratios of each metal in the 48 materials are displayed below in Figure 2.12 and listed in appendix table 1. Prior to synthesis, the ammonium metavanadate was dissolved in an aqueous solution of oxalic acid in the molar ratio of 1:2 respectively and left to stir overnight until a colour change from orange/yellow to deep blue was observed. The ammonium heptamolybdate tetrahydrate, ammonium niobate oxalate hydrate, ascorbic acid and sucrose were each individual dissolved in D.I. water. The quantities of each metal precursor needed to obtain the correct nominal ratio of elements were mixed together immediately before synthesis in the order, ascorbic acid, molybdenum, niobium, vanadium, carbon. The total concentration of all three metal salts in each material precursor solution was 0.3 mol dm^{-3}. The relative ratio of the metals to each other was used to name and identify each material (i.e., V = 0.1 Nb = 1 Mo = 0.1 → VNM111). The CHFS reactor utilised four diaphragm pumps (Primeroyal K, Milton Roy, France) at a pressure of 240 bar, P1 (flowrate: 80 ml min^{-1}) delivered the pre-heated D.I. water (450℃) while P2 and P3 (both at a flowrate of 40 ml min^{-1}) delivered the solution of metal salts and carbons to a Confined Jet Mixer (CJM, patent GB1008721), resulting in the formation of particles. P4 (flowrate of 160 ml min^{-1}) delivered a stream of room temperature D.I. water to the quench point where it met the stream of particles and rapidly reduced the temperature. The temperature of the solution was further reduced by a pipe-in-pipe counter current heat exchanger, after which the solutions of mixed vanadium niobium molybdenum oxides passed through a BPR and were collected. The post synthesis processing is described in section 2.5.7.

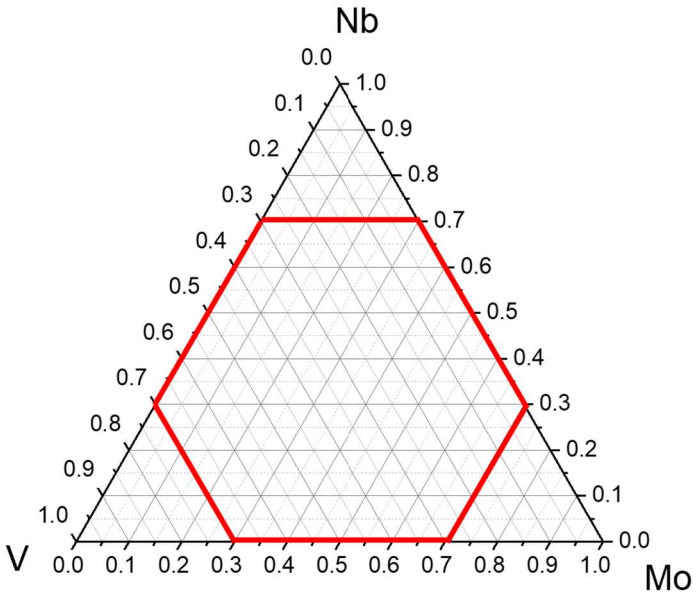

Figure 2.12: Ternary phase diagram of V-Nb-Mo with the compositional area investigated highlighted by a red hexagon.

2.4.3 Carbon Metal Oxide (Mixed V, Nb, Mo) Composite Materials

Precursors for Synthesis of Carbon Metal Oxide Composite Materials: Ammonium metavanadate (NH_4VO_3), ammonium heptamolybdate tetrahydrate ($(NH_4)_6Mo_7O_{24}.4H_2O$), ascorbic acid ($C_6H_8O_6$), oxalic acid ($C_2H_2O_4$), ammonium niobate oxalate hydrate ($C_4H_4NNbO_9.4.8H_2O$) and sucrose ($C_{12}H_{22}O_{11}$) were purchased from Sigma Aldrich (UK).

Mixed V, Nb and Mo oxide carbon composite materials were synthesised on a lab scale CHFS reactor using a Confined Jet Mixer (CJM, patent GB1008721) mixer and quench set up (appendix Figure 2). The nominal ratios of each metal and form of carbon are displayed in appendix table 6. Prior to synthesis, the ammonium metavanadate was dissolved in an aqueous solution of oxalic acid in the molar ratio of 1:2 respectively and left to stir overnight until the colour changed from orange/yellow to deep blue. The ammonium heptamolybdate tetrahydrate, ammonium niobate oxalate hydrate, ascorbic acid and sucrose were each individual dissolved in D.I. water. The quantities of each metal precursor needed to obtain the correct nominal ratio of elements were mixed together immediately before synthesis in the order, ascorbic acid, molybdenum, niobium, vanadium, carbon. The total concentration of all three metal salts in each material precursor

solution was 0.3 mol dm^{-3}. The CHFS reactor utilised four diaphragm pumps (Primeroyal K, Milton Roy, France) pumps at a pressure of 240 bar, P1 (80 ml min^{-1}) delivered the pre-heated D.I. water (450℃) while P2 and P3 (both 40 ml min^{-1}) delivered the solution of metal salts and carbons to the first CJM, resulting in the formation of particles. P4 (160 ml min^{-1}) delivered a stream of room temperature D.I. water to the second CJM acting as the quench point where it met the stream of particles and rapidly reduced the temperature of the solution. The temperature of the solution was further reduced by a pipe-in-pipe counter current heat exchanger, after which the solution of carbon vanadium niobium molybdenum oxide passed through a BPR and was collected. The post synthesis processing is described in section 2.5.7. The as collected powders were brown in colour, they were then subjected to a heat treatment in an Elite tube furnace (UK) with an inert atmosphere (N_2 gas) for 3h at 750℃ to graphitise the carbon.[213] The final materials were obtained as black powders.

2.4.4 Combinatorial Study of Mixed Fe, Mn and Zn Oxides, Carbon Coated Fe, Mn and Zn Oxides.

Precursors for Combinatorial Study of Mixed Fe, Mn and Zn Oxide Materials: Zinc nitrate ($Zn(NO_3)_2$) was purchased from Alfa Aesar (UK). Manganese acetate tetrahydrate ($Mn(C_2H_3O_2)_2.4H_2O$) and iron nitrate nonahydrate ($Fe(NO_3)_3.9H_2O$) were purchased from Sigma Aldrich (UK). Potassium hydroxide (KOH) was purchased from Fisher Scientific (Belgium).

A range of different individual, binary and tertiary Fe-Mn-Zn materials were synthesised from across the compositional space (Figure 2.13). A lab scale CHFS method using a balanced single mixer was used for the synthesis (appendix Figure 5). The relative molar ratios and the concentrations of the precursors used are outlined in appendix table 9. The lab CHFS used three diaphragm pumps (Primeroyal K, Milton Roy, France) to deliver feeds of deionised water heated to 450 ℃ (P1, flowrate 80 ml min^{-1}), metal salt solutions (P2, flowrate 40 ml min^{-1}) and KOH (P3, flowrate 40 ml min^{-1}) to a Confined Jet Mixer (CJM, patent GB1008721), which resulted in the formation of particles. The entire system was pressurised to 240 bar. The flow of particles was then fed through a counter current pipi-in-pipe cooler to reduce the temperature, after which it was passed through a BPR and collected as slurries. The post synthesis

processing procedure is detailed in section 2.5.7. The final products were collected as powders, with the colours detailed in appendix table 9.

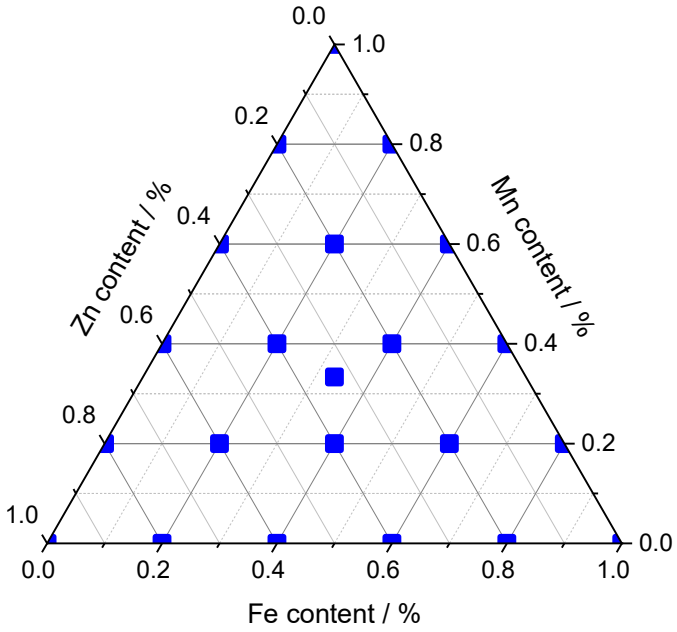

Figure 2.13: Ternary phase diagram of Fe, Mn and Zn with the individual, binary and tertiary mixed metal oxide compositions targeted.

Mixed Fe, Mn and Zn oxide carbon composite materials were synthesised using a lab scale balanced double mixer set up with a CJM and a quench (appendix Figure 6). The relative metal salt and sucrose ratios are outlined in appendix table 8. The CHFS set up utilised four diaphragm pumps (Primeroyal K, Milton Roy, France) that were pressurised to 240 bar. Two different approaches to the synthesis of the carbon metal oxide composites were taken. P1 delivered a feed of deionised water heated to 450 ℃ (flowrate 80 ml min^{-1}), P2 delivered a feed of metal salt and sucrose solutions (flowrate 40 ml min^{-1}), P3 delivered a feed of KOH (flowrate 40 ml min^{-1}) to a Confined Jet Mixer (CJM, patent GB1008721), which resulted in the formation of particles. P4 delivered a feed of room temperature deionised water as a quench to the second mixer (flowrate 160 ml min^{-1}). The stream of particles from the second mixer then flowed through a counter current pipe-in-pipe cooler to reduce the temperature and then through a BPR where they were collected as slurries. The post synthesis processing is outlined in section 2.5.7. Once collected as dry powders, the materials were

subjected to a heat treatment in an Elite tube furnace (UK) at 750 ℃ for 3 hours in an inert atmosphere (nitrogen) to convert the sucrose carbon to graphitic carbon. The final products were collected as black powders.

2.4.5 Post CHFS Processing

Once the slurries of the metal oxide particles were collected from the CHFS reactor, they were cleaned to remove any residual metal salts or ionic by-products left in solution. This was done by placing the slurries inside semi-permeable membrane bags (Medicell Membranes Ltd, UK), which were submerged in D.I. water to clean the materials by dialysis and remove any dissolved salt ions. The cleaning was repeated until the conductivity of the supernatant was reduced to below 100 μS as measured by a conductivity probe (Hanna Instruments, model H198311). The slurries of the metal oxide/carbon composite materials were cleaned by washing with D.I. water and centrifugation until the conductivity of the supernatant was determined to also be below 100 μS. The clean slurries were finally centrifuged to remove as much water as possible and give a paste that was then freeze-dried (Virtis Genesis 35XL, Biopharma Process Systems, UK) to give dry powders. These powders were either analysed directly or subjected to further processing as described in the above paragraphs.

3.0 Titanium Niobium Oxides and Carbon Composites; Electrochemical Properties and Li^+ Ion Diffusion Study

'It is not the mountain we conquer, but ourselves' – Edmund Hillary

3.1 Aims

Titanium niobium oxide ($TiNb_2O_7$) has been reported as a candidate for high power anodes due to its good capacity retention at high C-rates and minimal lattice strain upon insertion and removal of lithium ions. TNO however, suffers from low electronic conductivity which limits both the power and energy volumetric density. The aims of this chapter included investigating and showcasing the ability of continuous hydrothermal flow synthesis methods in creating targeted a targeted material of interest. As well as, to evaluate and understand the electrochemical and diffusion behaviours of smaller particle sized $TiNb_2O_7$ (TNO) A third objective was to investigate improving the high-power performance of CHFS TNO by forming carbon composite TNO materials in flow.

3.2 Introduction

In the pursuit of ever higher performing active Li^+ ion battery materials that are able to both store ever large amounts of charge and cycle at faster rates without suffering from capacity fading are attracting interest.[106] In spite of the fast ion mobility, low cost and high specific capacity of graphite (372 mAh g^{-1}), the low operating voltage limits it's use as an high-rate anode material due to the safety concerns surrounding lithium plating and dendrite formation.[82] Among the many possible candidates to replace graphite, various titanium and niobium based oxides are promising materials due to their high C-rate capabilities, very low structural strain upon lithiation/delithiation and inexpensive constituent elements.[156,214–216] In particular, the spinel $Li_4Ti_5O_{12}$ (LTO) as it is a "zero strain material" with good rate capability and long term stability that has a high working potential of ~1.55 V vs Li/Li^+, allowing it to avoid the formation of dendrites.[217] LTO however, suffers from a low specific capacity (175 mAh g^{-1}) and low intrinsic electronic conductivity.[218] Other commonly reported materials for anodes are the monoclinic and orthorhombic niobium pentoxides (T-Nb_2O_5 and H-Nb_2O_5 respectively).[200,214] Both of which utilise the redox couple Nb^{5+}/Nb^{4+} to give high

specific capacities of ~200 mAh g^{-1}. Due to the similarities in crystal structures, Ti atoms are able to replace Nb atoms to give mixed metal oxides which can further increases performance. Hydrothermally synthesised niobium doped titania ($Nb_{0.25}Ti_{0.75}O_2$) has also been reported as a high rate anode material that exhibits a specific capacity of 180 mAh g^{-1} at low C-rate (0.5 C) and retains 105 and 48 mAh g^{-1} at the high C-rates of 29 and 86 C respectively.[219]

The combination of titanium and niobium atoms in the same crystal morphology gives rise to a series of compounds that are of even greater interest due to their electrochemical performance, these are $TiNb_2O_7$,[220] $Ti_2Nb_{10}O_{29}$,[221] and $TiNb_{24}O_{62}$.[222] The structure of $TiNb_2O_7$ is a 3 X 3 sheared ReO_3 structure which consists of disordered Ti and Nb centred octahedrons of NbO_6 and TiO_6 that are both corner and edge sharing (Figure 3.1a and b) which form blocks.[223] Within the structure are shear plane units of octahedrons that are corner sharing, these are arranged along the *b*-axis forming layer planes between the blocks. The shear planes and are caused by the imbalance in oxygen nonstoichiometry in the material.[224] The presence of layers allows for lithium intercalation/deintercalation to occur in the spaces between the shear planes. Mixed Ti/Nb oxide materials are been reported to have specific capacities far in advance of LTO (~300 mAh g^{-1}) and a high working potential of ~1.65 V vs Li/Li^+.[225] The main physical attribute of titanium niobium oxides such as $TiNb_2O_7$ (TNO) is that the crystal lattice experiences almost zero strain upon intercalation and extraction of lithium, this is in part due to the shear planes which, provide crystal structure stability and reduce the deformation caused by lithium storage highlighting its potential as a

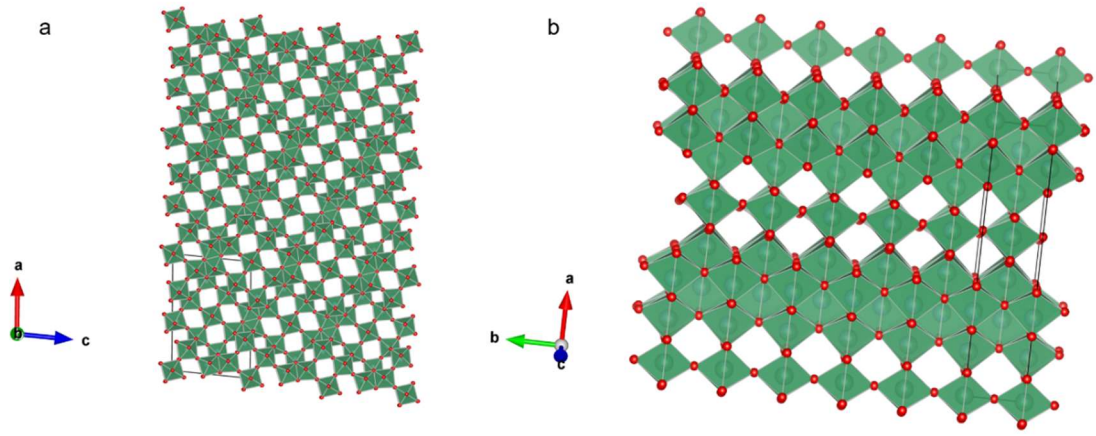

Figure 3.1: Schematics of the crystal structure of $TiNb_2O_7$ (a) along the *b*-axis, (b) along the *c*-axis. Generated from CIF file of ICSD collection code: 251796.

high-rate, high stability material.[10,220] Such is the potential of TNO that Toshiba Inc. developed a new lithium ion battery for use in EVs that had a TNO anode, which was found to have almost twice the volumetric energy density compared to an equivalent LTO cell (350 compared to 177 Wh L^{-1} respectively).[218]

Despite the many positive attributes of TNO, there are still several issues that must be overcome to fully realise its potential, such as the low intrinsic electronic conductivity (1 x 10^9 Ω cm at RT),[226,227] as well as the issue of gas evolution due to reactions occurring at the electrode/electrolyte interface.[228] Strategies to combat the low conductivity include nanosizing the particles to reduce the physical distance the electrons have to travel, this also has the beneficial effect of increasing the possibility for the material to store charge pseudocapacitively on the surface thereby increasing the specific capacity (213 mAh g^{-1} at 1 C). The other common technique is to synthesise the metal oxide in combination with a conductive additive or a substrate to form 3D conductive structures in order improve the high-rate performance.[229,230] For example, L. Fei *et al.* found that the addition of carbon nanotubes to TNO via a hydrolysis synthesis method gave a specific capacity of 218 mAh g^{-1} at 10 C after 100 cycles.[231] In contrast, the formation of 3D ordered porous TNO nanotubes using a sol-gel method, gave a high rate performance of 235 mAh g^{-1} at 5 C after 500 cycles.[232]

Understanding the lithium-ion diffusion kinetics of materials such as TNO is essential to understanding how and why they are able to offer high capacities at high C-rates. The diffusion coefficients of charge carriers such as Li^+ ions can also be determined electrochemically. The two most common practices are Electrochemical Impedance Spectroscopy (EIS) and Galvanostatic Intermittent Titration Technique (GITT). EIS uses the difference in phase between an input current pulse and the output voltage change to give information about the internal resistivities and from that the diffusion of charge carriers. GITT works via a similar principle in which the relaxation of the cell voltage to equilibrium after a current pulse is used to calculate the diffusion of charge carriers throughout the cell. Both methods have been extensively reported in literature for anode materials.[197,233]

Currently, the different synthesis methods for TNO that have been reported in literature include solid state synthesis methods,[234] sol-gel synthesis[235] and electrospinning.[236] Each of these methods have advantages and disadvantages

when the production rate is scaled up to kg/hr. Continuous Hydrothermal Flow Synthesis (CHFS) assisted methods represent a scalable and green method for production of metal oxide nanoparticles[157,173,213,219,237,238] including synthesis of lithium ion battery anode and cathode materials.[157,239,240] In the case off CHFS synthesised materials, they can be made either directly in CHFS without further processing, or CHFS can be used to make solid solutions of intimately mixed metal oxides, which can then be heat treated to form the desired final product, often with smaller particle sizes compared to more conventional methods.[240]

Herein, this chapter describes the use of a CHFS assisted method for the synthesis of nanoparticle precursors of TNO, the electrochemical evaluation of the CHFS assisted TNO as an anode material in lithium-ion batteries and hybrid capacitors, and the determination and comparison of lithium-ion diffusion coefficients determined by EIS and GITT. The use of CHFS assisted methods to synthesise a carbon-titanium/niobium mixed metal oxide composite with enhanced electrochemical performance is also investigated.

3.3 Experimental Methods

3.3.1 Synthesis of Titanium Niobium Oxides

The synthesis of the mixed titanium/niobium oxide materials are described in section 2.5.1. In the initial study of mixed Ti/Nb materials, KOH was used as the base with different relative concentrations of niobium salt precursor (samples K1-K5, appendix Table 2). The second set of materials synthesised via CHFS assisted methods (K6-K15) investigated the use of increasing amounts of KOH to give pH values of the precursor solutions between 7 and 14 (appendix Table 3). The third set of materials investigated used increasing concentrations of NaOH as the base to give pH values between 7 and 14 (N1-N9). All materials were subjected to heat treatments in air at 1000 ℃ for 3 hours.

3.3.2 Physical Characterisation

The physical characterisation methods used are described in section 2.1.

3.3.3 Electrochemical Characterisation

The construction of electrodes is described in section 2.2.1. The assembly of cells is described in section 2.2.2. The electrolyte used was 1M $LiPF_6$ in 1:1 v/v mixture

of EC/EMC. Hybrid capacitor cells were constructed using the same method as described in section 2.2.2.

The electrochemical characterisation of half-cells involved: Galvanostatic charge/discharge (GCD) cycling over a range of different specific currents including, 0.1, 0.5, 1, 2, 5, 10 and 15 A g^{-1} in the potential window 1 to 3 V vs Li/Li^+ completed by an Arbin Instrument (Model BT-2000 battery tester, US). Cyclic voltammetry (CV) was performed in the same potential window at range of increasing scan rates including 0.05, 0.1, 0.2, 0.5, 1, 2, 5, 10, 20, 50 and 100 mV s^{-1}. Potentiostatic EIS analysis was performed by a Gamry Interface 1000 Potentiostat, over the sinusoidal frequency range 100 kHz to 10 mHz. The oscillating alternating current voltage was set to 10 mV ms^{-1} with the area as 1 cm^2 and 10-point measurements.

The hybrid capacitor cells were electrochemically evaluated by GCD and CV testing. Both were performed by a Gamry Interface 1000 Potentiostat (Gamry Instruments, USA) over the voltage range window 1 to 4.2 V.

Galvanostatic Intermittent Titration Technique was performed by a Gamry Interface 1000 Potentiostat, initially two cycles at 0.1 A g^{-1}, followed by a charge GITT protocol from 0.05 to 3 V vs Li/Li^+ and then a discharge GITT protocol from 3 to 0.05 V vs Li/Li^+. The GITT protocol involved a 10 minute pulse of 0.1 A g^{-1}, followed by a 10 minute rest.

3.4 Results and Discussion

3.4.1 Physical Characterisation of Titanium Niobium Oxides

In the initial KOH study with increasing amounts of Nb precursor, the white/blue powders that were collected from the CHFS were analysed by PXRD. Before they materials were subjected to heat treatment, the PXRD pattern (Figure 3.2) indicated a highly amorphous material, with only a few characteristic peaks that could be potentially attributed to anatase TiO_2 (ICSD collection code: 9852),[241] suggesting a mixture of metal oxides and hydroxides being present.

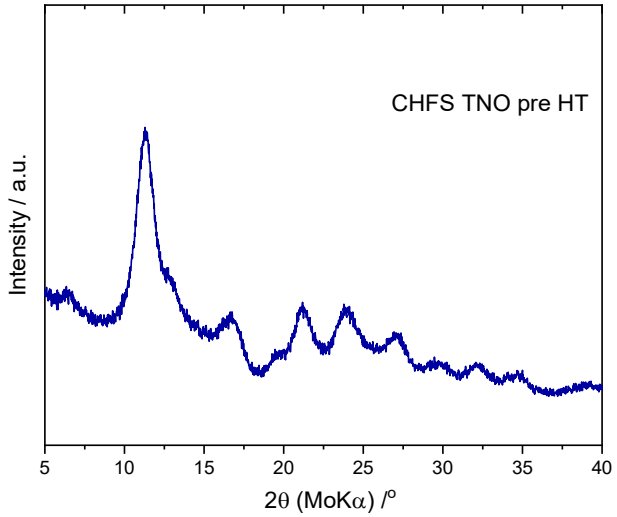

Figure 3.2: PXRD of the CHFS TNO (K1) material before heat treatment.

After heat treatment, all of the materials synthesised with potassium hydroxide (K1-5) gave PXRD patterns that were identical to each other (appendix Figure 6) with the main identifiable crystal phase being $KTiNbO_5$ (ICSD collection code 16557).[242]

The PXRD patterns of the materials (K6-K12) from the first base optimisation study are shown in Figure 3.3. It was observed that from pH 7 to 13 the heat treated materials all showed the characteristic peaks for monoclinic $TiNb_2O_7$, space group C 1 2/m 1 (ICSD collection code 48109).[243] Another very prominat peak at 2θ = 12.5 ° was observed in all of the materials, this was attibuted to an impurity of anatase TiO_2, the relative intensity of this impurity peak remained

consistant for all of the different pH values apart from pH 13 whereupon it became the dominant crystal phase present. The three materials K13-K15, were found to have PXRD patterns indicating no $TiNb_2O_7$ present and were a mixture of unidentified crystal phases and several potential potassiated titanium niobium oxides (appendix Figure 7).

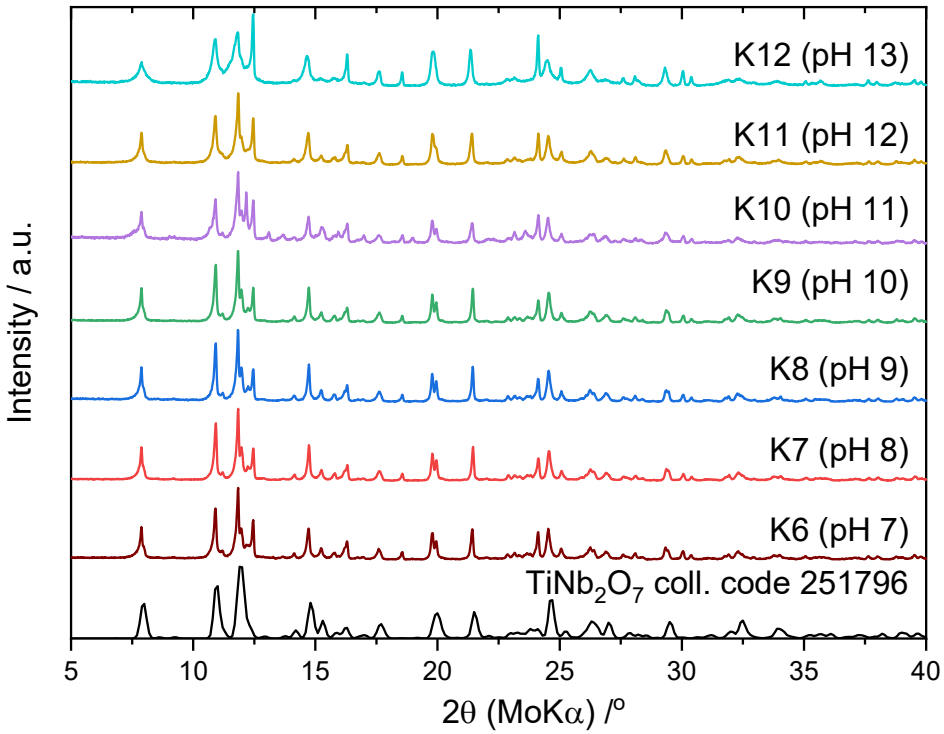

Figure 3.3: Graph showing the PXRD patterns for the TNO materials synthesised with increasing amounts of KOH to give higher pH values, and the $TiNb_2O_7$ reference pattern (ICSD collection no. 48109).

Due to the presence of an impurity crystal phase at the lower concentrations of KOH, and the undesired crystal phases being dominant at higher pH values, it was decided to switch base to sodium hydroxide and to perform a pH optimisation study again. After heat treatment, the materials synthesised at increasing concentrations of NaOH (N1-N9) were analysed by PXRD (Figure 3.4a). Except for one material, all were found to have PXRD patterns that could be indexed to monoclinic $TiNb_2O_7$ (ICSD collection code 48109).[243] When no additional base was added to the precursor solution (smaple N1), it was observed that for this sample the same impurity peak at $2\theta = 12.5°$ attributed to anatase TiO_2 was present again, and is marked on Figure 3.5a by an asterisk. The intensity of this impurity peak decreased as NaOH was added to increase the pH from 7 to 13 at

which point the impurity phase peak was no longer visible (sample N8). Once the pH was further increased to 14 (sample N9), however, no $TiNb_2O_7$ was observed and instead a mixture of TiO_2 and $NaNbO_3$ were identified.[244] The dependence on specific basic conditions for both crystal phase purity and high yields of metal oxides from metal salts has been reported for other materials in literature including Nb doped TiO_2 and yttrium aluminium garnet doped with Tb, both synthesised via CHFS.[219,245]

Taking the PXRD pattern which showed a phase pure material (N8) and applying a whole pattern fit using a Le Bail method and a C 1 2/m 1 space group yielded an excellent fit (R_p = 4.93, R_{wp} = 7.40). This gave corresponding lattice parameters *a* = 21.24 Å, *b* = 3.97 Å, *c* = 12.00 Å, α = γ = 90°, β = 120.82° and cell volume = 870.14 $Å^3$.These were in good agreement with previously reported data for TNO (Figure 3.4b).[226] The surface area of the $TiNb_2O_7$ (sample N8) was analysed by BET and was found that before heat treatment, it was 293 $m^2\ g^{-1}$. Post heat treatment, sample N8 was found to have a BET surface area of 5 $m^2\ g^{-1}$. This very large decrease in surface area, which has been reported for similar materials in literature, could be attributed to both the phase transformation of the high surface area, amorphous, nanosized titanium and niobium oxides and hydroxides converting to TNO as well as particle growth due to sintering during the heat treatment.[219]

The morphology of the particles of TNO (sample N8) were investigated by TEM. It can be observed that the particles of the CHFS mixed metal oxide prior to heat treatment are very small (possibly, less than 5 nm in diameter) which coalesce together to form larger agglomerates (Figure 3.5a). Post heat treatment, the TEM images reveal much larger primary particles which coalesce to form smaller agglomerates with diameters less than 100 nm (Figure 3.5b). When magnified (Figure 3.5c), the primary particles clearly display lattice planes with regular spacings of 0.346 nm (Figure 3.5c insert), these were found to be consistent with the interplanar spacing of the (003) plane for $TiNb_2O_7$.[246]

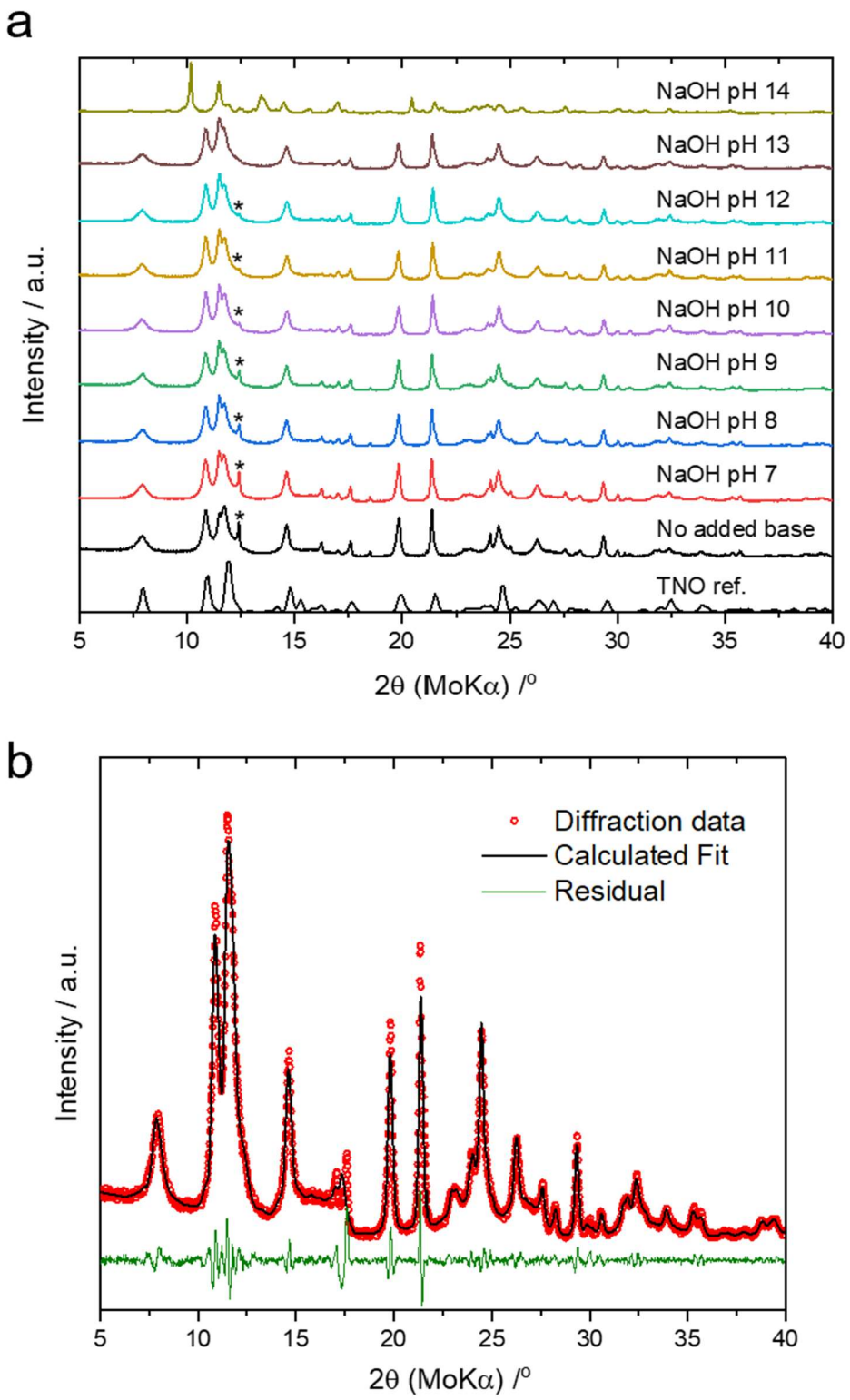

Figure 3.4: (a) PXRD patterns of all materials synthesised with NaOH at increasing pH values and the $TiNb_2O_7$ reference pattern (ICSD no. 48109), (b) PXRD pattern of TNO and Le Bail Whole pattern fitting of monoclinic $TiNb_2O_7$ C 1 2/m 1 space group (ICSD no. 48109). Calculated fit is shown as a black line with the residual shown as a green line.

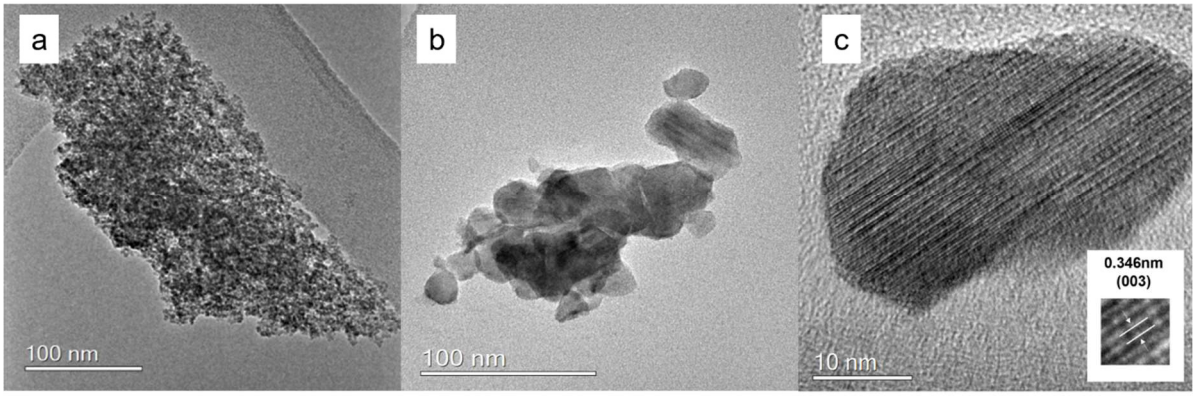

Figure 3.5: TEM images of (a) the mixed metal oxide from CHFS prior to heat treatment showing very small primary particles and large agglomerates, (b) particles of the heat treated CHFS TNO (N8) with sizes <100 nm, (c) high magnification image of a CHFS TNO (N8) particle with the interplanar spacing highlighted in the insert found to correspond to the (003) plane.

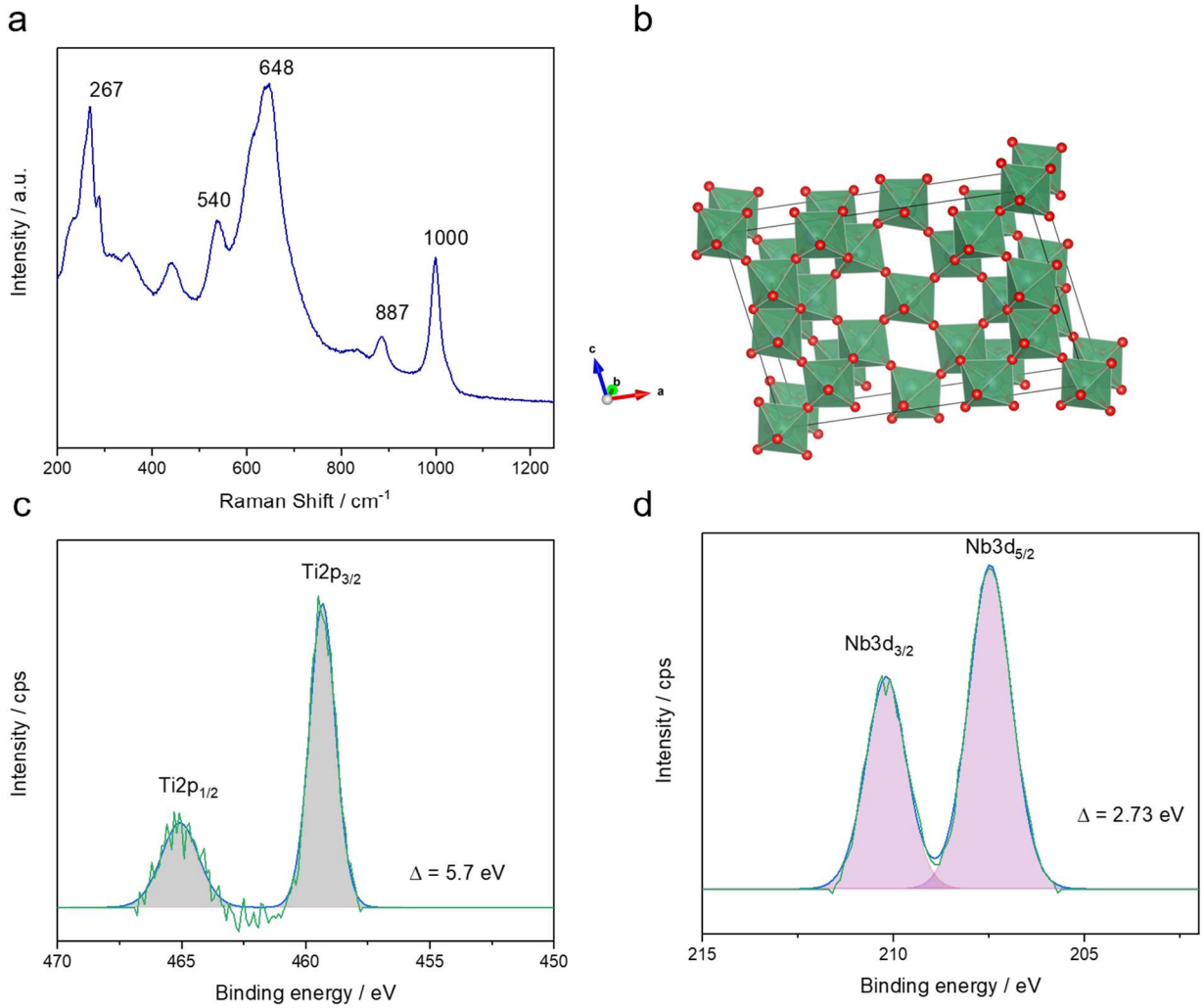

Figure 3.6: (a) Raman spectra of the CHFS TNO (sample N8) with the bands labelled, (b) crystal structure of monoclinic $TiNb_2O_7$, image generated by VESTA, (c) XPS spectra in the Ti2p region, (d) XPS spectra in the Nb3d region.

The structure of the CHFS TNO (sample N8) was further investigated by Raman spectroscopy (Figure 3.6a). The two bands highlighted at 887 and 1000 cm^{-1} were assigned to the symmetric stretching of the Nb-O bonds at the corner and edge sharing NbO_6 octahedra respectively.[247] The other bands at 540 and 648 cm^{-1} were attributed to the Ti-O vibrations of the TiO_6 octahedra, and the band at 267 cm^{-1} was attributed to the symmetric and asymmetric bending of both the O-Ti-O and O-Nb-O bonds.[248] The small peak at ~425 cm^{-1} and the shoulder on the left hand side of the peak at 648 cm^{-1} could be assigned to the stretching modes of rutile TiO_2.[249] The crystal structure of $TiNb_2O_7$ with the mixed occupancy Ti and Nb octahedra shown in green and the oxygen atoms in red is shown in Figure 3.6b.[250] XPS was unlisted to determine the valence states of the titanium and niobium ions present in the CHFS TNO (sample N8). The Ti $2p_{3/2}$ and $2p_{1/2}$ peaks were located at 459.2 and 464.9 eV respectively, giving a splitting of Δ = 5.7 eV, which is consistent with an oxidation state of +4 for Ti (Figure 3.6c).[251,252] The Nb $3d_{5/2}$ and $3d_{3/2}$ peaks were had a binding energy of 207.5 and 210.2 eV respectively and a splitting of Δ = 2.73 eV, all of which were consistent with an oxidation state of +5 for N (Figure 3.6d). These results were in good agreement with and confirmed the analysis by PXRD and Raman of the CHFS TNO.[253,254]

3.4.2 Electrochemical Characterisation of CHFS Titanium Niobium Oxides

3.4.2.1 Electrochemical Characterisation in Li-ion Half Cells

The electrochemical performance of sample N8 (referred to as CHFS TNO herein) was investigated by fabricating and testing half cells with lithium metal as the counter electrode, the detailed fabrication process is described in chapter 2 section 2.2.1 and 2.2.2. The half cells were first investigated by cyclic voltammetry over the potential range 1.0 to 3.0 V vs Li/Li^+ at increasing scan rates. The 0.5 mV s^{-1} CV curve, was found to exhibit several pairs of redox peaks, the major peaks at 1.56 and 1.71 V vs Li/Li^+ were assigned to the Nb^{5+}/Nb^{4+} redox couple (Figure 3.7a).[246] Two broad peaks were observed as shoulders at 1.81 and 1.90 V vs Li/Li^+, and were ascribed to the Ti^{4+}/Ti^{3+} redox reactions whilst the large broad peak at 1 to 1.4 V vs Li/Li^+ was credited to the Nb^{4+}/Nb^{3+} redox couple.[255] The outline of the CV curve was found to remain relatively consistent as the scan rates were increased, this suggests good electrochemical performance at fast charge/discharge rates (Figure 3.7b).

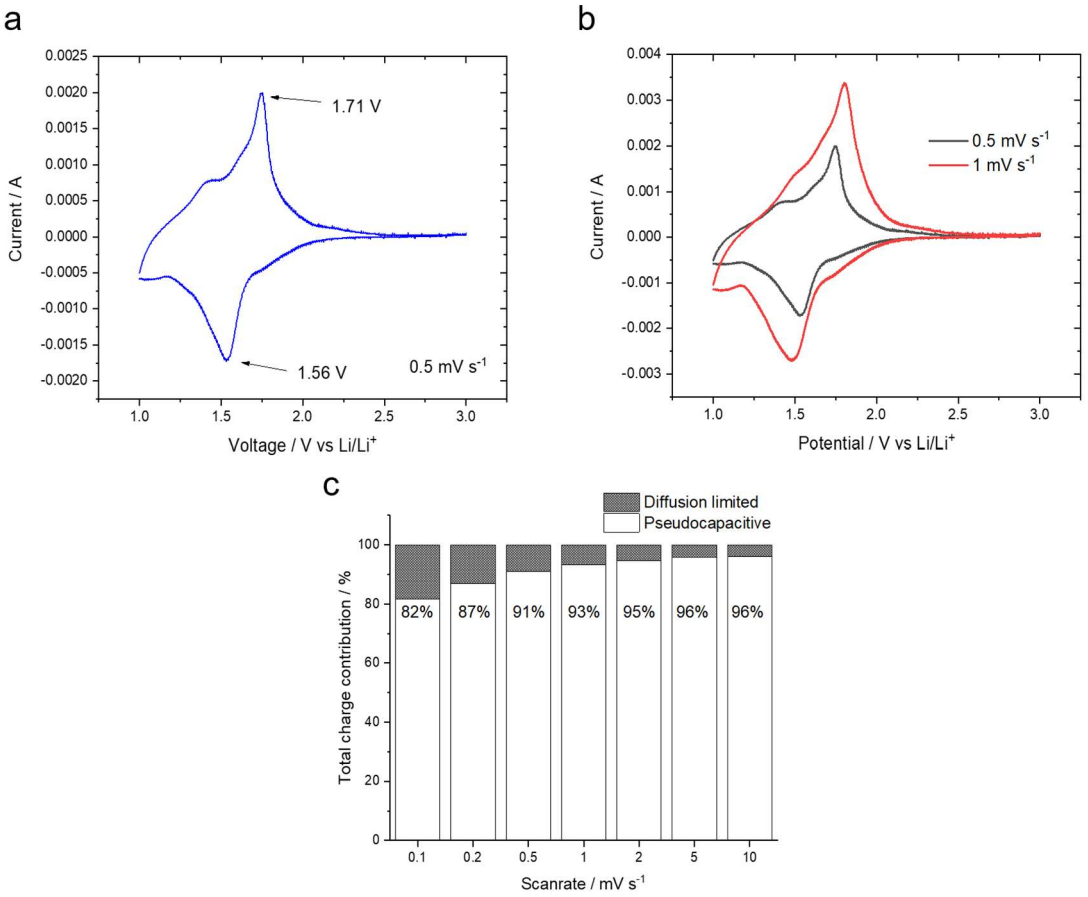

Figure 3.7: Cyclic voltammetry curves of CHFS TNO (sample N8) at (a) 0.5 mV s^{-1} (b) 0.5 and 1 mV s^{-1} (c) pseudocapacitive contribution as a percentage of the total charge stored, calculated vis the Trasetti methods.

A small increase in peak polarisation was observed at the faster scan rates, this could indicate some non-reversibility in the redox reactions occurring that could be associated with a wide range of factors, including potentially parasitic reactions between the TNO and the organic lithium salt electrolyte.[93,256] The contribution of different charge/discharge mechanisms to the performance of TNO was investigated via several methods that have been reported in literature.[93] The Trasetti method (described in section 1.2.4) was used to determine the pseudocapacitive contribution to charge storage as a percentage at increasing scan rates (Figure 3.7c).[83,93] At the slow scan rate of 0.1 mV s^{-1}, the pseudocapacitive contribution to charge storage was calculated to be very high at 82 %. This increased to 93 % and then to 96 % at the scan rates 1 and 10 mV s^{-1} respectively. These values were found to be higher than for those of similar materials reported in literature.[257]

The half cells of CHFS TNO (N8) were then analysed by galvanostatic charge/discharge cycling over the potential window 1.0 to 3.0 V vs Li/Li^+ at a range of increasing specific currents including 0.1, 0.5, 1.0, 2.0, 5.0, 10.0 and 15.0 A g^{-1}. The specific capacity for TNO was found to be 246, 220, 204, 188, 175, 143 and 120 mA h g^{-1} for the respective specific currents (Figure 3.8a). The coulombic efficiency for CHFS TNO was found to be remain very high at all specific currents (~99 %). After high current cycling, the CHFS TNO was returned to a specific current of 0.1 A g^{-1}, whereupon it was cycled for a further 120 cycles (Figure 3.8b). Over this period the CHFS TNO exhibited a very small capacity loss of 4 % whilst maintaining the same coulombic efficiency as before. This highlights the excellent cycling stability of the CHFS material even during and after high current cycling. The high capacities observed at a range of specific currents and the long term stability are very competitive with the other literature reports for TNO materials such as those reported by Zhang *et al*. for $TiNb_2O_7$ with oxygen vacancies that exhibited 145.7 mAh g^{-1} at a current of 1.6 A g^{-1}.[257] Other examples in literature of comparable materials include capacities of 150 mA h g^{-1} at 3.87 A g^{-1} (10 C) for microspheres of TNO prepared by solvothermal method.[258] A higher specific capacity of 174 mA h g^{-1} at 10C for TNO nanoparticles synthesised via a batch solvothermal method was reported by L. Buannic *et. at*.[259] The comparison of the high rate performance of CHFS TNO (N8) to literature values is highlighted in Table 3.2.[235] Electrochemical impedance spectroscopy (EIS) was utilised to probe the conductivity of the CHFS TNO. The nyquist plot is shown in Figure 3.8c, the plot was fitted to an equivalent circuit to obtain values of 88.4 ohms for the charge transfer resistance (R_{ct}). This was found to be similar to some values reported in literature for $TiNb_2O_7$ materials, but indicated that improvements to the intrinsic conductivity could be made through techniques such as the introduction of oxygen vacancies.[257]

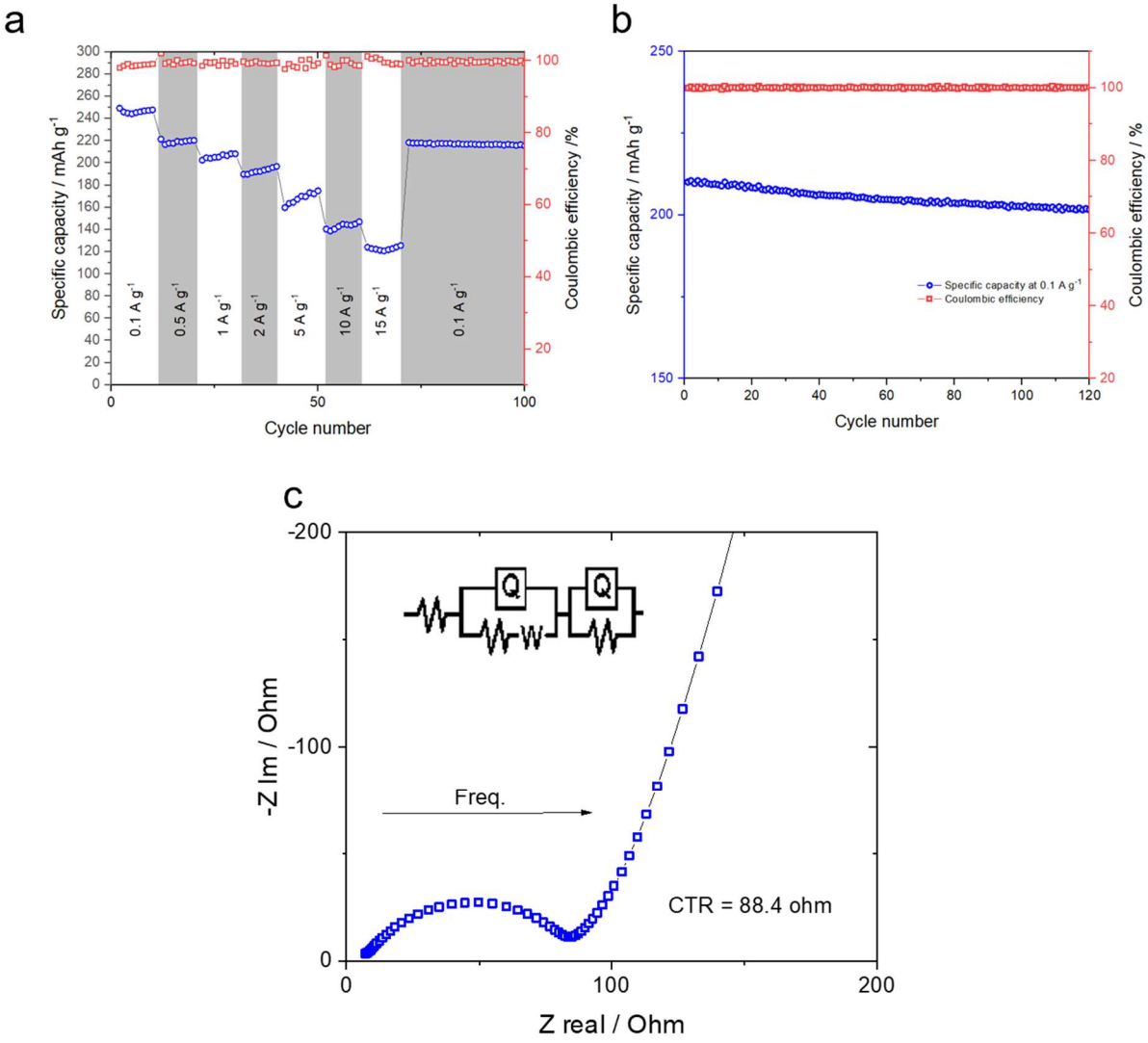

Figure 3.8: graphs of CHFS TNO (N8) showing (a) the specific capacities at increasing specific currents of GCD cycling (b) long term cycling performance over 120 cycles at 0.1 A g^{-1} (c) nyquist plot determined by EIS of CHFS TNO.

Anode	Manufacturing Process	Electrolyte	C-Rate/Current	Specific Capacity	Reference
Nano-$TiNb_2O_7$	CHFS method	1 M $LiPF_6$ (in 1:1 EC/DMC)	0.5 A g^{-1} (1.3C) 5 A g^{-1} (13C)	~220 mAh g^{-1} ~175 mAh g^{-1} after 70 cycles (1.0 - 3.0 V)	This work
Oxygen vacancy regulated $TiNb_2O_7$	Supercritical solvothermal method	1 M $LiPF_6$ (in 1:1 EC/DMC)	4.1 C (1600 mA g^{-1})	145.7 mAh g^{-1} after 50 cycles (1.0 - 3.0 V)	Electrochimica Acta, 2020, 330, 135299
Nanoporous $TiNb_2O_7$	Sol-gel method	1 M $LiPF_6$ (in 1:1 EC/DMC)	0.1C (38.7 mA g^{-1})	281 mAh g^{-1} (1.0-3.0 V)	Energy Environ. Sci., 2014, 7, 2220
Hierarchical $TiNb_2O_7$ nanotubes	Solvothermal method	1 M $LiPF_6$ (in 1:1 EC/DEC)	1 C (387 mA g^{-1})	170 mAh g^{-1} after 700 cycles	J. Mater. Chem. A, 2017, 15, 6958-6965
$TiNb_2O_7$ nanofibers	Electrospinning method	1 M $LiPF_6$ (in 1:1 EC/DEC)	0.1C (38.7 mA g^{-1})	170.1 mAh g^{-1} after 500 cycles (1.0-3.0 V)	J. Mater. Chem. A, 2015, 16, 8590-8596
$TiNb_2O_7$	Solid state method	1 M $LiPF_6$ (in 1:1:1 EC/DMC/DEC)	0.1C (38.7 mA g^{-1})	173.4 mAh g^{-1} after 200 cycles (1.0-3.0 V)	ACS Appl. Mater. Interfaces, 2018, 10, 27056-27062
$TiNb_2O_7$	Electrospinning method	1 M $LiPF_6$ (in 1:1 EC/DMC)	500 mA g^{-1}	~ 100 mAh g^{-1} after 100 cycles (1.0 - 3.0 V)	Nano Energy, 2015, 15, 104-115
3D ordered macroporous $TiNb_2O_7$	Sol-gel with polystyrene template method	1 M $LiPF_6$ (in 1:1 EC/DMC)	1C (387 mA g^{-1})	150 mAh g^{-1} after 50 cycles (1.0 - 3.0 V)	Nano Energy, 2017, 34, 15-25
$TiNb_2O_7$ nanowires	Sol-gel method	1 M $LiPF_6$ (in 1:1 EC/DEC)	0.4C (155 mA g^{-1})	199.6 mAh g^{-1} after 500 cycles (1.0-3.0 V)	Applied Surface Science, 2019, 475, 942-946
Nano-$TiNb_2O_7$	Solid state method	1 M $LiPF_6$ (in 1:1 EC/DMC)	10C (3.87 A g^{-1})	~180 mAh g^{-1} after 100 cycles (0.8 - 3.0 V)	Electrochimica Acta, 2018, 260, 65-72
Nano-$TiNb_2O_7$	Hydrothermal method	1 M $LiPF_6$ (in 1:1 EC/DMC)	300 mA g^{-1}	271 mAh g^{-1} after 100 cycles (0.7 - 3.0 V)	Solid State Ionics, 2018, 320, 7-15

Table 3.1: Table comparing the electrochemical performance of CHFS TNO with other similar materials reported in literature.

3.4.2.2 Electrochemical Performance in Li-ion Hybrid Capacitors

To investigate the possibility of CHFS TNO (sample N8) to be utilised to improve the energy density of capacitors, hybrid lithium-ion capacitor cells were fabricated using CHFS TNO as the anode and activated carbon (AC) as the cathode, a detailed description of the construction of the electrodes and cells can be found in section 2.2. In order to balance the electrodes and achieve the highest performing device possible, a method outlined by Wei *et al.*, was used to calculate the theoretical capacitance of a full cell (C_{LIHC}) from the capacitances and the relevant masses of the anode and cathode materials from their half-cell characterisation (C_{anode}, $C_{cathode}$, m_{anode} and $m_{cathode}$ respectively). Using equation 2.48, the theoretical peak capacitance was calculated to be for a mass ratio of 2:1 cathode to anode.[260]

The lithium-ion AC//TNO device was then subjected to galvanostatic cycling at a range of specific currents from 0.25 to 2 A g^{-1} over the potential range 1.2 to 4.2 V to investigate the electrochemical performance. It was observed that the overall shape of the GCD curves exhibit the triangular shape associated with fast faradaic charge storage but do not adhere perfectly to the response of purely capacitive behaviour which is seen for classical EDLC devices (Figure 3.9a and 3.9b).[261] At all specific currents tested, upon discharge an IR drop was observed (highlighted in Figure 3.9b). At the highest specific currents tested, the size of the IR drop was greater than 1V, this is suggestive of the charge transfer resistance being a limiting factor for the high power performance of the hybrid cell and highlights the need to focus on methods to improve the conductivity of the metal oxide electrodes for future research.[262]

EIS analysis of the AC//TNO hybrid was used to determine the time relaxation constant, this value represents the time taken for the cell exhibit a current response to a voltage stimulus as well as giving the maximum frequency of an AC sinusoidal current input that can be received before the device switches from capacitive to resistive behaviour.[210] The time relaxation constant and resonance frequencies have been reported as figures of merit for the performance of supercapacitors in literature. The plot of reactive power ([Q/S]) and active power ([P/S]) vs. log of frequency was used to identify the cross over point of the two

curves and subsequently the resonance frequency, which was determined to be 7.2 Hz (Figure 3.9c). Equation 1.47 was used to calculate the time relaxation constant to be 22.06 ms. Further analysis of the GCD testing showed the AC//TNO hybrid to have a specific energy of 134 Wh kg^{-1} at a specific power of 300 W kg^{-1}. At a high specific power of 2020 W kg^{-1}, the specific energy was found to be 12 Wh kg^{-1}. These energy and power values were compared to other hybrid devices of metal oxide/carbon composite materials such as titanium or niobium oxides with carbon nanotubes or graphene (Figure 3.9d). At low specific power, the AC//TNO hybrid has a higher specific energy than the m-Nb_2O_5-C//MSP-20 and G-LTO//G-SU materials plotted.[261,263] However, at high specific power, the performance of the metal oxide/carbon composites outstrips that of the AC//TNO, this further highlights the gains in electrochemical performance that could be attained from pursuing TNO/carbon composite materials in future research.[264]

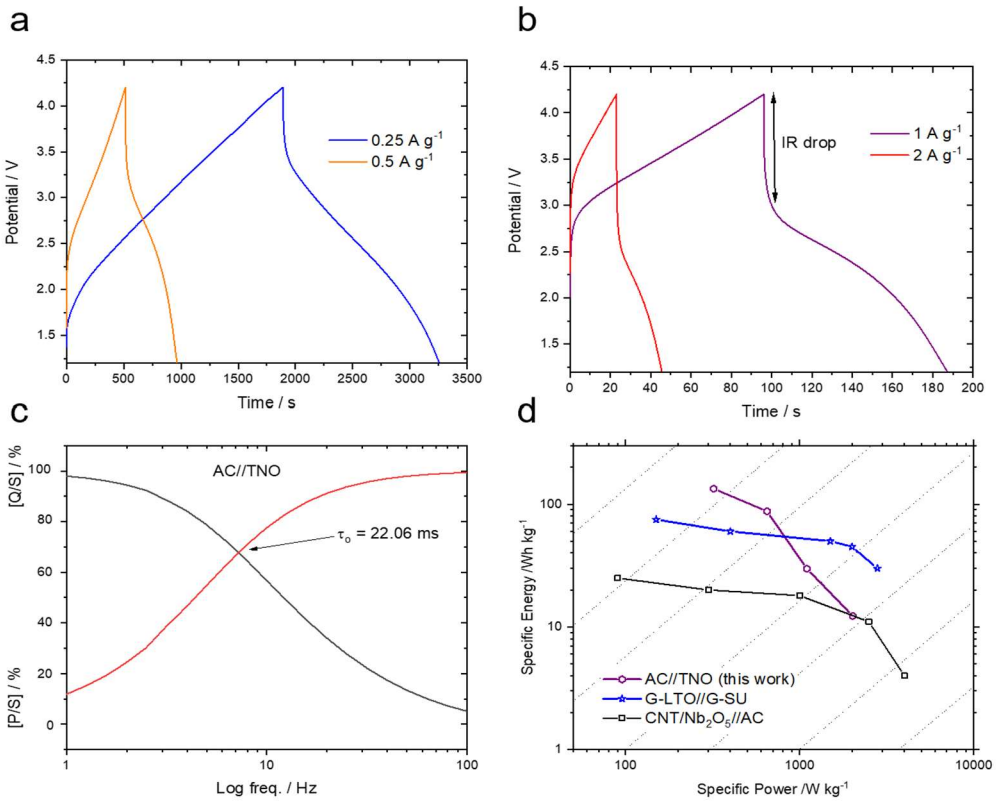

Figure 3.9: Graphs showing the GCD curves of the AC//TNO hybrid cells at specific currents of (a) 0.25 and 0.5 A g^{-1}, (b) 1.0 and 2.0 A g^{-1}. (c) a graph plotting the log frequency against the reactive (black) and active (red) power components, with the resonance frequency and its resulting time relaxation constant labelled. (d) Ragone plot comparing the specific energy and power metrics of AC//TNO hybrid cells against other similar hybrid cells reported in literature, data compiled from references [265,267].

3.4.3 Li^+ Diffusion Investigation

The method used to determine the diffusion coefficient of lithium ions through the CHFS TNO material was GITT analysis of the delithiation process (Figure 3.10a). The diffusion coefficients were calculated to be in the range of 10^{-15} cm^2 s^{-1} over the potential window during delithiation of the active material. As a function of potential, D_{Li} was observed to initially increase with potential up to a maximum of 1.88 $x10^{-15}$ at 1.5 V, beyond this the value decreased slowly until 1.8 V where a small fluctuation was seen and then the value dropped sharply by factor of 10 and remains there up to the maximum potential (Figure 3.10b). This behaviour mirrors that seen in the CV curves, where the highest values for D_{Li} are observed at the potentials where redox peaks are observed. The drop in D_{Li} seen after 1.8 V suggests that the phase change to fully delithiated crystal is complete and the concentration of lithium in the active material is as good as zero and is supported by the lack of charge storage visible in the CV curve at this potential. The average diffusion coefficient for the delithiation was found to be 3.08 $x10^{-15}$. Both the behaviour and calculated values are higher but within the same range compared to other values that have been reported in literature for GITT experiments of individual and mixed titanium niobium oxides.[265–268]

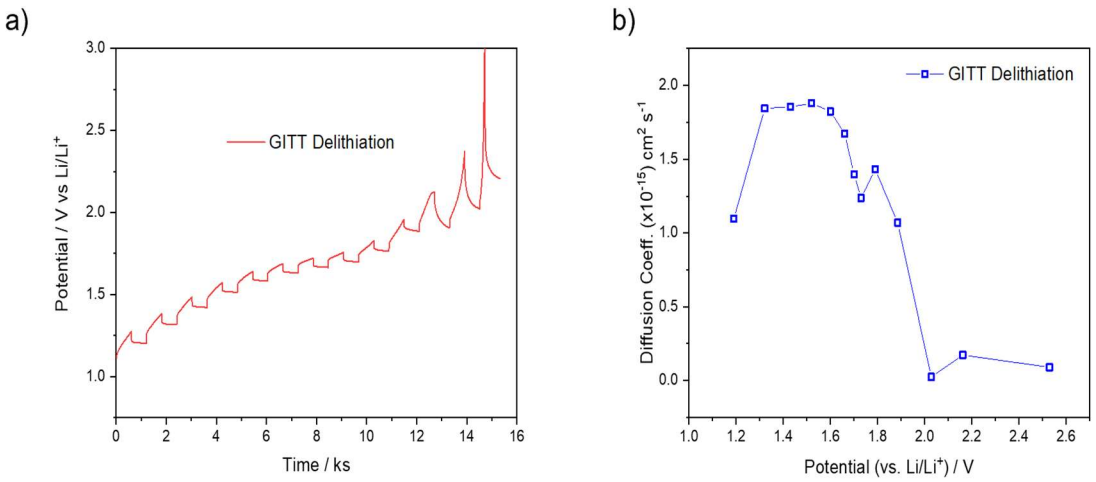

Figure 3.10: (a) Graph of the potential response vs. time for TNO with the GITT lithiation (red), (b) the calculated lithium diffusion coefficients as a function of potential (blue).

3.5 Carbon Titanium Niobium Oxide Composites

In order to further improve the electrochemical performance of the TNO materials synthesised via CHFS, a range of mixed titanium-niobium oxide carbon composite materials were synthesised using the procedure described in section 2.5.2. A range of increasing initial sucrose concentrations were investigated from 0.1 to 1.5 M (samples CTNO-1 to 7), the full table of metal salt and sucrose ratios synthesised are outlined in appendix Table 5.

3.5.1 Physical Characterisation of Carbon Titanium Niobium Oxide Composites

Post CHFS, the as-synthesised powders of carbon/titanium/niobium composites were subjected to a heat treatment protocol under nitrogen atmosphere at 750 ℃ for 3 hours to convert the carbonaceous material to graphitic carbon.[213] Initially, a wide range of increasing sucrose concentration materials from 0.1 to 1.75 M were synthesised, these samples were denoted as CTNO 1-6. The CTNO powders were analysed by PXRD post heat treatment (Figure 3.11), the diffraction patterns were found to be very broad in nature with only a few peaks observable in the materials with lower metal oxide to sucrose ratios. As the concentration of sucrose increased, the PXRD patterns were found to be become

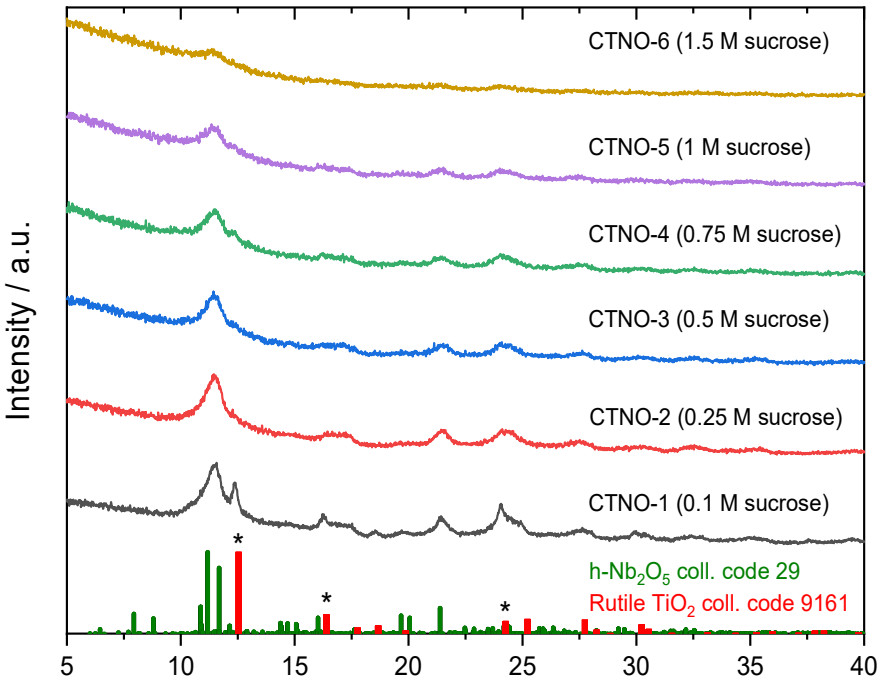

Figure 3.11: Graph showing the PXRD plots of the CTNO materials post heat treatment, with the reference patterns of niobium pentoxide (ICSD coll. code 29) and rutile titanium dioxide (ICSD coll. code 9161).

more broad and less well-defined. The peaks that were observable were located at 2θ = 11.4, 12.4, 16.2, 21.3 and 24.1 °. Identification of the peaks indicated a mixture of at least two different phases, with the peaks at 12.4, 16.2 and 24.1 ° being a close match for rutile TiO_2 (red and asterisked, ICSD collection code 9161),[269] and the peaks at 11.4 and 21.3 ° a potential match for monoclinic h-Nb_2O_5 (green, ICSD collection code 29).[270]

The diffraction values for the rutile TiO_2 were found to exhibit a slight shift to lower 2θ values compared to literature, this could be an indication of lattice expansion due to the substitution of niobium ions into the titania structure.[219] Due to the broad nature of the diffraction patterns, it was not possible to identify if any monoclinic $TiNb_2O_7$ was present in the materials.

To investigate if the lower temperatures employed for the carbonisation step were affecting the precipitation of the high performing $TiNb_2O_7$ crystal phase, the CTNO-3 (0.5 M sucrose) material was subjected to a heat treatment of 900 ℃ for 3 hours under a nitrogen atmosphere. PXRD analysis showed that the higher temperatures caused the rutile TiO_2 phase to become dominant with sharp well-defined peaks and the peaks for Nb_2O_5 to still be present but have a much smaller relative intensity (appendix Figure 8).

XRF was used to determine the relative ratios of the titanium and niobium ions, it was found that the presence of the sucrose in the aqueous solution prior to CHFS caused the precipitation of the metals to change. All CTNO materials showed a large decrease in the relative niobium content compared to the initial metal ratios before CHFS. At the lowest sucrose concentration of 0.1 M (CTNO-1), the atomic percentages of titanium and niobium were found to be 51.7 % and 48.3 % respectively. The titanium and niobium contents were found to shift towards higher amounts of titanium and lower amounts of niobium as the sucrose concentration increased, CTNO-3 was found to have a titanium content of 66.3 % and a niobium content of 33.7 %. This supports the PXRD findings of the dominant crystal phase being titanium dioxide and the possibility for niobium ions to have substituted into the titania structure due to the niobium content being high relative compared to the presence of pure niobium oxide phases. The full table of elements and their relative percentages for all CTNO materials is located in appendix Table 11.

TEM imaging of the different CTNO materials revealed large agglomerates of particles, which upon magnification revealed particles of metal oxide within a carbonaceous material (appendix Figure 9a and 9b). As the relative sucrose concentration was increased, the size of the agglomerates was found to increase with no well-defined lattice fringes observable (appendix Figure 9c and 9d).

EDS analysis of TEM images of CTNO-3 showed that the agglomerates contained titanium, niobium, carbon, and oxygen all intimately mixed (appendix Figure 10). The quantities of each metal were found to be a good match for the XRF data. This supports the concept of particles of mixed titanium and niobium oxides embedded in a carbon matrix. The nature of the carbon was investigated by Raman spectroscopy. It was found that for all of the CTNO materials post heat treatment, large bands at ~1380 and ~1590 cm^{-1} were observed, these were identified as the D and G bands, which correspond to the sp^3 and the sp^2 hybridised carbon respectively (Figure 3.12).[271] Carbon that was sp^3 hybridised would contain lower electronegative sigma C−C bonds and sp^2 hybridised carbon would contain higher electronegative pi C=C bonds. The intensity ratio between the D and G bands, I_D/I_G, has been reported to reflect the level of graphitisation of the carbon.[272] All of the CTNO materials were calculated to have intensity ratios

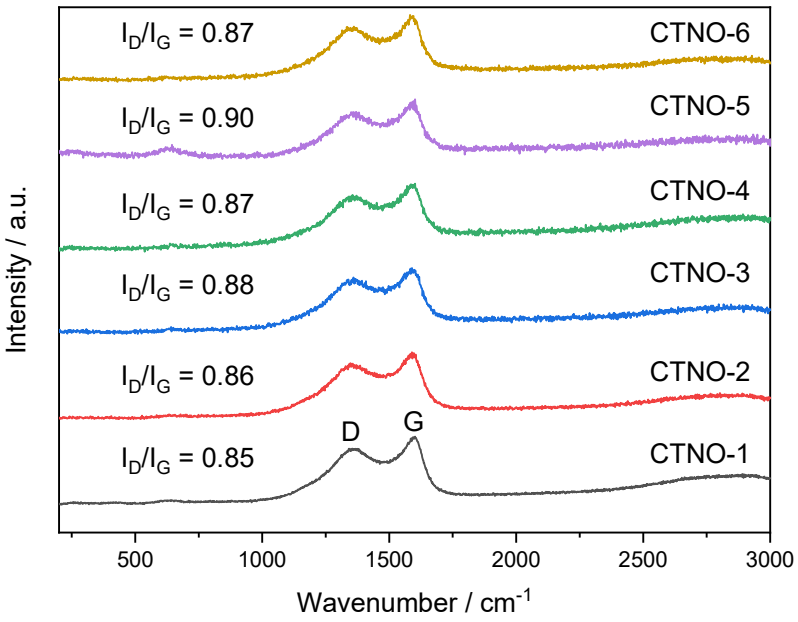

Figure 3.12: Graph showing the Raman plots of the CTNO materials post heat treatment with the D and G bands identified and the I_D/I_G ratio for each spectra shown.

between 0.85 and 0.90, suggesting high levels of graphitic sp^2 carbon was present. Previous studies of carbon coated LFP have shown that a low value for I_D/I_G corresponds to a higher electronic conductivity and therefore improved electrochemical performance.[273]

BET analysis showed a large increase in the surface area of the CTNO materials compared to the pure CHFS TNO. The surface areas of CTNO-1, CTNO-2, CTNO-3, CTNO-4, CTNO-5, and CTNO-6 were found to be 71.6, 256.4, 240.3, 225.9, 238.8 and 208.4 $m^2\ g^{-1}$ respectively.

3.5.2 Electrochemical Characterisation of Carbon Titanium Niobium Oxide Composites in Lithium-ion Batteries

The CTNO materials were manufactured into electrodes and tested in half-cell configurations against lithium metal counter electrodes over the voltage range 3-1 V vs. Li/Li^+. Cyclic voltammetry at a scanrate of 0.5 mV s^{-1} of CTNO-1 revealed a CV curve with a similar shape to that of CHFS TNO with a large area and broad anodic and cathodic peaks in the potential window of 2.1 to 1.1 V vs Li/Li^+. The overall broad shape was attributed to pseudocapacitive charge storage interactions with Nb_2O_5 particles that has been reported for similar materials with low crystallinity.[274] Within the CV, a pair of redox peaks at 1.91 and 1.42 V vs. Li/Li^+ were observed and assigned to the intercalation reaction of lithium ions into niobium oxide and the redox couple of Nb^{5+}/Nb^{4+} (Figure 3.13a).[246] A few other small shoulders were observed at 2.09 and 1.11 V vs Li/Li^+. These were attributed to the redox couples of Ti^{4+}/Ti^{3+} and Nb^{4+}/Nb^{3+} respectively.[268,275] This behaviour was found to be consistent for all other CTNO materials apart from CTNO-6 which had a large box-shape area and no well-defined redox peaks (appendix Figure 11). The CTNO materials were then subjected to long term cycling at the high specific current of 2 A g^{-1} to investigate the capacity retention (Figure 3.13b). It was found that all of the CTNO materials performed well with the initial specific capacities being 140, 253, 398, 241, 165 and 145 mAh g^{-1} for CTNO-1, 2, 3, 4, 5 and 6 respectively. It was observed that some of the materials displayed an increase in specific capacity over the first 20 to 30 cycles before stabilising, this could be associated with increased access of the electrolyte to active sites within the material due to wetting and formation of a stable SEI passivation layer.[276] Over the next 150 cycles, the capacity retentions were calculated to be 98, 83,

90, 93, 96, and 95 % respectively. The highest performing material, CTNO-3 at high specific currents of 5, 10 and 15 A g^{-1} gave specific capacities of 197, 145 and 108 mAh g^{-1}, all of which outperformed CHFS TNO at the same currents (Figure 3.13c). The low current capacity values of CTNO-3 was also found to outperform other carbon coated titanium/niobium oxide materials synthesised via different methods reported in literature.[277] EIS performed on the CTNO materials showed CTNO-1, 2, and 3 to have small semi-circles on the nyquist plots, but CTNO-4, 5 6 had much larger semi-circles and subsequent CTR values (appendix Figure 12). One possible explanation for this could be due to the large carbon content visible from TEM/EDS relative to the metal oxides, the interfacial distances between particles is too far for good electrical conductivity, suggesting that these materials would benefit from electrode engineering processes such as calendaring.[278]

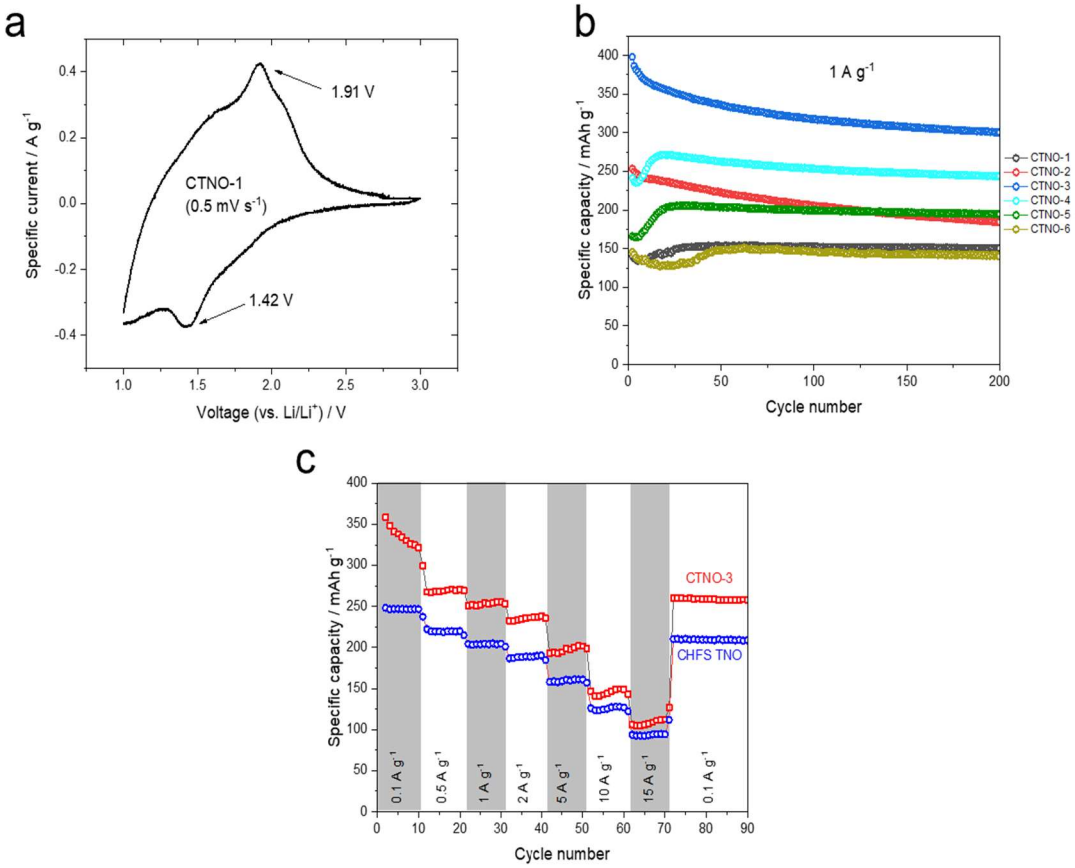

Figure 3.13: graphs showing (a) the CV curve at 0.5 mV s^{-1} for CTNO-1 (b) long term GCD cycling at 1 A g^{-1} for all six CTNO materials, and (c) specific capacity vs. cycle number plots of CTNO-3 and CHFS TNO.

3.6 Conclusions

A CHFS assisted synthesis method was used to create single phase monoclinic $TiNb_2O_7$, it was found that specific basic and heat treatment conditions played a significant role in the formation of the desired phase and in avoiding any impurities. TEM imaging identified particles with an average diameter <100 nm that exhibited high crystallinity. The BET surface area of the CHFS TNO was found to be 5 $m^2\ g^{-1}$. CHFS TNO was characterised electrochemically in lithium-ion half-cells, the CV curves were calculated to contain high proportions of pseudocapacitive charge storage at scan rates of 0.1 and 10 mV s^{-1} (82 and 96 % respectively). This high proportion of pseudocapacitive charge storage was attributed to the nanosized particles and the high surface area, which promoted more redox active centres to the surface of particles thereby enabling them to participate in fast faradaic charge transfer reactions. Galvanostatic cycling found the reversible capacity of CHFS TNO to be 248 mAh g^{-1} at 0.1 A g^{-1}, with a capacity retention of 76 % at a specific current of 2 A g^{-1}. This highlights the excellent rate performance of the CHFS TNO. Over long-term GCD cycling, the capacity retention was found to be 96% over 120 cycles at 0.1 A g^{-1}. The CHFS TNO was constructed into an anode material for hybrid lithium-ion capacitors with the cathode as activated carbon. This device was found to exhibit a specific energy of 134 Wh kg^{-1} at a specific power of 300 W kg^{-1}. When the specific power was increased to 2020 W kg^{-1}, the corresponding specific energy was found to be 12.3 Wh kg^{-1}. The kinetics of lithium diffusion through the CHFS TNO material were investigated by GITT delithiation, from which D_{Li} was calculated to be in the range of 10^{-15} $cm^2\ s^{-1}$. This was found to be higher than but within the same range than other literature values calculated using the same methods on related materials. One possible explanation for the improved diffusion coefficients could be the nano-sized particles reducing the physical distance travelled by the lithium ions.

The addition of sucrose to the CHFS process followed by a heat treatment protocol was used to synthesise a range of composite carbon-titanium/niobium oxide materials. PXRD indicated that the materials consisted of rutile TiO_2 with a slight peak shift suggesting Nb ions were doped into the structure, and a few very broad peaks that were assigned to poorly crystalline niobium oxide. TEM and

EDS revealed agglomerates of very small particles of intimately mixed titanium and niobium oxides within a carbon matrix. Raman analysis of the carbon indicated a high proportion of graphitic carbon was present. Cycling in lithium half-cells showed the CTNO materials had improved electrochemical performance compared to pure TNO at both low and high specific currents, with the capacity at 0.1 and 10 A g^{-1} being found as ~330 and 197 mAh g^{-1} respectively. These results have successfully investigated and showcased the application of CHFS to synthesise targeted nanomaterials for energy storage, explored the electrochemical properties and diffusion kinetics through a range of different methods, and shown the electrochemical benefits that can be achieved through in-flow formation of carbon/metal oxide composite materials. The excellent electrochemical performance of both CHFS TNO and CTNO as lithium-ion anode materials and the simplicity of scalability of the synthesis method all indicate the potential for these materials to be applied in high-energy, high-power devices.

3.7 Outlook

Following on from the research reported and discussed above, the benefits of using a continuous hydrothermal flow method for materials synthesis are clear to see for high performing anode materials such as TNO. Therefore, future work should focus on several avenues of research, the first is the application on the synthesis philosophy to other materials of interest that could benefit electrochemically from the process. Another area of research should be the scaling up from laboratory to pilot, as with many possible battery material candidates the issues of scale up are not considered or addressed and therefore are unable to have a meaningful, widespread impact on energy storage technology. Another large direction for future research is that of carbon/metal oxide composites, the ease of synthesis, ability to form complex multi-metal materials and achieve coated nanoparticles all aspects that could easily and successfully be applied to a wide range of other candidates. The use of different carbon sources and the integration of more complex carbon structures such as nanotubes or graphene sheets would be of interest for battery materials development.

4.0 Combinatorial Study of Mixed Vanadium, Niobium, Molybdenum Oxides for High Power Anodes

'*What man actually needs is not a tensionless state but rather the striving and struggling for some goal worthy of him*' – Viktor Frankl

4.1 Aims

The electrochemical performance of metal oxides such as VO_2 and MoO_2 have been shown to be improved by co-synthesising with other transition metals that can form the same crystal phase to give solid solutions. The aim of this work is to investigate the composition-performance relationships of the mixed metal oxides $V_xNb_yMo_zO_2$ (X + Y + Z = 1) to identify the best performing material at both low and high specific currents in Li-ion batteries and hybrid capacitors.

4.2 Introduction

In the design of high performing conversion mechanisms materials for anodes the issues surrounding low intrinsic conductivity and capacity fade due to volume changes during cycling must be addressed.[52] Of the possible metal oxides being investigated for use as anodic materials, molybdenum oxide (MoO_2 and MoO_3) have both been identified as very high capacity materials that exhibit a conversion mechanism.[54,279] These mechanisms gives molybdenum oxides very high specific capacities (838 mAh g^{-1} for the dioxide and 1117 mAh g^{-1} for the trioxide).[280] The equations for the conversion reaction of MoO_2 are given below in equation 4.1 and 4.2:

$$MoO_2 + \sim Li^+ + \sim e^- \leftrightarrow Li_{0.98}MoO_2 \quad (4.1)$$

$$Li_{0.98}MoO_2 + \sim 3Li^+ + \sim 3e^- \leftrightarrow Mo + 2Li_2O \quad (4.2)$$

However, it has been found that the conversion mechanism causes large volume changes upon lithiation and delithiation, which can cause pulverisation of the electrode. These effects are most pronounced in the bulk material.[281] Strategies to combat this have focused on producing nanostructured metal oxides as this can reduce the diffusion length, allow for a greater surface area between electrode and electrolyte, and help to reduce the destructive swelling effects of cycling.[282] An example of this were the yolk-shell MoO_2 nanostructures

synthesised by Zhang *et al.* which exhibited 847.5 mAh g^{-1} after 50 cycles at 0.5 A g^{-1}.[283] Different nanostructure morphologies have been reported, such as nanowires of α-$MoO_3.H_2O$ that gave a specific capacity of 954.8 mAh g^{-1}.[284] Other methods have included forming particles of mixed oxidation states which had a high capacity of 930.6 mAh g^{-1} and a cycle life of over 200 cycles.[280] Many examples of forming nanostructures of molybdenum oxides and conductive additives of coatings such as exfoliated graphene oxide/MoO_2,[285] MoO_2/MWCNT,[286] and MoO_2@carbon hollow nanospheres,[287] have all been reported with high capacities and improved cycling stability, however the formation of such complex nanostructures leads to difficulties when attempting to scale the synthesis as well as the reduction in density by introducing low capacity carbonaceous materials.[280]

In contrast to the conversion mechanism of molybdenum oxides, other transition metal oxides that are of high interest to researchers include vanadium and niobium oxides. Vanadium oxides such as vanadium dioxide (VO_2) are of interest due to the relatively low cost, ability to show multiple oxidation states, and form layered structures. However they suffer from low stability due to deformation during cycling.[288–290] Niobium oxides are also of high interest, this is due to the vast range of different morphologies that they can form, the ability to exhibit extrinsic pseudocapacitive charge storage, and critically they can intercalate lithium ions without massive volume changes. However they suffer from low intrinsic conductivity and lower capacities than other materials discussed here.[291,292]

Further developments in the performance of the transition metal oxides discussed above can be found when not just considering the individual materials but the binary and ternary iterations. The presence of different crystal morphologies, elements and oxidation states in the same particles together can lead to synergistic effects and interactions such as the sharing of electron density thereby changing the local electric structure, allowing for the creation of more accessible crystal morphologies and the promotion of different redox sites to the surfaces where they can more easily interact with charge carriers.[65,293] Due to the ability of both molybdenum and vanadium dioxide to form monoclinic crystal morphologies, the two materials are able to mix together as dopants in each in

other at low concentration and eventually as solid solutions at equal concentrations.[173] It was shown by Bauer *et al.* that nanoparticles of $Mo_{0.5}V_{0.5}O_2$ showed a solid solution morphology, as well as excellent electrochemical performance at both low and high currents (200 mAh g^{-1} at 10 A g^{-1}). This was attributed to high levels of pseudocapacitive charge storage. It was also found that the cycle life of the mixed metal oxides was improved, 480 mAh g^{-1} after 150 cycles at 0.5 A g^{-1}). Further examples include; a 3D hierarchically ordered VO_x/MoO_y[294] oxide which could deliver a specific capacity of 440 mAh g^{-1} over 400 cycles at 4 A g^{-1}; nanorods of $VO_x@MoO_3$ that were synthesised via electrochemical deposition onto carbon electrodes and were found to give an increase in the performance by a factor of 2 when compared to the same carbon electrodes with only molybdenum trioxide deposited.[293] These examples all highlight the performance benefits of creating mixed vanadium/molybdenum oxide materials, however other factors such as surface area and differences in testing protocols must be noted when making direct comparisons between studies.

Herein this chapter the use of CHFS for combinatorial chemistry as a method of materials discovery is reported. A range mixed V-Nb-Mo metal oxides across the compositional space of a ternary plot (Figure 4.1) where synthesised and characterised physically using methods such as PXRD, XRF, BET, TEM, EDS, Raman and XPS to elucidate correlations between composition and material properties. The mixed metal oxide materials were then characterised in lithium half-cells to evaluate their electrochemical performance, with relation to composition and identify materials that exhibit high capacity at both low and high currents. From this the high performing material $V_{0.3}Nb_{0.1}Mo_{0.6}$ was identified and investigated in depth to ascertain its applicability to both lithium and sodium ion high power and high energy storage devices.

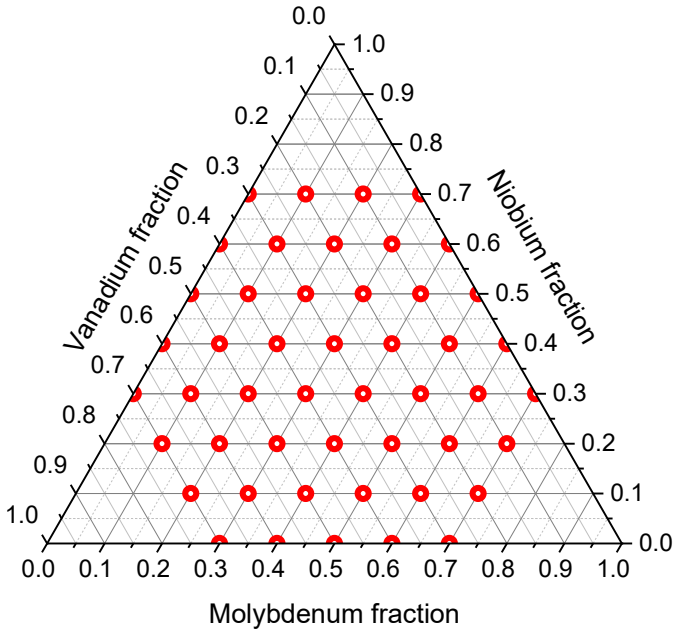

Figure 4.1: a) Ternary plot of vanadium, niobium and molybdenum with the compositions synthesised shown as red dots.

4.3 Experimental Methods

4.3.1 Synthesis of Mixed Vanadium, Niobium, Molybdenum Oxides

The compositions calculated from the ternary plot for both the first and second stages of the study were synthesised as described in section 2.4.2. The mixed V-Nb-Mo oxide materials herein were denoted using numbers to represent the relative nominal ratio of each of the metals at the point of synthesis, for example the material $V_{0.7}Nb_{0.2}Mo_{0.1}$ was labelled as VNM721.

4.3.2 Physical Characterisation

The physical characterisation methods utilised are described in section 2.1.

4.3.3 Electrochemical Characterisation

The formation of electrodes is described in section 2.2.1. The construction of half-cells and hybrid capacitor cells are described in section 2.2.2. The electrolyte used was 1M $LiPF_6$ in 1:1 v/v EC/EMC.

The electrochemical characterisation of half-cells involved: GCD cycling at a range of different specific currents including, 0.1, 0.2, 0.5, 1, 2, 5, and 10 A g^{-1} over the potential window 0.05 to 3 V vs Li/Li^+ performed by an Arbin Instrument (Model BT-2000 battery tester, US). Cyclic voltammetry (CV) was completed over

the same potential window at range of increasing scanrates including 0.05, 0.1, 0.2, 0.5, 1, 2, 5, 10, 20, 50 and 100 mV s^{-1}. Potentiostatic EIS was performed by a Gamry Interface 1000 Potentiostat, over the sinusoidal frequency range 100 kHz to 10 mHz. The oscillating alternating current voltage was set to 10 mV ms^{-1} with the area as 1 cm^2 and 10-point measurements.

The hybrid capacitor cells were electrochemically evaluated by GCD and CV analysis. Both were performed by a Gamry Interface 1000 Potentiostat (Gamry Instruments, USA) in the voltage window 1 to 4.2 V.

4.4 Results and Discussion

4.4.1 Physical Characterisation of Nominal Mixed Vanadium, Niobium, Molybdenum Oxides

All of the VNM materials were analysed by PXRD, Figure 4.2 shows a selection of the PXRD patterns from across the compositional space. All of the materials synthesised with high nominal concentrations of vanadium and niobium exhibited patterns with few peaks present apart from a few very broad peaks as shown by VNM172 and VNM613 (Figure 4.2).

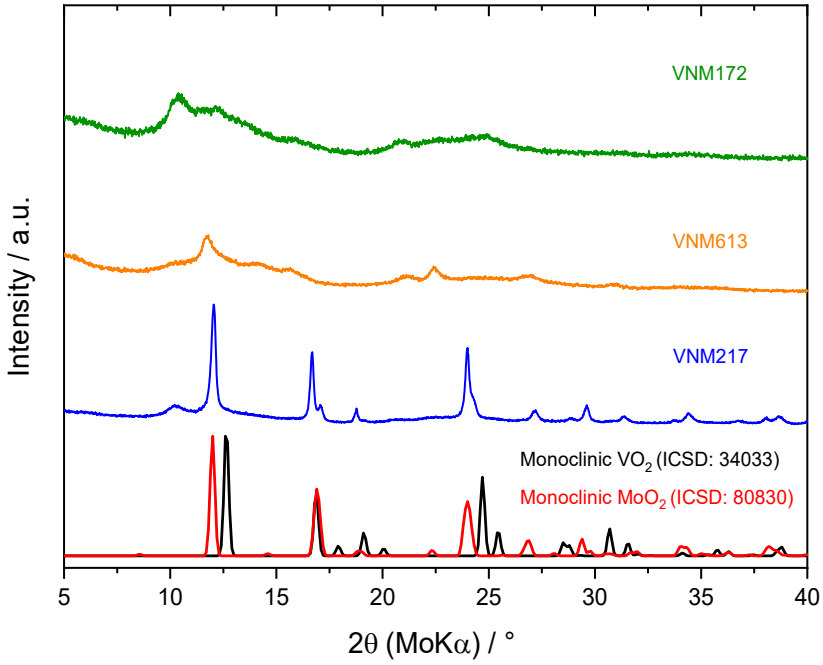

Figure 4.2: graph showing PXRD patterns of monoclinic VO_2 ICSD no. 34033 (black) VNM172 (green), VNM613 (orange) and VNM217 (blue).

This behaviour is suggestive of both small particle size and high levels of amorphous material, and has been reported previously for niobium oxide materials synthesised by a CHFS method.[167] The VNM materials with higher proportions of molybdenum present were found to exhibit the monoclinic MoO_2 crystal phase. The presence of this as the dominant crystal phase was unaffected by the addition of niobium to the mixed metal oxide. Figure 4.3 shows the PXRD plots of the niobium containing and niobium free analogue materials VNM316 and VNM406. Both materials display peaks at 2θ = 12.7, 16.9 and 24.7 °, which are characteristic of both monoclinic MoO_2 (ICSD no. 80830, space group $P1_{21/c1}$)[295] and monoclinic VO_2 (ICSD no. 34033).[296] The peaks present display a slight shift to higher angles for both materials from the MoO_2 reference pattern. The reference pattern for monoclinic VO_2 is almost identical to that of monoclinic MoO_2 except for two small peaks at 2θ = 19 and 25.5 ° which are present in the patterns for both VNM316 and VNM406 (marked by an asterisk).[296,297] This suggests that the crystal structure of both materials is a solid solution of both monoclinic MoO_2 and VO_2.

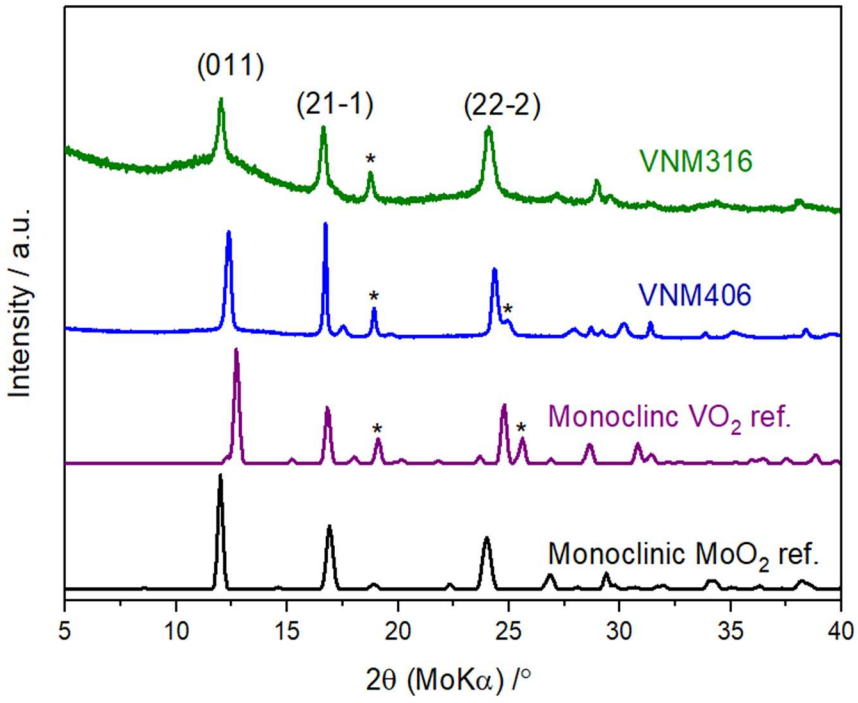

Figure 4.3: PXRD patterns of VNM316 (green), VNM406 (blue), monoclinic VO_2 (ref. 22, purple) and monoclinic MoO_2 (ref. 23, black).

The presence of the niobium ions was found to cause peak broadening in VNM316 compared to VNM406 and a peak shift in the (011) peak to a lower 2θ value by 0.33 °, this suggests that the Nb ions are doping into the crystal structure rather than forming a distinct phase or amorphous material that is separate from the V/Mo oxide.[298]

Whole pattern fitting was performed using a Le Bail method for both VNM316 and VNM406 PXRD patterns. Fitting to the space group $P1_{21/c1}$ gave lattice parameters which are reported below in Table 4.1 along with the reported lattice parameters for the reference patterns. It was found that the addition of niobium in the material VNM316 compared to VNM406 gave a slight increase in the size of the parameters a, b, angle β and cell volume, this further supports the theory that Nb ions are doping into the crystal structure.

	Lattice parameters				
Compound	a / Å	b / Å	c / Å	β / °	Cell vol. / Å^3
VO_2 ref. 26	5.7517	4.5378	5.3825	122.646	118.29
MoO_2 ref. 25	5.6096	4.8570	5.6259	120.912	131.51
VNM406	5.6555	4.6427	5.4066	124.180	117.44
VNM316	5.6873	4.7141	5.3939	125.015	118.44

Table 4.1: Table showing the reported lattice parameters for monoclinic VO_2 (ref 22) and MoO_2 (ref 23) compared to the calculated lattice parameters for VNM406 and VNM316 determined by Le Bail whole pattern fitting.

The BET surface area of a range of the VNM materials were measured and were found to vary across compositional space, with the materials VNM163, VNM145, VNM262, VNM226, VNM451, VNM433, VNM415 and VNM631 found to be ca. 218, 230, 182, 39, 97, 5, 3 and 15 $m^2\ g^{-1}$, respectively. The overall trends suggested that the higher the relative proportion of niobium present in the materials the higher the surface area, supporting the idea of greater levels of amorphous nature present in the high niobium materials.

The oxidation states of the metals present in selected samples of the VNM materials were analysed by XPS. The survey scan confirmed the presence of V, Nb, Mo and O in the samples. Figures 4.4a and 4.4b show the high-resolution scan for V2p of both VNM406 and VNM316 respectively. Both the $V2p_{1/2}$ and

$V2p_{3/2}$ peaks of the materials were fitted with two components for the V^{5+} and V^{4+} oxidation states.[299] For the material VNM406, the two components of the $V2p_{3/2}$ peak were located at 517.3 and 516.4 eV, these were assigned to the V^{5+} and V^{4+} oxidation states respectively and were found to have a relative ratio of 14:1. In comparison, the $V2p_{3/2}$ peak for VNM316 was deconvoluted to give the same oxidation states but with a relative ratio of 1.4:1 thereby indicating a far greater presence of V^{4+}. There was also a slight peak shift detected in the $V2p_{3/2}$ peak of VNM316, with the binding energies being 0.1 eV lower compared to VNM406. This suggests the presence of V-O-Nb interactions due to the lower electronegativity of vanadium compared niobium causing electron density to be pulled away from Nb and towards V changing their binding energies.[293] This trend was also seen in the high resolution scan for Mo3d for both VNM406 and VNM316 materials (Figures 4.4c and 4.4d correspondingly). The $Mo3d_{5/2}$ and $Mo3d_{3/2}$ peaks for VNM406 were found to have binding energies of 232.4 and 235.6 eV respectively, these were found to correspond to the Mo^{6+} oxidation state.[300] For VNM316, the $Mo3d_{5/2}$ and $Mo3d_{3/2}$ peaks were found to have shifted slightly to higher binding energies of 232.7 and 235.8 eV respectively suggesting the presence of Mo-O-Nb interactions through which niobium ions pull electron density away from molybdenum ions through the metal-oxygen-metal bonds. The high resolution scan of Nb3d for VNM316 identified a doublet of peaks, in which the $Nb3d_{5/2}$ peak was located at 206.9 eV with a spin orbit coupling of 2.78 eV, these correspond to the Nb^{5+} oxidation state (Figure 4.4e).[301]

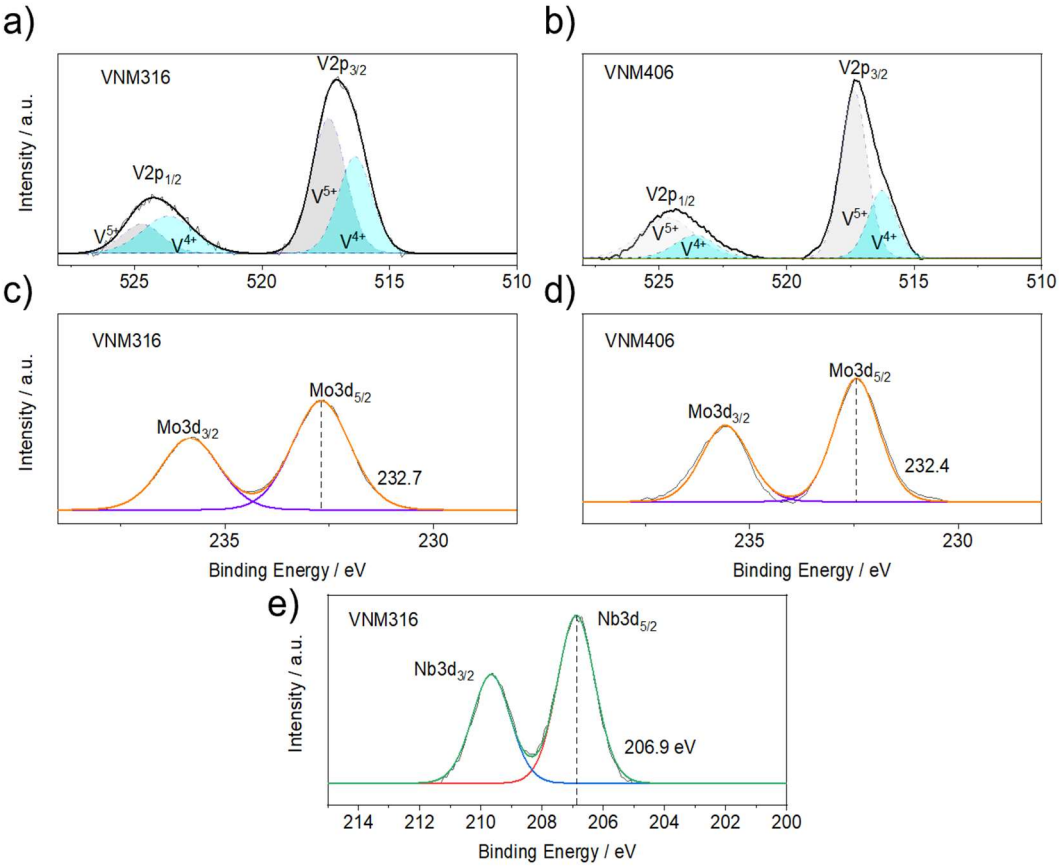

Figure 4.4: Fitted XPS spectra of high-resolution scans of V2p for (a) VNM316, (b) VNM406, fitted XPS spectra of high-resolution scans of Mo3d for (c) VNM316, (d) VNM406, (c) fitted XPS spectra of high-resolution scan of Nb3d of VNM316.

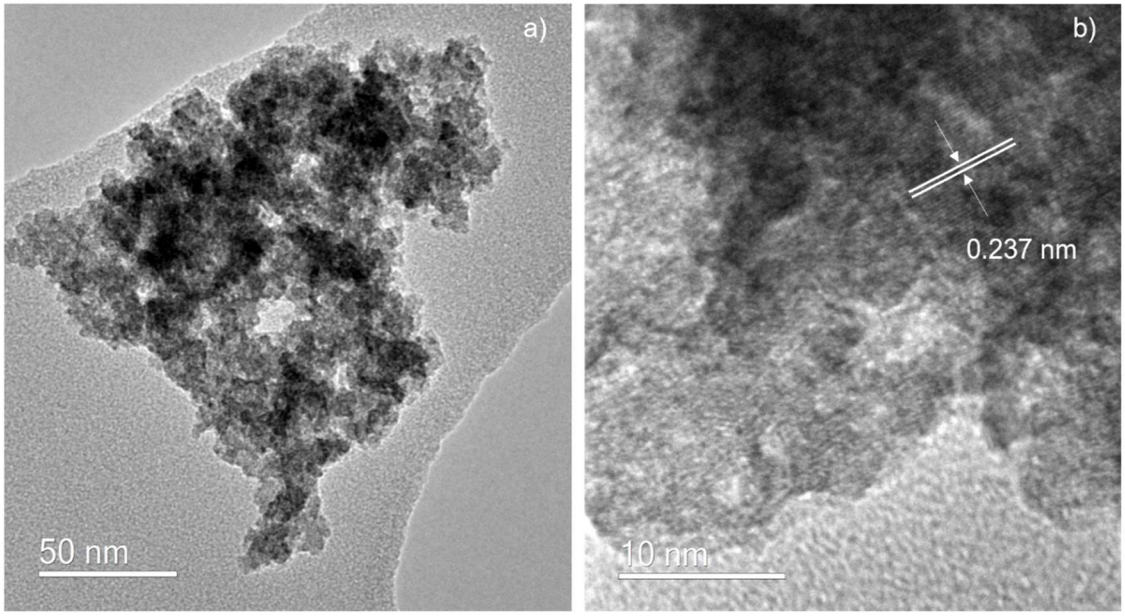

Figure 4.5: TEM images of (a) an agglomerate of VNM particles, (b) high-magnification image of a VNM particle with the lattice fringes and spacings highlighted.

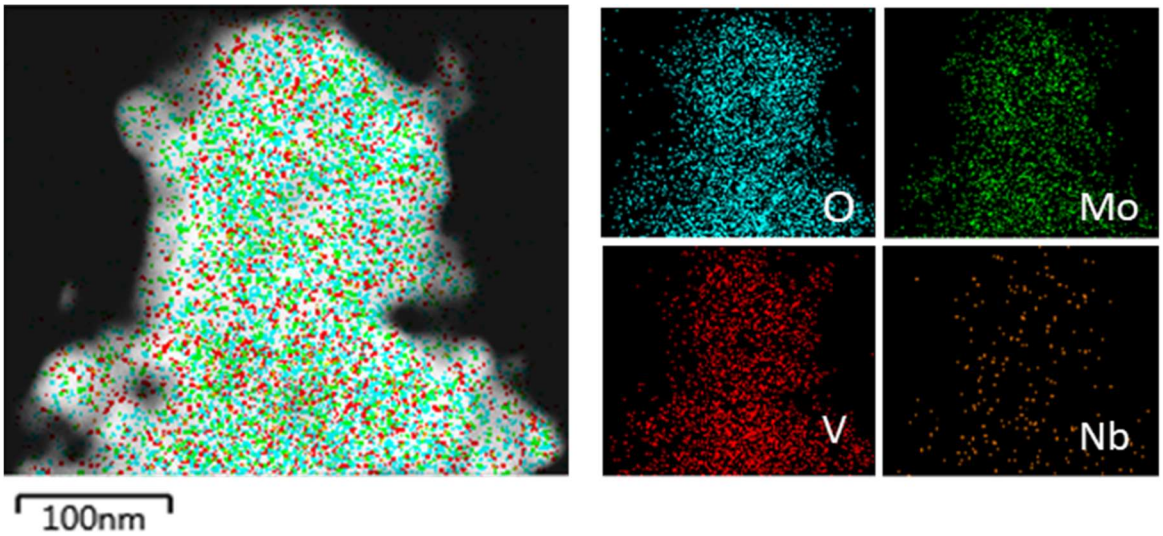

Figure 4.6: TEM/EDS scans of VNM316 for the elements O (blue), Mo (green), V (red) and Nb (orange).

TEM of the VNM316 material was used to investigate the morphology of the metal oxide particles. It was found that the particles were agglomerates of very small particles that had coalesced together (Figure 4.5a). Upon magnification, the particles displayed lattice planes with a lattice plane spacing measured as 0.237 nm, this was found to be fractionally smaller than the (111) plane of monoclinic MoO_2 (0.240 nm), and further supports the XRD findings that the additional V and Nb ions were doping into the crystal structure causing a change in the lattice parameters.[302]

EDS mapping of TEM images was used to investigate the dispersion of the three metal oxides throughout the observed particles. Figure 4.6 shows a TEM image of VNM316 with the EDS map overlayed and the induvial elemental scans for V, Nb, Mo and O shown in red, green, orange, and blue respectively. From the elemental mapping, it was observed that the particles contained a very homogenous dispersion of metals, further supporting the suggestion of XPS for the presence of direct V-O-Nb, V-O-Mo, and Nb-O-Mo interactions. The elemental composition of VNM316 was analysed by X-ray fluorescent spectroscopy and was found to be a good match to the nominal composition.

4.4.2 Electrochemical Characterisation of Mixed Vanadium, Niobium, Molybdenum Oxides

4.4.2.1 Electrochemical Characterisation in Li-ion Half Cells

The VNM materials were initially investigated electrochemically as anodes in lithium half cells. The specific capacity data gathered at the specific currents of 0.1 and 5 A g^{-1} were plotted as a heat map overlayed onto the nominal compositional ternary diagrams (Figure 4.7 and Figure 4.8 respectively).

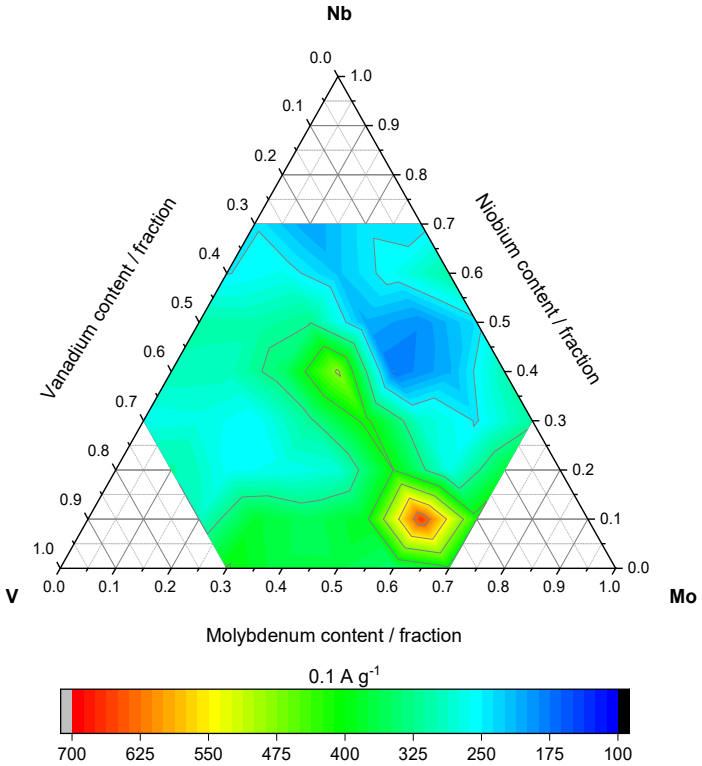

Figure 4.7: Ternary plot of nominal metal concentrations showing the specific capacity and crystal phase information of the VNM materials as a heat map for the specific currents 0.1 A g^{-1}.

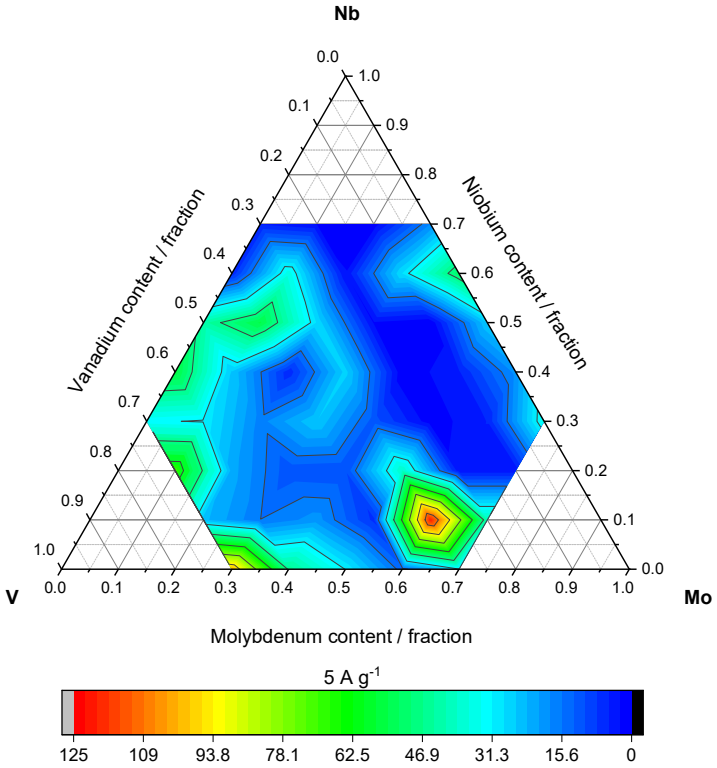

Figure 4.8: Ternary plot of nominal metal concentrations showing the specific capacity and the crystal phase information of the VNM materials as a heat map for the specific currents of 5 A g^{-1}.

The full range of heat maps of different specific currents tested can be found in appendix Figure 15a, 15b, 15c and 15d. Overall it can be observed that the materials that exhibit a single crystal phase show higher specific capacities that those that were found to be multiphasic or amorphous. The heat map ternary plots clearly identify the composition VNM316 as having the highest capacity for all the specific currents tested compared to all other VNM materials.

Due to the differences between the nominal compositions being 10 %, the topography of the heat maps is such that the highest performing composition of VNM316 appears to be a lone peak surrounded by much small peaks. In the pursuit of identifying high performing battery materials and investigating the relationships between composition, structure, and battery electrode performance, the 'lone peak' and its surrounding area require further investigation in greater detail to obtain a more complete picture of the topography as part of future work.

In order to investigate the good electrochemical performance exhibited initially by VNM316, half-cells of VNM316 and VNM406 with lithium metal counter electrodes were analysed by cyclic voltammetry (CV) across a range of scan rates in the potential range 3 to 0.05 V vs Li/Li^+. The first three cycles of VNM316 at a scan rate of 1 mV s^{-1} at shown in Figure 4.9a. Overall, the CV curves display a very broad nature with several electrochemical features observable. Over the first cycle, a pair of redox peaks at 1.6/1.5 and 1.1/1.0 V vs Li/Li^+ were observed. Both of these were attributed to the reversible charge storage reaction of molybdenum dioxide with lithium, in which the monoclinic MoO_2 undergoes a phase transition to orthorhombic partially lithiated Li_xMoO_2, then again to monoclinic $Li_{0.98}MoO_2$ and vice versa.[54] At much lower potentials, there is a large peak observable at 0.25 V vs Li/Li^+, this is characteristic of the conversion reaction of $Li_{0.98}MoO_2$ to Mo metal and Li_2O which can store large amounts of energy particularly at slower rates but has large volume changes and reduced long term stability associated with it. In addition to these redox peaks, there is one further very broad feature on the forward scan at 2.3 V vs Li/Li^+, however due to the broadness exhibited on the backwards scan, it is not possible to say with certainty if this feature represents a reversible process and the definition is being lost in the overall broad nature of the CV or if it is a non-reversible process.[237,280,286,303] Over the proceeding cycles the shape of the CV changes

very little with only very small changes in the size and position, this suggests the propensity for good cycling stability as well as the broad nature of the CVs indicating potential pseudocapacitive charge storage. When cycled at increasing scan rates (Figure 4.9b), the overall broad shape of the CVs stayed consistent indicating the possibility for good charge storage to occur at fast C-rates.[304]

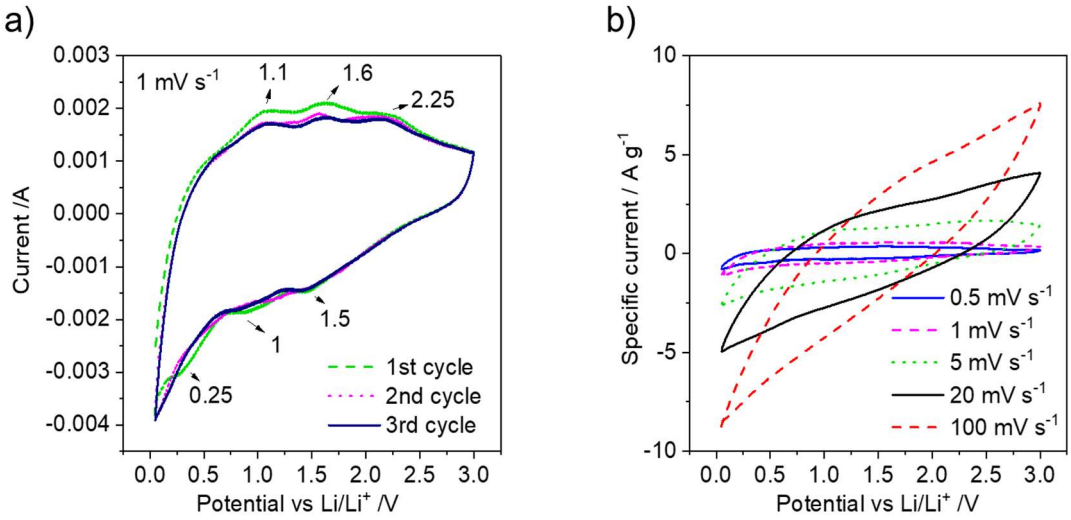

Figure 4.9: Graphs of cyclic voltammetry of VNM316in the potential window 3 to 0.05 V s Li/Li$^+$, a) the first three cycles at 1 mV s^{-1}, b) increasing scanrates from 0.5 to 100 mV s^{-1}.

When comparing the CV curves of the niobium containing VNM316 and the niobium free VNM406 (Figure 4.10a), VNM406 displays a very similar broad shape that is overall smaller and contains many of the same but not all the redox peaks of VNM316. These differences between the two persist at the higher scan rate of 20 mV s^{-1} (Figure 4.10b). The separation diffusion-limited and pseudocapacitive charge storage mechanisms to total charge storage for VNM316 and VNM406 were determined using the power law method.[90] From this, the CV curve attributed to purely pseudocapacitive mechanisms were overlayed as shaded areas onto the total CV curves (Figure 4.10c). It was found that VNM316 exhibited a higher percentage of pseudocapacitive charge storage relative to total charge, 82.7 % compared to 74.6 % for VNM406.

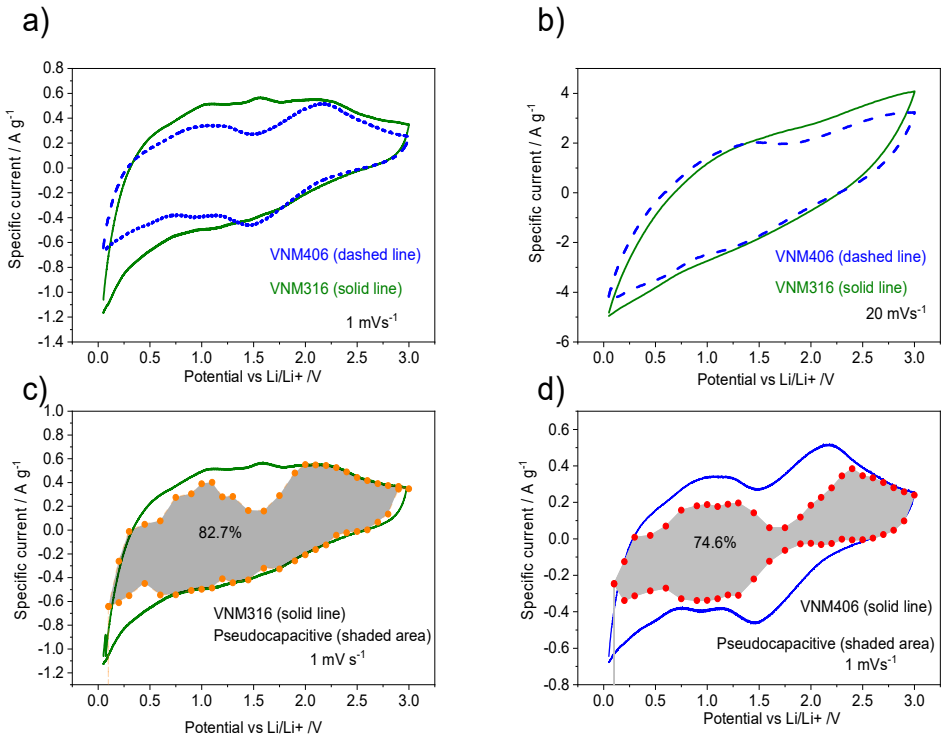

Figure 4.10: CV graphs of VNM316 and VNM406 at a) 1 mV s^{-1}, b) 20 mV s^{-1}, c) VNM316 with the calculated pseudocapacitive contribution overlayed as a grey shaded area, d) VNM406 with the calculated pseudocapacitive contribution overlayed as a grey shaded area.

The lithium half-cells were then analysed by galvanostatic charge/discharge (GCD) cycling, Figure 4.11a shows the GCD curves of the 2nd (red), 6th (blue) and 10th cycles of VNM316 at a specific current of 0.1 A g^{-1}. Immediately observable are the lack of any clear voltage plateaus, which support the suggestion of the CV data that pseudocapacitive charge storage mechanisms are dominant.[305] Over the ten cycles, it can be seen that the smooth shape of the GCD curves change very little, suggesting that any additional non-reversible electrochemical reactions are occurring in very small proportions. A specific capacity of 731.3 mAh g^{-1} with a coulombic efficiency of C.E. = 90 % was found initially at 0.1 A g^{-1}, this increased over the proceeding ten cycles to 786.9 mAh g^{-1} (C.E. = 93 %). It was observed that the gradual increase in capacity and coulombic efficiency continued as higher specific currents were applied, at a specific current of 0.5 A g^{-1} the specific capacity remained very high at 761.3 mAh g^{-1} with the C.E. increasing to 96 %. This gradual increasing capacity behaviour that is exhibited has been previously documented and reported for other transition metal oxide materials that exhibit conversion mechanisms, with two contributing factors

including an increase of the access of electrolyte within the porous active material and an improvement in the kinetics of the conversion reaction over cycling (Figure 4.11b).[52,306–308] For the material VNM316 over the specific currents 0.1, 0.2, 0.5, 1, 2, 5, and 10 A g^{-1}, the specific capacities achieved were 747, 761, 658, 542, 338, 185 and 83 mAh g^{-1} respectively (Figure 4.11c). After cycling at 10 A g^{-1}, the specific current was returned to 0.1 A g^{-1} whereupon the specific capacity of the material had increased to 829 mAh g^{-1}. These results highlight the excellent rate capability and cycling stability of the conversion material. When compared to the material VNM406, the specific capacities that were achieved were much lower across all specific currents tested, with no activation behaviour clearly observed. Over long-term cycling at 1 A g^{-1} (Figure 4.11d), VNM316 displayed an increase in capacity in the first 200 cycles, after which the capacity decreased slowly over the next 250 cycles to give 94 % of original capacity whilst maintaining a high C.E. The low and high specific capacities observed for VNM316 were found to compare favourably to other similar/related metal oxide materials that have been reported in literature such as.[173,293,294]

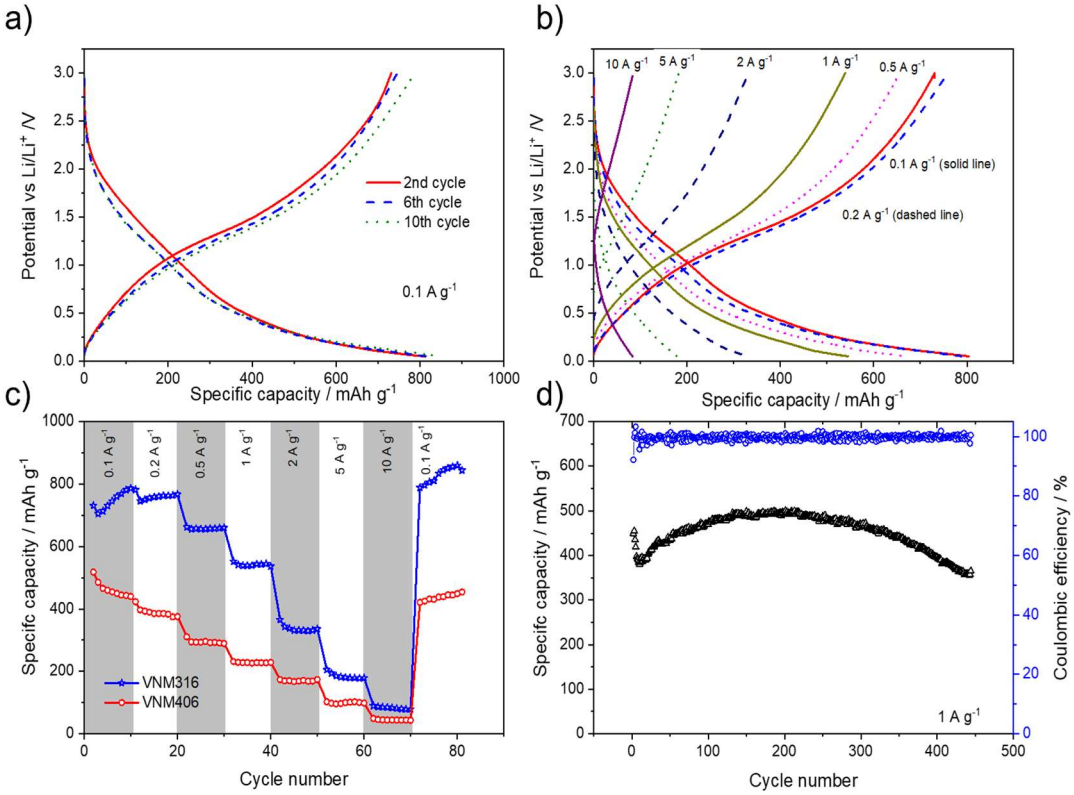

Figure 4.11: a) GCD curves of VNM316 in a lithium half-cell of the 2nd, 6th and 10th cycles at 0.1 A g^{-1}, b) GCD curves of VNM316 at increasing specific currents including 0.1, 0.2, 0.5, 1, 2, 5 and 10 A g^{-1}, c) Graph depicting the specific capacity of VNM316 (blue) and VNM406 (red) at increasing specific currents, d) long term cycling performance of VNM316 with specific capacity (black) and coulombic efficiency (blue) shown for 450 cycles at 1 A g^{-1}.

4.4.2.2 Electrochemical Characterisation in Li-ion Hybrid Capacitors

A lithium-ion hybrid capacitor device was constructed with activated carbon as the cathodic and VNM316 as the anodic active materials respectively. Using the method outlined by H-Y. Wei *et al.*, the cell was mass balanced with an anode to cathode ratio of 1:16.[260] The hybrid was cycled in the potential window 0.5-4.2 V. CV analysis of the hybrid at a scanrate of 5 mV s^{-1} displayed an overall large shape that is typical of capacitive behaviour (Figure 4.12a).[309] GCD cycling at specific currents of 0.1, 0.5 and 1 A g^{-1} was performed on the AC//VNM316 hybrid (Figure 4.12b), the shape of the GCD curves were found to be very triangular in nature, further suggestive of capacitive behaviour.[309] Power and energy analysis of the AC//VNM316 hybrid found a high energy density of 102 Wh kg^{-1} at a power density of 365 W kg^{-1}, and 10.3 Wh kg^{-1} at a high power density of 18.25 kW kg^{-1}. These results were found to compare very favourably against other hybrid capacitors that used molybdenum or titanium metal oxide materials, synthesised via hydrothermal methods, as anodes that have been reported in literature.[194,310] The results are plotted in a Ragone plot with the AC//VNM316 shown as red squares (Figure 4.12c).

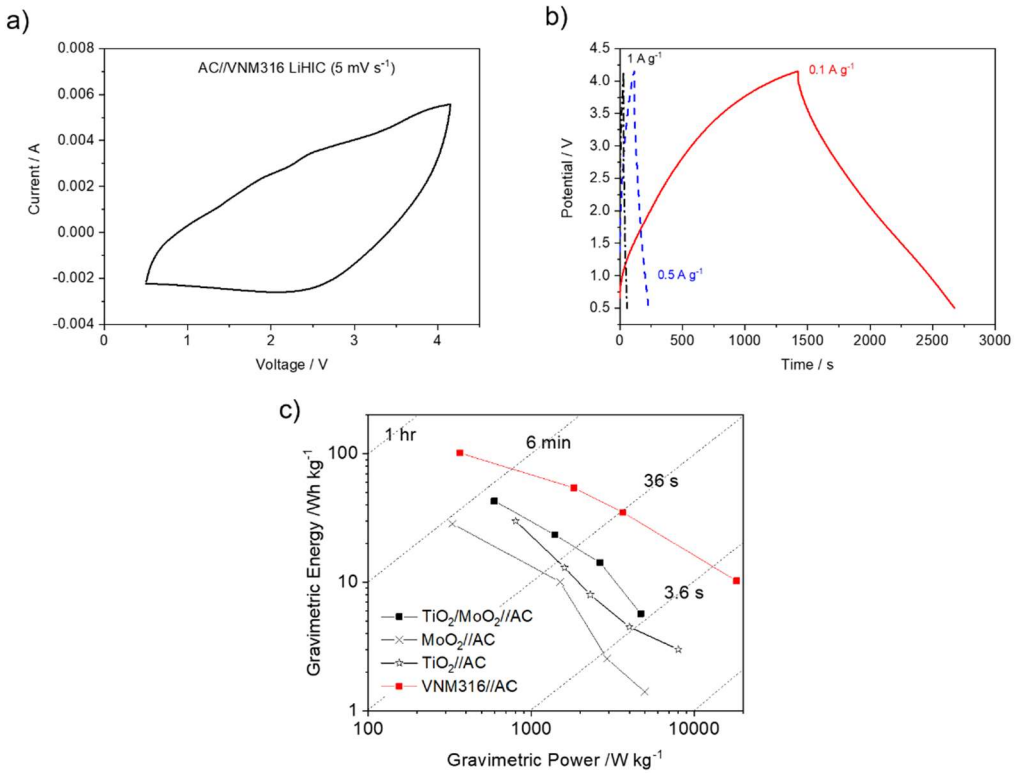

Figure 4.12: Graphs showing a) CV curve of AC//VNM316 at a scanrate of 5 mV s^{-1}, b) GCD curves of the LiHIC at different specific currents of 0.1 (red), 0.5 (blue) and 1 A g^{-1} (black), c) Ragone plot showing the energy and power performances of AC//VNM316 (red squares) compared to other reported HIC devices with titanium and molybdenum oxides as anodes. Sources [198, 314]

4.5 Conclusions

A large range of mixed vanadium-niobium-molybdenum oxides with different compositions from across ternary phase space were synthesised via a continuous hydrothermal flow method. The as-synthesised materials with high concentrations of niobium were found to have very amorphous crystal structures and high surface areas (up to 230 m^2 g^{-1}), whilst the higher V and Mo containing materials exhibited monoclinic crystal structures that were either VO_2 or MoO_2 or a solid solution of the two depending on the relative concentrations of metals. The lack of other crystal phases that were observed suggested the other elements were doping into the crystal structures instead of forming distinct phases. The specific surface areas of the monoclinic materials were all found to be lower than for the high Nb compositions. The mixed metal oxides were tested as anodic active materials in Li-ion half cells, mapping specific capacity at different specific currents as heat maps overlayed on ternary phase diagrams identified the

material $V_{0.3}Nb_{0.1}Mo_{0.6}$ (VNM316) as having the highest capacities at both low and high current cycling. At 0.1 A g^{-1} the specific capacity was found to be 747 mAh g^{-1}, and at the high current of 5 A g^{-1} the material retained 181 mAh g^{-1}. Over long-term cycling at a current of 1 A g^{-1} the capacity retention was found to be 94 % over 450 cycles. Cyclic voltammetry analysis showed clear redox peaks associated with intercalation and conversion-based energy storage mechanisms. Further analysis indicated a high contribution of pseudocapacitive charge storage for VNM316. The high specific capacity and pseudocapacitive charge storage compared to other similar compositions tested were attributed to several factors, such as multiple different redox centres being present in the material, EDS and XPS analysis also indicated the presence of interactions between Nb-O-V, Nb-O-Mo, and Mo-O-V with distribution of electronegativity along the bonds observed. The high surface area and small particle size observed by BET and TEM respectively have been previously associated with increasing pseudocapacitive charge storage and the reversible capacity and cycle life of conversion mechanism materials in literature. A Li-ion hybrid capacitor device utilising VNM316 as the anode and activated carbon as the cathode achieved an energy density of 102 Wh kg^{-1} at low power of 365 W kg^{-1} and retained an energy density of 10 Wh kg^{-1} at a high-power density of 18650 W kg^{-1}. The impressive electrochemical performance of VNM316 at a range of cycling currents, long term stability and ease of synthesise via CHFS identify this composition as a competitive anode material for use in Li-ion batteries and capacitors that warrants further investigation, development, and optimisation.

4.6 Outlook

Several different directions of future work for this study are worthy of pursuit. The first is the continued investigation of the interaction between the different metal ions and how they relate to electrochemical performance. Advanced techniques such as synchrotron based *in-operando* XRD and XAS would provide critical information regarding the structural and electronic changes occurring as lithium is intercalated and deintercalated, giving a deep insight into the exact nature of the redox reactions taking place. Comparison to the behaviour of other materials with different compositional ratios would allow for more information regarding elemental composition and electrochemical performance to be gathered. Despite

the higher intrinsic conductivity for molybdenum oxides compared to others, the conductivity of VNM316 as with other metal oxides is a barrier to good capacity retention at high power. Therefore, another future direction of investigation could focus on decreasing the resistivity of the material though introduction of carbon-based materials such as a nanotube, graphene sheets or carbon matrices for example. This avenue of research would lend itself well to this material due to the ability of CHFS to successfully incorporate carbons and metal oxides to form composites. A third potential avenue of investigation could be centred around the scaling-up of the synthesis of VNM316. Due to the scale-up of materials being such a large barrier to any materials of interest having a measurable impact on society, the need to design high performance materials with large scale synthesise methodologies considered is critical. In this regard CHFS has already successfully been scaled up to pilot scale, therefore the study of VNM316 would centre around investigating the conditions and processes required for parity between lab and pilot scale materials. Increased synthesis capabilities would then open up the opportunities to investigate the behaviour of VNM316 in much larger energy storage devices such as cylindrical and pouch cells where investigations in real-world situations and comparisons to industrial standards would be possible.

5.0 Improving the Performance of Mixed $V_{0.3}Nb_{0.1}Mo_{0.6}$ Oxides as Anodes Via Carbon Addition

'*The more difficult something is, the greater the attraction that comes from it*'

– Juan Manuel Fangio

5.1 Aims

The optimized mixed vanadium/niobium/molybdenum oxide anode material, $V_{0.3}Nb_{0.1}Mo_{0.6}O_x$, developed in Chapter 4 has been shown to have very high capacity at both low and high current cycling rates. However, the material displays low intrinsic conductivity and capacity fade over long term cycling (gradual electrode pulverization of the electrodes from the conversion mechanism) that must be overcome. In this chapter, the aim was to investigate the synthesis of a range of different carbon/VNM composite materials using coatings and additives. The hypothesis was that the coatings would reduce the capacity fade over cycling, whilst the carbon would also improve the conductivity to increase the capacity observed at high current in lithium-ion batteries and hybrid capacitors.

5.2 Introduction

Of the three main reported charge storage mechanisms for anode materials (intercalation, alloying and conversion) conversion materials present themselves as the most promising candidate for next generation battery anodes.[52,311] The reasons for this include, high achievable capacities and higher working potentials than graphite thereby decreasing the risk of lithium dendrite formation and increasing battery safety.[312,313] In addition to this, conversion mechanisms have been explored for a wide variety of different transition metal oxides, sulphides, selenides, nitrides and phosphides among others.[51,314,315] It has also been shown that conversion materials can exhibit tuneable potentials through manipulating the strength of the ionic bond between the transition metal (TM) cations and the anion species.[316]

However, there are several issues that must first be addressed before conversion materials are able to fulfil their full potential. These include low intrinsic ionic and electronic conductivity, reactivity with organic electrolytes (causing

decomposition over cycling), and large volume changes upon lithiation and delithiation.[312] Two metal oxides that are currently being investigated for potential use as conversion anodes are molybdenum oxides (MoO_2 and MoO_3), having been identified as both displaying very high specific capacities (838 mAh g^{-1} for the dioxide and 1117 mAh g^{-1} for the trioxide).[54,279,280] Vanadium oxides such as vanadium dioxide (VO_2) are also of interest due to the relatively low cost, ability to show multiple oxidation states, and the potential to form layered structures that are beneficial for intercalative charge storage. However suffer from low stability due to deformation during cycling.[288–290]

Improving the performance of conversion anodes can in part be addressed by nanoengineering.[52] It has been shown that reducing the particle size to the nanometre scale can reduce the distance ions have to diffuse thereby increasing the speed of charge storage, but can also reduce the swelling effects of lithiation which can improve the lifetime of the material.[47,317] Nanoengineering can encompass several different approaches each with their own benefits and costs. these include nanostructuring of 0D, 1D and 2D structures,[318–322] forming hierarchical structures, the formation of hollow structures,[323,324] and forming hybrid composites with carbons through coating, growing or embedding.[47,283,325,326] As previously discussed in Chapter 4, binary and ternary iterations have been shown to have improved performance over individual metal oxide materials. The presence of different crystal morphologies, elements and oxidation states in the same particles together can lead to synergistic effects and interactions through bonds between ions of different electronegativity.[327] This can lead to the changing of the local electric structure, which alters the consequent interactions with charge carrier ions.[328–330] There is also the possibility of promotion of different redox sites to the surface of particles, where they can more easily interact with charge carriers for the creation of more accessible crystal morphologies due to the mixed ion materials.[65,293] Due to the ability of both molybdenum and vanadium dioxide to form monoclinic crystal morphologies, the two materials are able to mix together as dopants in each in other at low concentration and eventually as solid solutions at equal concentrations.[173] Previously, Bauer *et al.* showed that nanoparticles of $Mo_{0.5}V_{0.5}O_2$ formed a solid solution of both MoO_2 and VO_2 crystal structures, as well as excellent

electrochemical performance at both low and high currents (200 mAh g^{-1} at 10 A g^{-1}). This was attributed to high levels of pseudocapacitive charge storage. It was also found that the cycle life of the mixed metal oxides was improved, 480 mAh g^{-1} after 150 cycles at 0.5 A g^{-1}). Further examples of the performance benefits of creating mixed vanadium/molybdenum oxide materials include a 3D hierarchically ordered VO_x/MoO_y oxide which could deliver a specific capacity of 440 mAh g^{-1} over 400 cycles at 4 A g^{-1}.[294]

These methods have dramatically improved the electrochemical performance of conversion type metal oxides; however, the issues of conductivity and long-term cycle stability still remain as large problems. Another area of research that has received a lot of attention in the past few years is the formation of carbon composite materials. These offer a path to composite materials with individual particles interconnected by a three-dimensional matrix of carbon which can vastly improve the transfer of electrons from the redox active sites to the metal current collector. The carbon material present can further act as a buffer to reduce the impact of volume changes as well as inhibiting the electrode/electrolyte degradation reactions which can cause capacity loss over time.[213,331] Further to this, carbon composite materials also require far less complex synthesis procedures than those for creating intricate hierarchical or low dimensionality materials.[332,333]

In general, the approach to forming carbon coatings on nanoparticles, involves the use of a carbon-containing precursor, which initially coats the particles, followed by a heat treatment in inert atmosphere to graphitise the carbon.[334] The use of glucose and fructose as the precursor coating solutions has been reported as an effective method of forming highly conductive carbon layers on nanoparticulate metal oxides.[213] More recently, other forms of carbon containing monomers have been successfully used, such as dopamine hydrochloride as a precursor to polydopamine (PDA) to form different composite morphologies such as nano sized “peapods” of carbon encapsulated MnO, which were found to exhibit capacities of over 525 mAh g^{-1} at a high specific current of 2 A g^{-1} for 1000 cycles without displaying obvious pulverisation of the electrodes.[335,336] Another example was shown by D Bresser *et al*., where nanoparticles of the conversion material $ZnFe_2O_4$ were coated in a carbon shell from a sucrose

precursor.[332] It was found that the carbon shell provided both improved conductivity (which in turn assisted in the high specific capacity of 310 mAh g^{-1} at a current of 7.78 A g^{-1}) and inhibited particle fragmentation over long term cycling reducing capacity loss observed.

The creation of a transition metal oxide embedded into a conductive carbon matrix has also been reported as a promising technique. Zhu *et al.* reported the formation of microspheres of composite carbon and titanium niobate that were shown to have improved electrochemical performance.[230] The precursors for the metal oxide were mixed with a carbon precursor and then subject to a heat treatment protocol in an inert atmosphere to produce graphitic carbon and the transition metal oxide microspheres. The highly uniform composite particles were found to have an increased capacity of 35 % when compared to the pure metal oxide. A more recent example was shown for improving the performance of Nickle phosphides (Ni_2P), in which nanoparticles of carbon coated Ni_2P were embedded into an echinus-like porous carbon structure.[337] These large structures provided very high surface areas and tunnels for facile lithium ion diffusion, and also structural stability that could reduce the swelling experienced upon lithiation. This gave the carbon metal phosphide material excellent reversible capacity at both low and high currents (807.7 and 236.4 mAh g^{-1} at 0.2 and 1 A g^{-1} respectively).

Another carbon material that has received a lot of focus as an additive in electrodes is reduced graphene oxide (rGO). This is due to it having a very high conductivity and a very high surface area on which functional groups can have favourable interactions with non-organic particles.[338] A multitude of reports have been reported in which graphene oxide sheets are used to either coat nanoparticles or provide nucleation sites from which ceramic nanoparticles can be grown on and anchored to. This has been shown for a wide range of metal oxides such as MnO_2 and $TiNb_2O_7$.[339,340] Another example of the electrochemical benefits of rGO was shown by using it to form a three-dimensional composite material with iron oxide nanoparticles (α-Fe_2O_3/rGO).[341] It was shown that the two components could inhibit agglomeration over cycling as well as improving electrical conductivity and promotion of active sites. All of which were critical in providing far improved specific capacities over a wide range of currents when

compared to nanoparticles of only α-Fe_2O_3, 1418.2 and 804.5 mAh g^{-1} compared to 1218.6 and 411.5 mAh g^{-1} at specific currents of 0.1 and 5 A g^{-1}.

A further source of carbonaceous material that can improve the electrochemical performance of ceramics are carbon nanotubes (CNTs) through either growth or deposition of battery materials onto the surfaces of the nanotubes.[342] This has been shown for a wide range of materials such as manganese oxide deposited onto vertically aligned CNTs which greatly improved the capacity, long term cycling stability and mechanical strength of the metal oxide.[343] It was also reported that the C-rate performance of the promising anode material $Li_4Ti_5O_{12}$ (LTO) could be improved by a forming a composite with graphitised CNTs to give a capacity retention of 86 % after 100 cycles at the very high specific current of 10 A g^{-1}.[344]

The potential benefits of synthesising composite carbon ceramic materials are clear and represent an exciting avenue of research for the improvement of electrochemical energy storage. However, to be able to permit these promising materials to greatly expand and accelerate battery and capacitor performance they must also meet the requirements of a commercial material. These include facile material production at large scale, low cost and low environmental impact. The ability to balance the requirements of improving material performance through addition of different forms of carbon without sacrificing the energy density is a further challenge for industrial battery manufactures especially those in the automotive industry.[10,35,218]

Chapter 4 outlines the results of a combinatorial study investigating the relationship between composition of mixed V/Nb/Mo oxides and their electrochemical performance as anodes in lithium-ion devices. It was found that a key composition, $V_{0.3}Nb_{0.1}Mo_{0.6}$ (VNM316) outperformed the other compositions at all currents tested (>650 mAh g^{-1} at 0.1 A g^{-1} and 120 mAh g^{-1} at 10 A g^{-1}). Studies on the electronic conductivity and long-term cycling stability suggested that the VNM316 material would benefit from the addition of carbon-based materials, potentially in the form of coatings or porous matrices similar to those discussed above.

In this chapter is reported the synthesis of a carbon-VNM316 composite anode material using a heat treatment assisted CHFS synthesis process, tested as an anode material in both lithium and sodium ion batteries and hybrid capacitors. These materials were characterised physically using methods such as PXRD, XRF, BET, TEM, EDS, Raman and XPS to analyse the nature of the carbon present, its interaction with the metal oxide, and elucidate correlations between composition and material properties. The materials were then characterised in lithium half-cells to evaluate their electrochemical performance as well as investigate the effect of the carbon in the composite materials. The highest performing material was then fabricated into hybrid capacitor devices to investigate the power and energy metrics and evaluate its applicability as an anode material for future research and usage.

5.3 Experimental Methods

5.3.1 Synthesis of Carbon/VNM Composite Materials

The different carbon-VNM materials that were synthesised are described in section 2.4.3. The labelling used herein follows as such, pure $V_{0.3}Nb_{0.1}Mo_{0.6}$ is referred to by VNM316, the un-coated material post heat treatment is referred to by [VNM316]HT, the carbon coated materials are referred to as CVNM-X (where X = 1-8 sequentially for the incremental sucrose concentrations investigated) reported herein. The full table of materials synthesised can be found in the appendix (appendix Table 6).

5.3.2 Physical Characterisation

The techniques used to characterise the CVNM materials are described in section 2.1.

5.3.3 Electrochemical Characterisation

The construction of electrodes is described in section 2.2.1, the formation of half-cells and hybrid capacitor cells are described in section 2.2.2. The electrolytes used in lithium half-cells was 1M $LiPF_6$ in 3:7 v/v EC/EMC. The electrolyte used in the hybrid capacitor cells was 1M $LiPF_6$ in 1:1 v/v EC/EMC.

The electrochemical characterisation of half-cells involved: GCD cycling at a range of different specific currents including, 0.1, 0.2, 0.5, 1, 2, 5, and 10 A g^{-1} over the potential window 0.05 to 3 V vs Li/Li^+ performed by an Arbin Instrument

(Model BT-2000 battery tester, US). CV analysis was performed in the same potential window at range of increasing scanrates including 0.05, 0.1, 0.2, 0.5, 1, 2, 5, 10, 20, 50 and 100 mV s^{-1}. Potentiostatic EIS was performed by a Gamry Interface 1000 Potentiostat, over the sinusoidal frequency range 100 kHz to 10 mHz. The oscillating alternating current voltage was set to 10 mV ms^{-1} with the area as 1 cm^2 and 10-point measurements. The hybrid capacitor cells were electrochemically evaluated by GCD and CV testing. Both were performed by a Gamry Interface 1000 Potentiostat (Gamry Instruments, USA) over the potential window 1 to 4.2 V.

5.4 Results and Discussion

5.4.1 Physical Characterisation of Composite CVNM Materials

The CVNM materials as collected immediately after synthesis were brown coloured powders, post heat treatment in inert atmosphere they changed to black powders and were initially analysed by PXRD. Prior to heat treatment, the CVNM materials were found to be a good match for monoclinic MoO_2 ICSD no. 80830, just as with the non-sucrose containing material VNM, with a slight peak shift to lower angles due to the presence of V and Nb in the structure (Figure 5.1a).[295,345] The PXRD patterns of the CVNM materials post HT are shown in Figure 5.1b, the CVNM materials post heat treatment all exhibited peaks at 2θ = ~12, ~16.5 and ~24°. These were found to be a still be a good fit for monoclinic MoO_2.[295] This retention of the monoclinic crystal phase after the heat treatment process is a noteworthy point, one possible explanation could be that as the sucrose coated on the particle surfaces undergoes a graphitisation reaction, this protects the metal oxide crystal phase from the heat of the furnace. For comparison, pure VNM316 metal oxide powder was heat treated by the same protocol, it was observed that without the carbon from the sucrose precursor, the [VNM316]HT underwent a phase change from monoclinic VO_2 to triclinic $V_{0.97}Mo_{0.95}O_5$ (Figure 5.1c).[346]

The quantification of the ratios of transition metals within the materials was performed by XRF. It was determined that the atomic percentage of vanadium, niobium, and molybdenum in the CVNM materials were a good match to the nominal concentrations of pre-cursors prior to the CHFS process, CVNM-6 was found to have the composition V:Nb:Mo 28%, 12% and 60% respectively. CHN

analysis was performed to quantify the carbon content of the composite materials, it was found that CVNM-6 had a carbon content of 1.12 %.

To further characterise the CVNM materials, BET and BJH analysis were performed, Figure 5.4a shows the isotherm of CVNM-1. The specific surface area was found to increase for CVNM-6 due to the heat treatment process from 26 to 85 $m^2\ g^{-1}$. This can be explained by the transformation of large amorphous carbonaceous particles converting to distinct carbon coatings on nanoparticles, thus increasing the surface area. This trend was consistent across all the carbon to metal oxide ratios investigated, however there was no significant difference in surface area as the carbon content of the precursor solutions were increased with the other CVNM-X materials, 1, 2, 3, 4, 6, 7 and 8, exhibiting surface areas of 30, 71, 39, 76, 85, 91 and 74 $m^2\ g^{-1}$ respectively. This could be due to a non-linear relationship between initial sucrose concentration and final carbon content, further investigation is needed to understand the impact of precursor concentration, heat treatment parameters and synthesis conditions on final carbon content and surface area. BJH pore size analysis identified a narrow distribution of pore sizes, with the average diameter being 3.7 nm for all materials, this is indicative that the heat treatment process is central to the formation of the pores (Figure 5.2b).[347] A good interaction between the active material and the electrolyte could therefore be achieved because of the large BET surface area and average pore size, thus improving the electrochemical performance.[44,344]

In order to investigate the nature of the carbon present in the materials post heat treatment, Raman spectroscopy was performed. Figure 5.3 shows the spectra for CVNM-6 collected prior to heat treatment, in which the broad feature visible at 1400 cm^{-1} and the broad peak at 1600 cm^{-1} were assigned to the D and G bands which correspond respectively to disorder along the c-axis of graphitic carbon materials and of the C−C stretch along the plane of carbon sheets.[44] Post heat treatment, the sharpness of the peaks increases suggesting the formation of more graphitic carbon within the material, the intensity of the G band is also greater than the D band, this suggests a higher proportion of sp^2 hybridised carbon (C=C bonds) present in the material. A high ratio of G:D band intensity has been shown to correspond to improved electrochemical performance of the composite materials.[332,348]

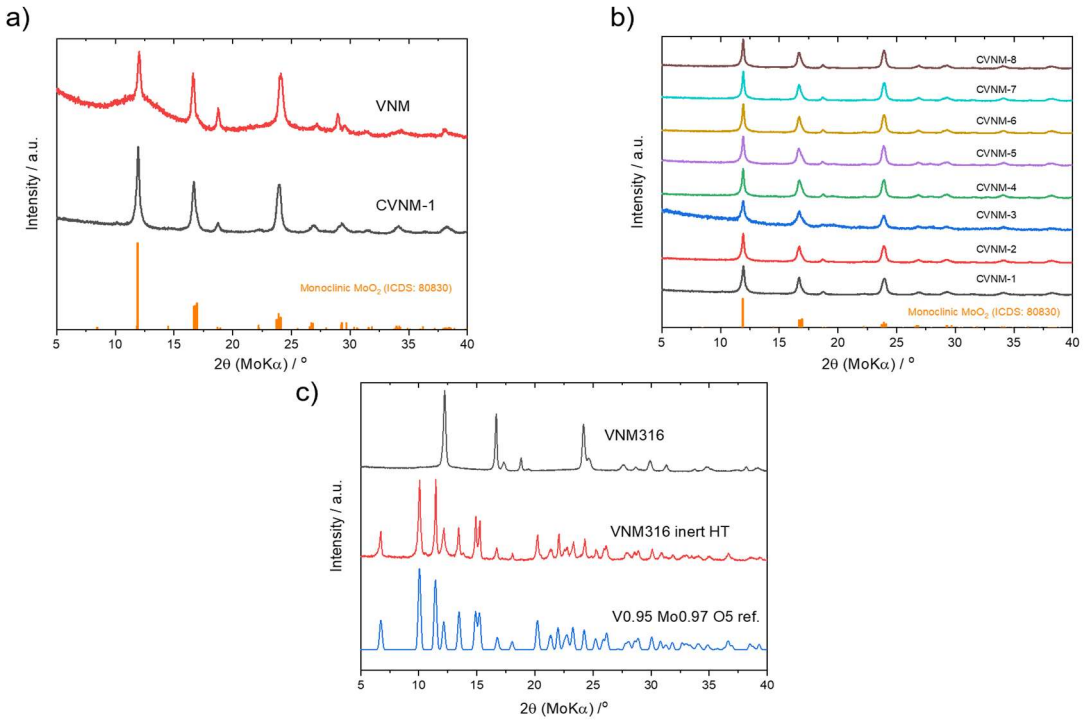

Figure 5.1: PXRD patterns of (a) VNM316 (red) and CVNM-1 (black) prior to heat treatment, (b) CVNM-X materials post heat treatment with the reference pattern for monoclinic MoO_2 (orange), (c) VNM316 (black) and [VNM316]HT (red) and the reference pattern for triclinic $V_{0.95}Mo_{0.97}O_5$ source [350].

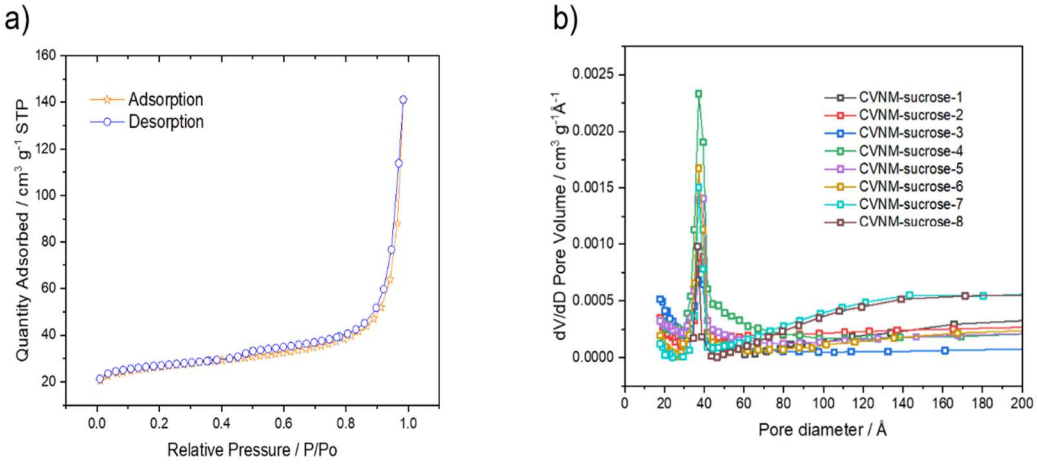

Figure 5.2: (a) BET isotherm of CVNM-1, (b) BJH pore diameter graph for all CVNM-X materials.

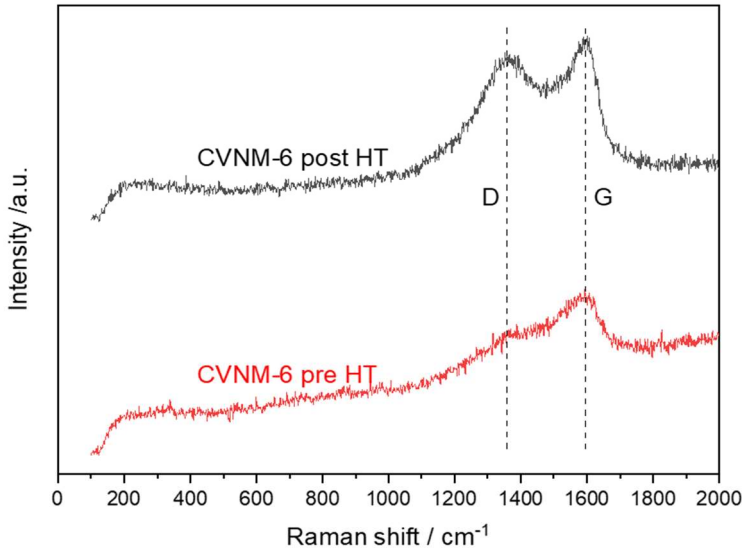

Figure 5.3: Raman scattering of CVNM-6 before heat treatment (red) and post heat treatment (black) with the D and G bands highlighted.

The topography and morphology of the particles of the CVNM material were investigated by TEM. The images revealed the CVNM-sucrose materials consisted of particles of metal oxide embedded into a carbon matrix (Figure 5.4a). Upon higher magnification, lattice fringe planes orientations were observed with lattice plane spacings of 0.34 nm, which correspond to the (1 -1 -1) plane of monoclinic MoO_2 (Figure 5.4b).[295] Further to this, the particles imaged were measured to have a carbon coating with an average thickness of 5.8 nm (Figure 5.4c). The small particle size observed suggests that the presence of the carbon inhibits agglomeration of particles or sintering during the graphitisation process.[230]

The composition and spatial dispersion of the constituent elements within the carbon coated materials were mapped by EDS. The scans for vanadium, niobium molybdenum, oxygen and carbon are shown in Figure 5.5. This not only confirmed the presence of all four elements but also highlighted the homogeneity of the mixing of all three transition metals within each particle, suggesting the integration of the different elements into the same crystal structure, supporting the PXRD data which was unable to identify any additional crystal phases. The scan for carbon confirmed that the particles were coated, and the lack of any

clear voids suggests complete coverage and good integration between the ceramic and carbon materials.

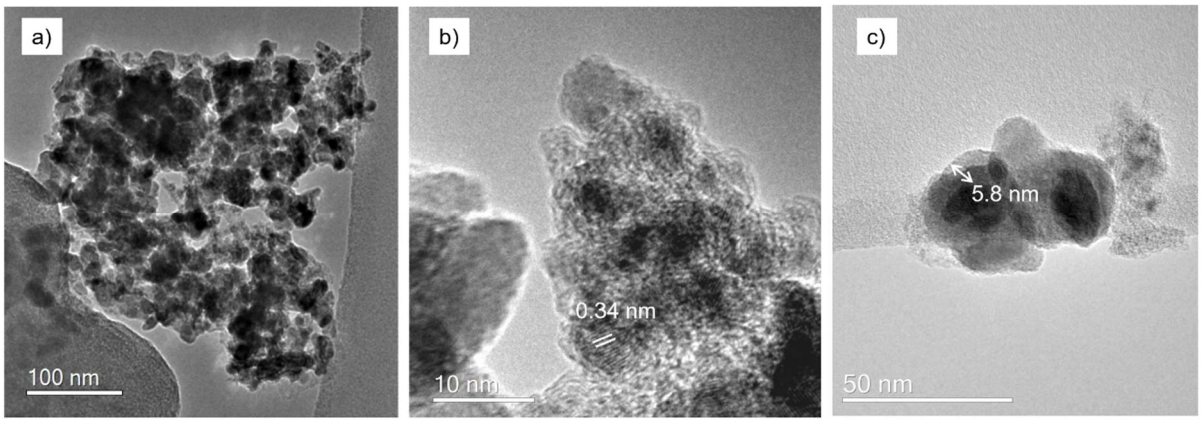

Figure 5.4: (a) TEM image of a cluster of CVNM-6 particles, (b) HRTEM image of CVNM-6 with lattice spacings highlighted, (c) HRTEM image of CVNM-6 particles with the carbon coating layer thickness measured.

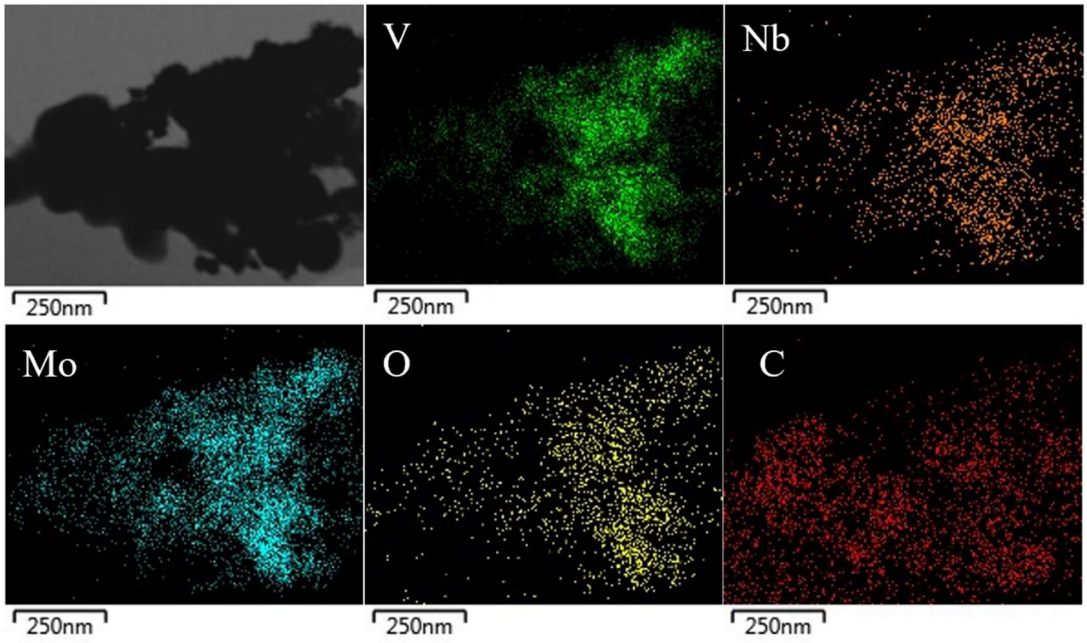

Figure 5.5: Dark field TEM image of a cluster of particles of CVNM-6 and EDS scans for V (green), Nb (orange), Mo (blue), O (yellow) and C (red).

XPS was used to investigate the oxidation states of the transition metals present and give information regarding the electronic structure of the CVNM materials, with the survey scan of CVNM-6 recognising peaks for V, Nb, Mo, O and C. High resolution scanning of the V2p area revealed two peaks at 523.7 and 516.4 eV with a spin-orbit splitting between them of Δ = 7.33 eV, these peaks were assigned to the $V2p_{3/2}$ and $V2p_{1/2}$ peaks respectively and were matched to the V^{5+} oxidation state (Figure 5.6).[349] The high resolution scan for Mo3d found three distinct peaks, which when deconvoluted were found to consist of three sets of doublets that each displayed a spin-orbit splitting of Δ = 3.15 eV (Figure 5.7). The $Mo3d_{5/2}$ peaks of each of the sets of doublets were located at 229.8, 231.4 and 232.6 eV, which were assigned to the Mo^{4+}, Mo^{5+} and Mo^{6+} oxidation states respectively.[350] Analysis of the peak area gave a composition of oxidations states of 33%, 20% and 47% respectively. The presence of additional oxidation states other than only Mo^{6+} is different to the XPS findings of the non-carbon coated VNM (Figure 5.8), which was found to have two peaks that were located at 232.7 eV and 235.8 eV and a spin-orbit coupling of Δ = 3.15 eV. These were assigned to the $Mo3d_{5/2}$ and $Mo3d_{3/2}$ peaks respectively for only the oxidation state Mo^{6+}. This suggests that the carbon coating of CVNM is providing partial protection from oxidation.[351] The high resolution scan for Nb3d gave a doublet of peaks at 209.9 and 207.2 eV with a spin-orbit splitting of Δ = 2.58 eV, these were assigned to the $Nb3d_{3/2}$ and $Nb3d_{5/2}$ peaks respectively for the Nb^{5+} oxidation state.[352]

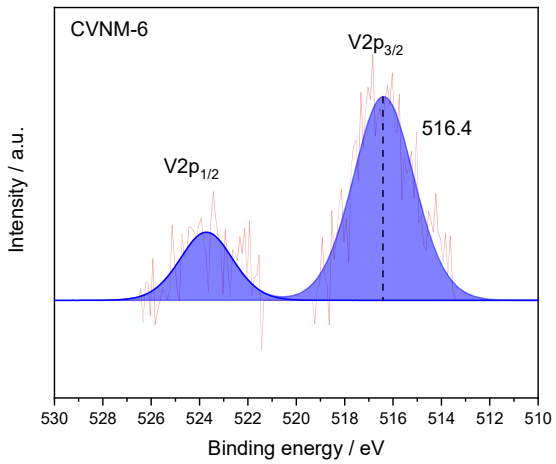

Figure 5.6: High resolution XPS scan of V2p of CVNM-6, with the peaks for the oxidation state V(5+) shown in blue.

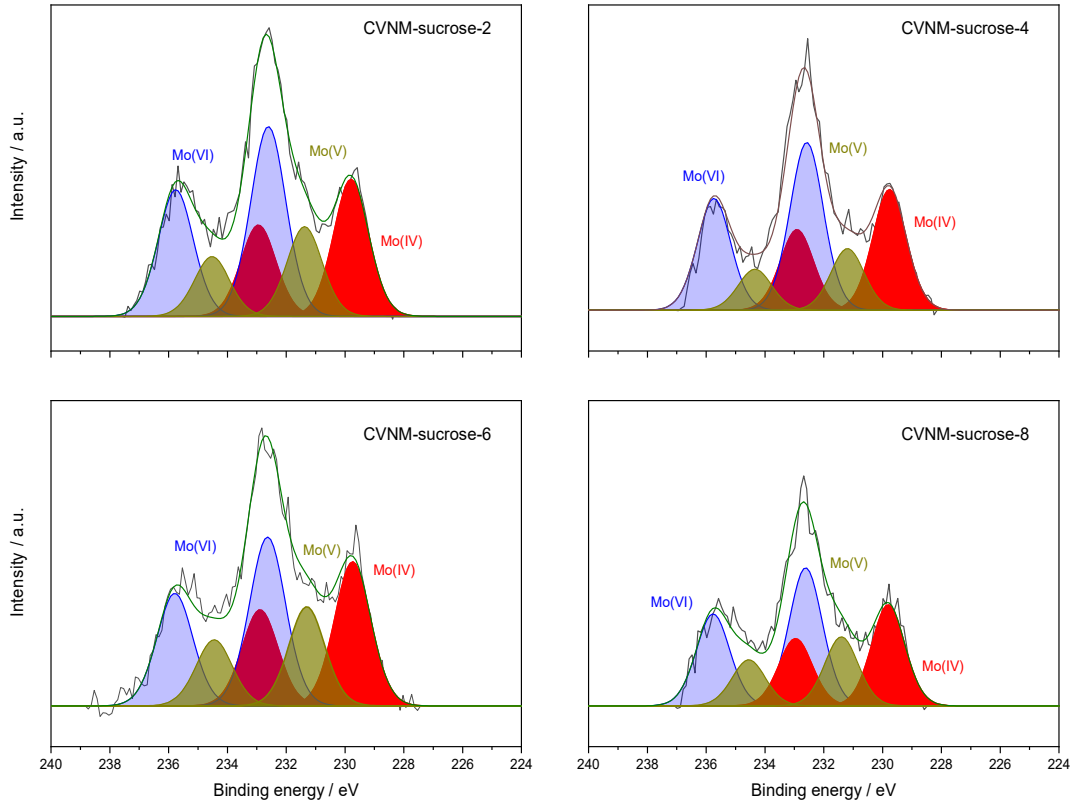

Figure 5.7: High resolution Mo3d scans from XPS of different CVNM materials with the doublets for Mo(VI), Mo(V) and Mo(IV) shown in blue, yellow, and red respectively.

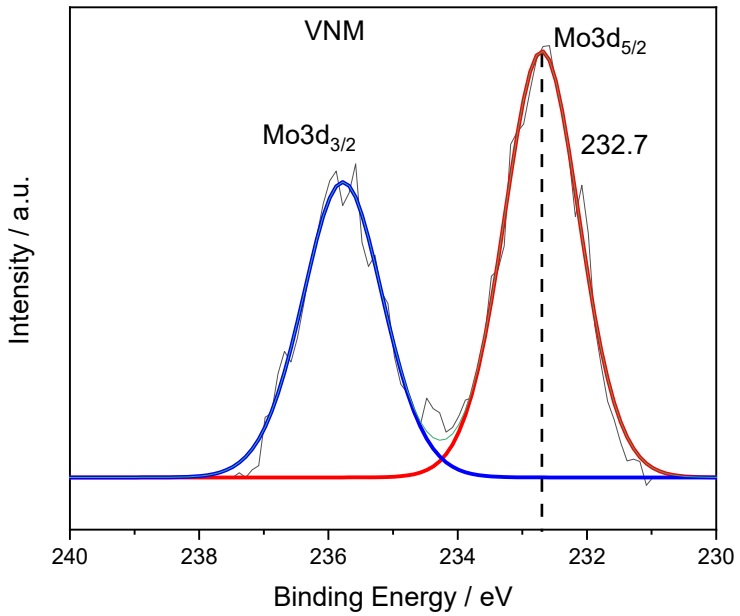

Figure 5.8: High resolution XPS scan of Mo3d of non-carbon coated VNM.

The exact binding energies of both V2p and Mo3d were shifted to lower and higher values respectively compared to literature values, this is suggestive of Nb-O-V and Nb-O-Mo interactions being present in the material and the differences in electronegativity between the three metals causing electron density to be pulled away from molybdenum ions towards niobium, and away from niobium towards vanadium ions.[293] This supports the findings of the EDS analysis, that of highly intimate mixing between the metal oxides within the same particles. Across the different CVNM materials synthesised, all were found to have the same oxidation states present for V, Nb and Mo with the relative ratios of the different oxidation states of Mo remaining very consistent. No effect between the sucrose concentration and oxidation states detected was found across the materials. Understanding the nature of the interaction between the carbon coating and the core metal oxide particles is very challenging, current adhesion science suggests that chemical and physical interactions at the interface are important for structural integrity and reducing delamination.[353] The lack of direct metal-carbon bonds observed by XPS does suggest a highly physical interaction for the CVNM materials at the interface. Further investigation into the size and shape of the carbon coatings during cycling and how the changes in volume impact them could be used to probe the interaction further. Some studies have shown that FTIR could be used to probe the interfacial interactions between polymers and metal oxides, however, due to the angle of incidence being a key factor, the technique was only applicable to ultrathin deposited layers.[354]

In summary, the physical properties of the CVNM materials have confirmed the presence of sp^2 hybridised carbon coatings on nanoparticles of mixed V/Nb/Mo oxide which is mainly uniform across all particles but does not make up a large percentage of the total mass of the material. The CVNM materials were found to match the crystal structure and elemental ratio of the non-carbon coated VNM material previously reported.

5.4.2 Electrochemical Characterisation of Composite CVNM Materials as Lithium-Ion Anodes

The lithium-ion insertion/extraction properties and the electrochemical cycling performance of the CVNM materials as anodes were analysed in half cell configurations with lithium metal as the counter electrode. Figures 5.9a and b display the first cycle GCD curves for CVNM-1 and CVNM-8 respectively. The first initial discharge and charge specific capacities of CVNM-1 were found to be 871 and 450 mAh g^{-1} respectively. These were marginally larger than the capacity values for the material CVNM-8 (743 and 397 mAh g^{-1} correspondingly). The first cycle coulombic efficiencies of CVNM-1 and CVNM-8 were found to be 52 and 53 % respectively. All the CVNM materials were found to exhibit similar initial charge and discharge capacities and first cycle efficiencies with very little variation between them as the carbon content increased. The large capacity losses experienced and the low coulombic efficiency on the first cycle could be attributed to the decomposition of electrolyte involved in the formation of the solid electrolyte interface layers (SEI) on the surface of the active material.[355] For all CVNM materials tested, the shape of the GCD curves were found to all display a smooth curve with two smaller plateaus at 1.35 and 1.70 V vs Li/Li^+ and a larger plateau below 0.25 V vs Li/Li^+. The high-rate performance of the CVNM materials was measured at increasing specific currents from 0.1 to 10 A g^{-1} (Figure 5.9c). The overall trend followed such that rate performance increased with carbon concentration up the sucrose metal ratio of 2:1, after which it decreased again. At low and medium specific currents (0.2, 0.5 and 1 A g^{-1}) CVNM-4 exhibited the highest reversible capacities of 638, 666 and 646 mAh g^{-1} respectively. However, at high specific currents (5 and 10 A g^{-1}) CVNM-6 was found to far outperform the others with capacities of 366 and 197 mAh g^{-1} respectively (Figure 5.9d). One interesting trend observed was the slow increase in capacity over cycling at low current that was displayed by all CVNM materials., CVNM-6 increased from 522 to 604 mAh g^{-1} over 10 cycles at 0.2 A g^{-1}. This increase in performance is well documented for other conversion materials and was attributed to an activation process of the conversion reaction between molybdenum oxide and lithium, and to the increase in the number of active sites available for charge storage reactions.[306,308,356] This effect was further observed once the specific current was returned from 10 back to 0.1 A g^{-1}, upon which the reversible capacity of CVNM-

6 was found to have increased to 803 mAh g^{-1}. The long-term cycling stability for CVNM-6 was investigated by cycling at the high current of 5 A g^{-1}. After 100 cycles, the capacity had retained ~300 mAh g^{-1}, after 400 cycles this had decreased slowly and plateaued at ~110 mAh g^{-1}. The GDC high-rate performance and long-term cycling stability for CVNM-6 compare very well to other carbon/metal oxide composite materials that have been reported in literature (Table 5.1). The applicability of CVNM-6 as a high-performance anode material is further bolstered when taking the ease of scalability of synthesis into account.

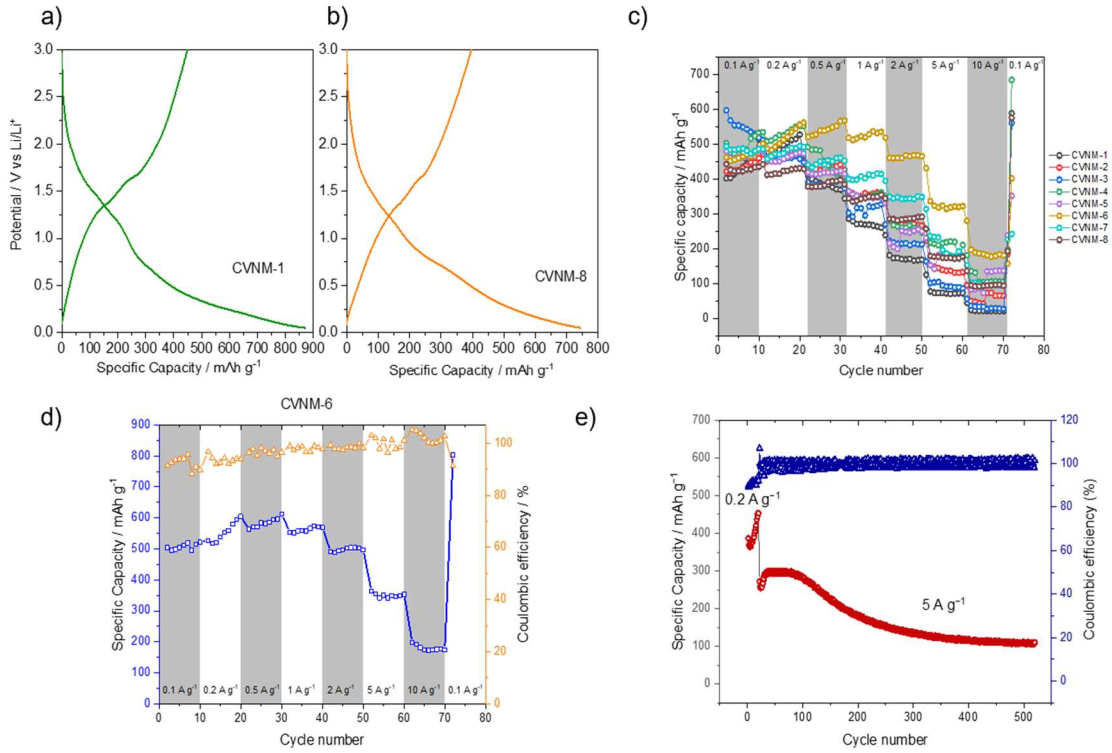

Figure 5.9: (a) GCD first cycle graphs of CVNM-1 (green), (b) GCD first cycle graphs of CVNM-8 (orange), (c) specific capacity vs. cycle number graphs of all CVNM materials at increasing specific currents, (d) specific capacity vs. cycle number at increasing specific currents or CVNM-6, (e) long-term cycling specific capacity graph of CVNM-6 at a high specific current of 5 A g^{-1}.

Anode Material	Electrolyte	C-Rate/Current	Specific Capacity	Reference
Carbon-VNbMoO$_2$ by CHFS method	1 M LiPF$_6$ (in 3:7 EC/DMC)	5 A g^{-1}	366 mAh g^{-1} after 60 cycles (0.05-3 V vs Li/Li$^+$)	This work
Carbon coated MoO$_3$-NiO microspheres	1 M LiPF$_6$ (in 1:1:1 EC/DMC/EMC)	2 mA g^{-1}	481 mAh g^{-1} after 2000 cycles (0.01-3 V vs Li/Li$^+$)	Materials Letters, 2019, **246**, 141-143
Carbon Li$_4$Ti$_5$O$_{12}$ via solid state method	1 M LiPF$_6$ (in 1:1:1 EC/DMC/EMC)	20C (3.2 A g^{-1})	126 mAh g^{-1} after 50 cycles (1-3 V vs Li/Li$^+$)	Energy Environ. Sci., 2011, **4**, 4016
Cylindroid-like Li$_4$Ti$_5$O$_{12}$ mesocrystals by sol-gel method	1 M LiPF$_6$ (in 1:1 EC/DEC)	20C (3.2 A g^{-1})	167 mAh g^{-1} after 3000 cycles (1-2.5 V vs Li/Li$^+$)	ChemNanoMat, 2020, **6**, 1-7
MnO$_2$ on carbon nanotubes by aq. Redox reaction	1 M LiPF$_6$ (in 1:1 EC/DEC)	2 A g^{-1}	630 mAh g^{-1}	Carbon, 2018, **139**, 145-155
3D carbon V$_2$O$_3$ microspheres via a solvothermal method	1 M LiPF$_6$ (in 1:1 EC/DMC)	2 A g^{-1}	216 mAh g^{-1} after 9000 cycles (0.01-3 V vs Li/Li$^+$)	Nano Res., 2016, **9**, 128-138
Carbon coated MnMoO$_4$ nanorods via a hydrothermal method	1 M LiPF$_6$ (in 1:1 EC/DEC)	5 A g^{-1}	362 mAh g^{-1} after 30 cycles (0.05-3 V vs Li/Li$^+$)	Electrochimica Acta, 2016, **190**, 354-359
Carbon supported V$_2$O$_5$ nanosheets by precipitation reaction	1 M LiPF$_6$ (in 1:1 EC/DEC)	1 A g^{-1}	802 mAh g^{-1} after 200 cycles (0.01-3 V vs Li/Li$^+$)	J. Mater. Chem A, 2016, **4**, 13907-13915
Carbon coated MoO$_2$ nanobelts by a hydrothermal method	1 M LiPF$_6$ (in 1:1:1 EC/DMC/DEC)	100 mA g^{-1}	615 mAh g^{-1} after 30 cycles (0.01-3 V vs Li/Li$^+$)	J. Mater. Chem., 2012, **22**, 13148-13152
Nitrogen rich Carbon nanosheet wrapped TiO$_2$ by hydrothermal method	1 M LiPF$_6$ (in 1:1 EC/DMC)	5C (1.68 A g^{-1})	136 mAh g^{-1} after 500 cycles (1-3 V vs Li/Li$^+$)	Electrochimica Acta, 2017, **255**, 417-427
Carbon-shell Nb$_2$O$_5$ core nanoparticles via a hydrothermal method	1M LiClO$_4$ (in PC)	5C (1 A g^{-1})	100 mAh g^{-1} after 4000 cycles (1-3 V vs Li/Li$^+$)	Electrochimica Acta, 2017, **240**, 316-322
TiNb$_2$O$_7$/C microspheres by spray dry method	1 M LiPF$_6$ (in 1:1 EC/DEC)	5C (1.935 A g^{-1})	260 mAh g^{-1} after 1000 cycles (0-3 V vs Li/Li$^+$)	ACS Appl. Mater. Interfaces, 2017, **9**, 41258-41264
TiNb$_2$O$_7$ by solid state method	1 M LiPF$_6$ (in 1:1:1 EC/DMC/DEC)	0.1C (38.7 mA g^{-1})	173.4 mAh g^{-1} after 200 cycles (1-3 V vs Li/Li$^+$)	ACS Appl. Mater. Interfaces, 2018, **10**, 27056-27062

Table 5.1: Table showing comparable carbon/metal oxide materials and their electrochemical performance reported in literature.

To analyse the electrochemical dynamics and kinetics of the charge storage mechanisms occurring in the CVNM composite materials cyclic voltammetry was performed. Within the CV curve of CVNM-6 at the scan rate of 1 mV s^{-1}, two pairs of cathodic/anodic peaks were observed at ≈ 1.2/1.45 and 1.5/1.8 V vs. Li/Li^+ (Figure 5.10a). These were both assigned to the reversible crystal phase transition of partially lithiated molybdenum oxide (Li_xMoO_2) from monoclinic-to-orthorhombic-to-monoclinic that occurs as lithium intercalates and de-intercalates from the structure.[357] Below the potential 0.5 V vs. Li/Li^+ a large peak is well defined, this was attributed to the conversion reaction of molybdenum oxide and lithium to Mo^0 and Li_2O which provides large amounts of charge storage.[313] Figure 5.10b shows the first, tenth and fiftieth cycles at 1 mV s^{-1} of CVNM-6. During the initial cycle, the overall area of the CV curve is noticeably smaller and there is a very large peak on the backward portion of the scan at 1.17 V vs Li/Li^+ which was assigned to non-reversible reactions involved in the formation of the SEI. By the tenth cycle, the area of the CV has increased, and the shape has a more pronounced box shape. As can be seen the shape and features change very little by the fiftieth cycle with the redox peaks only decreasing in size slightly, this demonstrates the stability of the CVNM materials over cycling and their ability to retain structural integrity whilst storing charge via the conversion reaction and its associated volume expansion and contraction.[70,345,358] When the scan rate is increased up to 100 mV s^{-1}, the shape of the CV curves becomes more box-like with less well defined redox peaks and some peak polarisation observable, however it is clear that even at the very high scan rates charge is still being stored by the same mechanisms (Figure 5.10c).

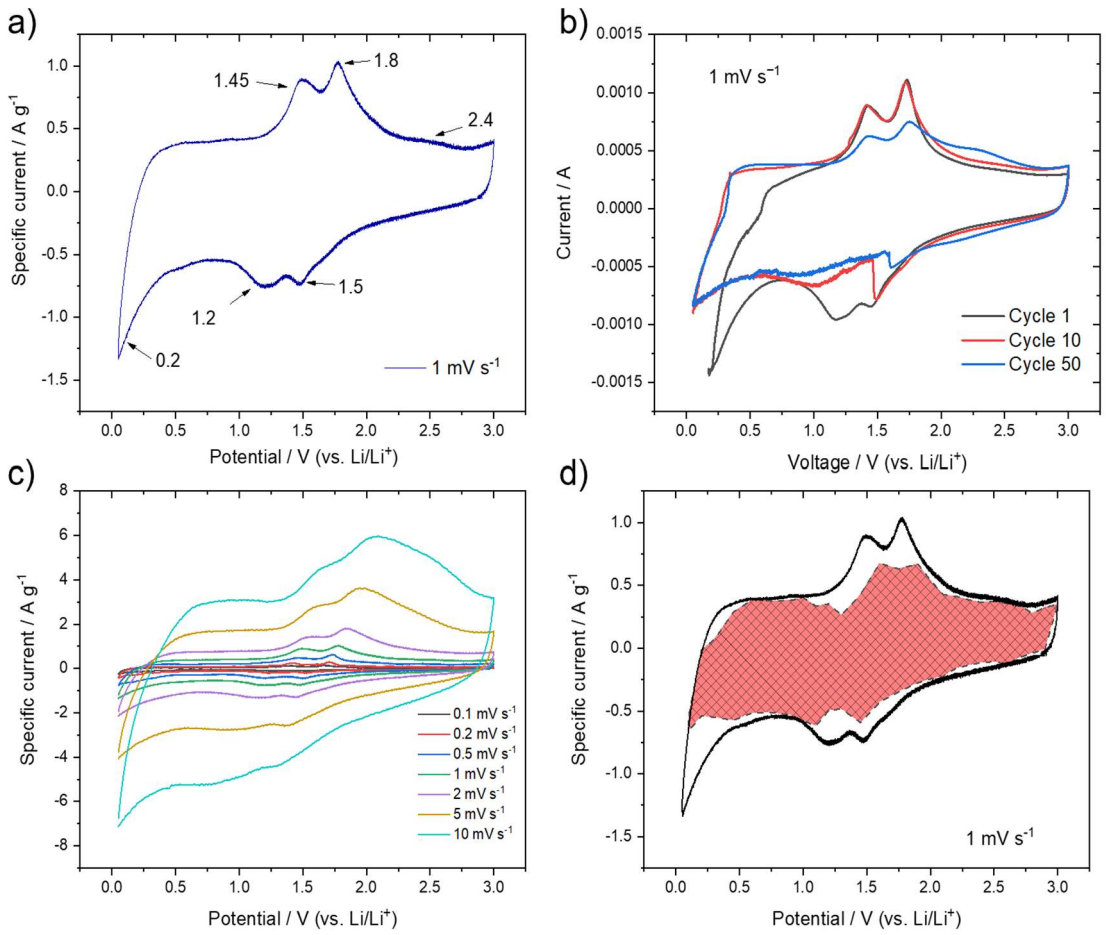

Figure 5.10: (a) CV graph of CVNM-6 at a scan rate of 1 mV s^{-1} with the redox peaks labelled, (b) CV graph showing the curves for the 1st, 10th and 50th cycles from long term cycling at 1 mV s^{-1}, (c) CV graphs at increasing scan rates, (d) CV curved of CVNM-6 at 1 mV s^{-1} (black) with the calculated capacitive

The combination of diffusion-limited charge storage mechanisms such as conversion and intercalation, and capacitive processes are what represents the area under the CV curve, with the box-like shape of the overall CV curve suggesting pseudocapacitive charge storage occurring alongside the redox peaks discussed earlier.[90,345] The method described in section 1.2.4 for calculating an approximation of the proportion of charge storage occurring by the different mechanisms was applied to the CV curve at 1 mV s^{-1} (Figure 5.10d, black) to which the calculated capacitive contribution was overlayed (red shaded area), this suggests that a large proportion of the charge stored can be attributed to capacitive processes. This was further supported by applying the Trasetti *et al*. method which approximates the capacitive contribution at increasing scan rates as a percentage of the total charge stored.[83]

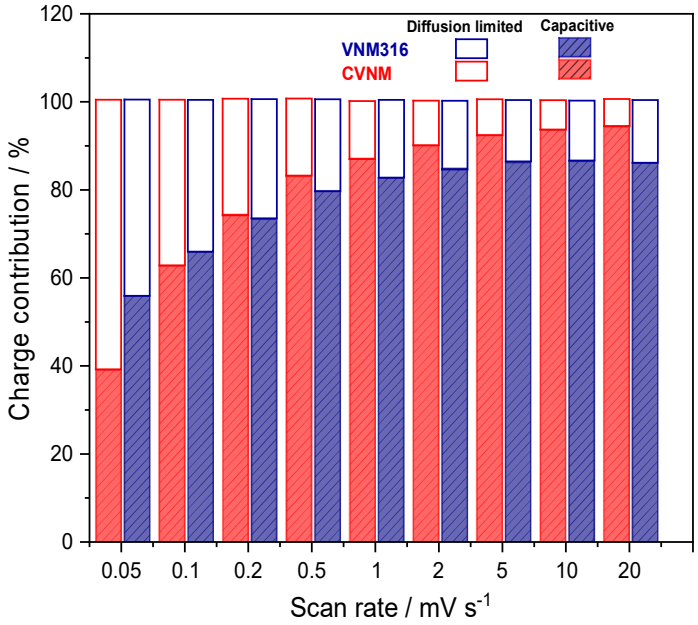

Figure 5.11: Bar graph showing the percentages of diffusion-limited (clear) and capacitive (shaded) charge storage mechanisms for CVNM-6 (red) and VNM316(blue).

From Figure 5.11 it is clearly observable that this method suggests that as the scan rate is increased, the proportion of capacitive charge storage increases for CVNM-6 (red shaded), this matches the same analysis applied to pure VNM, however the percentages were found to be marginally higher for CVNM, potentially due to the carbon playing a role in capacitively storing charge as well as the metal oxide. To further investigate how continuous long-term cycling affected the performance of CVNM-6, EIS was performed initially before cycling, followed by 100 cycles of cyclic voltammetry at a scan rate of 1 mV s^{-1} with EIS analysis repeated every 10 cycles. The compiled EIS results are plotted in Figure 5.12 and individual nyquist plots after 0, 10 and 100 cycles in Figure 5.13a, b and c respectively. Initially the charge transfer resistance was determined to be 5.22 ohms, over the proceeding cycles the size of the semi-circle of the nyquist plots increase steadily to 19.44 ohms after ten cycles and then up to a maximum of 165.6 ohms after one hundred cycles. This increase in the CTR over long term CV cycling suggests that the CVNM-6 material, despite showing markedly improved stability than the non-carbon coated metal oxide, still suffers from degradation to the integrity of the electrode as is characteristic of conversion

mechanism molybdenum oxide based materials.[280] The diffusion coefficients of lithium ions were calculated for each of the EIS analyses over the long term CV cycling (Figure 5.14) through the manipulation of the Warburg coefficient (error determined to be ±6 %).[207] The diffusion coefficient was found to initially to be 1.03 x 10^{-13} cm^2 s^{-1}, this increased by more than a factor of two over the first thirty cycles to a maximum of 5.73 x 10^{-13} cm^2 s^{-1}. It then decreased gradually over the proceeding seventy cycles to just below the initial value to a minimum of 8.59 x 10^{-14} cm^2 s^{-1}. The initial improvement in lithium ion kinetics can be ascribed to a combination of increased penetration of the electrolyte into the electrode, and to the activation process of the molybdenum oxide conversion mechanism.[359] The subsequent decrease in diffusion coefficients observed indicates the possible loss of structural integrity of the mixed metal oxide electrodes due to the large volume expansion of the conversion mechanism, this highlights the need for further development of the carbon-metal oxide composite to improve on the long term stability achieved here as well as fundamental understanding of the changes in physical structure experienced during cycling, which could be achieved by in-situ XRD and high resolution imaging of individual particles after cycling.

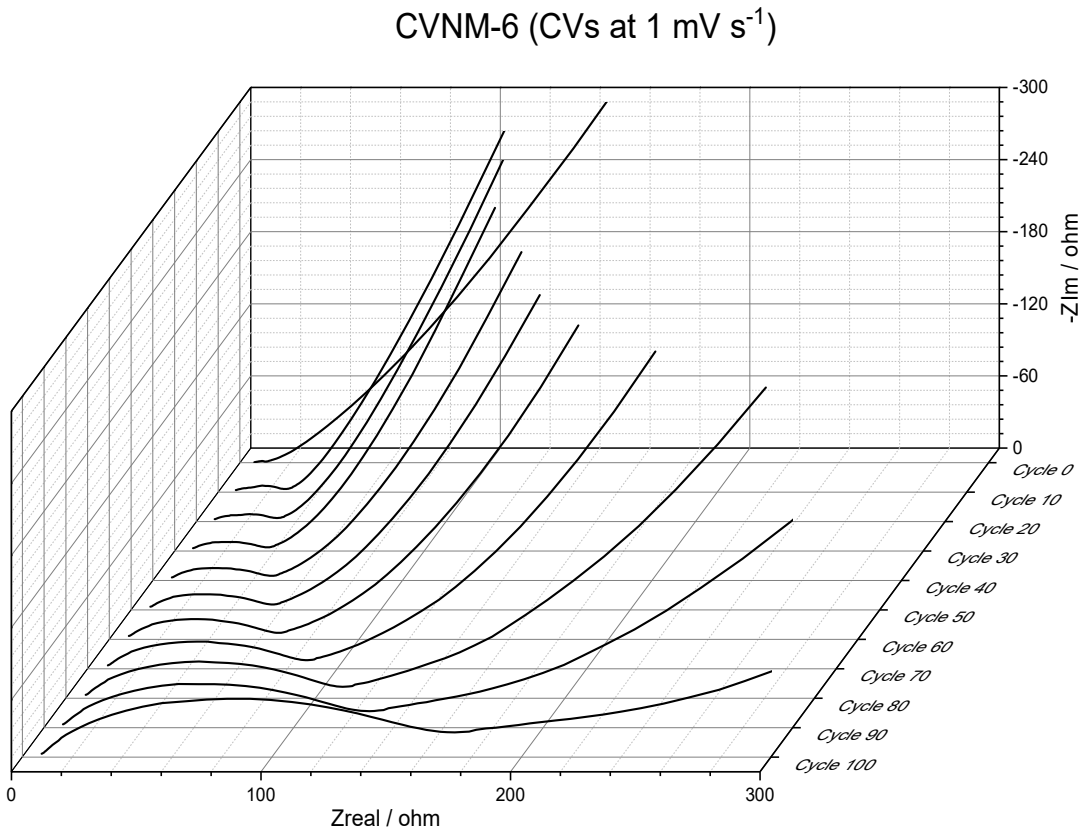

Figure 5.12: Time series graph showing the nyquist plots taken every 10th cycle over 100 CV cycles at 1 mV s^{-1}.

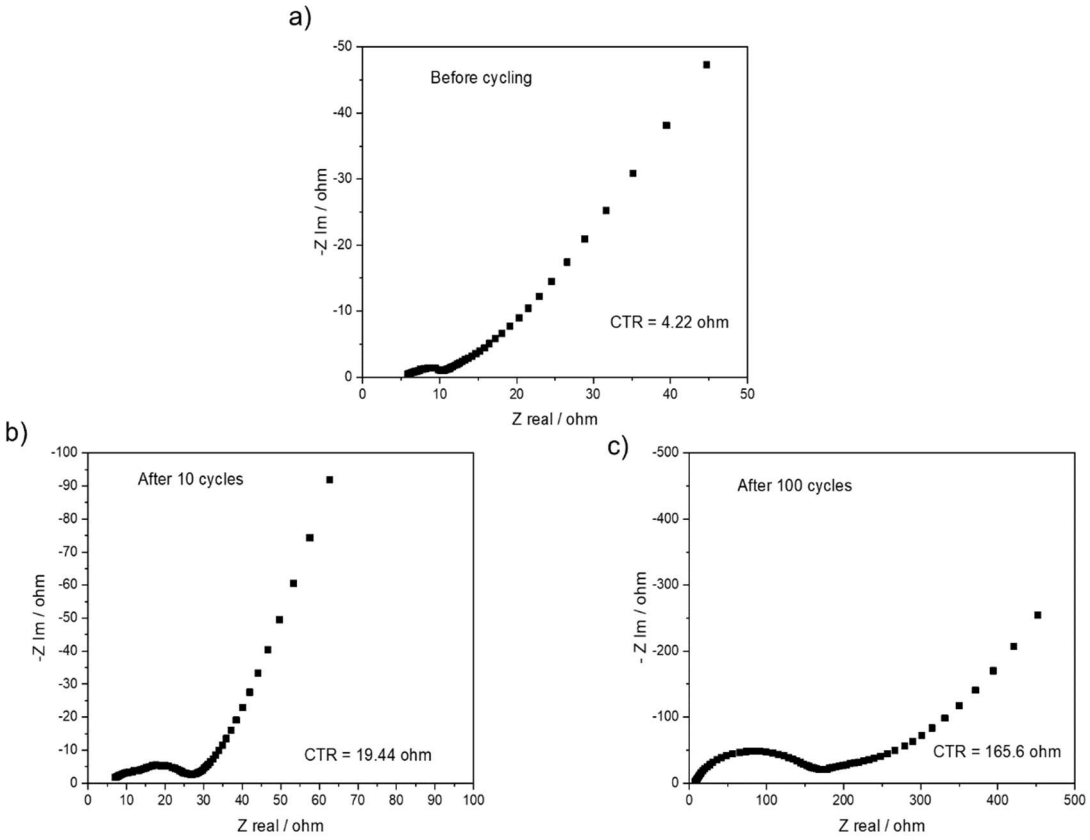

Figure 5.13: Nyquist plots of CVNM-6 taken at (a) 0 CV cycles, (b) 10 CV cycles, (c) 100 CV cycles of 1 mV s^{-1}.

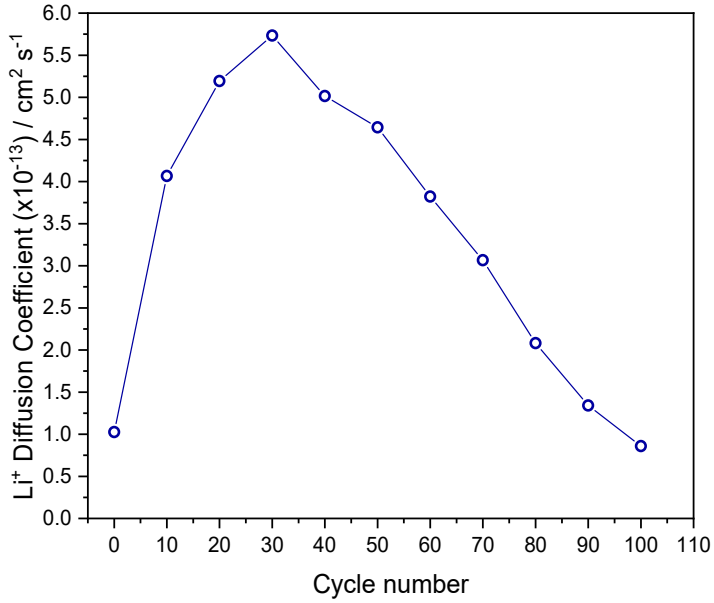

Figure 5.14: Graph of the lithium-ion diffusion coefficients calculated from the Warburg impedance vs. the cycle number for CVNM-6.

5.4.3 Galvanostatic Intermittent Titration Technique Analysis of Composite CVNM-6 Materials in Lithium-Ion Half-Cells

The diffusion coefficient of lithium ions throughout the CVNM-6 material as a function of potential was analysed by galvanostatic intermittent titration technique (GITT) for both lithiation and delithiation (Figure 5.15a). The GITT test protocol constituted a current pulse of 0.1 A g^{-1} for 10 minutes, followed by a rest period of 10 minutes (Figure 5.15b). The Li^+ diffusion coefficients were calculated to be in the range of 10^{-16} cm^2 s^{-1} (error determined to be ±7 %) over the potential window (Figure 5.15c), this was lower than the diffusion coefficients determined by EIS. On the lithiation scan, the diffusion coefficient increased gradually with the potential from 0.15 to 1.13 (10^{-16}) cm^2 s^{-1} at 1 V vs Li/Li^+. However, it then displayed a drop between ~1.0 to ~1.5 V vs Li/Li^+ to 0.96 (10^{-16}) cm^2 s^{-1}, after which it continued to increase rapidly up to 3.36 (10^{-16}) cm^2 s^{-1} at the maximum potential. On the delithiation scan, the diffusion coefficient displayed similar behaviour with a gradual increase as the potential decreased from 0.19 to 1.16 (10^{-16}) cm^2 s^{-1} until ~1.5 V vs Li/Li^+ whereupon it too experienced a small decrease to 1.01 (10^{-16}) cm^2 s^{-1}. Beyond this, the coefficient increased rapidly to 3.95 (10^{-16}) cm^2 s^{-1} as the potential reached a value of 0.27 V vs. Li/Li^+. The decreases in diffusion coefficient experienced in the potential window correlate well with the redox peak locations observed on the CV scans and could therefore be explained by phase transitions occurring within the structure, as has been reported in literature for similar behaviours of other active materials.[197,198] The differences in exact values for the diffusion coefficients calculated from both GITT and EIS techniques highlights the complexity involved in comparing different methods that utilise different parameters, however this does not detract from the scientific insight gained from observation of the coefficients as functions of potential or cycle number respectively.

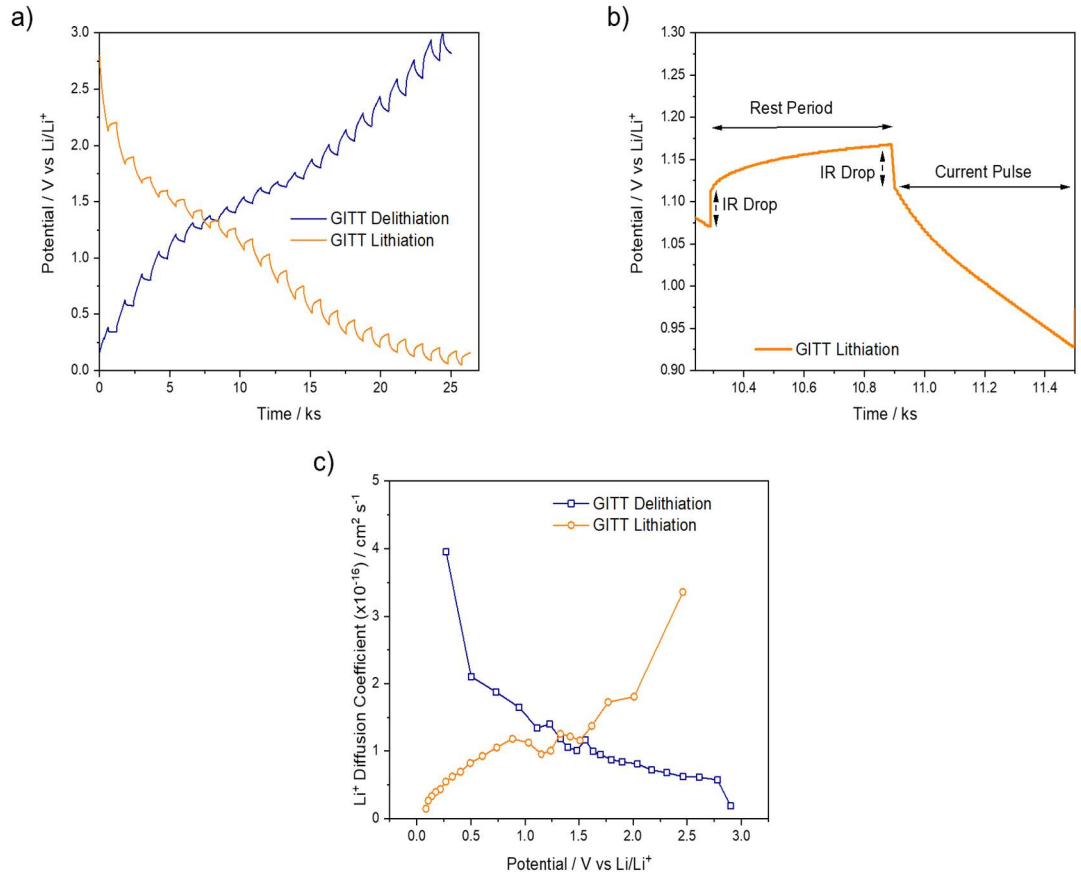

Figure 5.15: Graphs of CVNM-6 showing (a) the GITT delithiation (blue) and lithiation (orange) tests performed, (b) a single GITT lithiation step with the current pulse, rest period and IR drops labelled, (c) graph of the calculated Li^+ diffusion coefficients as a function of potential vs Li/Li^+ for both delithiation (blue) and lithiation (orange) GITT steps.

5.4.5 Electrochemical Performance of Composite CVNM Materials in Lithium-Ion Hybrid Capacitors

The electrochemical performance of CVNM-6 in a half cell against lithium metal highlighted its potential as an anode in energy storage devices. In order to investigate this application, hybrid lithium-ion capacitor devices were constructed with CVNM-6 electrodes as the anode and activated carbon as the cathode. The electrodes were balanced in order to give the HIC the best possible performance, the optimal ratio of cathode material to anode material was determined to be 2.5:1 as shown in Figure 5.16. The AC//CVNM-6 hybrid ion capacitor underwent GCD cycling in the voltage window 1 to 4.2 V. Overall the shape of the GCD curves at all four specific currents tested (0.5, 1, 2 and 5 A g^{-1}) were found to be triangular in nature as is typical for capacitor like behaviour (Figure 5.17a and b). When compared to the non-carbon coated pure AC//VNM316 HIC in Chapter 4, at a current of 0.5 A g^{-1}, the IR drop for AC//CVNM-6 was found to be less than half the value for AC//VNM316 (0.11 and 0.32 V respectively). This clearly shows the benefit of the carbon coating to both the conductivity and subsequent energy and power performance. However, the size of the IR drop is still a limiting factor for the performance especially at high currents. To further investigate the electronic conductivity of the AC//CVNM-6 HIC, EIS was performed which gave a value of 12.56 ohms for the charge-transfer resistance and a value of 10 ohms for the resistivity of the device itself (ESR, Figure 5.17c). Both of these resistivity values are large when compared to commercial EDLC devices, however they are analogous to other metal oxide HIC devices reported in literature that have not undergone specific electrode optimisation.[360,361] Complex power analysis was also performed, this yielded a plot of complex active and reactive power vs. logarithmic frequency (Figure 5.17d). From the cross over point of the two plots (the resonance frequency), a value for the time relaxation constant was calculated to be t_o = 0.29 s. The discharge data from GCD cycling was converted into metrics of energy and power density, at a specific power of 1270 W kg^{-1} the AC//CVNM-6 HIC gave a specific energy of 81 Wh kg^{-1}. At a very high power of 8500 W kg^{-1} the specific energy was determined to be 11 Wh kg^{-1}. These results were plotted into a Ragone plot with other similar carbon/metal oxide composite materials that have been reported in literature (Figure 5.18).[194,261,362]

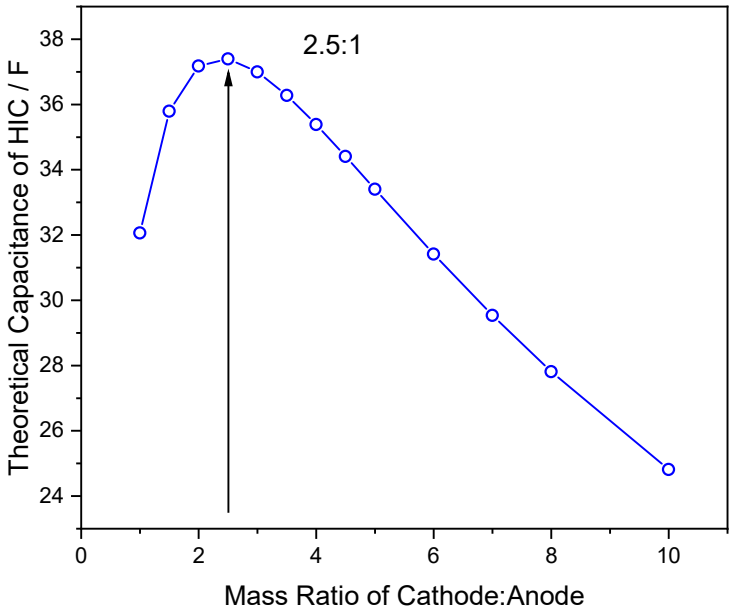

Figure 5.16: Graph showing the calculated theoretical capacity of a HIC device with different cathode to anode (CVNM-6) mass ratios.

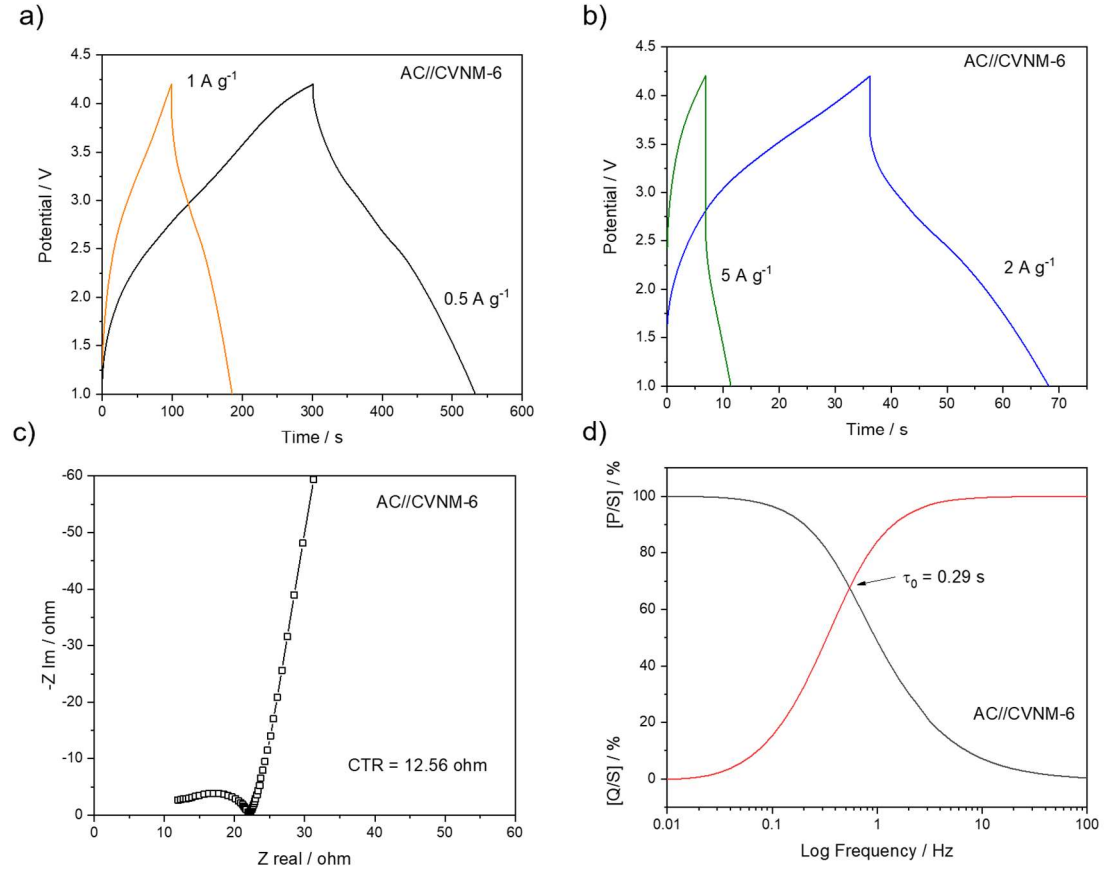

Figure 5.17: Graphs of the AC//CVNM-6 HIC showing the (a) GCD curves of 0.5 (black) and 1 (red) A g^{-1}, (b) GCD curves of 2 (blue) and 5 (green) A g^{-1}, (c) nyquist plot from EIS, (d) calculated complex active (red) and reactive power (black) vs. log frequency with the time relaxation constant labelled.

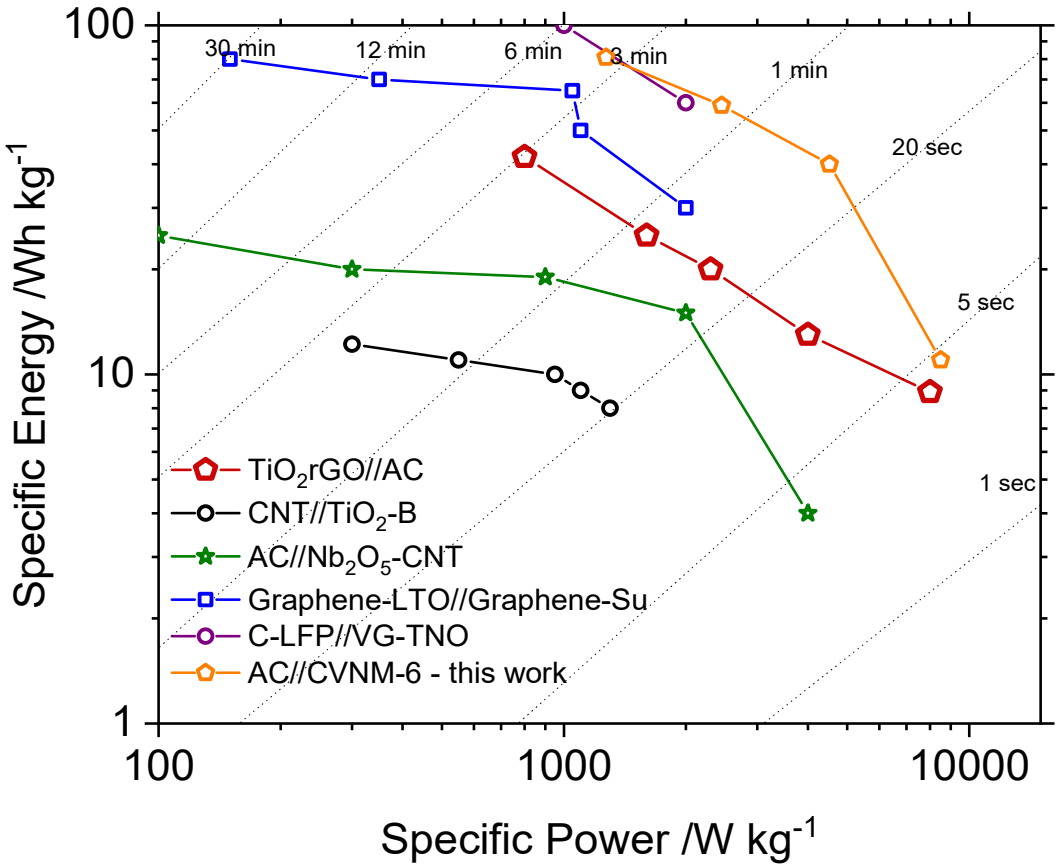

Figure 5.18: Ragone plot of logarithmic specific energy and specific power of HICs of carbon/metal oxide composite materials reported in literature, and AC//CVNM-6 HIC (orange) Data compiled from sources [194, 261, 362].

5.7 Conclusions

In summary, a heat treatment in inert atmosphere assisted CHFS synthesis method was used to create composite materials of carbon and mixed vanadium, niobium and molybdenum oxide. PXRD analysis determined that the presence of the carbon allowed for the protection of the monoclinic MoO_2 crystal phase from the heat treatment. Transmission electron microscopy identified nanosized particles of metal oxide that were both coated in a layer of carbon and embedded into a carbon matrix, with different levels of interaction that was heavily dependent on the ratio of carbon to metal oxide precursors prior to heat treatment. The heat treatment was also found to cause the composite materials to exhibit a large increase in BET surface area, Raman spectroscopy confirmed that the carbon coatings and matrix were graphitic in nature due to the ratio of D and G bands

measured. The electrochemical characterisation and cycling performance were performed in lithium-ion half-cells. Cyclic voltammetry highlighted several well-defined redox peaks, a large redox peak assigned to conversion mechanism charge storage and a pseudocapacitive contribution to overall charge storage of 72, 92 and 97 % at scan rates of 0.1, 1 and 20 mV s^{-1}. The material CVNM-6 with a carbon to metal oxide precursor ratio of 1.5:1, was found to have the best GCD cycling performance. At specific currents of 0.1, 0.2, 0.5 1, 2, 5, and 10 A g^{-1} the reversible capacity was found to be 505, 546, 584, 567, 506, 366, and 197 mAh g^{-1} respectively. Long term CV cycling was found by EIS analysis to increase the value of charge transfer resistance from 4.22 to 165.6 ohms over 100 cycles at 1 mV s^{-1}. The diffusion coefficient was determined to initially improve from 1.49 $x10^{-16}$ to 3.53 $x10^{-16}$ cm^2 s^{-1} over the first 30 cycles (±6 % error), and then slowly decrease to 1.37 $x10^{-16}$ cm^2 s^{-1} after 100 cycles (±6 % error), this indicates the impact of long term cycling on the stability of the material and highlights the need to further improve the electronic and ionic conductivity, and the stability of the material to degradative processes such as volume changes during cycling. Galvanostatic Intermittent Titration Technique determined the Li^+ ion diffusion coefficient to lie in the range 10^{-16} to 10^{-17} cm^2 s^{-1} (±7 % error) agreeing with the EIS analysis. The variation of the diffusion coefficient was found to vary with potential, with the large changes corresponding to redox peaks identified by CV.

A hybrid capacitor of AC//CVNM-6 was fabricated and cycled in the voltage window 1 - 4.2 V. Complex power analysis of the impedance data found the value for the time relaxation constant was 0.29 s. It was found that over galvanostatic charge/discharge cycling, at a medium specific power of 1270 W kg^{-1} the specific energy was 81 Wh kg^{-1}, at a very high power of 8500 W kg^{-1} the specific energy was found to be 11 Wh kg^{-1}. These values performed well when compared to other similar composite carbon-metal oxide anodes in hybrid capacitors. The electrochemical performance of composite carbon-V-Nb-Mo oxide materials reported here identifies the as candidates for use as high-power anodes in lithium-ion batteries and hybrid capacitors and warrants further investigation into the application to larger energy storage devices.

5.7 Outlook

The addition of graphitic carbon to mixed V-Nb-Mo oxides and the resultant improvement of the electrochemical performance has indicated itself as a successful method for producing potential candidates for high power and high energy anodes. In order to further improve the performance, the issues surrounding low conductivity and long-term stability must be addressed. Possible routes of investigation for these could include the addition of highly conductive carbons such as single-wall nanotubes or graphene sheets, which by introducing to the metal oxide in conjunction with a sucrose-based carbon coating could create an intricate 3D matrix in which the nanotubes or graphene provide the increase in conductivity required for high power performance and the carbon coating continues to improve the long-term cycling stability. Another potential direction of investigation could focus on the heat treatment conditions and carbon precursor ratio with the aim of optimising the coating on individual particles and understanding the relationship between time, temperature, coating thickness and levels of agglomeration. In order to improve the interaction between the carbonaceous materials and mixed metal oxides, the effect of the carbon coatings and/or additives on the structural changes which occur during lithiation/delithiation must be investigated using techniques such as in-situ XRD and XPS during cycling to give the results as a function of potential and state of charge. One further area of research should focus on the scale up of both the CHFS method and the heat treatment process to synthesise reproducible materials that match the performance of lab scale ones. This importance of addressing this challenge is large due to the well-known difficulties of scaling up, and the inability of any high-performance material to influence industrial lithium-ion battery and hybrid capacitor devices without a process which can produce material on the scale needed. An initial investigation into the scale-up of this material via CHFS has proven successful, however far more research is required to take it to fruition.

6.0 Materials Discovery and Development of Mixed Iron, Manganese and Zinc Oxides as Lithium-Ion Anodes

'*The real purpose of the scientific method is to make sure nature hasn't mislead you into thinking you know something you actually don't know*'

– Robert M. Persig

6.1 Aims

The aims of this chapter are to investigate ternary Fe, Mn and Zn mixed metal oxides produced by CHFS as anode materials for lithium-ion batteries. The application of carbon composite formation techniques learned from previous work applied to the highest performing compounds to improve the specific capacity, capacity retention at high current and long-term stability.

6.2 Introduction

As the prevalence of lithium-ion batteries in society increases, the need for developments in battery technology is critical.[102,363,364] However, as research efforts are directed at greater energy and power densities, two other aspects that must be considered in parallel are sustainability and cost. As discussed in the introduction (Chapter 1), the sales of lithium-ion batteries are forecast to increase by more than threefold in the next 10 years, therefore the amounts of raw materials that must be extracted to meet this demand are also set to increase.[3] This means that the identity of the elements used in the active materials can have serious implications regarding financial cost, environmental impact and energy security concerns.[365] Future research of new active materials should focus on elements that are abundant, have a low environmental impact and low cost of extraction and processing (Figure 6.1). Many of the first and second row transition metals satisfy these criteria and are also of interest electrochemically as metal oxides.[34,56,366] Examples include Fe, Mn, and Zn based oxides.[53,54,313,367,368] However, as previously discussed there are several drawbacks to conversion mechanism materials that must be addressed before they are applied to large scale energy storage. These include characteristics such as large volume expansion and contraction during cycling which can lead to rapid capacity fading, as well as low electronic conductivity and poor performance at fast rates.[34,369]

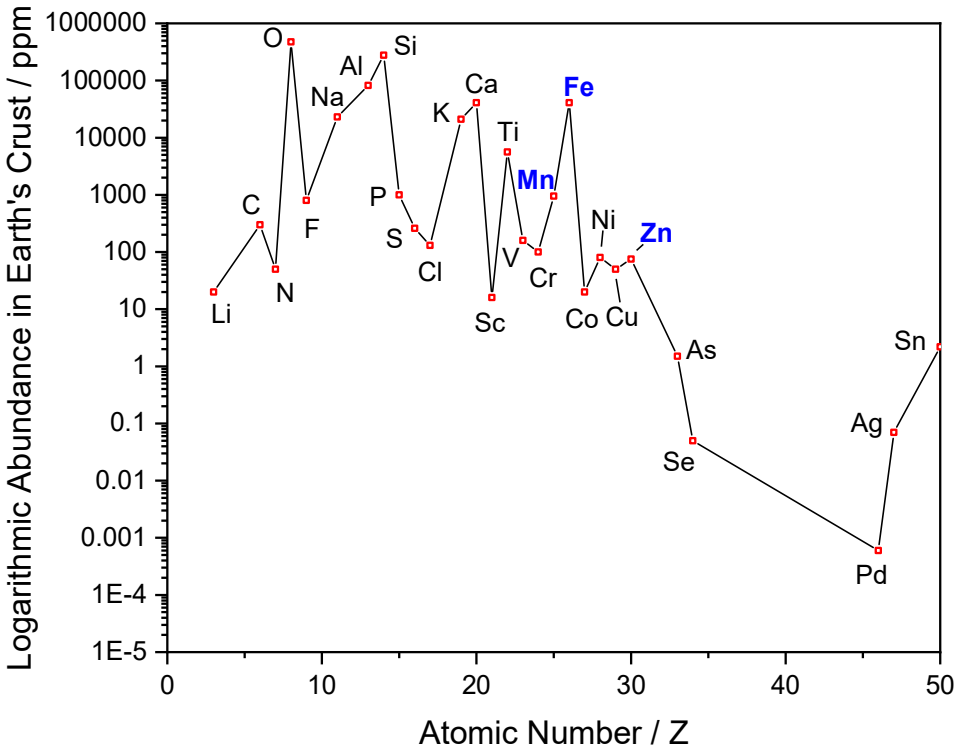

Figure 6.1: Graph showing the logarithmic abundance of a range of different elements in the earth's crust. The elements focused on in this chapter are highlighted in blue. Data adapted from results by K. Barbalace [368].

Certain iron oxides (Fe_3O_4 and Fe_2O_3) present themselves as candidates of interest due to having theoretical capacities of 926 and 1008 mAh g^{-1} respectively, having a low environmental impact and being naturally abundant in the earth's crust.[370–373] However they suffer from very low intrinsic conductivity, capacity loss over long term cycling as well as the reduction of available iron through the reaction with lithium not exhibiting any electrochemical behaviour.[341] The method of forming composites of metal oxide and carbon based materials has been discussed in depth throughout this thesis for a range of different materials. It has also found to be successful for iron oxides as a way to address the inherent issues.[374] One example of this was reported by Jiang *et al.*, where porous nano-frameworks of Fe_2O_3/graphene were formed and utilised as a flexible anode in lithium-ion batteries, which showed a high capacity of 1129 mAh g^{-1} at 0.2 A g^{-1} after 130 cycles.[375] Another example reported by Li *et al.* was graphene oxide encapsulated Fe_2O_3 nanoparticles which displayed a specific capacity of ca. 890 mAh g^{-1} at 0.1005 A g^{-1} after 50 cycles and retained 405 mAh g^{-1} after 1000 cycles at 1.005 A g^{-1}.[376]

Examples for Fe_3O_4 materials include an aerogel formed from partially reduced graphene oxide with nanoparticles of Fe_3O_4 deposited that displayed a reversible capacity of 2083 to 2136 mAh g^{-1} after 100 cycles at a specific current of 0.5 A g^{-1}.[377] One further example was shown with an aligned Fe_3O_4/graphene architecture formed using a upward magnetostatic field, that was found to have greatly improved lithium storage properties with 700 and 610 mAh g^{-1} at 3 and 10 A g^{-1} respectively after 1000 cycles.[378]

Manganese oxides have also drawn significant interest as electrode materials in lithium-ion batteries due to their high prevalence on earth, low cost, ability to display many different oxidation states and form various crystal structures.[47] Several different manganese oxides have been identified as possible anodic candidates such as MnO, MnO_2 and Mn_2O_3, as they can undergo conversion reactions with lithium ions, giving them high theoretical specific capacities of 756, 1232 and 1018 mAh g^{-1} respectively.[379] Once again progress has been made by combining these materials with conductive carbonaceous materials, such as a hydrothermally synthesised nitrogen doped cauliflower-like porous MnO@C/N composite were found to have a capacity of 837 mAh g^{-1} at 0.5 A g^{-1}.[380] Further to this, a hybrid material of MnO_2 grown directly onto fabrics of carbon nanotube fibres gave very high capacities at low and high current, 1100 and 500 mAh g^{-1} at 0.025 and 5 A g^{-1} respectively, and a good capacity retention of 97 % after 1500 cycles at 5 A g^{-1}.[381] These improvements in performance as lithium-ion electrode materials were also reported for the material Mn_2O_3, reduced graphene oxide was used to form a composite Mn_2O_3/rGO that displayed a porous microcube structure containing interconnected particles.[382] These microcube composites gave a very high capacity of 1015 mAh g^{-1} at 0.23 A g^{-1} (0.5C) over 130 cycles.

Another method of improving the electrochemical performances of individual iron and manganese oxides is to substitute in an additional transition metal atoms to give mixed metal oxides that have a spinel structure of AB_2O_4 (A/B = Zn, Ni, Cu, Fe, Co, Mn, Mo, Sn).[57] The reasons for this include higher ionic and electronic conductivities, easy methods of synthesis and high theoretical capacities. In general spinels store charge through the combination of conversion reactions from metal oxide to nanocrystals of metal and lithium dioxide and an

alloying/dealloying process of the second metal species with lithium. This is the case for zinc which can undergo alloying with lithium ions thereby giving a theoretical capacity of ~1000 mAh g^{-1} for the compound $ZnFe_2O_4$ by increasing the number of lithium atoms that can be hosted per formula unit from 8 to 9 (Equations 6.1 and 6.2).[332]

$$ZnB_2O_4 + 8Li^+ + 8e^- \rightarrow 2B^0 + 4Li_2O + Zn^0) \quad (6.1)$$

$$Zn^0 + Li^+ + e^- \rightarrow LiZn \quad (6.2)$$

The general formula of a spinel (AB_2O_4) consists of divalent (A^{2+}) and trivalent (B_2^{3+}) cations which form a unit cell that contains 64 tetrahedral cations and 32 octahedral cations.[383] The spinel structure can be further separated into normal, inverse and mixed spinels, each of which are differentiated by the cation occupancy.[384] The normal spinel structure consists of the A cations sitting in the tetrahedral sites and the B cations sitting in the octahedral sites preferentially and is denoted by the formula $[A^{2+}][B_2^{3+}]O_4$. In the inverse spinel crystal structure, the octahedral sites are inhabited by all of the A cations and half of the B cations and the remining B cations sit on the tetrahedral sites, they are denoted by the formula $[B^{3+}][A^{2+}B^{3+}]O_4$ and examples include the materials $CoFe_2O_4$ and $NiFe_2O_4$.[385,386] The third form of spinels, the mixed spinel, as the name suggest contains both the A and B cations occupying both the octahedral and tetrahedral sites. Mixed spinel's are denoted by the chemical formula $[A_x^{2+}B_{1-x}^{3+}][A_{1-x}^{2+}B_{1+x}^{3+}]O_4$, examples include the materials $MnCo_2O_4$ and $CoMn_2O_4$.[387]

Ferrite based spinel's, AFe_2O_4 (A = Zn, Mn, Cu and Co) are one type of spinel that show interesting magnetic and electrochemical properties, as well as being highly abundant on earth and environmentally friendly.[388] The zinc ferrites mentioned above ($ZnFe_2O_4$) display a normal spinel structure, despite having a theoretical capacity far above graphite, the charge storage mechanisms can cause major capacity fading over short term cycling.[121] This therefore makes them prime candidates for material engineering techniques such as nanostructuring and formation of composites. It was shown by Won *et al*. that by forming $ZnFe_2O_4$ into yolk-shell architectures through a spray drying process, a high specific capacity of 862 mAh g^{-1} after 200 cycles at 0.5 A g^{-1} could be achieved.[389] When investigated as anodic materials in full lithium-ion cells Varzi

et al.[390] reporting a maximum gravimetric energy of 202 Wh kg^{-1} at low current and a maximum gravimetric power of 3.72 kW kg^{-1} at high current cycling for carbon coated nanoparticles of $ZnFe_2O_4$ as the anode in conjunction with $LiFePO_4$/CNT composite as the cathode.

Manganese ferrites ($MnFe_2O_4$) are another promising set of materials for energy storage applications with a theoretical capacity of 928 mAh g^{-1} that is provided by a conversion mechanism that can accommodate eight lithium or sodium ions per formula unit.[383] The electrochemical performance of $MnFe_2O_4$ was found to be greatly improved by synthesising microspheres.[391] The porous microspheres were found to display a reversible capacity of 712 mAh g^{-1} after 50 cycles at 0.2 C, this was accounted for by the ability of the porous structure to withstand the volume changes. The long term cycling stability was improved on through the formation of carbon coated nanoparticles of $MnFe_2O_4$ arranged into hollow microsphere architectures via an emulsion based process.[392] These were found to retain a very high specific capacity of 730 mAh g^{-1} after 300 cycles at 2 A g^{-1}, and could exhibit 433 mAh g^{-1} at the very high current of 10 A g^{-1}. The benefits of carbon-$MnFe_2O_4$ composites has also been found in sodium ion batteries as well, Kollu *et al*. showed that a nanocomposite of $MnFe_2O_4$/rGO could not only deliver a stable capacity of 905 mAh g^{-1} at 0.1C versus Li/Li^+ but also a very impressive 258 mAh g^{-1} at the same rate versus Na/Na^+.[393]

Other similar spinel examples include $ZnMn_2O_4$ which was reported to give a specific capacity of 896 mAh g^{-1} at 0.2 A g^{-1} and retained 800 mAh g^{-1} after 300 cycles at 0.5 A g^{-1} when synthesised as porous microspheres.[394] Composites of $ZnMn_2O_4$/graphene nanosheets were found to improve on this performance with a capacity retention of 650 mAh g^{-1} after 1500 cycles at 2 A g^{-1}.[395]

From the work reported herein this thesis and throughout the wider literature, there are also major benefits in electrochemical performance to be obtained through the formation of tertiary mixed metal oxides with metal ions of different valences.[65] Synergistic effects in the local electronic structure can be induced in particles through the sharing of electron density between ions of different electronegativities, which can lead to the preferential promotion of different redox sites to the surfaces and thereby different interactions with lithium ions.[396]

The work in this chapter describes the use of CHFS to synthesise a range of individual, binary and tertiary mixed metal oxides with the constituent elements Fe, Mn, and Zn. The physical characterisation of the nanomaterials, as well as the electrochemical analysis as anode materials for lithium-ion batteries is also explored and discussed. The materials that displayed high specific capacities at both low and high current, as well as those that exhibited greater long term cycling stability were identified and then subjected to the formation of a graphitic carbon coating to further improve the electrochemical performance. The nature of the interaction between the different oxidation states, crystal phases and the carbonaceous elements were investigated and used to deepen the understanding of the mechanisms occurring, how they relate to electrochemical performance and how to manipulate them to obtain high energy and high anode material for lithium-ion energy storage devices.

6.3 Experimental Methods

6.3.1 Synthesis Methods

The experimental set-ups and synthesis parameters are described in detail in section 2.3.4.

6.3.2 Physical Characterisation

The techniques and methods used to characterise the physical properties are described in section 2.1.

6.3.3 Electrochemical Characterisation

The formation of electrodes and half cells are described in section 2.2.1 and 2.2.2 respectively. The electrolyte used in the lithium-ion half-cells was 1M $LiPF_6$ in 3:7 v/v EC/EMC. GCD cycling was performed at a range of specific currents over the potential window 0.05 to 3 V vs. Li/Li^+ by an Arbin Instrument (Model BT-2000 battery tester, USA). CV and potentiostatic EIS analysis were both performed on a Gamry Interface 1000 Potentiostat (Gamry Instruments, USA). CVs were conducted at different scan rates in the voltage window 0.05 to 3 V vs. Li/Li^+, EIS was performed over the frequency range 100 kHz to 10 mHz, the oscillating AC voltage was 10 mV ms^{-1}, for 10-point measurements.

6.4 Results and Discussion – Materials Discovery Study of Mixed Fe/Mn/Zn Oxides

6.4.1 Synthesis of Mixed Fe/Mn/Zn Oxides

The ratios of the different constituent metals were selected to give a picture of the composition/structure/performance relationships. The nominal target materials are shown in Figure 6.2. The full list of nominal ratios and detailed information regarding the synthesis conditions are found in section 2.4.4. The materials were denoted by the relative ratios of the metals, e.g., Fe = 0.33, Mn = 0.33 and Zn = 0.33 is referred to as FMZ111. The materials were obtained post CHFS, cleaned by centrifugation and then freeze-dried. The final materials were

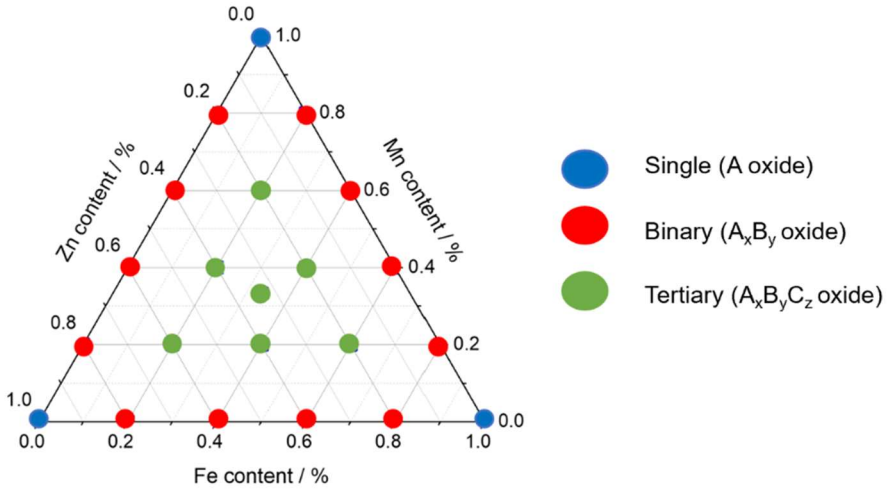

Figure 6.2: Ternary diagram of Fe, Mn and Zn with the target compositions for single metal oxides (blue dots), binary metal oxides (red dots) and tertiary metal oxides (green dots) highlighted.

collected as black, grey, and yellow powders depending on the concentrations of the metals. For the synthesis of carbon composite FMZ materials (denoted herein CFMZ), the carbon source (sucrose) was introduced to the CHFS process in-flow, the as-collected materials were, cleaned by centrifugation, freeze-dried, and subjected to heat treatment under nitrogen atmosphere. The final materials were collected as black powders.

6.3.2 Physical Characterisation of Mixed Fe/Mn/Zn Oxides

The as-synthesised materials were initially analysed by XRF to determine the ratios of constituent metals. It was found that the ratios of metals determined by XRF were a good match to the target composition ratios as shown by Figure 6.3. There was a trend observed for the tertiary materials, in which the relative amounts of manganese were found to be slightly lower than expected (~1%), this was attributed to several factors including not all the manganese reacting in the CHFS process, as well as the hydroscopic nature of manganese nitrate that could alter the mass of manganese in the precursor solutions.

All materials were initially investigated by PXRD. For the single metal oxides, the CHFS iron oxide was found to have well defined peaks at 2θ = 15.08, 16.19, 22.21 and 24.14 ° that were indexed to a trigonal corundum Fe_2O_3 structure (Figure 6.4, ICSD collection code: 7797).[397] The CHFS manganese oxide was also found to have sharp peaks at 2θ = 8.26, 13.18, 14.71 and 16.39 ° that were indexed to a tetragonal spinel Mn_3O_4 structure (Figure 6.5, ICSD collection code: 257346).[398] The CHFS zinc oxide was found to be a good match for hexagonal ZnO with peaks at 2θ = 14.5, 15.68 and 16.48 ° (Figure 6.6, ICSD collection code: 26170).[399]

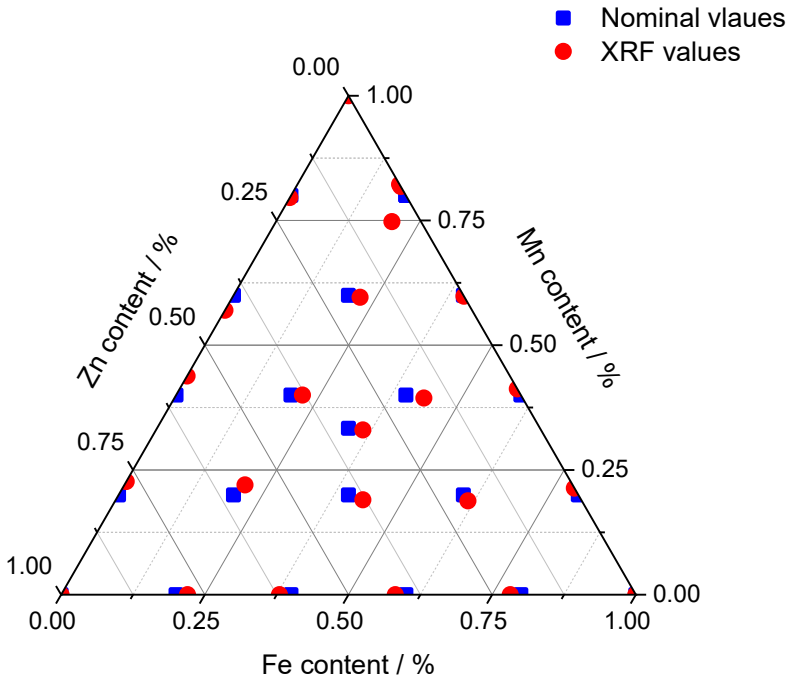

Figure 6.3: Ternary diagram showing the target compositions (blue squares) and the compositions of metals determined by XRF (red dots).

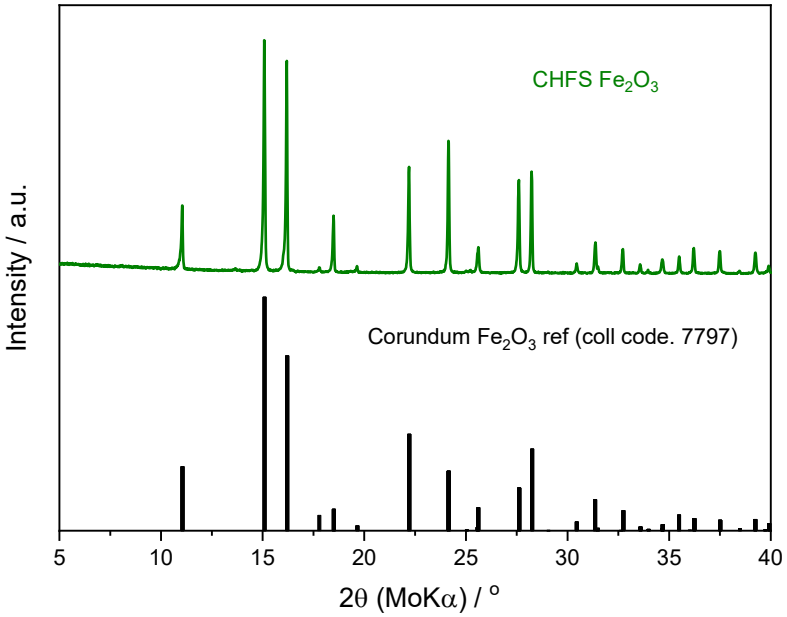

Figure 6.4: Graph showing the PXRD pattern for CHFS iron oxide (green) and the reference pattern for corundum Fe_2O_3 (ICSD coll. code: 7797).

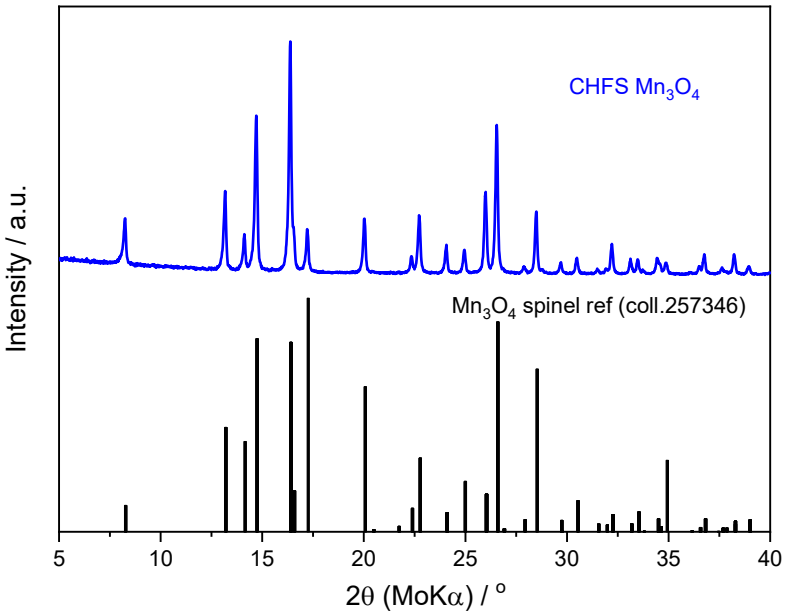

Figure 6.5: Graph showing the PXRD pattern for CHFS manganese oxide (blue) and the reference pattern for spinel Mn_3O_4 (ICSD coll. code: 257346).

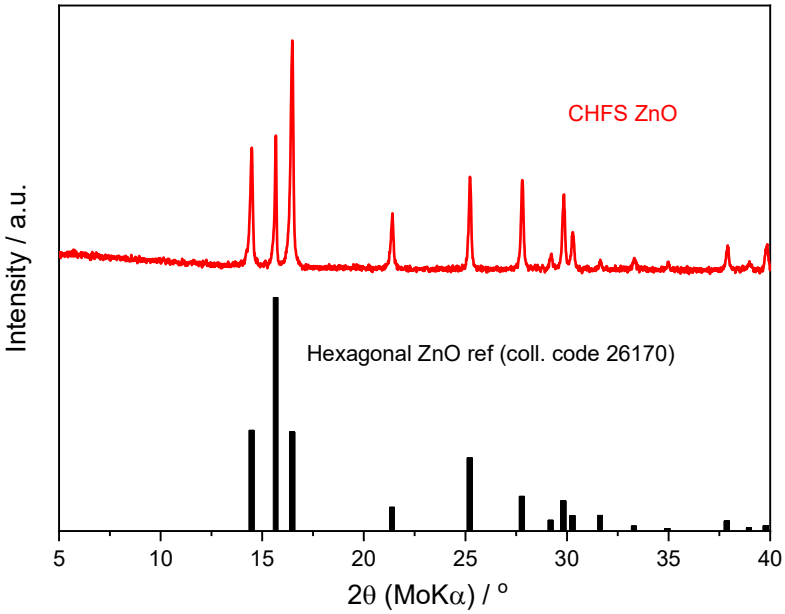

Figure 6.6: Graph showing the PXRD pattern for CHFS zinc oxide (red) and the reference pattern for hexagonal ZnO (ICSD coll. code: 26170).

PXRD analysis of the binary metal oxides revealed sharp, well-defined peaks for all the materials synthesised. Along the Zn-Mn binary line (Figure 6.7), the material ZnMn41 was found to be a good match for hexagonal ZnO,[399] with a few very small peaks/shoulders visible of an additional second phase. As the concentration of Mn was increased through the materials ZnMn32 and ZnMN23, the small peak at 2θ = 13.14 ° grew significantly in intensity and was matched to spinel Mn_3O_4.[398] The relative intensities of the two phases in ZnMn23 suggest equal amounts of the two were present in the material. For the higher Mn concentration material ZnMn14, the spinel Mn_3O_4 phase become dominant as was to be expected.

For the materials along the Zn-Fe binary line however (Figure 6.8), the high iron material ZnFe14 was not matched to corundum Fe_2O_3 in contrast to the single metal oxide. The peaks at 2θ = 13.7 and 16 ° of the dominant phase were found to be a spinel $ZnFe_2O_4$ structure,[400] the disparity between the crystal structure and the stoichiometry also suggests the possibility of iron atoms also sitting on the A sites as well as the B sites.[401] As the concentration of zinc was increased,

the peak at 2θ = 16.5 ° for ZnO grew significantly to give roughly equal proportions of the two crystal phases in the materials ZnFe32 and ZnFe23, for the material ZnFe41 the dominant phase was determined to be ZnO, however there was a small peak at 2θ = 16 ° indicating the presence of a small amount of $ZnFe_2O_4$ that remained.

The materials along the final binary line of Fe-Mn were analysed to have a mixture of crystal phases (Figure 6.9). At either end of the compositional line, high concentrations of Mn gave a multitude of diffraction peaks, some of which were a match to spinel Mn_3O_4 and others that indicated the presence of several other phases. High concentrations of iron were found to give predominantly peaks that were matched to spinel $MnFe_2O_4$ (ICSD collection code:155275),[402] with some small impurity peaks from other crystal phases present. For the materials FeMn23 and FeMn32, the PXRD patterns were much cleaner and showed that $MnFe_2O_4$ was the dominant phase with almost no visible impurity peaks.

The PXRD patterns for the tertiary metal oxides (Figure 6.10) were found to have predominantly two crystal phases present, peaks at 2θ = 15.68 and 16.48 ° were observed for materials with high concentrations of zinc and were indexed to hexagonal ZnO,[399] however these peaks were small in relative intensity suggesting it was a secondary phase. The larger peaks at 2θ = 13.7 and 16 ° were seen for all of the mixed ZnFeMn materials, these were found to be a good match for the spinel crystal structure of AFe_2O_4 (A = Zn and Mn) with mixed occupancy of the A site with Zn and Mn reflective of the overall stoichiometry.[400,402]

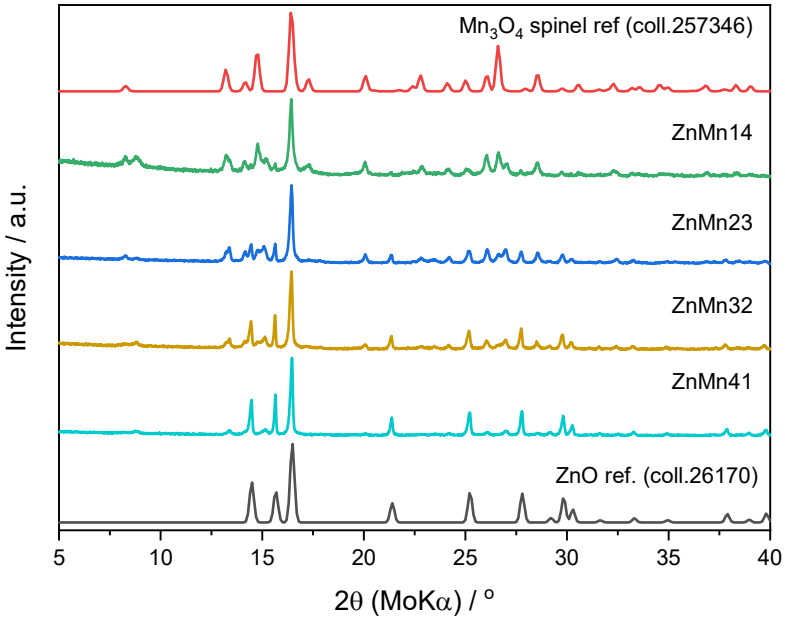

Figure 6.7: Graph showing the PXRD patterns for the binary Zn-Mn materials with the reference patterns of ZnO (black) and spinel Mn_3O_4 (red) plotted.

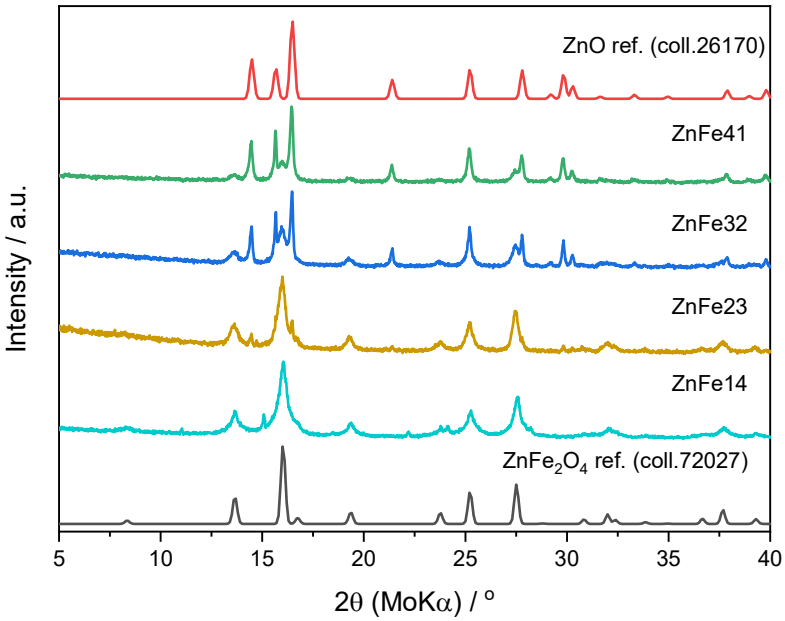

Figure 6.8: Graph showing the PXRD patterns for the binary Zn-Fe materials with the reference patterns of ZnO (red) and spinel $ZnFe_2O_4$ (red) plotted.

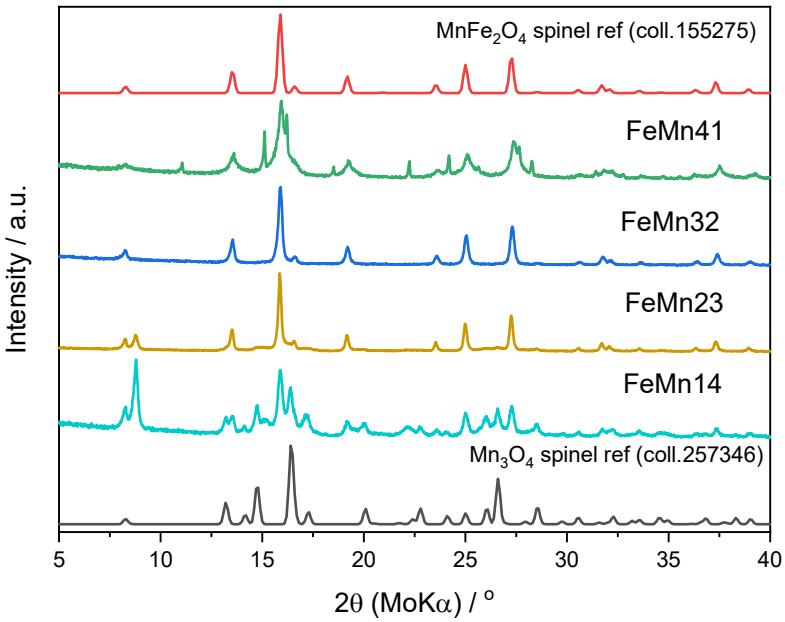

Figure 6.9: Graph showing the PXRD patterns for the binary Fe-Mn materials with the reference patterns of Mn_3O_4 (black) and $MnFe_2O_4$ (red) plotted.

Scherrer crystallite size analysis was performed for all FMZ samples, the most intense peak of the dominant crystal phase was selected for use in the analysis. All the mixed metal oxide materials were found to have small crystallite sizes between 6-53 nm (Figure 6.11). These small sizes combined with the sharp nature of the PXRD patterns suggests that the particle sizes will also be small (<100 nm), this is supported by previous findings of similar materials synthesised by CHFS.[174,403,404] It was observed that the smallest Scherrer sizes were found in general for those materials with lower than 50 % Zn content as seen by the large blue swathe on the heat map, whilst the largest crystallite sizes were calculated to be for pure CHFS Mn oxide and for high Zn content materials.

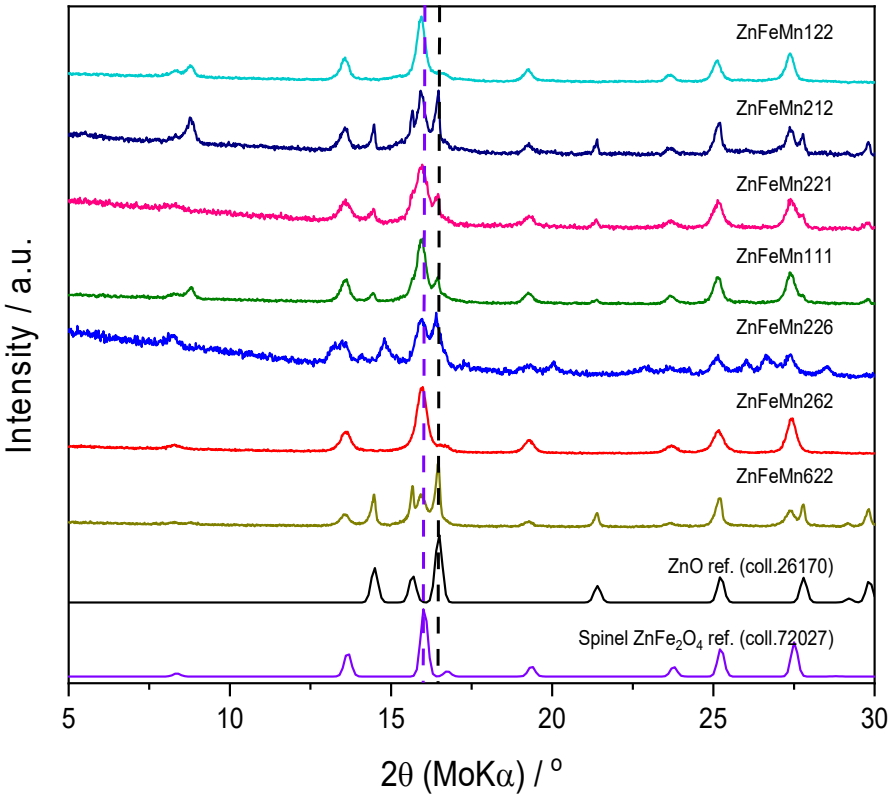

Figure 6.10: Graph showing the PXRD patterns of the tertiary Zn-Fe-Mn materials with the reference patterns for ZnO (black) and $ZnFe_2O_4$ (lilac) plotted

The BET specific surface areas (SSA) of all the FMZ materials were found to quite low across compositional space. For example, the SSAs for ZnO, FeO, MnO, ZnFe23, FeMn23, ZnMn23 and FeMnZn111 were found to be 16.6, 8.8, 22.7 39.3, 32.8, 17.5 and 53.5 $m^2\ g^{-1}$ respectively.

Further physical characterisation of the materials was found to be challenging. Due to the vast majority of the materials displaying magnetic properties, imaging of the particles through Transmission Electron Microscopy was not possible without advanced techniques such as Lorentz microscopy or electron holograpy.[405] The presence of iron in the samples was also determined to make the determination of the valence states of the metals exceptionally difficult. This is due to the $2p_{3/2}$ peak of Fe (II) and high-spin Fe (III) compounds displaying

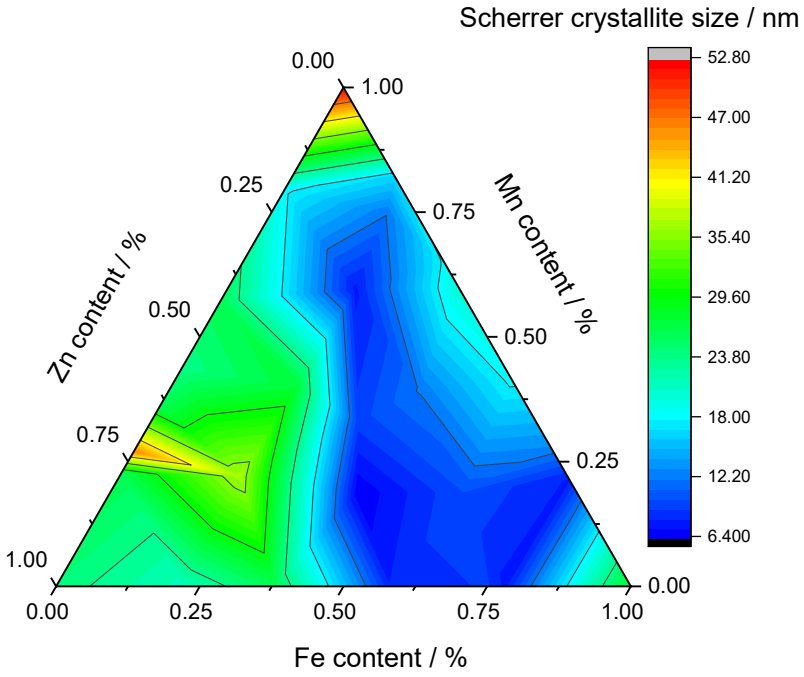

Figure 6.11: Ternary diagram with the calculated Scherrer crystallite sizes plotted as a heat map, red as the largest and blue as the lowest.

broader peaks that for low spin Fe (III). This is a result of spin-orbit coupling between the 2p core hole and unpaired 3d electrons, crystal field interactions and electrostatic interactions, creating multiplet splitting such as those calculated by Gupta and Sen.[406] The fitting of Fe (III) peaks is only made more complex by the presence of other forms of Fe being present in the sample as shown by M. C. Biesinger *et al.*[407] The addition of other metal ions with their own complex electronic structures such as Manganese, being present in the material and interacting with the Fe ions, only exacerbates the issue. In order for the accurate, reliable fitting of a spectra to elucidate oxidation states, the spectra of standards of similar mixed metal materials with known oxidation states would be required in order to build a model for comparison.[408] The construction and optimisation of this model is outside the current remit of this thesis and would be an avenue for potential future research.

6.3.3 Electrochemical Characterisation of Mixed Fe/Mn/Zn Oxides

The average specific capacities over 10 cycles at currents of 0.1, 0.5 and 1 A g^{-1} were plotted as a heat map overlayed onto ternary plots of composition (Figure 6.12a, b and c correspondingly). At the low specific current of 0.1 A g^{-1}, the majority of the mixed Fe/Mn/Zn materials displayed high average specific capacities between ~300 to ~500 mAh g^{-1}, the lowest specific capacities were found to be at the very edges of the ternary plots for the individual metal oxides. Overall, the distribution of specific capacities loosely followed the opposite to the Scherrer size plot (Figure 6.11), potentially suggesting a correlation between small particle size/amorphous nature and higher specific capacity, as has been reported previously for metal oxide materials displaying pseudocapacitance.[304,409] All of the Fe/Mn/Zn materials were found to display sever capacity loss over cycling, with the effect more pronounced at higher specific currents. This behaviours of capacity loss has been reported previously for similar materials.[317] The specific capacities were all found to be lower than the theoretical capacities for individual metal oxides and some spinel materials discussed above, this could be associated to the low levels of crystallinity achieved by CHFS alone, as seen by PXRD analysis, and suggests these material could benefit from a post-synthesis heat treatment protocol to improve the crystallinity as has been shown previously in this thesis.

To investigate the cycling behaviour across compositional space further, the GCD plots of specific capacity vs. potential of $Zn_{0.4}Fe_{0.6}$, $Zn_{0.4}Mn_{0.6}$, $Fe_{0.4}Mn_{0.6}$ and $Fe_{0.33}Mn_{0.33}Zn_{0.33}$ were constructed (appendix Figure 16), from these differential capacity plots (dQ/dV vs. potential) were created for cycles 2, 3, 5 and 10 at a specific current of 0.1 A g^{-1} (Figure 6.13a, 6.14b, 6.13c and 6.13d respectively. Analysis of the plots revealed several peaks that relate to capacity, in three different areas that were attributed to different charge storage mechanisms: Region (a) has been attributed in literature to electrolyte decomposition providing additional capacity;[58,410] Region (b) contains the largest charge storage peaks that were attributed to conversion reactions from oxide to elemental metal and back again for both Fe and Mn oxides;[373] Region (c) was associated with charge storage by reversible lithium intercalation into the crystal structures for Fe, Mn and Zn oxides.[411–413] The size and location of the peaks and therefore for the regions was determined by the onset and cut off potentials of the intercalation

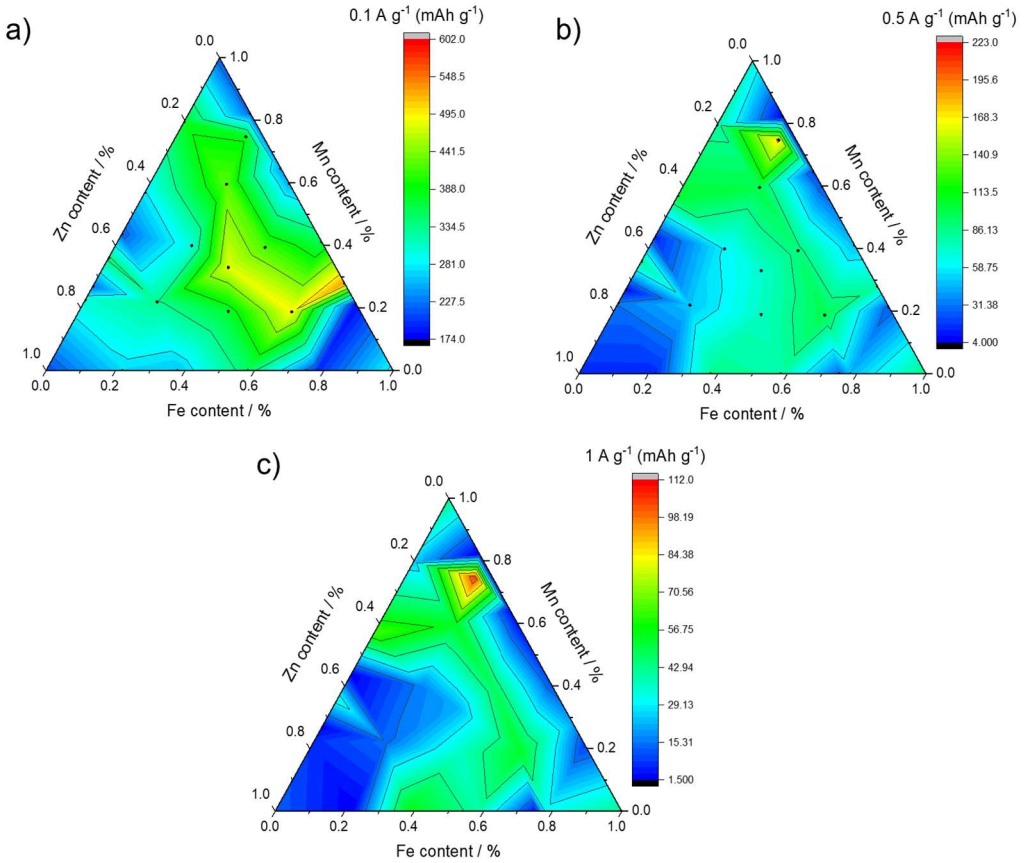

Figure 6.12: Compositional ternary diagrams with specific capacity overlayed as a heat map at specific currents of a) 0.1 A g^{-1}, b) 0.5 A g^{-1} and c) 1 A g^{-1}.

and conversion peaks. These were found to vary with composition, $Zn_{0.4}Fe_{0.6}$ displayed both a sharp peak for conversion storage (region b) and the highest potential window of ~0.75-1.25 V vs. Li/Li^+ (Figure 6.13a). In comparison, the conversion peak for $Zn_{0.4}Mn_{0.6}$ was found to be much broader and over a lower potential window (~0.25-0.90 V vs. Li/Li^+, Figure 6.13b). The composition of $Fe_{0.4}Mn_{0.6}$ was found to be at an even lower potential window of ~0.25-0.50 V vs. Li/Li^+ (Figure 6.13c). The tertiary composition $Fe_{0.33}Mn_{0.33}Zn_{0.33}$ displayed the largest potential windows for both regions b and c (conversion and intercalation respectively), which is expected due to the presence of the three different metals having different onset potentials for reaction with lithium ions. All four types of material display a significant decrease in the size of all of the different peaks between cycle 2 and cycle 10, this reduction in capacity could be associated with irreversible changes to the crystal structure and particles due to volume changes upon the insertion and removal of lithium associated with conversion reactions.[414]

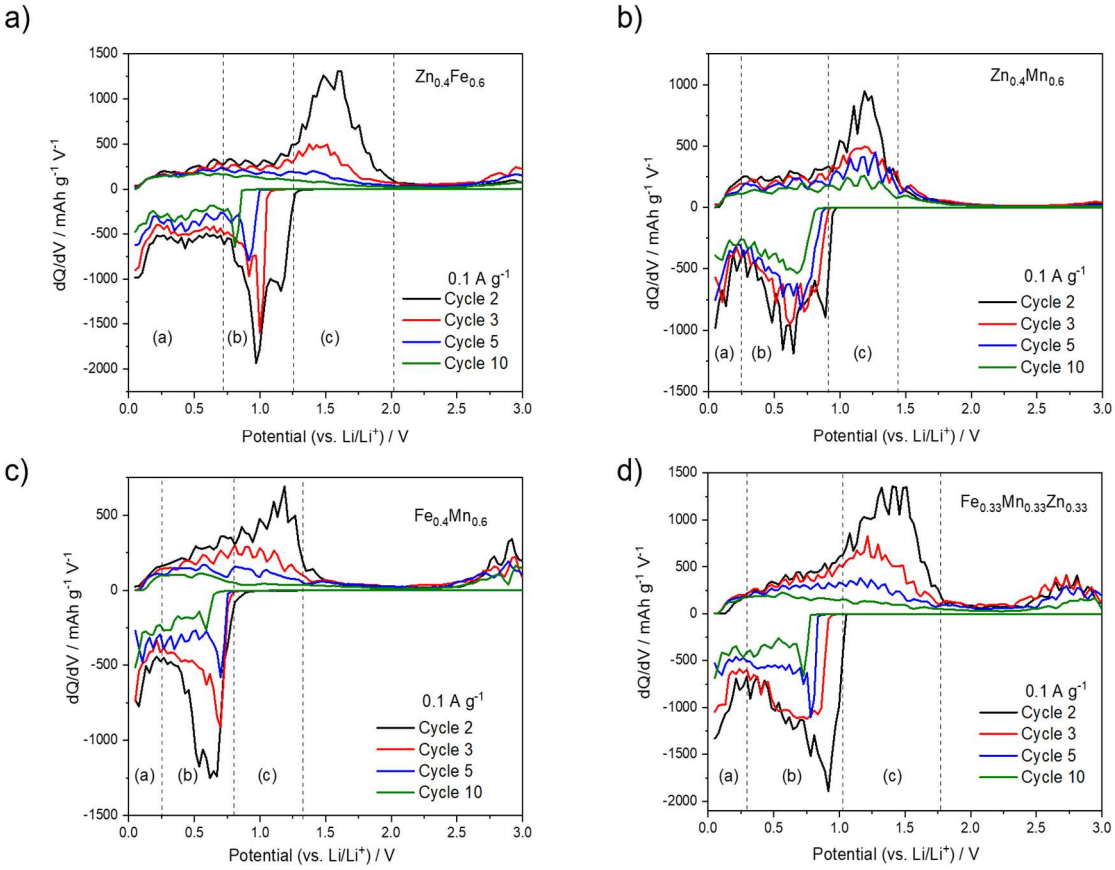

Figure 6.13: Differential capacity plots (dQ/dV vs. potential) of cycles 2, 3, 5 and 10 (black, red, blue and green respectively) at a specific current of 0.1 A g^{-1} for a range of different FMZ materials from across ternary compositional space. (a) $Zn_{0.4}Fe_{0.6}$ (b) $Zn_{0.4}Mn_{0.6}$ (c) $Fe_{0.4}Mn_{0.6}$ (d) $Fe_{0.33}Mn_{0.33}Zn_{0.33}$.

The highest specific capacity of the materials tested was found to be 531 mAh g^{-1} for FeMn41 ($Fe_{0.8}Mn_{0.2}$). As the specific current was increased to 0.5 and 1 A g^{-1}, the composition $Fe_{0.2}Mn_{0.75}Zn_{0.05}$ was identified as having specific capacities of 172 and 105 mAh g^{-1} respectively (shown by the hot spot on the ternary heat maps), displaying greater capacity retention and more stable cycling compared to all other compositions tested including the zinc free analogue material $Fe_{0.2}Mn_{0.8}$, highlighting it as a composition of interest for further development and investigation. At high specific currents (>1 A g^{-1}) the capacity decreased dramatically (Figure 6.14a), this was suggestive of poor conductivity limiting high current performance, as well as low stability due to the volume expansion associated with the conversion reaction of both Mn and Fe oxides and lithium.[415,416] The GCD curves of $Fe_{0.2}Mn_{0.75}Zn_{0.05}$ show large voltage plateaus between 1-1.5 V vs Li/Li^+ on the charge step and 0.75-0.2 V vs. Li/Li^+ on the discharge step of the first cycle. This behaviour was found to be consistent on the 2nd and even 10th cycles (Figure 6.14b) despite the drop in capacity observed overall. The subsequent differential capacity plot identified the same peaks and regions for intercalation, conversion, and additional charge storage as for the other compositions discussed above. However, it was observed that the size of the dQ/dV vs. Potential plots did not decrease very much between cycle 2 and cycle 10, this improved capacity retention indicates the possible effects of pulverisation by volume fluctuations were reduced for this material. One possible explanation for this could be the doping of Zn into the crystal structures, this has been shown in literature to introduce oxygen vacancies and to assist in the conversion reactions.[417] Further work and specialised techniques are needed to elucidate the atomic structure and interactions with lithium of these materials to fully understand the trends that are observed.[418,419]

The voltage hysteresis of the Mn/Mn^{2+} redox couple was analysed (Figure 6.14d), it was found that at a 50 % state of charge (SOC), the charge (delithiation) and discharge (lithiation) voltages were 1.208 and 0.525 V vs Li/Li^+ respectively, giving a difference of 0.683 V vs Li/Li^+. The presence of voltage hysteresis, or overvoltage, has previously been assigned as one of the main causes for a drop in performance over cycling.[420] Voltage hysteresis results from a range of different effects. Thermodynamic hysteresis within an active material

corresponds to varying rates of lithium insertion into particles, which has been reported to be directly correlated to the operating temperature.[421] This can occur in conjunction with mechanical hysteresis and physical stress caused by differences in the lattice parameters at the boundaries of different crystal phases at different levels of lithiation.[422] The large structural differences between the unlithiated metal oxide, partially lithiated metal oxide and elemental metal and lithium oxide that are all associated with the conversion charge storage mechanisms of Fe and Mn oxides are likely to have played a role in the hysteresis observed.[423,424]

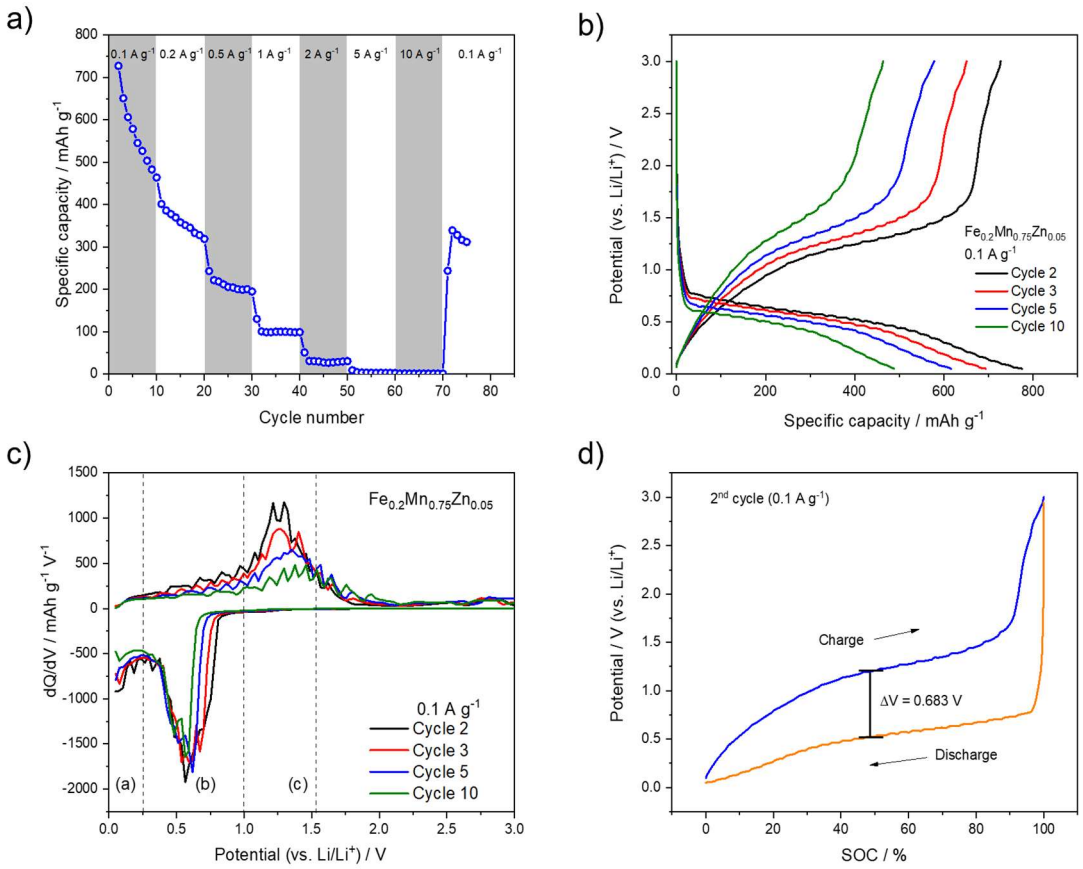

Figure 6.14: Graphs of $Fe_{0.2}Mn_{0.75}Zn_{0.05}$ oxide in lithium-ion half cells showing a) the specific capacity at different specific currents, b) the GCD curves for the 2nd (black) 3rd (red), 3rd (blue) and 10th cycles (green) at 0.1 A g^{-1}, c) the dQ/dV vs. potential plot, d) the GCD curves of SOC vs. potential of the 2nd cycle at 0.1 A g^{-1} with the voltage hysteresis highlighted.

6.4 Results and Discussion– Carbon Composite Mixed Fe/Mn/Zn Oxide Materials

6.4.1 Synthesis of Carbon Composite Mixed Fe/Mn/Zn Oxides

The materials $Fe_{0.2}Mn_{0.75}Zn_{0.05}$ and $Fe_{0.2}Mn_{0.8}$ were identified and selected for investigation into methods of improving its electrochemical performance particularly at high current cycling to make them applicable for applications such as HICs. A range of different carbon/metal oxide materials were synthesised *in-flow* where sucrose (the carbon source), and the metal salt precursors in the relative compositions outlined above, were dissolved at different sucrose: metal ratios and passed through the CHFS reactor. The as-collected powders after cleaning and drying were heat treated in a nitrogen atmosphere at 750 ℃ for 3 hours and the final products were collected as black powders. Ratios for each material can be found below (Table 6.1). The materials were referred to by $C(Fe_aMn_bZn_c)$-XHT, where C denotes the carbon from sucrose, a, b, and c are the relative atomic percentages determined by XRF, X denotes the ratio of sucrose to metal and HT refers to post heat treatment.

Sucrose to Metal Molar Ratio	**FMZ Sample Name**	**FM Sample Name**
1:2	$C(Fe_aMn_bZn_c)$-0.5HT	$C(Fe_aMn_b)$-0.5HT
1:1	$C(Fe_aMn_bZn_c)$-1HT	$C(Fe_aMn_b)$-1HT
2:1	$C(Fe_aMn_bZn_c)$-2HT	$C(Fe_aMn_b)$-2HT
3:1	$C(Fe_aMn_bZn_c)$-3HT	$C(Fe_aMn_b)$-3HT
4:1	$C(Fe_aMn_bZn_c)$-4HT	$C(Fe_aMn_b)$-4HT
5:1	$C(Fe_aMn_bZn_c)$-5HT	$C(Fe_aMn_b)$-5HT

Table 6.1: Table showing the different sucrose to metal oxide ratios and the sample names.

6.4.2 Physical Characterisation of Carbon Composite Mixed Fe/Mn/Zn Oxides

Initially, all materials were investigated by XRF prior to heat treatment to investigate the effect of sucrose on the precipitation of the metal oxides. It was observed that the four lowest carbon to metal ratios, C(FeMnZn)-0.5 to C(FeMnZn)-3, and C(FeMn)-0.5 to C(FeMn)-3 all gave elemental ratios that matched the initial metal salt concentrations of Fe = 0.2, Mn = 0.75 and Zn = 0.05 for the zinc containing samples, and Fe = 0.2 and Mn = 0.8 for the zinc free samples. However, both C(FeMnZn)-4 and C(FeMnZn)-5, and C(FeMn)-4 and C(FeMn)-5 were found to have different ratios of metals post synthesis (Table 6.2). The high relative concentrations of the sucrose have affected the precipitation of the metals, reducing the amount of Mn, and increasing the amounts of Fe and Zn present in the materials.

	Pre-CHFS, aqueous solution			**Post-CHFS XRF values**		
	[Fe] / % of Total Molarity	**[Mn] / % of Total Molarity**	**[Zn] / % of Total Molarity**	**[Fe] / at. %**	**[Mn] / at. %**	**[Zn] / at. %**
C($Fe_aMn_bZn_c$)-4HT	20	75	5	66	21	11
C($Fe_aMn_bZn_c$)-5HT	20	75	5	72	17	9
C(Fe_aMn_b)-4HT	20	80	0	69	30	N/A
C(Fe_aMn_b)-5HT	20	80	0	77	21	N/A

Table 6.2: Table showing the initial percentage content of the three metals in aqueous solution before CHFS and the elemental percentages of the as-collected CFMZ materials as determined by XRF.

PXRD was performed on the materials both pre and post heat treatment. Prior to heat treatment, both the Zn containing and Zn free materials at low sucrose ratio (0.5-3) all showed a range of peaks that was suggestive of multiple phases being present (Appendix Figure 17-19). The high sucrose ratio samples (4 and 5) of both sets of materials were found to exhibit very broad patterns with few discernible peaks. Post heat treatment, the differences between low and high sucrose concentrations were found to still be present. At low sucrose

concentrations (X = 0.5-3HT) the Zn free materials all displayed well-defined peaks at 2θ = 15.9 and 18.4 ° (Figure 6.15a), which were indexed to a cubic FeO/MnO crystal structure (ICSD collection code: 60685).[425] Some other very small peaks were observed that suggested the presence of a small amount of another phase being present. For the Zn containing materials (Figure 6.15b), the same peaks for cubic FeO/MnO were observed. Both sets of materials displayed a small peak shift in 2θ values, this was attributed to all three metals sitting on the same sites in the crystal.[426]

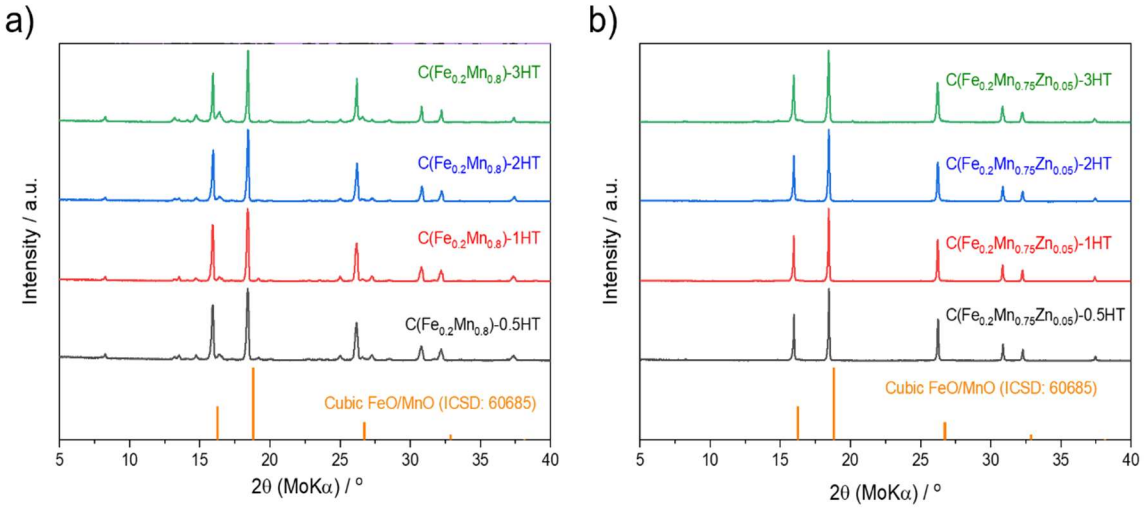

Figure 6.15: XRD patterns post heat treatment of low sucrose containing materials (0.5-3HT) for (a) Zn free materials, and (b) Zn containing materials. Reference pattern for cubic FeO/MnO (ICSD coll. code: 60685) shown in orange.

The PXRD patterns for the high sucrose concentration samples were found to be different to the lower concentration iterations (Figure 6.16a). C($Fe_{0.69}Mn_{0.3}$)-4HT was found to be primarily cubic FeO/MnO with several other peaks present indicating it to be multiphasic. The highest sucrose concentration material, C($Fe_{0.78}Mn_{0.21}$)-5HT, was found to have peaks at 2θ = 13.7, 16.0, 25.2 and 27.5 ° that were found to be a good match for the mixed Fe and Mn tetragonal spinel crystal structure ($Mn_{1.7}Fe_{1.3}O_4$, ICSD collection code: 76612).[427] Both materials, C($Fe_{0.66}Mn_{0.21}Zn_{0.11}$)-4HT and C($Fe_{0.72}Mn_{0.17}Zn_{0.09}$)-5HT, were also found to have peaks that corresponded to tetragonal spinel. However, it was observed that an extra set of peaks at 2θ = 20.2, 28.7 and 35.3 ° were present. The relative peak intensities were low for C($Fe_{0.66}Mn_{0.21}Zn_{0.11}$)-4HT but were far greater for C($Fe_{0.72}Mn_{0.17}Zn_{0.09}$)-5HT, the peaks were found to correspond to cubic metal Fe (Figure 6.16b, ICSD collection code: 14754).[428] This suggests that during the heat

treatment process to graphitise the sucrose, a carbothermal reduction reaction was occurring which led to the presence of metal Fe.[351] It has been described in literature that the doping of Zn into metal oxides enhanced that ability to perform catalytic reactions, this could potentially be a factor in facilitating the reduction of Fe oxide to metallic Fe in the composite materials containing Zn and why none is observed for the Zn free materials.[429] Further analysis with specialised techniques required to investigate the nature of the metallic Fe within the metal oxide particles and how the presence of Zn affects the heat treatment process.

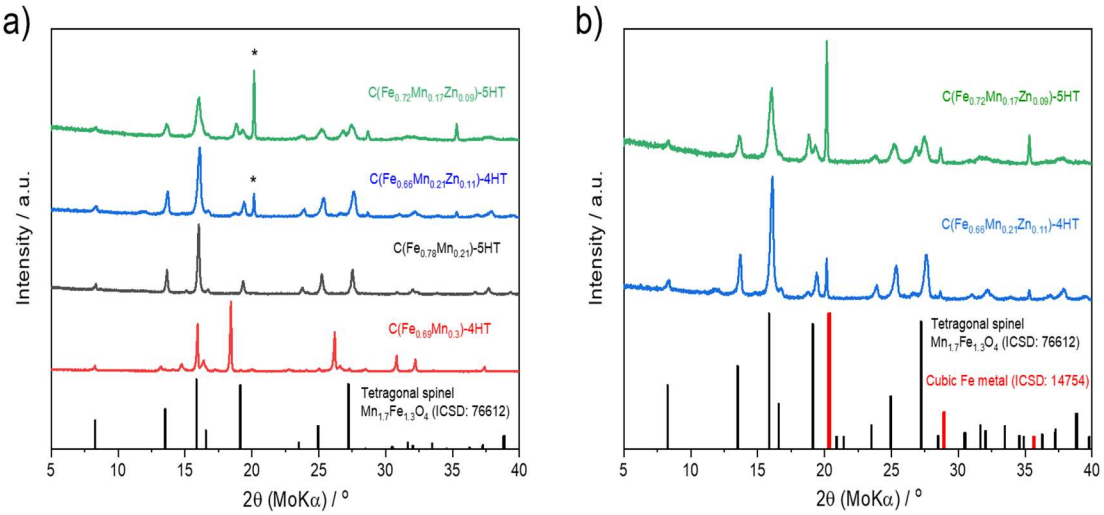

Figure 6.16: (a) PXRD patterns of the high sucrose concentration materials (X = 4HT and 5HT) for both Zn free and Zn containing materials. The reference pattern of tetragonal spinel (ICSD collection code: 76612) is shown in black. The extra peak at 20.2 ° is highlighted by an asterisk. (b) the PXRD patterns of C($Fe_{0.66}Mn_{0.21}Zn_{0.11}$)-4HT and C($Fe_{0.72}Mn_{0.17}Zn_{0.09}$)-5HT are shown with the reference patterns for tetragonal spinel (black) and cubic Fe metal (red, ICSD collection code: 14754).

The nature of the carbon was investigated by Raman spectroscopy (Figure 6.18) for the CFMZ materials. It was found that for the C(Fe_aMn_b) materials, at the lowest concentration of sucrose (Figure 6.17a), that no D or G bands of carbon were detected. This is suggestive that potentially not enough carbon survived the CHFS process to be coated onto the particles to be observable. At the highest sucrose concentration pre-heat treatment (Figure 6.17b), a large peak at ~1500 cm^{-1} was observed with a slight shoulder at ~1250 cm^{-1}, these were assigned to the G and D bands respectively. The large G band with respect to the D band indicates a high proportion of non-graphitic carbon present, as has been shown for similar carbon composite materials direct from CHFS before in this thesis.[44]

Post-heat treatment, the spectra was found to only contain unidentifiable peaks in the low wavenumber region and no D or G. This behaviour was mirrored for the C($Fe_aMn_bZn_c$) materials with no D or G bands identified in the low sucrose material both before and after heat treatment (Figure 6.17c), and with only the pre-heat treatment scan of the highest sucrose concentration material displaying absorption from carbon (Figure 6.17d). Another possible explanation for the lack of graphitic carbon detected, is that despite the heat treatment taking place in an inert atmosphere, the carbothermal reduction rection that has been postulated as a reason for the presence of Fe metal in the XRD pattern, converted all of the carbon to carbon dioxide in the process.[430]

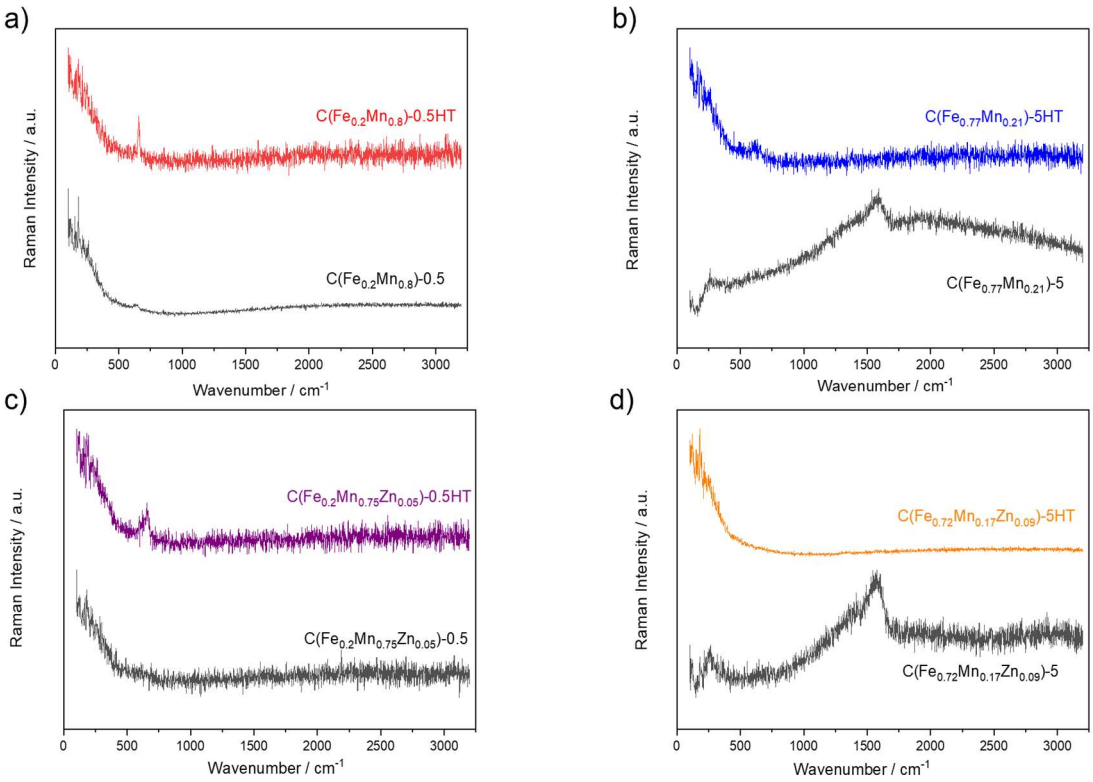

Figure 6.17: Raman spectra of (a) C($Fe_{0.2}Mn_{0.8}$)-0.5 for pre-(black) and post-(red) heat treatment, (b) C($Fe_{0.77}Mn_{0.21}$)-5 for pre- (black) and post-(blue) heat treatment, (c) C($Fe_{0.2}Mn_{0.75}Zn_{0.05}$)-0.5 pre-(black) and post-(purple) heat treatment, (d) C($Fe_{0.72}Mn_{0.17}Zn_{0.09}$)-5 pre-(black) and post-(orange) heat treatment.

6.4.3 Electrochemical Characterisation of Carbon Composite Mixed Fe/Mn/Zn Oxides

The C(Fe_aMn_b)-XHT and C($Fe_aMn_bZn_c$)-XHT materials were investigated electrochemically as anode materials in lithium-ion half cells. GCD cycling at a low specific current of 0.1 A g^{-1} revealed that the lower sucrose concentration materials, C($Fe_aMn_bZn_c$)-XHT (X = 0.5, 1, 2 and 3) exhibited specific capacities of 410, 421, 385 and 314 mAh g^{-1} respectively (Figure 6.18a). The materials C($Fe_{0.66}Mn_{0.21}Zn_{0.11}$)-4HT and C($Fe_{0.72}Mn_{0.17}Zn_{0.09}$)-5HT were found to outperform the other materials by a large margin at both low and high specific currents, with the specific capacities at 0.1, 0.5, 1 and 2 A g^{-1} were found to be 932, 685, 460 and 271 mAh g^{-1}, and 715, 460, 338 and 202 mAh g^{-1} correspondingly. For the C(Fe_aMn_b)-XHT materials, the specific capacities at the low current of 0.1 A g^{-1} were found to be 493, 404, 262, 360 and 442 for the lower sucrose concentrations of X = 0.5, 1, 2, 3 and 4HT respectively (Figure 6.18b). The material with the highest sucrose concentration, C($Fe_{0.77}Mn_{0.21}$)-5HT displayed far superior specific capacities at both low and high current cycling. At specific currents of 0.1, 0.5, 1 and 2 A g^{-1}, the reversible specific capacities were found to be 776, 616, 493, 362 mAh g^{-1} correspondingly. These results show clearly the greater electrochemical cycling performance of the spinel crystal structure over the cubic FeO/MnO crystal structure materials, as well as presence of metallic Fe being associated with improved cycling ability as has been reported in literature for similar Iron oxide materials.[431]

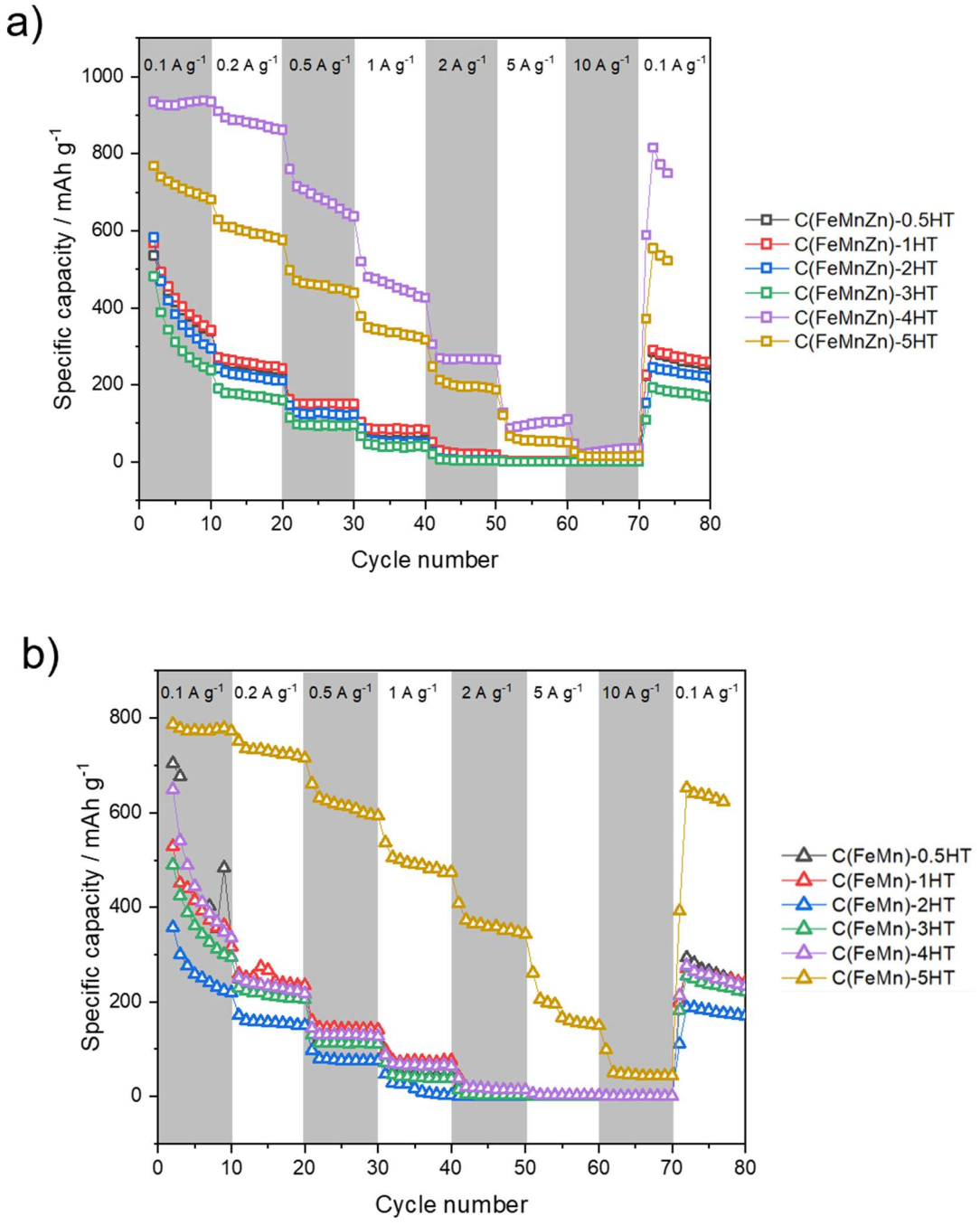

Figure 6.18: Graphs of specific capacity vs. cycle number for the (a) $C(Fe_aMn_bZn_c)$-XHT materials, (b) $C(Fe_aMn_b)$-XHT materials, at different specific currents.

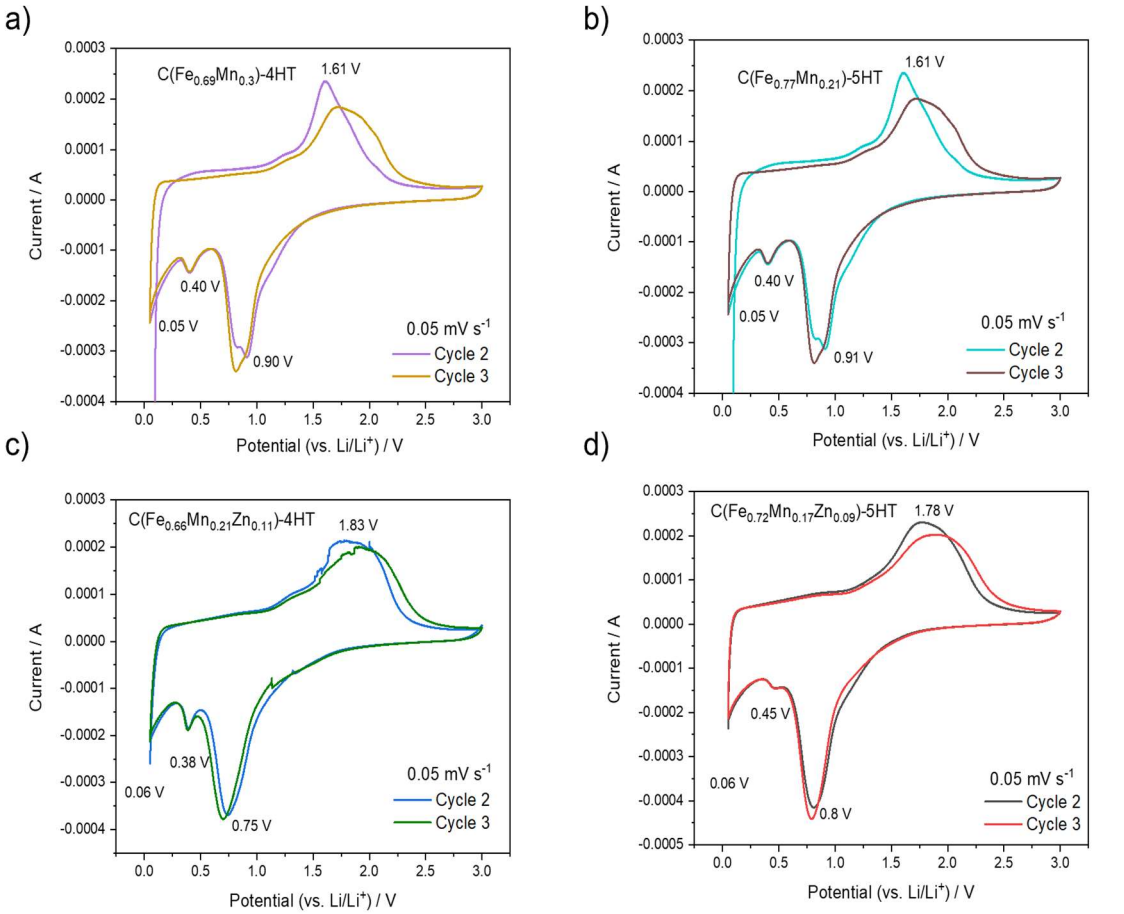

Figure 6.19: the first and second cycle CV curves at a scan rate of 0.05 mV s^{-1} for (a) $C(Fe_{0.69}Mn_{0.3})$-4HT, (b) $C(Fe_{0.77}Mn_{0.21})$-5HT, (c) $C(Fe_{0.66}Mn_{0.21}Zn_{0.11})$-4HT, and (d) $C(Fe_{0.72}Mn_{0.17}Zn_{0.09})$-5HT.

To investigate the electrochemistry of the high performing materials further, cyclic voltammetry was performed (Figure 6.19) All of the materials displayed CV curves that were coherent with other similar Mn/Fe oxide materials reported in literature. At a scan rate of 0.05 mV s^{-1} on the second cycle (first full cycle), $C(Fe_{0.69}Mn_{0.3})$-4HT and $C(Fe_{0.77}Mn_{0.3})$-5HT (Figure 6.19a and 6.19b) both displayed a large peak on the forward scan at 1.61 V and a small shoulder at 2.07 vs. Li/Li^+, these were attributed with the reversible oxidation of Fe^0 to Fe^{2+} and to Fe^{3+}.[376] Another small shoulder at 1.25 V vs. Li/Li^+ was also observed, this along with the peak at 2.07 V were a good match for the oxidation of Mn^0 to Mn^{2+} and Mn^{2+} to higher valance states respectively.[432] On the backward scan, two peaks at 0.9 and 0.4 V vs. Li/Li^+ were observed and assigned to the conversion of Fe_2O_3/Fe and MnO/Mn respectively.[433,434] For the peaks on the backward scan,

there was little change observed between the second and third cycles, this indicates good reversibility of the materials. For the oxidation peaks on the forward scan, the shapes of the peaks were found to broaden between the first and second cycles, as well as a slight shift to higher potentials. This could be explained by polarisation of the active materials and a promotion of Mn^{2+} to higher Mn valence states for charge storage as a result of cycling.[392,435] The materials C($Fe_{0.66}Mn_{0.21}Zn_{0.11}$)-4HT and C($Fe_{0.72}Mn_{0.17}Zn_{0.09}$)-5HT (Figure 6.19c and 6.19d) were found to display very similar CV curves to the Zn free materials. The large oxidation peaks on the forward scan were found at 1.83 and 1.78 V vs. Li/Li^+, with a small shoulder at 1.30 and 1.29 V vs. Li/Li^+. The shoulders were attributed once again with the oxidation of Mn^0 to Mn^{2+}, the broad peaks covered the potential window for the oxidation of Fe^0 to Fe^{2+} to Fe^{3+} and Mn^{2+} to higher Mn valence states. The peaks on the backward scan at 0.75 and 0.38, 0.8 and 0.45 V vs. Li/Li^+ were attributed to the conversion reactions of Fe_2O_3/Fe and MnO/Mn respectively. The shift in to higher and lower potentials for the oxidation and reduction reactions for the C($Fe_aMn_bZn_c$)-XHT materials, could possibly be explained by the differences in composition and presence of Zn doped into the crystal structure affecting the electronic local environment and introducing vacancies and defects.[436,437] The C($Fe_aMn_bZn_c$)-XHT materials were also found to display improved cycling reversibility as there was very little change in the peaks between the second and third cycles.

To investigate the effect of long-term cycling on the performance, the four materials were subjected to 100 cycle of CV testing at a scan rate of 1 mV s^{-1}, with an EIS experiment performed every 10th cycle. For the material C($Fe_{0.66}Mn_{0.21}Zn_{0.11}$)-4HT, the first cycle was found to contain a very large peak at 0.37 V vs. Li/Li^+ that was attributed to the decomposition of electrolyte and the formation of the SEI layer.[438] All of the same peaks observed at 0.05 mV s^{-1} were also seen at 1 mV s^{-1} (Figure 6.20a). Over the next 10 cycles, the oxidation peaks at ~1.8 V vs. Li/Li^+ were observed to broaden and shift to a higher potential, with the large reduction peaks at ~0.5 V vs. Li/Li^+ were observed to slowly decrease in size and shift to a lower potential (Figure 6.20a and 6.20b). This behaviour and the corresponding reduction in specific capacity could be attributed to the formation of an accumulative passivation internal phase within the active material

and the outer SEI layer acting as a rate-limiting diffusion barrier, as was shown by Li *et al.* in iron oxides.[439] Another contributing factor could be changes to the crystal structure and morphology due to volume changes upon lithium insertion and extraction.[373,435] Between cycle 10, cycle 50 and cycle 100 the overall size of the CV and the definition of the redox peaks decrease in the same trend of behaviour (Figure 6.20c) as before. The Nyquist plots, taken every 10 cycles, show a rapid change between 10 and 20 cycles, with the tail of the Nyquist plot experiencing a large drop in gradient. This supports the suggestion of passive internal and external surface layers forming and limiting diffusion. As the material is cycled up to 100 cycles, the size of the semi-circle and thereby the charge transfer were found to increase by more than a factor or two, while the tails continued to reduce in gradient. This same behaviour was also seen for the other materials, C($Fe_{0.69}Mn_{0.3}$)-4HT, C($Fe_{0.77}Mn_{0.21}$)-5HT and C($Fe_{0.72}Mn_{0.17}Zn_{0.09}$)-5HT, analysed (appendix Figure 20, 21 and 22). The specific capacity values exhibited by these materials highlight them as high performing, this combined with the trends displayed by CV and EIS analysis showing the degradation of the active material, all highlight the potential that these materials have as well as that further development of these materials is required to in order to reduce the effects of long-term cycling and extract the best performance.

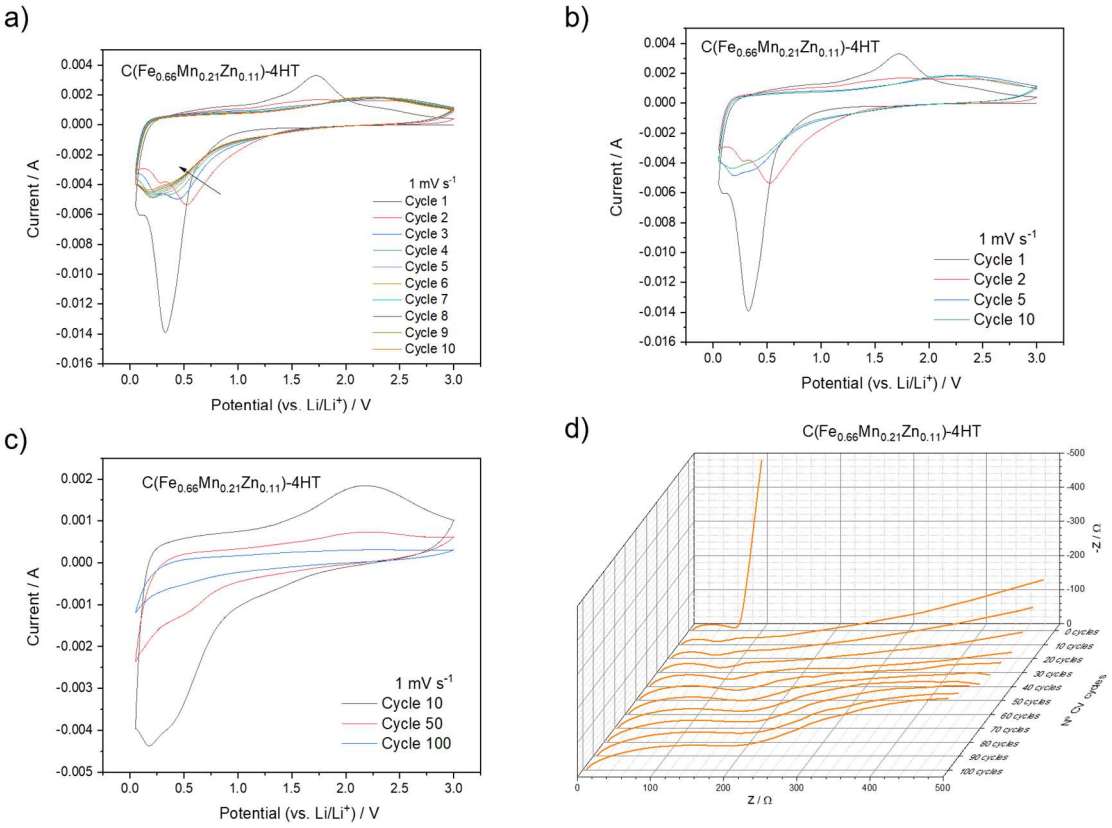

Figure 6.20: Graphs of $C(Fe_{0.66}Mn_{0.21}Zn_{0.11})$-4HT showing (a) the CV curves for the first 10 cycles at 1 mV s^{-1}, (b) CV cycles 1, 2, 5 and 10, (c) CV cycles 10, 50 and 100, (d) the Nyquist plots taken every 10th cycle between cycle 0 and cycle 100.

6.5 Conclusions

In conclusion, a range of Fe, Mn and Zn based single, binary, and tertiary mixed metal oxides were synthesised from across ternary space in a materials discovery study. It was found that the individual Fe, Mn, and Zn oxides has well defined PXRD patterns suggesting high levels of crystallinity. Along the Zn-Mn binary line, the PXRD patterns were found to be a mixture of two major phases of either cubic ZnO or spinel Mn_3O_4, the proportion of which was dependant on the composition. This was also observed along the Zn-Fe line for ZnO and spinel MFe_2O_4, and along the Mn-Fe line between Mn_3O_4 and $MnFe_2O_4$ spinels. For the tertiary metal oxides, the PXRD patterns were found to be a mixture of spinels. Analysis of the Scherrer crystallite size found the higher the Zn concentration, the larger the calculated value. Electrochemical characterisation in lithium half-cells of the FMZ materials found that there was a correlation between small Scherrer size and

higher specific capacity at low current cycling. Analysis of the differential capacity plots from across compositional space identified both intercalation and conversion mechanisms of charge storage, as well as a decrease in the redox peak size and the resultant specific capacity over short term cycling. At low current, the material $Fe_{0.8}Mn_{0.2}$ was found to have the highest specific capacity of 531 mAh g^{-1}, at the higher currents of 0.5 and 1 A g^{-1} the material $Fe_{0.2}Mn_{0.75}Zn_{0.05}$ was found to outperform the others with corresponding capacities of 172 and 105 mAh g^{-1}. Analysis of the GCD curves revealed a large voltage hysteresis of 0.68 V between charge and discharge, which was attributed in part to the reason for capacity fade being observed.

Based off the high current cycling performance, the compositions $Fe_{0.2}Mn_{0.8}$ and $Fe_{0.2}Mn_{0.75}Zn_{0.05}$ were used in the formation of carbon-metal oxide composite materials via an inert atmosphere heat treatment assisted CHFS method. Sucrose was used as the carbon precursor at a range of different concentrations. XRF studies showed good agreement between the elemental compositions of the materials and the initial concentrations of metal salt precursors for the three lowest sucrose concentrations. PXRD analysis of the materials found that they all displayed the crystal phase of cubic FeO/MnO without any impurity phases. The two highest sucrose concentrations were found by XRF to affect the precipitation of Mn, leading to the materials displaying a high Fe and low Mn composition. PXRD of these materials found that the dominant crystal phase was a tetragonal spinel, it was also found that the Zn containing materials contained metallic Fe, this was hypothesised as being a result from the Zn facilitating the carbothermal reduction of iron oxide to metallic iron. Raman analysis of all of the $C(Fe_aMn_b)$ and $C(Fe_aMn_bZn_c)$ materials found that for the lower sucrose concentration materials (0.5-3 M) did not have any D or G bands of carbon present, suggesting that it was not high enough to survive the conditions of CHFS. The high sucrose concentration materials (4 and 5 M) were found to contain D and G bands that indicated amorphous carbon in the materials pre-HT. Post-HT, there were no D or G bands identified, this suggested that all the carbon had been lost in the furnace. Electrochemical characterisation of the materials as anodes in lithium half cells showed low specific capacities for the cubic FeO/MnO materials. The composite materials $C(Fe_{0.77}Mn_{0.21})$-5HT, $C(Fe_{0.66}Mn_{0.21}Zn_{0.11})$-

4HT and C($Fe_{0.72}Mn_{0.17}Zn_{0.09}$)-5HT were found to greatly outperform the other iterations at all specific currents tested at. The specific capacities at 0.1, 0.5, 1 and 2 A g^{-1} were found to be: 776, 616, 493 and 362; 932, 685, 460 and 271; and 715, 460, 338 and 202 respectively. Long term CV studies over 100 cycles at 1 mV s^{-1} showed the materials undergoing degradation through polarisation and broadening of redox peaks. EIS analysis taken every 10 cycles showed large changes to the charge transfer resistance as well as to the tail of the Nyquist plots, suggesting a reduction in the diffusion kinetics. The high specific capacities of the C($Fe_{0.77}Mn_{0.21}$)-5HT, C($Fe_{0.66}Mn_{0.21}Zn_{0.11}$)-4HT and C($Fe_{0.72}Mn_{0.17}Zn_{0.09}$)-5HT highlight these as conversion materials of interest for use as anodes in lithium-ion storage devices, that warrant further investigation to improve the long-term cycling as well as the capacity at very high cycling rates.

6.6 Outlook

The use of CHFS as a method for the discovery of novel material compositions was shown to be successful for the elements Fe, Mn, and Zn. In a broad view, further work on this technique could focus on different families of elements as well as the ability to infer composition-property relationships through detailed analysis. For the highest performing mixed metal oxides reported here, future work should focus on improving both the capacity retention over long term cycling and the intrinsic conductivity to reduce the degradation observed and increase the capacity at high cycling rates. Possible avenues to achieve these aims could centre around the use of other coatings of additives to reduce the impact of volume fluctuations during operation, or the use of other elements as dopants to introduce vacancies that improve the electronic conductivity. The formation of more porous nanostructures to improve ionic diffusion could also prove to be a direction of research of interest. The addition of sucrose in an assisted CHFS method to form high-capacity conversion anode materials was successful. In-situ analysis of the materials during cycling would be challenging due to the magnetic nature of the materials but could shed light on the role of the metallic Fe in cycling and the structural nature of the degradation. Both of which could be applied successfully to other similar materials. Further optimisation of the sucrose concentration and heat treatment parameters could allow for the improvement of the conductivity and long term cyclability.

7.0 Thesis Conclusions, Outlook and Future Work

7.1 Summary of Thesis Conclusions

The work reported and discussed in this thesis has centred around the use of CHFS (assisted and un-assisted) methods as tools for the formation of mixed metal oxides and composite carbon-metal oxide materials for use as high capacity and high-power anodic materials in lithium-ion storage devices. The materials examined in this thesis all benefited from small particle sizes, homogenous mixing of different metal ions and a high synthesis rate.

In Chapter 3, an assisted CHFS method was successfully utilised, for the first time as far as the author is aware, for the synthesis of $TiNb_2O_7$, a promising anode material reported in literature. Characterisation of the material with TEM identified particle sizes with average diameters below 100 nm. Cyclic voltammetry showed clearly defined redox peaks at both slow and fast scan rates. This was found to equate to high specific capacity and good retention at high current cycling with the CHFS TNO exhibiting 248 mAh g^{-1} at 0.1 A g^{-1} and retaining 76 % specific capacity at 2 A g^{-1} during galvanostatic cycling. The CHFS TNO was then investigated as an anode material in a lithium-ion HIC, where at a specific power of 300 W kg^{-1} the specific energy was identified to be 134 Wh kg^{-1}, and at the high specific power of 2020 W kg^{-1} the hybrid displayed a specific energy of 12.3 Wh kg^{-1}. These results showed the ability of assisted CHFS methods for the targeted synthesis of high performance nanosized metal oxides for energy storage.

The CHFS TNO material was taken forward to investigate the addition of carbonaceous compounds to the CHFS flow followed by a heat treatment in inert atmosphere to form carbon-titanium/niobium oxide nanomaterials (CTNO). It was found that the use of sucrose as a carbon precursor affected the precipitation of the two metal salt precursors leading to post-HT materials displaying PXRD patterns that suggested both rutile TiO_2 and poorly crystalline Nb_2O_5 were both present. Raman spectroscopy identified graphitic carbon, TEM and EDS found agglomerates of very small particles of homogenously mixed titanium and niobium oxide within a carbon matrix. Galvanostatic cycling of the composite CTNO materials found a large increase in the specific capacity at both low and high current cycling. At 0.1 A g^{-1} the best performance was found to be ~330

mAh g^{-1} and at the high specific current of 10 A g^{-1} the capacity was found to be 197 mAh g^{-1}, outperforming the non-carbon containing CHFS TNO materials. These results highlighted the benefit to electrochemical performance gained through carbon metal oxide composite materials synthesised via in-flow CHFS, as well as the importance for further work optimising the synthesis conditions to achieve optimal elemental ratios and crystal phase purity.

Chapter 4 reported the use of CHFS to create a library of ternary mixed metal oxides for the purpose of materials discovery. Building on previous research on mixed vanadium and molybdenum oxides, the addition of the third element Niobium was examined. A range of mixed V-Nb-Mo oxides from across ternary compositional space were successfully synthesised and investigated as anode materials for lithium-ion batteries. Heat maps of specific capacities at specific current cycling were constructed and used to identify the high performing composition $V_{0.3}Nb_{0.1}Mo_{0.6}$ (VNM316). This material was found to have nanosized particles with homogenous mixing of the metals and a single monoclinic crystal phase. VNM316 was found to have a capacity of 747 mAh g^{-1} at a current of 0.1 A g^{-1}, at the high current of 5 A g^{-1} VNM316 retained a capacity of 181 mAh g^{-1}. Cyclic voltammetry identified both intercalation and conversion mechanisms of charge storage as well indicating a high proportion of charge stored pseudocapacitively. Techniques such as EDS, XPS, TEM and BET all suggested that homogenous metal ion distribution, multiple redox states, synergistic electronic interactions, small particle size and high surface areas all contributed to the high electrochemical performance of VNM316 compared to other compositions investigated. The application of the conversion nanomaterial VNM316 as an anode in a lithium hybrid ion capacitor was shown to be successful with specific energies of 102 and 10 Wh kg^{-1} at low and high specific powers of 365 and 18650 W kg^{-1} respectively.

Chapter 5 investigated the application of carbon precursors in-flow to form composite carbon-metal oxide materials to the mixed V-Nb-Mo material discovered in Chapter 4 (VNM316). The synthesis method followed the same pathway as before with sucrose, as the carbonaceous precursor, added to the metal salt precursors in-flow at different molar ratios, followed by a heat treatment in inert atmosphere. Through PXRD, it was revealed that the heat treatment process induced a phase change from monoclinic MoO_2 to multiple higher

oxidation states for non-carbon containing VNM316, in contrast the composite carbon-VNM316 (CVNM) materials were found to be protected by the presence of the carbon and retained the desired monoclinic phase. TEM identified the composite materials as consisting of nanosized particles that were both individually coated with carbon and embedded within a carbonaceous matrix. XRF and TEM-EDS showed that, unlike in previous work, the presence of sucrose did not affect the precipitation of the metals and the CVNM materials displayed homogenous mixing of three metals within each nanoparticle. Raman spectroscopy was used to identify that, post heat treatment, the carbon was graphitic in nature. Cyclic voltammetry in lithium half-cells, identified redox peaks that were assigned to both intercalation and conversion energy storage mechanisms. It was shown by GCD cycling in lithium half-cells, that the addition of graphitic carbon decreased the specific capacity at low currents, but greatly increased the capacity at high currents. The material CVNM-6, with a carbon to metal oxide molar ratio of 1.5:1, at 0.1 A g^{-1} exhibited 505 mAh g^{-1} and retained 197 mAh g^{-1} at 10 A g^{-1}. This high-performance material was successfully used as an anode in a lithium-ion hybrid capacitor that exhibited 81 Wh kg^{-1} at a specific power of 1270 W kg^{-1} and at a high specific power of 8500 W kg^{-1} retained a specific energy of 11 Wh kg^{-1}. These results show composite carbon-V-Nb-Mo oxide materials as candidates for high energy and high-power anode materials for lithium-ion energy storage devices that warrant further investigation and development. The results also display the use of assisted CHFS methods for synthesising nanosized conversion mechanism metal oxide materials that have improved electrochemical cycling behaviour.

Chapter 6 applied lessons learnt in previous chapters regarding the benefits of multiple mixed metals and the addition of graphitic carbon in-flow to the ternary system of Fe-Mn-Zn oxides (FMZ). A range of single, binary, and tertiary metal oxides from across ternary compositional space were successfully synthesised by a CHFS method. PXRD analysis of the as-synthesised materials found high levels of crystallinity compared to other materials synthesised via CHFS without a subsequent heat treatment protocol, with the major crystal phases being identified as Mn and mixed Mn/Fe spinels and cubic ZnO. Calculation of the Scherrer crystallite sizes found that the size was correlated with the proportion of Zn in the material. Electrochemical investigation of the FMZ materials as anodes

in lithium half-cells identified a correlation between smaller Scherrer size and lower Zn content and higher specific capacity. At low current GCD cycling, the material $Fe_{0.8}Mn_{0.2}$ displayed the highest specific capacity of 531 mAh g^{-1}. At higher currents of 0.5 and 1 A g^{-1} the composition $Fe_{0.2}Mn_{0.8}Zn_{0.05}$ outperformed the others with capacities of 172 and 105 mAh g^{-1} correspondingly. All the materials were found to have reversible capacities below the theoretical values, as well as displaying large capacity loss at currents above 1 A g^{-1} and gradual capacity fade over continued cycling at low currents. Analysis of the GCD curves revealed a large voltage hysteresis of over 0.5 V between charge and discharge that was associated in part with the capacity loss being observed.

The compositions $Fe_{0.2}Mn_{0.8}$ and $Fe_{0.2}Mn_{0.75}Zn_{0.05}$ were re-synthesised with varying concentrations of sucrose in-flow, followed by an inert atmosphere heat treatment to form carbon-metal oxide composite materials. Through XRF studies, it was found that at the lower concentrations of sucrose (0.5-3 M) did not affect the precipitation of the metals, however the higher concentrations investigated (4 and 5 M) did affect the final composition by inhibiting the precipitation of Manganese. PXRD of the lower sucrose samples post heat treatment found the dominant crystal phase to be cubic FeO/MnO, which suggests that the materials had undergone a carbothermal reduction. PXRD of the highest sucrose samples, which had high Fe and low Mn content, displayed a tetragonal spinel structure. PXRD also discovered the presence of metallic Fe in the materials that also had Zn. This was suggested as being potentially the result of the Zn facilitating the carbothermal reduction of iron oxide. Raman spectroscopy indicated that only the highest concentrations of sucrose gave materials prior to heat treatment that displayed D and G bands for carbon. Post heat treatment it was found that no bands were detected, suggesting that any carbon present had been lost in the furnace. Electrochemical investigation of the CFMZ materials as anodes in lithium half-cells found poor specific capacities for the cubic FeO/MnO materials. The materials $C(Fe_{0.77}Mn_{0.21})$-5HT, $C(Fe_{0.66}Mn_{0.21}Zn_{0.11})$-4HT and $C(Fe_{0.72}Mn_{0.17}Zn_{0.09})$-5HT were found to display greater capacities at all currents tested compared to all other FMZ and CFMZ materials. At 0.1, 0.5, 1 and 2 A g^{-1} were found to be: 776, 616, 493 and 362; 932, 685, 460 and 271; and 715, 460, 338 and 202 mAh g^{-1} for the three materials respectively. Analysis of CV plots indicated that conversion and intercalation mechanisms were the main source of

reversible capacity. The degradation of these materials over long term cycling was investigated over 100 CV cycles with EIS measurements every 10th cycle. It was observed that redox polarisation increased over cycling as well as changes in the Nyquist plots that were suggestive of a reduction in diffusion kinetics. The specific capacities identified indicate C($Fe_{0.77}Mn_{0.21}$)-5HT, C($Fe_{0.66}Mn_{0.21}Zn_{0.11}$)-4HT and C($Fe_{0.72}Mn_{0.17}Zn_{0.09}$)-5HT as materials of interest as anodes for lithium-ion energy storage devices.

7.2 Outlook and Future Work

The research reported and discussed here offers a wide range of different avenues for future work to pursue. The utilisation of CHFS for the synthesis of libraries of different compositions for materials discovery was shown to be successful. The application of this technique to different groups of transition metals, in combination with computational techniques such as structure prediction and advanced AI systems, could be very effective at increasing the speed of discovering high performing compositions and providing a feedback loop of real-world data that can help inform more accurate future computer models. For the specific groups of materials reported herein, further compositional work should be performed to develop a more high-resolution picture of the hotspots. This would potentially allow for further high-performing compositions to be discovered. It would also allow the relationships between composition, the localised interactions between different elements and electrochemical behaviours to be investigated and understood at a higher level.

The use of carbonaceous materials in-flow was shown to be a successful technique for improving the performance of the materials reported here. One possible direction for future research could focus on the use of more complex carbon motifs in-flow, such as nanotubes or graphene sheets. Some initial investigations into this suggested that the CHFS conditions required optimisation for other carbon sources to survive the synthesis process. Other approaches such as the addition of carbonaceous materials to the CHFS nanomaterials post-synthesis through methods such as sol-gel or incipient wetness could allow for improved metal oxide-carbon interactions/coatings to be achieved whilst retaining the nanosized particles and homogenous mixing of elements created by CHFS. A few initial forays in this direction performed on the CVNM materials suggested

that the techniques were successful but required further work to develop the processes for greater control and increased complexity of composite to improve the electrochemical performance.

Another area that could benefit from further work is the investigation of the role of metallic Fe in the charge storage process for carbon-Fe-Mn-Zn oxide materials. In-depth analysis using synchrotron techniques could provide key insights into the mechanisms of charge storage and the extent to which Fe nanoparticles play a role. The addition of Fe to other mixed metal oxides followed by carbothermal reduction to form Fe could improve the electrochemical performance through increasing the intrinsic conductivity of materials.

Although the use of coin cells provides invaluable information on the electrochemical behaviours, performances, and kinetics of battery materials, the scale-up to cylindrical, single-layer or multi-layer pouch or prismatic cells would provide more representative analysis of materials in real-world situations. Some effects of materials could possibly only present at larger scale, such as issues with gas evolution during formation. This would also provide cell data directly comparable to the current technology on the market allowing for more accurate evaluation of potential candidates.

8.0 Bibliography, Abbreviations, Lists of Figures and Tables

8.1 Bibliography

1 E. Pomerantseva, F. Bonaccorso, X. Feng, Y. Cui and Y. Gogotsi, *Science (80-.).*, , DOI:10.1126/science.aan8285.

2 NOAA, NOAA National Centers for Environmental information, Climate at a Glance: Global Time Series, published November 2020, https://www.ncdc.noaa.gov/cag/, (accessed 8 December 2020).

3 C. Pillot, in *Niobium-Based Materials for Advanced Electrochemical Energy Storage*, 2019, pp. 18–30.

4 J. Blosiu, R. Bugga, E. Brandon, M. Smart, J. Elliott, J. Castillo, T. Yi, L. Lee, M. Piszczor, T. Miller, C. Reid, C. Taylor, S. Liu, U. S. Army, E. Plichta, C. Iannello, P. M. Beauchamp and J. A. Cutts, *Energy Storage Technologies for Future Planetary Science Missions Work Performed under the Planetary Science Program Support Task*, 2017.

5 M. C. Smart, B. V. Ratnakumar, R. C. Ewell, S. Surampudi, F. J. Puglia and R. Gitzendanner, *Electrochim. Acta*, 2018, **268**, 27–40.

6 M. Winter and R. J. Brodd, *Chem. Rev.*, 2004, **104**, 4245–4270.

7 J. M. Tarascon and M. Armand, *Nature*, 2001, **414**, 359–367.

8 R. A. Marsh, S. Vukson, S. Surampudi, B. V. Ratnakumar, M. C. Smart, M. Manzo and P. J. Dalton, *J. Power Sources*, 2001, **97**–**98**, 25–27.

9 NASA, Mars Curiosity Rover, https://mars.nasa.gov/msl/mission/science/results/.

10 J. Ding, W. Hu, E. Paek and D. Mitlin, *Chem. Rev.*, 2018, **118**, 6457–6498.

11 T. Pandolfo, V. Ruiz, S. Sivakkumar and J. Nerkar, *Mater. Syst. Appl.*, 2013, 69–109.

12 M. Armand and J. M. Tarascon, *Nature*, 2008, **451**, 652–657.

13 J. B. Goodenough and K. S. Park, *J. Am. Chem. Soc.*, 2013, **135**, 1167–1176.

14 P. Simon, Y. Gogotsi and B. Dunn, *Science (80-.).*, 2014, **343**, 1210–1211.

15 D. P. Dubal, O. Ayyad, V. Ruiz and P. Gómez-Romero, *Chem. Soc. Rev.*, 2015, **44**, 1777–1790.

16 P. W. Atkins, T. I. Overton, J. P. Rourke, M. T. Weller and F. A. Armstrong, Oxford University Press, Oxford, fifth., 2010, p. 150.

17 P. Atkins and J. De Paula, in *Atkin's Physical Chemistry*, Oxford University Press, Oxford, Ninth., 2010, p. 928.

18 K. Mizushima, P. C. Jones, P. J. Wiseman and J. B. Goodenough, *Mater. Res. Bull.*, 1980, **15**, 783–789.

19 M. S. WHITTINGHAM, *Science (80-.).*, 1976, **192**, 1126–1127.

20 A. Yoshino, *Angew. Chemie Int. Ed.*, 2012, **51**, 5798–5800.

21 A. K. Padhi, K. S. Nanjundaswamy and J. B. Goodenough, *J. Electrochem. Soc.*, 1997, **144**, 1188–1194.

22 M. M. Thackeray, W. I. F. David, P. G. Bruce and J. B. Goodenough, *Mater. Res. Bull.*, 1983, **18**, 461–472.

23 F. Yu, T. Huang, P. Zhang, Y. Tao, F. Z. Cui, Q. Xie, S. Yao and F. Wang, *Energy Storage Mater.*, 2019, **22**, 235–255.

24 C. Liu, G. Neale, Zachary and G. Cao, *Mater. Today*, 2016, **19**, 109–123.

25 F. Lin, I. Markus, D. Nordlund, T.-C. Weng, M. D. Asta, H. L. Xin and M. M. Doeff, *Nat. Commun.*, , DOI:10.1038/ncomms4529.

26 P. Chandan, C. Chang, K. Yeh, C. Chiu, D. Wu, T. Huang, P. M. Wu, P. Chi, W. Hsu, K. Su, Y. Lee, H. Chang, M. Wang, H. Wu, H. Tang and M. Wu, *Commun. Chem.*, 1–7.

27 Z. Ahsan, B. Ding, Z. Cai, C. Wen, W. Yang, Y. Ma, S. Zhang, G. Song and M. S. Javed, 2021, **18**, 1–18.

28 A. C. Wagner, N. Bohn, H. Geßwein, M. Neumann, M. Osenberg, A. Hilger, I. Manke, V. Schmidt and J. R. Binder, , DOI:10.1021/acsaem.0c02494.

29 G. Chen, L. Yan, H. Luo and S. Guo, *Adv. Mater.*, 2016, **28**, 7580–7602.

30 G. Liu and W. Lu, *J. Electrochem. Soc.*, 2017, **164**, A1826–A1833.

31 F. Lambert, Breakdown of raw materials in Tesla's batteries and possible bottlenecks, https://electrek.co/2016/11/01/breakdown-raw-materials-tesla-batteries-possible-bottleneck/, (accessed 4 May 2021).

32 N. Takami, K. Ise, Y. Harada, T. Iwasaki, T. Kishi and K. Hoshina, *J. Power Sources*, 2018, **396**, 429–436.

33 C. Chen, R. Agrawal and C. Wang, *Nanomaterials*, 2015, **5**, 1469–1480.

34 S. Fang, D. Bresser and S. Passerini, *Adv. Energy Mater.*, , DOI:10.1002/aenm.201902485.

35 B. Li, J. Zheng, H. Zhang, L. Jin, D. Yang, H. Lv, C. Shen, A. Shellikeri, Y. Zheng, R. Gong, J. P. Zheng and C. Zhang, *Adv. Mater.*, 2018, **30**, 1–19.

36 F. C. Strobridge, H. Liu, M. Leskes, O. J. Borkiewicz, K. M. Wiaderek, P. J. Chupas, K. W. Chapman and C. P. Grey, *Chem. Mater.*, 2016, **28**, 3676–3690.

37 M. Wagemaker and F. M. Mulder, *Acc. Chem. Res.*, 2013, **46**, 1206–1215.

38 G. K. Singh, G. Ceder and M. Z. Bazant, *Electrochim. Acta*, 2008, **53**, 7599–7613.

39 M. Wagemaker, A. P. M. Kentjens and F. M. Mulder, *Nature*, 2002, **418**, 397–399.

40 G. Chen, X. Song and T. J. Richardson, *Electrochem. Solid-State Lett.*, 2006, **9**, 295–298.

41 J. Xiao, X. Yu, J. Zheng, Y. Zhou, F. Gao, X. Chen, J. Bai, X.-Q. Yang and J.-G. Zhang, *J. Power Sources*, 2013, **242**, 736–741.

42 M. A. Tarselli, *Nat. Publ. Gr.*, 2013, **5**, 2013.

43 Y. R. Jhan and J. G. Duh, *J. Power Sources*, 2012, **198**, 294–297.

44 L. Shen, X. Zhang, E. Uchaker, C. Yuan and G. Cao, *Adv. Energy Mater.*, 2012, **2**, 691–698.

45 X. Wang, X. Zuo and S. Yin, 2021, 1–9.

46 L. Yan, X. Rui, G. Chen, W. Xu, G. Zou and H. Luo, *Nanoscale*, 2016, **8**, 8443–8465.

47 K. Zhang, X. Han, Z. Hu, X. Zhang, Z. Tao and J. Chen, *Chem. Soc. Rev.*, 2015, **44**, 699–728.

48 K. J. Griffith, K. M. Wiaderek, G. Cibin, L. E. Marbella and C. P. Grey, *Nature*, 2018, **559**, 556–563.

49 W. Ye, H. Yu, X. Cheng, H. Zhu, R. Zheng, T. Liu, N. Long, M. Shui and J. Shu, *Electrochim. Acta*, 2018, **292**, 331–338.

50 X. Y. Yu, L. Yu and X. W. Lou, *Adv. Energy Mater.*, 2016, **6**, 1–14.

51 X. Xu, W. Liu, Y. Kim and J. Cho, *Nano Today*, 2014, **9**, 604–630.

52 Y. Lu, L. Yu and X. W. (David) Lou, *Chem*, 2018, **4**, 972–996.

53 L. Zhang, H. Bin Wu and X. W. Lou, *Adv. Energy Mater.*, 2014, **4**, 1–11.

54 W. Tang, C. X. Peng, C. T. Nai, J. Su, Y. P. Liu, M. V. V. Reddy, M. Lin and K. P. Loh, *Small*, 2015, **11**, 2446–2453.

55 Q. Liu, X. Su, D. Lei, Y. Qin, J. Wen, F. Guo, Y. A. Wu, Y. Rong, R. Kou, X. Xiao, F. Aguesse, J. Bareño, Y. Ren, W. Lu and Y. Li, *Nat. Energy*, 2018, **3**, 936–943.

56 P. Poizot, S. Laruelle, S. Grugeon, L. Dupont and J. Tarascon, .

57 D. Bresser, S. Passerini and B. Scrosati, *Energy Environ. Sci.*, 2016, **9**, 3348–3367.

58 J. Cabana, L. Monconduit, D. Larcher and M. R. Palacín, *Adv. Mater.*, 2010, **22**, 170–192.

59 H. Bin Wu, G. Zhang, L. Yu and X. W. Lou, *Nanoscale Horizons*, 2016, **1**, 27–40.

60 W. Xu, J. Wang, F. Ding, X. Chen, E. Nasybulin, Y. Zhang and J.-G. Zhang, *Energy Environ. Sci.*, 2014, **7**, 513–537.

61 M. Ge, J. Rong, X. Fang and C. Zhou, *Nano Lett.*, 2012, **12**, 2318–2323.

62 H. Tian, F. Xin, X. Wang, W. He and W. Han, *J. Mater.*, 2015, **1**, 153–169.

63 X. Zhang, D. Wang, X. Qiu, Y. Ma, D. Kong, K. Müllen, X. Li and L. Zhi, *Nat. Commun.*, 2020, **11**, 1–9.

64 G. Berdichevsky and G. Yushin, *The Future of Energy Storage*, 2020.

65 Y. Xie, X. W. Lou, C. Yuan, H. Bin Wu, Y. Xie, X. Wen and D. Lou, 2014, 1488–1504.

66 L. Cong, H. Xie and J. Li, *Adv. Energy Mater.*, , DOI:10.1002/aenm.201601906.

67 P. Trogadas, V. Ramani, P. Strasser, T. F. Fuller and M. O. Coppens, *Angew. Chemie - Int. Ed.*, 2016, **55**, 122–148.

68 C. Liu, F. Li, L.-P. Ma and H.-M. Cheng, *Adv. Mater.*, 2010, **22**, E28–E62.

69 J. Qi, X. Lai, J. Wang, H. Tang, H. Ren, Y. Yang, Q. Jin, L. Zhang, R. Yu, G. Ma, Z. Su, H. Zhao and D. Wang, *Chem. Soc. Rev.*, 2015, **44**, 6749–6773.

70 L. Yu, H. Hu, H. Bin Wu and X. W. D. Lou, *Adv. Mater.*, , DOI:10.1002/adma.201604563.

71 G. Nava, J. Schwan, M. G. Boebinger, M. T. Mcdowell and L. Mangolini, *Nano Energy*, 2019, **19**, 7236–7245.

72 J. Shi, X. Jiang, B. Ban, J. Li and J. Chen, *Electrochim. Acta*, 2021, **381**, 138269.

73 S. Chen, X. Yang, J. Zhang, J. Ma, Y. Meng, K. Tao, F. Li and J. Geng, *Electrochim. Acta*, 2021, **368**, 137626.

74 A. Manthiram, *Nat. Commun.*, 2020, **11**, 1550.

75 M. Azevedo, N. Campagnol, T. Hagenbruch, K. Hoffman, A. Lala and O. Ramsbottom, *Lithium and Cobalt - a tale of two commodities*, 2018.

76 K. H. Wedepohl, *Geochim. Cosmochim. Acta*, 1995, **7**, 1217–1232.

77 R. I. Gruar, C. J. Tighe and J. A. Darr, *Ind. Eng. Chem. Res.*, 2013, **52**, 5270–5281.

78 A. Jana and R. E. García, *Nano Energy*, 2017, **41**, 552–565.

79 T. A. Atia, G. Elia, R. Hahn, P. Altimari and F. Pagnanelli, *J. Energy Chem.*, 2019, **35**, 220–227.

80 Q. Dai, J. C. Kelly, L. Gaines and M. Wang, *Batteries*, 2019, **5**, 48.

81 S. Ma, M. Jiang, P. Tao, C. Song, J. Wu, J. Wang and T. Deng, *Prog. Nat. Sci. Mater. Int.*, 2018, **28**, 653–666.

82 P. Simon and Y. Gogotsi, *Nat. Mater.*, 2008, **7**, 845–854.

83 S. Trasatti and G. Buzzanca, *J. Electroanal. Chem. Interfacial Electrochem*, 1971, **29**, 1–5.

84 R. Kotz and M. Carlen, *Electrochim. Acta*, 2000, **45**, 2483–2498.

85 B. E. Conway, *Electrochemical Supercapacitors: Scientific Fundamentals and Technological Applications*, Kluwer Academic, 1999.

86 L. Zhang, D. P. Wilkinson, Z. Chen and J. Zhang, *Lithium-Ion Supercapacitors*, Taylor & Francis Group, Boca Raton, 2018.

87 Z. Chen, V. Augustyn, J. Wen, Y. Zhang, M. Shen, B. Dunn and Y. Lu, *Adv. Mater.*, 2011, **23**, 791–795.

88 Y. P. Gao, K. J. Huang, C. X. Zhang, S. S. Song and X. Wu, *J. Alloys Compd.*, 2018, **731**, 1151–1158.

89 A. K. Thakur, R. Bilash, M. Majumder and G. Gupta, *Electrochim. Acta*, 2017, **251**, 532–545.

90 J. Wang, J. Polleux, J. Lim and B. Dunn, *J. Phys. Chem. C*, 2007, **111**, 14925–14931.

91 M. Catti and M. R. Ghaani, *Phys. Chem. Chem. Phys.*, 2014, **16**, 1385–1392.

92 V. Augustyn, P. Simon and B. Dunn, *Energy Environ. Sci.*, 2014, **7**, 1597–1614.

93 V. Augustyn and B. Dunn, *Energy Env.*, 2014, **7**, 1597–1614.

94 M. Lübke, A. Sumboja, L. McCafferty, C. F. Armer, A. D. Handoko, Y. Du, K. McColl, F. Cora, D. Brett, Z. Liu and J. A. Darr, *ChemistrySelect*, 2018, **3**, 2613–2622.

95 W. Wang, S. Guo, I. Lee, K. Ahmed, J. Zhong, Z. Favors, F. Zaera, M. Ozkan and C. S. Ozkan, *Sci. Rep.*, 2014, **4**, 9–14.

96 M. Okubo, E. Hosono, J. Kim, M. Enomoto, N. Kojima, T. Kudo, H. Zhou and I. Honma, *J. Am. Chem. Soc.*, 2007, **129**, 7444–7452.

97 Z. Tong, J. Hao, K. Zhang, J. Zhao, B.-L. Su and Y. Li, *J. Mater. Chem. C*, 2014, **2**, 3651.

98 A. R. Armstrong, G. Armstrong, J. Canales, R. García and P. G. Bruce, *Adv. Mater.*, 2005, **17**, 862–865.

99 B. E. Conway, *J. Electrochem. Soc.*, 1991, **138**, 1539–1548.

100 W. Yan, J. Y. Kim, W. Xing, K. C. Donavan, T. Ayvazian and R. M. Penner, *Chem. Mater.*, 2012, **24**, 2382–2390.

101 S. Ardizzone, G. Fregonara and S. Trasatti, *Electrochim. Acta*, 1989, **35**, 263–267.

102 C. Choi, D. S. Ashby, D. M. Butts, R. H. DeBlock, Q. Wei, J. Lau and B. Dunn, *Nat. Rev. Mater.*, 2020, **5**, 5–19.

103 J. H. Ku, J. H. Ryu, S. H. Kim, O. H. Han and S. M. Oh, *Adv. Funct. Mater.*, 2012, **22**, 3658–3664.

104 R. A. Dougal, S. Liu and R. E. White, *IEEE Trans. Components Packag. Technol.*, 2002, **25**, 120–131.

105 Jian Cao and A. Emadi, *IEEE Trans. Power Electron.*, 2012, **27**, 122–132.

106 P. Simon and Y. Gogotsi, *Nat. Mater.*, 2020, **19**, 1151–1163.

107 H. Wang, C. Zhu, D. Chao, Q. Yan and H. J. Fan, *Adv. Mater.*, 2017, **29**, 1–18.

108 M. Yang, Y. Zhong, J. Ren, X. Zhou, J. Wei and Z. Zhou, *Adv. Energy Mater.*, 2015, **5**, 1–7.

109 Formula1, Re-writing the F1 rulebook - Part 4: ‘cleaner’ cars, KERS and the return of slicks, https://www.formula1.com/en/latest/article.re-writing-the-f1-rulebook-part-4-cleaner-cars-kers-and-return-of-slicks.1NUrjfG83a6aE0QSuAkGK8.html.

110 J. Partridge and D. I. Abouelamaimen, *Energies*, , DOI:10.3390/en12142683.

111 A. González-Gil, R. Palacin and P. Batty, *Energy Convers. Manag.*, 2013, **75**, 374–388.

112 J. Doling, *Feasibility Study of On-Car Regenerative Braking System (RBS) for Electric Rail Applications*, Bohemia, NY, 2013.

113 K. Fleurbaey, N. Omar, J. Ronsmans, P. Van Den Bossche and J. Van Mierlo, 2007, 1–6.

114 J. M. Baptista, J. Sagu, U. W. KG and K. Lobato, *Chem. Eng. J.*, 2019, **374**, 1153–1179.

115 L. Li, Y. Zheng, S. Zhang, J. Yang, Z. Shao and Z. Guo, *Energy Environ. Sci.*, 2018, **11**, 2310–2340.

116 L. Li, Y. Zheng, S. Zhang, J. Yang, Z. Shao and Z. Guo, *Energy Environ. Sci.*, 2018, **11**, 2310–2340.

117 L. Xiao, H. Lu, Y. Fang, M. L. Sushko, Y. Cao, X. Ai, H. Yang and J. Liu, *Adv. Energy Mater.*, 2018, **8**, 1–7.

118 D. Chao, C. Zhu, P. Yang, X. Xia, J. Liu, J. Wang, X. Fan, S. V. Savilov, J. Lin, H. J. Fan and Z. X. Shen, *Nat. Commun.*, 2016, **7**, 1–8.

119 E. M. Lotfabad, P. Kalisvaart, A. Kohandehghan, D. Karpuzov and D. Mitlin, *J. Mater. Chem. A*, 2014, **2**, 19685–19695.

120 L. G. H. Staaf, P. Lundgren and P. Enoksson, *Nano Energy*, 2014, **9**, 128–141.

121 S. J. An, J. Li, C. Daniel, D. Mohanty, S. Nagpure and D. L. Wood, *Carbon N. Y.*, 2016, **105**, 52–76.

122 N. Xu, X. Sun, F. Zhao, X. Jin, X. Zhang, K. Wang, K. Huang and Y. Ma, *Electrochim. Acta*, 2017, **236**, 443–450.

123 S. S. Zhang, *J. Power Sources*, 2017, **343**, 322–328.

124 M. Watanabe, M. L. Thomas, S. Zhang, K. Ueno, T. Yasuda and K. Dokko, *Chem. Rev.*, 2017, **117**, 7190–7239.

125 M. Watanabe, M. L. Thomas, S. Zhang, K. Ueno, T. Yasuda and K. Dokko, *Chem. Rev.*, 2017, **117**, 7190–7239.

126 C. Wolff, S. Jeong, E. Paillard, A. Balducci and S. Passerini, *J. Power Sources*, 2015, **293**, 65–70.

127 K. Karuppasamy, J. Theerthagiri, D. Vikraman, C. J. Yim, S. Hussain, R. Sharma, T. Maiyalagan, J. Qin and H. S. Kim, *Polymers (Basel).*, 2020, **12**, 1–37.

128 M. Broussely, P. Biensan, F. Bonhomme, P. Blanchard, S. Herreyre, K. Nechev and R. J. Staniewicz, *J. Power Sources*, 2005, **146**, 90–96.

129 K. Xu, *Chem. Rev.*, 2004, **104**, 4303–4417.

130 A. Wang, S. Kadam, H. Li, S. Shi and Y. Qi, *npj Comput. Mater.*, 2018, **15**, 1–26.

131 D. L. Wood, J. Li and C. Daniel, *J. Power Sources*, 2015, **275**, 234–242.

132 P. Verma, P. Maire and P. Novák, *Electrochim. Acta*, 2010, **55**, 6332–6341.

133 N. Takenaka, Y. Suzuki, H. Sakai and M. Nagaoka, *J. Phys. Chem. C*, 2014, **118**, 10874–10882.

134 G. Gachot, P. Ribie, D. Mathiron, S. Grugeon, M. Armand, J. Leriche, S. Pilard and S. Laruelle, *Anal. Chem.*, 2011, **83**, 478–485.

135 S. F. Lux, J. Chevalier, I. T. Lucas and R. Kostecki, *ECS Electrochem. Lett.*, 2013, **2**, A121–A123.

136 J. Wu, N. Membreno, W. Y. Yu, J. D. Wiggins-Camacho, D. W. Flaherty, C. B. Mullins and K. J. Stevenson, *J. Phys. Chem. C*, 2012, **116**, 21208–21215.

137 F. Joho, B. Rykart, A. Blome, P. Novák, H. Wilhelm and M. E. Spahr, *J. Power Sources*, 2001, **97**–**98**, 78–82.

138 S. S. Zhang, *J. Power Sources*, 2006, **162**, 1379–1394.

139 N. Schulz, J. E. Soc, N. Schulz, C. Wittich and L. Dimesso, *J. Electrochem. Soc.*, 2018, **165**, A833–A846.

140 M. Wagemaker, W. J. H. Borghols, E. R. H. Van Eck, A. P. M. Kentgens, G. J. Kearley and F. M. Mulder, *Chem. - A Eur. J.*, 2007, **13**, 2023–2028.

141 N. Liu, Z. Lu, J. Zhao, M. T. Mcdowell, H. W. Lee, W. Zhao and Y. Cui, *Nat. Nanotechnol.*, 2014, **9**, 187–192.

142 X. Wang, J. Feng, Y. Bai, Q. Zhang and Y. Yin, *Chem. Rev.*, 2016, **116**, 10983–11060.

143 W. J. Zhang, *J. Power Sources*, 2011, **196**, 13–24.

144 P. S. Aithal and S. Aithal, *Int. J. Eng. Manuf.*, 2016, **6**, 15–25.

145 W. Lin, Y. wern Huang, X. D. Zhou and Y. Ma, *Toxicol. Appl. Pharmacol.*, 2006, **217**, 252–259.

146 A. Boldrin, S. F. Hansen, A. Baun, N. I. B. Hartmann and T. F. Astrup, *J. Nanoparticle Res.*, 2014, **16**, 2394.

147 K. Rogers and P. Dobson, Nanoparticle.

148 K. Zaghib, M. Simoneau, M. Armand and M. Gauthier, *J. Power Sources*, 1999, **81**–**82**, 300–305.

149 T. V. S. L. Satyavani, A. S. Kumar and P. S. V. S. Rao, *Eng. Sci. Technol. an Int. J.*, 2016, **19**, 178–188.

150 K. S. Smirnov, V. A. Zhorin and N. A. Yashtulov, *Russ. J. Appl. Chem.*, 2013, **86**, 603–605.

151 A. Nakahira, T. Kubo and C. Numako, *Inorg. Chem.*, 2010, **49**, 5845–5852.

152 X. Zhang, P. He, X. Zhang, C. Li, H. Liu, S. Wang and F. Dong, *Electrochim. Acta*, 2018, **276**, 92–101.

153 H. Li, Y. Zhang, Y. Tang, F. Zhao, B. Zhao, Y. Hu, H. Murat, S. Gao and L. Liu, *Appl. Surf. Sci.*, 2019, **475**, 942–946.

154 C. Piccirillo, R. Binions and I. P. Parkin, *Eur. J. Inorg. Chem.*, 2007, 4050–4055.

155 S. Shen, W. Guo, D. Xie, Y. Wang, S. Deng, Y. Zhong, X. Wang, X. Xia and J. Tu, *J. Mater. Chem. A*, 2018, **6**, 20195–20204.

156 D. Bauer, A. J. Roberts, S. G. Patnaik, D. J. L. Brett, P. R. Shearing, E. Kendrick, N. Matsumi and J. A. Darr, *J. Electrochem. Soc.*, 2018, **165**, A1662–A1670.

157 J. A. Darr, J. Zhang, N. M. Makwana and X. Weng, *Chem. Rev.*, 2017, **117**, 11125–11238.

158 T. Adschiri, Y. W. Lee, M. Goto and S. Takami, *Green Chem.*, 2011, **13**, 1380–1390.

159 C. I. Krau, D. Kuhn and T. Schulenberg, in *International Youth Nuclear Congress*, 2008, pp. 20–26.

160 I. Pioro and S. Mokry, *Thermophysical Properties at Critical and Supercritical Conditions*, 20111.

161 Nuclear-Power, Prop. Supercrit. Water, https://www.nuclear-power.net/nuclear-engineering/materials-nuclear-engineering/properties-steam-what-is-steam/supercritical-fluid-supercritical-water/properties-of-supercritical-water/#:~:text=the specific enthalpy of supercritical,25MPa and 500°C), (accessed 9 May 2021).

162 D. Kashchiev, *J. Chem. Phys.*, 1982, **76**, 5098–5102.

163 D. Kashchiev and G. M. Van Rosmalen, *Cryst. Res. Technol.*, 2003, **38**, 555–574.

164 C. J. Tighe, R. I. Gruar, C. Y. Ma, T. Mahmud, X. Z. Wang and J. A. Darr, *J. Supercrit. Fluids*, 2012, **62**, 165–172.

165 V. K. Lamer and R. H. Dinegar, *J. Am. Chem. Soc.*, 1950, **72**, 4847–4854.

166 J. Polte, *CrystEngComm*, 2015, **17**, 6809–6830.

167 M. Lübke, A. Sumboja, I. D. Johnson, D. J. L. Brett, P. R. Shearing, Z. Liu and J. A. Darr, *Electrochim. Acta*, 2016, **192**, 363–369.

168 C. J. Tighe, R. Q. Cabrera, R. I. Gruar and J. A. Darr, *Ind. Eng. Chem. Res.*, 2013, **52**, 5522–5528.

169 P. W. Dunne, A. S. Munn, C. L. Starkey, T. A. Huddle and E. H. Lester, *Philos. Trans. R. Soc. A Math. Phys. Eng. Sci.*, 2015, **373**, 20150015.

170 A. A. Galkin, B. G. Kostyuk, V. V. Lunin and M. Poliakoff, *Angew. Chemie - Int. Ed.*, 2000, **39**, 2738–2740.

171 T. Adschiri, K. Kanazawa and K. Arai, *J. Am. Chem. Soc.*, 1992, **75**, 2615–2618.

172 S. Kubota, T. Morioka, M. Takesue, H. Hayashi, M. Watanabe and R. L. Smith, *J. Supercrit. Fluids*, 2014, **86**, 33–40.

173 D. Bauer, T. E. Ashton, D. J. L. Brett, P. R. Shearing, N. Matsumi and J. A. Darr, *Electrochim. Acta*, 2019, **322**, 134695.

174 A. R. Groves, T. E. Ashton and J. A. Darr, , DOI:10.1021/acscombsci.0c00094.

175 X. Weng, J. K. Cockcroft, G. Hyett, M. Vickers, P. Boldrin, C. C. Tang, S. P. Thompson, J. E. Parker, J. C. Knowles, I. Rehman, I. Parkin, J. R. G. Evans and J. A. Darr, *J. Comb. Chem.*, 2009, **11**, 829–834.

176 I. D. Johnson, M. Loveridge, R. Bhagat and J. A. Darr, *ACS Comb. Sci.*, 2016, **18**, 665–672.

177 W. H. Bragg and W. L. Bragg, *Proc. R. Soc. London. Ser. A, Contain. Pap. a Math. Phys. Character*, 1913, **88**, 428–438.

178 L. E. Smart and E. A. Moore, *Solid State Chemistry*, Taylor & Francis Group, Boca Raton, 4th edn., 2012.

179 P. Scherrer, in *Kolloidchemie Ein Lehrbuch*, Springer Berlin Heidelberg, Berlin, Heidelberg, 1912, pp. 387–409.

180 U. Holzwarth and N. Gibson, *Nat. Nanotechnol.*, 2011, **6**, 534–534.

181 M. Wojdyr, *J. Appl. Crystallogr.*, 2010, **43**, 1126–1128.

182 K. Momma and F. Izumi, *J. Appl. Crystallogr.*, 2011, **44**, 1272–1276.

183 J. L. F. A. Le Bail , H. Duroy, *Mat. Res. Bull.*, 1988, **23**, 447–452.

184 P. Brouwer, *Theory of XRF*, PANalytical BV, Almelo, Netherlands, 2006.

185 B. S. Mitchell, *An Introduction to Materials Engineering and Science*, John Wiley & Sons, Inc., Hoboken, NJ, USA, 2003.

186 D. Chen, J. H. Wang, T. F. Chou, B. Zhao, M. A. El-Sayed and M. Liu, *J.*

Am. Chem. Soc., 2017, **139**, 7071–7081.

187 A. C. Ferrari and J. Robertson, *Philos. Trans. R. Soc. A Math. Phys. Eng. Sci.*, 2004, **362**, 2477–2512.

188 S. Brunauer, P. H. Emmett and E. Teller, *J. Am. Chem. Soc.*, 1938, **60**, 309–319.

189 J. B. Condon, in *Surface Area and Porosity Determinations by Physisorption*, Elsevier, 2006, pp. 1–27.

190 E. P. Barrett, L. G. Joyner and P. P. Halenda, *J. Am. Chem. Soc.*, 1951, **73**, 373–380.

191 R. Bardestani, G. S. Patience and S. Kaliaguine, *Can. J. Chem. Eng.*, 2019, **97**, 2781–2791.

192 M. L. Ojeda, J. M. Esparza, A. Campero, S. Cordero, I. Kornhauser and F. Rojas, *Phys. Chem. Chem. Phys.*, 2003, **5**, 1859–1866.

193 P. W. Atkins and J. De Paula, *Atkins' Physical Chemistry*, Oxford University Press, Oxford, 9th edn., 2010.

194 D. Bauer, A. J. Roberts, N. Matsumi and J. A. Darr, *Nanotechnology*, 2017, **28**, 195403–195413.

195 S. B. Tang, M. O. Lai and L. Lu, 2008, **449**, 300–303.

196 A. A. Moya, *J. Power Sources*, 2018, **397**, 124–133.

197 Y. S. Lee and K. S. Ryu, *Sci. Rep.*, 2017, **7**, 1–13.

198 A. Verma, K. Smith, S. Santhanagopalan, D. Abraham, K. P. Yao and P. P. Mukherjee, *J. Electrochem. Soc.*, 2017, **164**, A3380–A3392.

199 W. Weppner and R. A. Huggins, *J. Electrochem. Soc.*, 1977, **124**, 1569–1578.

200 M. V. Reddy, R. Jose, A. Le Viet, K. I. Ozoemena, B. V. R. Chowdari and S. Ramakrishna, *Electrochim. Acta*, 2014, **128**, 198–202.

201 A. Lasia, *Electrochemical impedance spectroscopy and its applications*, 2014, vol. 9781461489.

202 G. K. Jr Lewis, G. K. Sr Lewis and W. Olbricht, *Meas Sci Technol.*, 2008,

19, 105102.

203 A. A. Moya, *J. Power Sources*, 2018, **397**, 124–133.

204 E. Barsoukov and J. R. Macdonald, *Impedance Spectroscopy*, John Wiley & Sons, Inc., Third., 2018.

205 R. J. Cava, D. W. Murphy and S. M. Zahurak, *J. Electrochem. Soc.*, 1983, **130**, 2345–2351.

206 T. Jacobsen and K. West, *Elecrrochimiccr Acta*, 1995, **40**, 255–262.

207 M. Shi, Z. Chen and J. Sun, *Cem. Concr. Res.*, 1999, **29**, 1111–1115.

208 A. Allagui, A. S. Elwakil, M. E. Fouda and A. G. Radwan, *J. Power Sources*, 2018, **390**, 142–147.

209 P. L. Taberna, P. Simon and J. F. Fauvarque, *J. Electrochem. Soc.*, 2003, **150**, 292–300.

210 V. Ganesh, S. Pitchumani and V. Lakshminarayanan, *J. Power Sources*, 2006, **158**, 1523–1532.

211 J. Kasnatscheew, T. Placke, B. Streipert, S. Rothermel, R. Wagner, P. Meister, I. C. Laskovic and M. Winter, *J. Electrochem. Soc.*, 2017, **164**, A2479–A2486.

212 T. Placke, A. Heckmann, R. Schmuch, P. Meister, K. Beltrop and M. Winter, *Joule*, 2018, **2**, 2528–2550.

213 I. D. Johnson, E. Blagovidova, P. A. Dingwall, D. J. L. Brett, P. R. Shearing and J. A. Darr, *J. Power Sources*, 2016, **326**, 476–481.

214 K. Kim, S. G. Woo, Y. N. Jo, J. Lee and J. H. Kim, *Electrochim. Acta*, 2017, **240**, 316–322.

215 J. T. Han and J. B. Goodenough, *Chem. Mater.*, 2011, **23**, 3404–3407.

216 R. Monteiro, in *Niobium-Based Materials for Advanced Electrochemical Energy Storage*, CBMM, 2019, pp. 31–44.

217 C. Lin, X. Fan, Y. Xin, F. Cheng, M. O. Lai, H. Zhou and L. Lu, *J. Mater. Chem. A*, 2014, **2**, 9982–9993.

218 N. Takami, K. Ise, Y. Harada, T. Iwasaki, T. Kishi and K. Hoshina, *J.*

Power Sources, 2018, **396**, 429–436.

219 M. Lübke, J. Shin, P. Marchand, D. Brett, P. Shearing, Z. Liu and J. A. Darr, *J. Mater. Chem. A*, 2015, **3**, 22908–22914.

220 J. T. Han and J. B. Goodenough, *Chem. Mater.*, 2011, **23**, 3404–3407.

221 X. Xia, S. Deng, S. Feng, J. Wu and J. Tu, *J. Mater. Chem. A*, 2017, **5**, 21134–21139.

222 C. Yang, S. Deng, C. Lin, S. Lin, Y. Chen, J. Li and H. Wu, *Nanoscale*, 2016, **8**, 18792–18799.

223 H. Wang, R. Qian, Y. Cheng, H.-H. Wu, X. Wu, K. M. Pan and Q. Zhang, *J. Mater. Chem. A*, 2020, **8**, 18425–18463.

224 K. J. Griffith, A. C. Forse, J. M. Griffin and C. P. Grey, *J. Am. Chem. Soc.*, 2016, **138**, 8888–8899.

225 T. Yuan, L. Soule, B. Zhao, J. Zou, J. Yang, M. Liu and S. Zheng, *Energy & Fuels*, 2020, **34**, 13321–13334.

226 B. Guo, X. Yu, X. G. Sun, M. Chi, Z. A. Qiao, J. Liu, Y. S. Hu, X. Q. Yang, J. B. Goodenough and S. Dai, *Energy Environ. Sci.*, 2014, **7**, 2220–2226.

227 K. J. Griffith, I. D. Seymour, M. A. Hope, M. M. Butala, L. K. Lamontagne, M. B. Preefer, C. P. Koçer, G. Henkelman, A. J. Morris, M. J. Cliffe, S. E. Dutton and C. P. Grey, *J. Am. Chem. Soc.*, 2019, **141**, 16706–16725.

228 L. Buannic, J. F. Colin, M. Chapuis, M. Chakir and S. Patoux, *J. Mater. Chem. A*, 2016, **4**, 11531–11541.

229 H. Park, H. Bin Wu, T. Song, X. W. Lou and U. Paik, *Adv. Energy Mater.*, 2015, **5**, 1401945.

230 G. Zhu, Q. Li, Y. Zhao and R. Che, *ACS Appl. Mater. Interfaces*, 2017, **9**, 41258–41264.

231 L. Fei, Y. Xu, X. Wu, Y. Li, P. Xie, S. Deng, S. Smirnov and H. Luo, *Nanoscale*, 2013, **5**, 11102–11107.

232 H. Li, L. Shen, J. Wang, S. Fang, Y. Zhang, H. Dou and X. Zhang, *J. Mater. Chem. A*, 2015, **3**, 16785–16790.

233 J. Zhu, J. Chen, H. Xu, S. Sun, Y. Xu, M. Zhou, X. Gao and Z. Sun, *ACS Appl. Mater. Interfaces*, 2019, **11**, 17384–17392.

234 K. Ise, S. Morimoto, Y. Harada and N. Takami, *Solid State Ionics*, 2018, **320**, 7–15.

235 J. T. Han, Y. H. Huang and J. B. Goodenough, *Chem. Mater.*, 2011, **23**, 2027–2029.

236 H. Park, D. H. Shin, T. Song, W. Il Park and U. Paik, *J. Mater. Chem. A*, 2017, **5**, 6958–6965.

237 D. Bauer, A. J. Roberts, C. L. Starkey, R. Vedarajan, D. Brett, P. Shearing, N. Matsumi and J. A. Darr, *Int. J. Electrochem. Sci.*, 2018, **13**, 5120–5140.

238 D. Bauer, T. E. Ashton, A. R. Groves, A. Dey, S. Krishnamurthy, N. Matsumi and J. A. Darr, *Energy Technol.*, , DOI:10.1002/ente.201900692.

239 A. E. D. M. van der Heijden, *Chem. Eng. J.*, 2018, **350**, 939–948.

240 T. E. Ashton, P. J. Baker, D. Bauer, A. R. Groves, C. Sotelo-Vazquez, T. Kamiyama, T. Matsukawa, K. M. Kojima, K. M. Kojima and J. A. Darr, *J. Mater. Chem. A*, 2020, **8**, 11545–11552.

241 M. Horn, C. F. Schwerdtfeger and E. P. Meagher, *Zeitschrift für Krist.*, 1972, **136**, 273–281.

242 A. D. Wadsley, *Acta Crystallogr.*, 1964, **17**, 623–628.

243 M. Gasperin, *J. Solid State Chem.*, 1984, **53**, 144–147.

244 P. Seidel and W. Hoffman, *Zeitschrift fuer Krist.*, 1976, **143**, 444–459.

245 Y. Hakuta, K. Scino, H. Ura, T. Adschiri, H. Takizawa and K. Aral, *J. Mater. Chem.*, 1999, **9**, 2671–2674.

246 S. Lou, X. Cheng, Y. Zhao, A. Lushington, J. Gao, Q. Li, P. Zuo, B. Wang, Y. Gao, Y. Ma, C. Du, G. Yin and X. Sun, *Nano Energy*, 2017, **34**, 15–25.

247 Y. Yang, Z. Li, R. Zhang, Y. Ding, H. Xie, G. Liu, Y. Fan, Z. Yang and X. Liu, *Electrochim. Acta*, 2021, **368**, 137623.

248 S. Lou, X. Cheng, Y. Zhao, A. Lushington, J. Gao, Q. Li, P. Zuo, B. Wang,

Y. Gao, Y. Ma, C. Du, G. Yin and X. Sun, *Nano Energy*, 2017, **34**, 15–25.

249 O. Frank, M. Zukalova, B. Laskova, J. Kürti, J. Koltai and L. Kavan, *Phys. Chem. Chem. Phys.*, 2012, **14**, 14567–14572.

250 L. Perfler, V. Kahlenberg, C. Wikete, D. Schmidmair, M. Tribus and R. Kaindl, *Inorg. Chem.*, 2015, **54**, 6836.

251 I. T. Chashechnikova, V. M. Vorotyntsev, V. V. Borovik, G. I. Golodets, I. V. Plyuto and A. P. Shpak, *Theor. Eksp. Khim.*, 1992, **28**, 216.

252 J. L. Sullivan, S. O. Saied and I. Bertoti, *Vacuum*, 1991, **42**, 1203.

253 A. Darlinski and J. Halbritter, *Surf. Interface Anal.*, 1987, **10**, 223.

254 N. Ozer, T. Barreto, T. Buyuklimanli and C. M. Lampert, *Sol. Energy Mater. Sol. Cells*, 1995, **36**, 433.

255 Q. Cheng, S. Tang, J. Liang, J. Zhao, Q. Lan, C. Liu and Y. C. Cao, *Results Phys.*, 2017, **7**, 810–812.

256 X. Wu, S. Lou, X. Cheng, C. Lin, J. Gao, Y. Ma, P. Zuo, C. Du, Y. Gao and G. Yin, *ACS Appl. Mater. Interfaces*, 2018, **10**, 27056–27062.

257 Y. Zhang, M. Zhang, Y. Liu, H. Zhu, L. Wang, Y. Liu, M. Xue, B. Li and X. Tao, *Electrochim. Acta*, 2020, **330**, 135299.

258 W. Li, X. Li, M. Chen, Z. Xie, J. Zhang, S. Dong and M. Qu, *Electrochim. Acta*, 2014, **139**, 104–110.

259 L. Buannic, J. F. Colin, M. Chapuis, M. Chakir and S. Patoux, *J. Mater. Chem. A*, 2016, **4**, 11531–11541.

260 H. Y. Wei, D. S. Tsai and C. L. Hsieh, *RSC Adv.*, 2015, **5**, 69176–69183.

261 X. Wang and G. Shen, *Nano Energy*, 2015, **15**, 104–115.

262 A. Noori, M. F. El-Kady, M. S. Rahmanifar, R. B. Kaner and M. F. Mousavi, *Chem. Soc. Rev.*, 2019, **48**, 1272–1341.

263 T. Gu and B. Wei, *Nanoscale*, 2015, **7**, 11626–11632.

264 S. Fleischmann, A. Tolosa and V. Presser, *Chem. - A Eur. J.*, 2018, **24**, 12143–12153.

265 M. Yang, S. Li and J. Huang, *ACS Appl. Mater. Interfaces*, 2021, **13**, 39501–39512.

266 X. Hua, Z. Liu, M. G. Fischer, O. Borkiewicz, P. J. Chupas, K. W. Chapman, U. Steiner, P. G. Bruce and C. P. Grey, *J. Am. Chem. Soc.*, 2017, **139**, 13330–13341.

267 R. Inada, R. Kumasaka, S. Inabe, T. Tojo and Y. Sakurai, *J. Electrochem. Soc.*, 2019, **166**, A5157–A5162.

268 B. Babu and M. M. Shaijumon, *Electrochim. Acta*, 2020, **345**, 136208.

269 W. H. Baur and A. A. Khan, *Acta Crystallogr.*, 1971, **27**, 2133–3139.

270 K. Kato, *Acta Cryst.*, 1976, **32**, 764–767.

271 S. Hsu, T. Huang, Y. Wu, C. Lu, H. C. Weng, J. Huang and T. Liu, *Polymers (Basel).*, 2021, **13**, 1672.

272 J. Mondal and S. K. Srivastava, *ACS Appl. Nano Mater.*, 2020, **3**, 11048–11059.

273 J. D. Wilcox, M. M. Doeff, M. Marcinek and R. Kostecki, *J. Electrochem. Soc.*, 2007, **154**, A389.

274 E. Lim, C. Jo, H. Kim, M. H. Kim, Y. Mun, J. Chun, Y. Ye, J. Hwang, K. S. Ha, K. C. Roh, S. Yoon and J. Lee, *ACS Nano*, 2015, **9**, 7497–7505.

275 X. Du, Q. Wang, T. Feng, X. Chen, L. Li, L. Li, X. Meng, L. Xiong, X. Sun, L. Lu and Y. Xu, *Sci. Rep.*, 2016, **6**, 1–8.

276 X. Wu, S. Lou, X. Cheng, C. Lin, J. Gao, Y. Ma, P. Zuo, C. Du, Y. Gao and G. Yin, *ACS Appl. Mater. Interfaces*, 2018, **10**, 27056–27062.

277 H. Lyu, H. Lyu, J. Li, T. Wang, B. P. Thapaliya, B. P. Thapaliya, S. Men, C. J. Jafta, C. J. Jafta, R. Tao, X. G. Sun and S. Dai, *ACS Appl. Energy Mater.*, 2020, **3**, 5657–5665.

278 A. Van Bommel and R. Divigalpitiya, *J. Electrochem. Soc.*, 2012, **159**, 1791–1795.

279 U. Kumar Sen, A. Shaligram and S. Mitra, *ACS Appl. Mater. Interfaces*, 2014, **6**, 14311–14319.

280 D. Wu, R. Shen, R. Yang, W. Ji, M. Jiang, W. Ding and L. Peng, *Sci. Rep.*, 2017, **7**, 1–9.

281 H. J. Zhang, T. H. Wu, K. X. Wang, X. Y. Wu, X. T. Chen, Y. M. Jiang, X. Wei and J. S. Chen, *J. Mater. Chem. A*, 2013, **1**, 12038–12043.

282 Y. Sun, X. Hu, W. Luo and Y. Huang, *ACS Nano*, 2011, **5**, 7100–7107.

283 X. Zhang, X. Song, S. Gao, Y. Xu, X. Cheng, H. Zhao and L. Huo, *J. Mater. Chem. A*, 2013, **1**, 6858–6864.

284 Z. Yuan, L. Si, D. Wei, L. Hu, Y. Zhu, X. Li and Y. Qian, *J. Phys. Chem. C*, 2014, **118**, 5091–5101.

285 S. Petnikota, K. W. Teo, L. Chen, A. Sim, S. K. Marka, M. V. Reddy, V. V. S. S. Srikanth, S. Adams and B. V. R. Chowdari, *ACS Appl. Mater. Interfaces*, 2016, **8**, 10884–10896.

286 A. Bhaskar, M. Deepa and R. Narasinga, *ACS Appl. Mater. Interfaces*, 2013, **5**, 255–2566.

287 X. Liu, D. Wu, W. Ji and W. Hou, *J. Mater. Chem. A*, 2015, **3**, 968–972.

288 N. A. Chernova, M. Roppolo, A. C. Dillon and M. S. Whittingham, *J. Mater. Chem.*, 2009, **19**, 2526.

289 W. Chen, J. Peng, L. Mai, H. Yu and Y. Qi, *Chem. Lett.*, 2004, **33**, 1366.

290 P. Poizot, S. Laruelle, S. Grugeo and L. Dupont, *Ionics (Kiel).*, 2000, **6**, 321–330.

291 E. Lim, H. Kim, C. Jo, J. Chun, K. Ku, S. Kim, H. I. Lee, I. S. Nam, S. Yoon, K. Kang and J. Lee, *ACS Nano*, 2014, **8**, 8968–8978.

292 M. Lubke, A. Sumboja, I. Johnson, D. Brett, P. Shearing, Z. Liu and J. A. Darr, *Electrochim. Acta*, 2016, **192**, 363–369.

293 S.-Q. Wang, X. Cai, Y. Song, X. Sun and X.-X. Liu, *Adv. Funct. Mater.*, 2018, **28**, 1803901.

294 D. Zhao, J. Qin, L. Zheng and M. Cao, *Chem. Mater.*, 2016, **28**, 4180–4190.

295 A. A. Bolzan, B. J. Kennedy and C. J. Howard, *Aust. J. Chem.*, 1995, **48**,

1473–1477.

296 J. M. Longo and P. Kierkegaard, *Acta Chem. Scand.*, 1970, **24**, 420–426.

297 M. Ghedir, H. Vincent, M. Marezio and J. C. Launay, *J. Solid State Chem.*, 1977, **22**, 423–438.

298 J. Papavasiliou, G. Avgouropoulos and T. Ioannides, *Appl. Catal. B Environ.*, 2007, **69**, 226–234.

299 J. Kasperkiewicz, J. A. Kovacich and D. Lichtman, *J. Electron Spectrosc. Relat. Phenom.*, 1983, **32**, 128.

300 N. S. McIntyre, D. D. Johnston, L. L. Coatsworth, R. D. Davidson and J. R. Brown, *Surf. Interface Anal.*, 1990, **15**, 265.

301 Nefedov V.I, D. Gati, B. . Dzhurinskii, N. P. Sergushin and Y. V Salyn, *Zh. Neorg. Khimii*, 1975, **20**, 2307.

302 C. Guo, C. Wei, Y. Shen, X. Cui and Q. Xu, *ChemNanoMat*, 2020, **6**, 779–782.

303 V. Pralong, V. Gopal, V. Caignaert, V. Duffort and B. Raveau, *Chem. Mater.*, 2012, **24**, 12–14.

304 A. González, E. Goikolea, J. A. Barrena and R. Mysyk, *Renew. Sustain. Energy Rev.*, 2016, **58**, 1189–1206.

305 H. Li, J. Chen, B. Yang, K. Wang, X. Zhang, T. Zhang, L. Zhang, W. Liu and X. Yan, *Electrochim. Acta*, 2019, **299**, 163–172.

306 L. Guo and Y. Wang, *J. Mater. Chem. A*, 2015, **3**, 4706–4715.

307 X.-Y. Xue, Z.-H. Chen, L.-L. Xing, S. Yuan and Y.-J. Chen, *Chem. Commun.*, 2011, **47**, 5205.

308 Y. Luo, J. Luo, J. Jiang, W. Zhou, H. Yang, X. Qi, H. Zhang, H. J. Fan, D. Y. W. Yu, C. M. Li and T. Yu, *Energy Environ. Sci.*, 2012, **5**, 6559.

309 R. B. Rakhi, W. Chen, D. Cha and H. N. Alshareef, *Nano Lett.*, 2012, **12**, 2559–2567.

310 H. Kim, *Adv. Energy Mater.*, 2013, **3**, 1500–1506.

311 A. C. Forse, C. Merlet, J. M. Griffin and C. P. Grey, *J. Am. Chem. Soc.*,

2016, **138**, 5731–5744.

312 S. Goriparti, E. Miele, F. De Angelis, E. Di Fabrizio, R. Proietti Zaccaria and C. Capiglia, *J. Power Sources*, 2014, **257**, 421–443.

313 K. Cao, T. Jin, L. Yang and L. Jiao, *Mater. Chem. Front.*, 2017, **1**, 2213–2242.

314 C. Yuan, H. Bin Wu, Y. Xie and X. W. Lou, *Angew. Chemie - Int. Ed.*, 2014, **53**, 1488–1504.

315 S. Dong, X. Chen, X. Zhang and G. Cui, *Coord. Chem. Rev.*, 2013, **257**, 1946–1956.

316 A. S. Aricò, P. Bruce, B. Scrosati, J.-M. Tarascon and W. van Schalkwijk, *Nat. Mater.*, 2005, **4**, 366–377.

317 B. Ng, X. Peng, E. Faegh and W. E. Mustain, *J. Mater. Chem. A*, 2020, **8**, 2712–2727.

318 S. Pinilla, S.-H. Park, K. Fontanez, F. Márquez, V. Nicolosi and C. Morant, *Nanomaterials*, 2020, **10**, 515.

319 H. Li, L.-J. Wu, S.-G. Zhang, C. Yao, C.-Y. Chao, H.-W. Yue and H.-H. Fan, *J. Alloys Compd.*, 2020, **832**, 155008.

320 X. Ren, D. Ai, R. Lv, F. Kang and Z.-H. Huang, *Electrochim. Acta*, 2020, **336**, 135723.

321 D. Adekoya, S. Zhang and M. Hankel, *ACS Appl. Mater. Interfaces*, 2020, **12**, 25875–25883.

322 P. Yan, L. Ji, X. Liu, Q. Guan, J. Guo, Y. Shen, H. Zhang, W. Wei, X. Cui and Q. Xu, *Nano Energy*, 2021, **86**, 106139.

323 M. Trukawka, K. Wenelska, L. Singer, R. Klingeler, X. Chen and E. Mijowska, *J. Alloys Compd.*, 2021, **853**, 156700.

324 Q. Dai, C. Gu, Y. Xu, Y. Zhang, Y. Hong, S. Woo Joo and J. Huang, *J. Electroanal. Chem.*, 2021, **898**, 115653.

325 H. Geng, Y. Peng, L. Qu, H. Zhang and M. Wu, *Adv. Energy Mater.*, 2020, **10**, 1–34.

326 L. Liang, X. Sun, J. Zhang, L. Hou, J. Sun, Y. Liu, S. Wang and C. Yuan, *Adv. Energy Mater.*, 2019, **9**, 1–15.

327 M. Nurul Islam, T. B. Ghosh, K. L. Chopra and H. N. Acharya, *Thin Solid Films*, 1996, **280**, 20–25.

328 Y. Ma, Y. Ma, G. Giuli, T. Diemant, R. J. Behm, D. Geiger, U. Kaiser, U. Ulissi, S. Passerini and D. Bresser, *Sustain. Energy Fuels*, 2018, **2**, 2601–2608.

329 S. Le, S. Wen, Z. Zou and Y. Li, *J. Nanosci. Nanotechnol.*, 2019, **19**, 7421–7426.

330 A. Birrozzi, J. Asenbauer, T. E. Ashton, A. R. Groves, D. Geiger, U. Kaiser and J. A. Darr, *Batter. Supercaps*, 2020, **3**, 284–292.

331 M. K. Kim, W. H. Shin and H. M. Jeong, *Appl. Surf. Sci.*, 2019, **467**–**468**, 926–931.

332 D. Bresser, E. Paillard, R. Kloepsch, S. Krueger, M. Fiedler, R. Schmitz, D. Baither, M. Winter and S. Passerini, *Adv. Energy Mater.*, 2013, **3**, 513–523.

333 Y. Teng, H. Zhao, Z. Zhang, Y. Li and H. Liu, *Mater. Lett.*, 2019, **246**, 141–143.

334 W. Wei, S. Yang, H. Zhou, I. Lieberwirth, X. Feng and K. Müllen, *Adv. Mater.*, 2013, **25**, 2909–2914.

335 H. Jiang, Y. Hu, S. Guo, C. Yan, P. S. Lee and C. Li, *ACS Nano*, 2014, **8**, 6038–6046.

336 Y. Liu, K. Ai and L. Lu, *Chem. Rev.*, 2014, **114**, 5057–5115.

337 Z. Chen and H. Li, *Nanotechnology*, , DOI:10.1088/1361-6528/ab71b7.

338 X. Huang, X. Qi, F. Boey and H. Zhang, *Chem. Soc. Rev.*, 2012, **41**, 666–686.

339 A. G. Ashish, P. Arunkumar, B. Babu, P. Manikandan, S. Sarang and M. M. Shaijumon, *Electrochim. Acta*, 2015, **176**, 285–292.

340 S. Chen, J. Zhu, X. Wu, Q. Han and X. Wang, *ACS Nano*, 2010, **4**, 2822–

2830.

341 X. Zhang, S. Li, S. A. El-Khodary, B. Zou, S. Yang, D. H. L. Ng, X. Liu, J. Lian and H. Li, *Nanotechnology*, 2020, **31**, 145404.

342 C. Lin, L. Hu, C. Cheng, K. Sun, X. Guo, Q. Shao, J. Li, N. Wang and Z. Guo, *Electrochim. Acta*, 2018, **260**, 65–72.

343 X. Li, Y. Zhao, W. Chu, Y. Wang, Z. Li, P. Jiang, X. Zhao, M. Liang and Y. Liu, *RSC Adv.*, 2015, **5**, 77437–77442.

344 X. Li, M. Qu and Z. Yu, *Solid State Ionics*, 2010, **181**, 635–639.

345 Z. Hao, Q. Chen, W. Dai, Y. Ren, Y. Zhou, J. Yang, S. Xie, Y. Shen, J. Wu, W. Chen and G. Q. Xu, *Adv. Energy Mater.*, 2020, **10**, 1–8.

346 L. . Plyasova, L. . Soloveva, G. . Kryukova, V. . Zabolotnyi and I. . Olenkova, *Zhurnal Strkturnoi Khimii*, 1991, **32**, 110–115.

347 M. Zhi, C. Xiang, J. Li, M. Li and N. Wu, *Nanoscale*, 2013, **5**, 72–88.

348 M. M. Doeff, J. D. Wilcox, R. Yu, A. Aumentado, M. Marcinek and R. Kostecki, *J. Solid State Electrochem.*, 2008, **12**, 995–1001.

349 G. Silversmit, D. Depla, H. Poelman, G. B. Marin and R. De Gryse, *J. Electron Spectros. Relat. Phenomena*, 2004, **135**, 167–175.

350 J. Baltrusaitis, B. Mendoza-Sanchez, V. Fernandez, R. Veenstra, N. Dukstiene, A. Roberts and N. Fairley, *Appl. Surf. Sci.*, 2015, **326**, 151–161.

351 M. Bystrzejewski, *J. Solid State Chem.*, 2011, **184**, 1492–1498.

352 N. Ozer, M. D. Rubin and C. M. Lampert, *Sol. Energy Mater. Sol. Cells*, 1996, **40**, 256.

353 S. Pletincx, L. L. I. Fockaert, M. C. Mol, Johannes, T. Hauffman and H. Terryn, *npj Mater. Degrad.*

354 M. Ohman and D. Perrson, *Electrochim. Acta*, 2007, **52**, 5159–5171.

355 L. Liu, P. Guan and C. Liu, *J. Electrochem. Soc.*, 2017, **164**, A3163–A3173.

356 W. Ai, J. Jiang, J. Zhu, Z. Fan, Y. Wang, H. Zhang, W. Huang and T. Yu,

Adv. Energy Mater., 2015, **5**, 1–8.

357 W. Tang, C. X. Peng, C. T. Nai, J. Su, Y. P. Liu, M. V. V. Reddy, M. Lin and K. P. Loh, *Small*, 2015, **11**, 2446–2453.

358 J. Ding, W. Hu, E. Paek and D. Mitlin, *Chem. Rev.*, 2018, **118**, 6457–6498.

359 B. Guo, X. Fang, B. Li, Y. Shi, C. Ouyang, Y. S. Hu, Z. Wang, G. D. Stucky and L. Chen, *Chem. Mater.*, 2012, **24**, 457–463.

360 A. Ramadoss and S. J. Kim, *Carbon N. Y.*, 2013, **63**, 434–445.

361 A. Burke and M. Miller, *J. Power Sources*, 2011, **196**, 514–522.

362 S. Shen, W. Guo, D. Xie, Y. Wang, S. Deng, Y. Zhong, X. Wang, X. Xia and J. Tu, *J. Mater. Chem. A*, 2018, **6**, 20195–20204.

363 A. Sharma and G. Shapps, Government takes historic step towards net-zero with end of sale of new petrol and diesel cars by 2030, https://www.gov.uk/government/news/government-takes-historic-step-towards-net-zero-with-end-of-sale-of-new-petrol-and-diesel-cars-by-2030#:~:text=The UK has taken another,in the UK by 2030., (accessed 26 February 2021).

364 VW, Volk-swa-gen sig-nif-i-cantly raises elec-tric car pro-duc-tion fore-cast for 2025, https://www.volkswagen-newsroom.com/en/press-releases/volkswagen-significantly-raises-electric-car-production-forecast-for-2025-5696, (accessed 26 February 2021).

365 FCAB, *National Blueprint for Lithium Batteries 2021-2030*, Washington, DC, 2021.

366 K. Barbalace, Periodic Table of Elements, https://environmentalchemistry.com/yogi/periodic/, (accessed 23 August 2021).

367 B. Zhao, X. Z. Fu, R. Sun and C. P. Wong, *Sustain. Energy Fuels*, 2017, **1**, 2145–2154.

368 S. Zheng, X. Li, B. Yan, Q. Hu, Y. Xu, X. Xiao, H. Xue and H. Pang, *Adv. Energy Mater.*, 2017, **7**, 1–27.

369 R. Xue, W. Hong, Z. Pan, W. Jin, H. Zhao, Y. Song, J. Zhou and Y. Liu, *Electrochim. Acta*, 2016, **222**, 838–844.

370 P. L. Taberna, S. Mitra, P. Poizot, P. Simon and J. M. Tarascon, *Nat. Mater.*, 2006, **5**, 567–573.

371 S. Mitra, P. Poizot, A. Finke and J. M. Tarascon, *Adv. Funct. Mater.*, 2006, **16**, 2281–2287.

372 W. M. Zhang, X. L. Wu, J. S. Hu, Y. G. Guo and L. J. Wan, *Adv. Funct. Mater.*, 2008, **18**, 3941–3946.

373 J. Tang, C. E. Zavala Lugo, S. F. Acuña Guzmán, G. Daniel, V. G. Kessler, G. A. Seisenbaeva and V. G. Pol, *J. Mater. Chem. A*, 2016, **4**, 18107–18115.

374 M. Li, H. Du, L. Kuai, K. Huang, Y. Xia and B. Geng, *Angew. Chemie - Int. Ed.*, 2017, **56**, 12649–12653.

375 T. Jiang, F. Bu, X. Feng, I. Shakir, G. Hao and Y. Xu, *ACS Nano*, 2017, **11**, 5140–5147.

376 H. Li, X. Zhu, H. Sitinamaluwa, K. Wasalathilake, L. Xu, S. Zhang and C. Yan, *J. Alloys Compd.*, 2017, **714**, 425–432.

377 B. Bulut Kopuklu, A. Tasdemir, S. Alkan Gursel and A. Yurum, *Carbon N. Y.*, 2021, **174**, 158–172.

378 F. Wang, X. Qi, L. Mao and J. Mao, *ACS Appl. Energy Mater.*, 2021, **4**, 331–340.

379 J. Yoon, W. Choi, T. Kim, H. Kim, Y. Seok Choi, J. Man Kim and W.-S. Yoon, *J. Energy Chem.*, 2021, **53**, 276–284.

380 T. Chen, Z. Wu, W. Xiang, E. Wang, T. Chen, X. Guo, Y. Chen and B. Zhong, *Electrochim. Acta*, 2017, **246**, 931–940.

381 M. Rana, V. Sai Avvaru, N. Boaretto, V. A. De La Peña O'Shea, R. Marcilla, V. Etacheri and J. J. Vilatela, *J. Mater. Chem. A*, 2019, **7**, 26596–26606.

382 H. S. Jadhav, G. M. Thorat, B. B. Kale and J. G. Seo, *Dalt. Trans.*, 2017, **46**, 9777–9783.

383 S. Yuvaraj, R. K. Selvan and Y. S. Lee, *RSC Adv.*, 2016, **6**, 21448–21474.

384 G. Pilania, V. Kocevski, J. A. Valdez, C. R. Kreller and B. P. Uberuaga, *Commun. Mater.*, 2020, **1**, 1–11.

385 M. Houshiar, F. Zebhi, Z. J. Razi, A. Alidoust and Z. Askari, *J. Magn. Magn. Mater.*, 2014, **371**, 43–48.

386 R. Tiwari, M. De, H. S. Tewari and S. K. Ghoshal, *Results Phys.*, 2020, **16**, 102916.

387 Y. Xu, X. Wang, C. An, Y. Wang, L. Jiao and H. Yuan, *J. Mater. Chem. A*, 2014, **2**, 16480–16488.

388 K. Malaie and M. R. Ganjali, *J. Energy Storage*, 2021, **33**, 102097.

389 J. M. Won, S. H. Choi, Y. J. Hong, Y. N. Ko and Y. C. Kang, *Sci. Rep.*, 2014, **4**, 5857.

390 A. Varzi, D. Bresser, J. Von Zamory, F. Müller and S. Passerini, *Adv. Energy Mater.*, 2014, **4**, 1400054.

391 Z. Zhang, Y. Wang, Q. Tan, Z. Zhong and F. Su, *J. Colloid Interface Sci.*, 2013, **398**, 185–192.

392 Y. Yan, G. Guo, T. Li, D. Han, J. Zheng, J. Hu, D. Yang and A. Dong, *Electrochim. Acta*, 2017, **246**, 43–50.

393 P. Kollu, P. R. Kumar, C. Santosh, D. K. Kim and A. N. Grace, *RSC Adv.*, 2015, **5**, 63304–63310.

394 X. Zhong, X. Wang, H. Wang, Z. Yang, Y. Jiang, J. Li and Z. Tian, *Nano Res.*, 2018, **11**, 3814–3823.

395 P. Xiong, B. Liu, V. Teran, Y. Zhao, L. Peng, X. Wang, G. Yu, M. Science, E. Program, M. Engineering, U. States, S. Chemistry, F. Materials and C. Engineering, *ACS Nano*, 2014, 0–6.

396 D. Liu, Z. Kong, X. Liu, A. Fu, Y. Wang, Y. G. Guo, P. Guo, H. Li and X. S. Zhao, *ACS Appl. Mater. Interfaces*, 2018, **10**, 2515–2525.

397 C. Gökhan Ünlü, M. Burak Kaynar, T. Şimşek, A. Tekgül, B. Kalkan and

Ş. Özcan, *J. Alloys Compd.*, 2019, **784**, 1198–1204.

398 T. L. Christiansen, E. D. Bøjesen, M. Søndergaard, S. Birgisson, J. Becker and B. B. Iversen, *CrystEngComm*, 2016, **18**, 1996–2004.

399 S. C. Abrahams and J. L. Bernstein, *Acta Crystallogr. Sect. B Struct. Crystallogr. Cryst. Chem.*, 1969, **25**, 1233–1236.

400 H. S. C. O'neill, *Eur. J. Mineral.*, 1992, **4**, 571–580.

401 W. Jian, R. Jia, J. Wang, H.-X. Zhang and F.-Q. Bai, *Inorg. Chem. Front.*, 2019, **6**, 2810–2816.

402 C. Wende, K. Olimov, H. Modrow, F. E. Wagner and H. Langbein, *Mater. Res. Bull.*, 2006, **41**, 1530–1542.

403 Y. Xu, D. Bauer, M. Lübke, T. E. Ashton, Y. Zong and J. A. Darr, *J. Power Sources*, 2018, **408**, 28–37.

404 D. Bauer, T. E. Ashton, A. R. Groves, A. Dey, S. Krishnamurthy, N. Matsumi and J. A. Darr, *Energy Technol.*, 2020, **8**, 1900692.

405 D.-T. Ngo and L. T. Kuhn, *Adv. Nat. Sci. Nanosci. Nanotechnol.*, 2016, **7**, 045001.

406 R. P. Gupta and S. K. Sen, *Phys. Rev. B*, 1975, **12**, 15–19.

407 M. C. Biesinger, B. P. Payne, A. P. Grosvenor, L. W. M. Lau, A. R. Gerson and R. S. C. Smart, *Appl. Surf. Sci.*, 2011, **257**, 2717–2730.

408 G. H. Major, T. G. Avval, B. Moeini, G. Pinto, D. Shah, V. Jain, V. Carver, W. Skinner, T. R. Gengenbach, C. D. Easton, A. Herrera-Gomez, T. S. Nunney, D. R. Baer and M. R. Linford, *J. Vac. Sci. Technol. A*, 2020, **38**, 061204.

409 B. Akinwolemiwa, C. Peng and G. Z. Chen, *J. Electrochem. Soc.*, 2015, **162**, A5054–A5059.

410 L. Fan, B. Li, D. W. Rooney, N. Zhang and K. Sun, *Chem. Commun.*, 2015, **51**, 1597–1600.

411 B. Koo, H. Xiong, M. D. Slater, V. B. Prakapenka, M. Balasubramanian, P. Podsiadlo, C. S. Johnson, T. Rajh and E. V. Shevchenko, *Nano Lett.*,

2012, **12**, 2429–2435.

412 Q. Li, H. Zhang, S. Lou, Y. Qu, P. Zuo, Y. Ma, X. Cheng, C. Du, Y. Gao and G. Yin, *Ceram. Int.*, 2017, **43**, 11998–12004.

413 J. H. Park, W. Y. Choi, S. Lee, T.-S. Kim and J. W. Lee, *Electrochim. Acta*, 2020, **348**, 136310.

414 J. P. Pender, G. Jha, D. H. Youn, J. M. Ziegler, I. Andoni, E. J. Choi, A. Heller, B. S. Dunn, P. S. Weiss, R. M. Penner and C. B. Mullins, *ACS Nano*, 2020, **14**, 1243–1295.

415 G. Zeng, N. Shi, M. Hess, X. Chen, W. Cheng, T. Fan and M. Niederberger, *ACS Nano*, 2015, **9**, 4227–4235.

416 K. Malaie and F. Scholz, *Colloids Surfaces A Physicochem. Eng. Asp.*, 2019, **577**, 576–582.

417 Q. Li, Z. Liu, C. Wang, Y. Zhao and R. Che, *Small*, 2017, **14**, 1702574.

418 X. Hua, P. K. Allen, H. S. Geddes, P. G. Bruce and A. L. Goodwin, *Cell Reports Phys. Sci.*, 2021, **2**, 100543.

419 C. Dong, W. Dong, X. Lin, Y. Zhao, R. Li and F. Huang, *EnergyChem*, 2020, **2**, 100045.

420 V. J. Ovejas and A. Cuadras, *Sci. Rep.*, 2019, **9**, 14875.

421 M. A. Roscher, O. Bohlen and J. Vetter, *Int. J. Electrochem.*, 2011, **2011**, 1–6.

422 W. Dreyer, J. Jamnik, C. Guhlke, R. Huth, J. Moškon and M. Gaberšček, *Nat. Mater.*, 2010, **9**, 448–453.

423 Y. Wu, L. Xie, X. He, L. Zhuo, L. Wang and J. Ming, *Electrochim. Acta*, 2018, **265**, 115–120.

424 Y.-T. Lee, C.-T. Kuo and T.-R. Yew, *ACS Appl. Mater. Interfaces*, 2021, **13**, 570–579.

425 A. H. Jay and K. W. Andrews, *J. Iron Steel Inst.*, 1945, **152**, 15–18.

426 W. Zhang, Y. Gong, N. P. Mellott, D. Liu and J. Li, *J. Power Sources*, 2015, **276**, 39–45.

427 D. Jarosch, *Zeitschrift fuer Krist.*, 1988, **185**, 605.

428 A. Machida, H. Saitoh, T. Hattori, A. Sano-Furukawa, K. Funakoshi, T. Sato, S. Orimo and K. Aoki, *Sci. Rep.*, 2019, **9**, 12290.

429 K. Bejtka, N. B. D. Monti, A. Sacco, M. Castellino, S. Porro, M. A. Farkhondehfal, J. Zeng, C. F. Pirri and A. Chiodoni, *Materials (Basel).*, 2021, **14**, 2354.

430 M. Bystrzejewski, *J. Solid State Chem.*, 2011, **184**, 1492–1498.

431 M. Lübke, N. M. Makwana, R. Gruar, C. Tighe, D. Brett, P. Shearing, Z. Liu and J. A. Darr, *J. Power Sources*, 2015, **291**, 102–107.

432 C.-G. Han, C. Zhu, Y. Aoki, H. Habazaki and T. Akiyama, *Green Energy Environ.*, 2017, **2**, 377–386.

433 Y. Zhao, Z. Feng and Z. J. Xu, *Nanoscale*, 2015, **7**, 9520–9525.

434 B. Liu, X. Hu, H. Xu, W. Luo, Y. Sun and Y. Huang, *Sci. Rep.*, 2015, **4**, 4229.

435 H. Bin Wu, J. S. Chen, H. H. Hng and X. Wen (David) Lou, *Nanoscale*, 2012, **4**, 2526.

436 K. Zhang, P. Guo, M. Zeng, Y. Zhang, Y. Bai and J. Li, *Mater. Lett.*, 2020, **280**, 128558.

437 S. Guo, H. Wang, W. Yang, H. Fida, L. You and K. Zhou, *Appl. Catal. B Environ.*, 2020, **262**, 118250.

438 S. Liu, J. Xie, Q. Su, G. Du, S. Zhang, G. Cao, T. Zhu and X. Zhao, *Nano Energy*, 2014, **8**, 84–94.

439 J. Li, S. Hwang, F. Guo, S. Li, Z. Chen, R. Kou, K. Sun, C.-J. Sun, H. Gan, A. Yu, E. A. Stach, H. Zhou and D. Su, *Nat. Commun.*, 2019, **10**, 2224.

8.2 List of Abbreviations

μSR – Muon Spin Relaxation spectroscopy

AC – Activated Carbon

BET – Brunauer Emmett Teller surface area analysis

BJH – Barrat Joyner Halenda

BPR – Back Pressure Regulator

C.E – Coulombic Efficiency

CHFS – Continuous Hydrothermal Flow Synthesis

CHN – Carbon Hydrogen Nitrogen analysis

CJM – Confined Jet Mixer

CNT – Carbon Nanotubes

CTNO – Carbon Titanium Niobium Oxide

CTR – Charge Transfer Resistance

CV – Cyclic Voltammetry

CVNM – Carbon Vanadium Niobium Molybdenum oxide

D.I. – Deionized Water

DEC – Diethyl Carbonate

D_{Li} – Diffusion coefficient of Lithium

DMC – Dimethyl Carbonate

EC – Ethylene Carbonate

EDLC – Electric Double Layer Capacitor

EDS – Energy dispersive x-ray spectroscopy

EIS – Electrochemical Impedance Spectroscopy

EV – Electric Vehicle

FEC – Fluoroethylene Carbonate

FEG-SEM – Field Emission Gun SEM

FMZ – Iron Manganese Zinc oxides

GCD – Galvanostatic Charge Discharge

GITT – Galvanostatic Intermittent Titration Technique

GO – Graphene Oxide

HIC – Hybrid Ion Capacitor

HOMO – Highest Occupied Molecular Orbital

HR-TEM – High Resolution Transmission Electron Microscopy

HT – Heat Treated

ICE – Internal Combustion Engine

ICSD – Inorganic Crystal Structure Database

IL – Ionic Liquid

IR – Internal Resistance

KERS – Kinetic Energy Recovery System

KOH – Potassium Hydroxide

LFP – Lithium Iron Phosphate

LIB – Lithium Ion Battery

LIC – Lithium-Ion Capacitor

LiNCA – Lithium Nickel Cobalt Aluminum Oxide

LiNMC – Lithium Nickel Manganese Cobalt Oxide

LTO – Lithium Titanium Oxide

LUMO – Lowest Unoccupied Molecular Orbital

NaOH – Sodium Hydroxide

NIB – Sodium Ion Battery

NIC – Sodium Ion Capacitor

NMP – N-Methyl Pyrrolidone

PDA – Polydopamine

PVDF – Polyvinylidene fluoride

PXRD – Powder X-ray Diffraction

rGO – Reduced Graphene Oxide

SCH_2O – Supercritical water

SEI – Solid Electrolyte Interphase layer

SEM – Scanning electron Microscopy

SHE – standard hydrogen electrode

SOC – state of charge

SSA – Specific Surface Area

TCD – thermal conductivity detector

TEM – Transmission Electron Microscopy

TIBALD – Titanium Bis (Ammonium Lactate) Dihydroxide

TNO – Titanium Niobium Oxide

VC – Vinylene Carbonate

VNM – Vanadium Niobium Molybdenum oxide

XAS – X-ray Absorption Spectroscopy

XPS – X-ray Photoelectron Spectroscopy

XRF – X-ray Fluorescence Spectroscopy

8.3 List of Figures

Ce, Zr and Y are proportional to the amount of red, green and blue colours respectively. (b) The different crystal phases identified by PXRD, fluorite (grey), monoclinic zirconium oxide (ZrO_2, yellow), tetragonal zirconium oxide (ZrO_2, red), bixbyite (blue) and a 2x2x2 pseudo-Y_2O_3 fluorite superstructure that has oxygen-vacancy ordering (green). Single colour hexagons indicate a single-phase material, three dots indicate two-phase behaviour, and stripes indicate a single-phase region with a smooth transition between the fluorite and the 2x2x2 fluorite superstructure. (c) Lattice parameter information regarding mean volume per unit ($MO_{2-\delta}$) displaying a smooth pseudolinear variation with composition. The volume at each nominal point can be approximated with the linear equation V = 40.3x + 33.5y + 37.5z. (d) The relative crystallite sizes calculated from the Scherrer equation and shown proportionally by the size of the blue circles. Reprinted with permission from X. Wang et al. J. Comb. Chem. Copyright 2013 American Chemical Society. (**53**)

Figure 1.25 (a): Ternary phase diagram of $LiMn_{1-x-y}Fe_xV_yPO_4$ with the compositional area investigated shown with a green triangle. (b) The unit cell volume for each material overlayed as a heat map onto the green triangle area. (c) Specific capacity values at C/2 cycling shown as a heat map. (d) Specific capacity values at 5C cycling shown as a heat map. Adapted and reprinted with permission from I. D. Johnson *et al. ACS Combi Chem*, https://pubs.acs.org/doi/10.1021/acscombsci.6b00035. Copyright 2016 American Chemical Society. Further permission related to this material excerpted should be directed to the ACS. (**54**)

Figure 2.1: Diagram showing the process that enables XRF, including the expulsion of an inner shell electron by an incident x-ray photon, the transfer of a higher shell electron to fill the hole and the resulting photon of excess energy released. (**57**)

Figure 2.2: Diagram showing the different types of scattering that occur during Raman spectroscopy. (**59**)

Figure 2.3: Diagram showing the internal components of a coin cell. (**64**)

8.4 List of Tables

9.0 – Appendix

9.1 Supplementary for Chapter 2

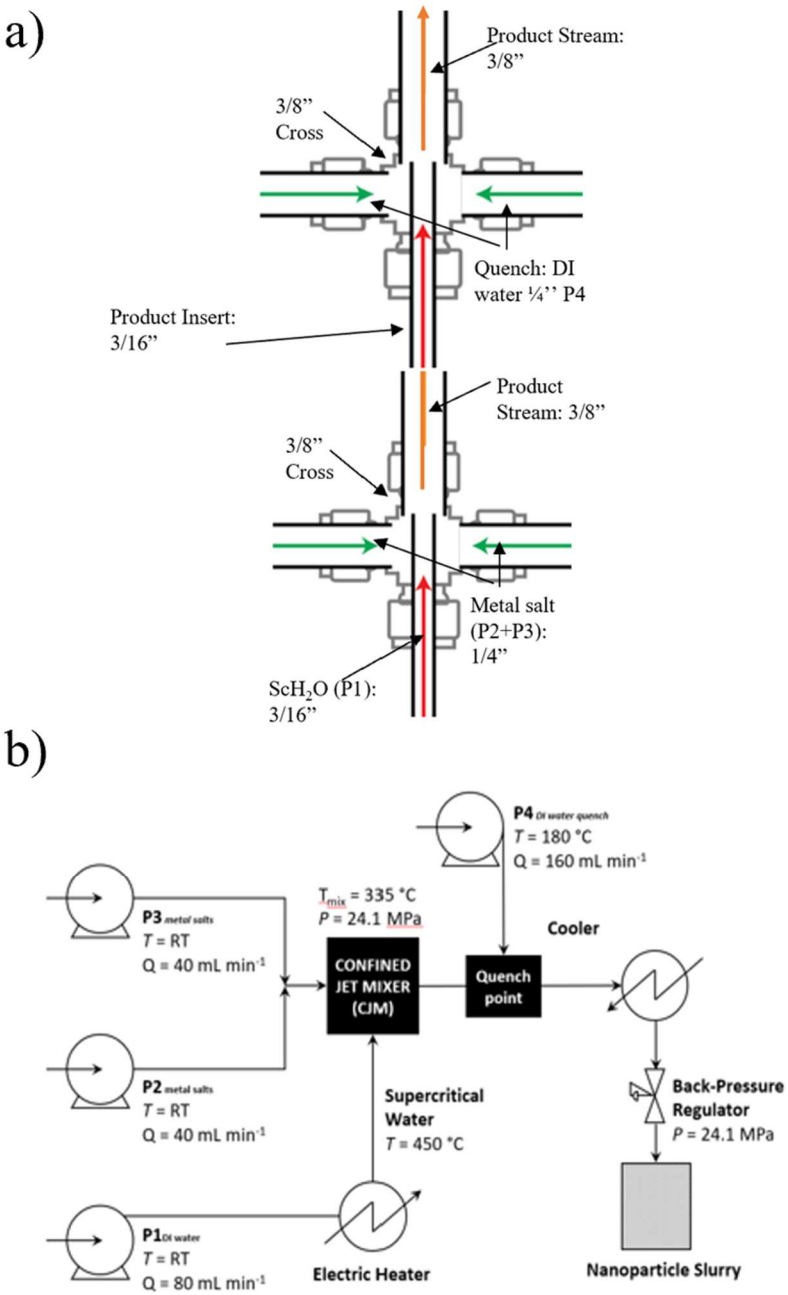

Figure 1 (a): Diagram of the lab scale CHFS reactor with quench used to synthesise mixed VNM oxide materials. (b) Schematic of the CHFS lab reactor.

Sample	Material	NH_4VO_3 / mol dm^{-3}	$NH_4NbC_4O_9.xH_2O$ / mol dm^{-3}	$(NH_4)_6Mo_7O_{24}.4H_2O$ / mol dm^{-3}	Ascorbic acid / mol dm^{-3}
1	$V_{0.7}Nb_{0.3}$	0.21	0.09	0.0	0.0
2	$V_{0.7}Nb_{0.2}Mo_{0.2}$	0.21	0.06	0.00857	0.0343
3	$V_{0.7}Nb_{0.2}Mo_{0.1}$	0.21	0.06	0.00429	0.0172
4	$Nb_{0.3}Mo_{0.7}$	0.0	0.09	0.03	0.12
5	$V_{0.6}Nb_{0.4}$	0.18	0.12	0.0	0.0
6	$V_{0.6}Nb_{0.1}Mo_{0.3}$	0.18	0.03	0.0129	0.0516
7	$V_{0.6}Nb_{0.2}Mo_{0.2}$	0.18	0.06	0.00857	0.0343
8	$V_{0.6}Nb_{0.3}Mo_{0.1}$	0.18	0.09	0.00429	0.0172
9	$Nb_{0.4}Mo_{0.6}$	0.0	0.12	0.0257	0.1028
10	$V_{0.5}Nb_{0.5}$	0.15	0.15	0.0	0.0
11	$V_{0.5}Nb_{0.1}Mo_{0.4}$	0.15	0.03	0.0171	0.0684
12	$V_{0.5}Nb_{0.2}Mo_{0.3}$	0.15	0.06	0.0129	0.0516
13	$V_{0.5}Nb_{0.3}Mo_{0.2}$	0.15	0.09	0.00857	0.0343
14	$V_{0.5}Nb_{0.4}Mo_{0.1}$	0.15	0.12	0.00429	0.0172
15	$Nb_{0.5}Mo_{0.5}$	0.0	0.15	0.0214	0.0856
16	$V_{0.4}Nb_{0.6}$	0.12	0.18	0.0	0.0
17	$V_{0.4}Nb_{0.1}Mo_{0.5}$	0.12	0.03	0.0214	0.0856
18	$V_{0.4}Nb_{0.2}Mo_{0.4}$	0.12	0.06	0.0171	0.0684
19	$V_{0.4}Nb_{0.3}Mo_{0.3}$	0.12	0.09	0.0129	0.0516
20	$V_{0.4}Nb_{0.4}Mo_{0.2}$	0.12	0.12	0.00857	0.0343
21	$V_{0.4}Nb_{0.5}Mo_{0.1}$	0.12	0.15	0.00429	0.0172
22	$Nb_{0.6}Mo_{0.4}$	0.0	0.18	0.0171	0.0684
23	$V_{0.3}Nb_{0.7}$	0.09	0.21	0.0	0.0
24	$V_{0.3}Nb_{0.1}Mo_{0.6}$	0.09	0.03	0.0257	0.1028
25	$V_{0.3}Nb_{0.2}Mo_{0.5}$	0.09	0.06	0.0214	0.0856
26	$V_{0.3}Nb_{0.3}Mo_{0.4}$	0.09	0.09	0.0171	0.0684
27	$V_{0.3}Nb_{0.4}Mo_{0.3}$	0.09	0.12	0.0129	0.0516
28	$V_{0.3}Nb_{0.5}Mo_{0.2}$	0.09	0.15	0.00857	0.0343
29	$V_{0.3}Nb_{0.6}Mo_{0.1}$	0.09	0.18	0.00429	0.0172
30	$Nb_{0.7}Mo_{0.3}$	0.0	0.21	0.0129	0.0516

31	$V_{0.2}Nb_{0.1}Mo_{0.7}$	0.06	0.03	0.03	0.12
32	$V_{0.2}Nb_{0.2}Mo_{0.6}$	0.06	0.06	0.0257	0.1028
33	$V_{0.2}Nb_{0.3}Mo_{0.5}$	0.06	0.09	0.0214	0.0856
34	$V_{0.2}Nb_{0.4}Mo_{0.4}$	0.06	0.12	0.0171	0.0684
35	$V_{0.2}Nb_{0.5}Mo_{0.3}$	0.06	0.15	0.0129	0.0516
36	$V_{0.2}Nb_{0.6}Mo_{0.2}$	0.06	0.18	0.00857	0.0343
37	$V_{0.2}Nb_{0.7}Mo_{0.1}$	0.06	0.21	0.00429	0.0172
38	$V_{0.1}Nb_{0.2}Mo_{0.7}$	0.03	0.06	0.03	0.12
39	$V_{0.1}Nb_{0.3}Mo_{0.6}$	0.03	0.09	0.0257	0.1028
40	$V_{0.1}Nb_{0.4}Mo_{0.5}$	0.03	0.12	0.0214	0.0856
41	$V_{0.1}Nb_{0.5}Mo_{0.4}$	0.03	0.15	0.0171	0.0684
42	$V_{0.1}Nb_{0.6}Mo_{0.3}$	0.03	0.18	0.0129	0.0516
43	$V_{0.1}Nb_{0.7}Mo_{0.2}$	0.03	0.21	0.00857	0.0343
44	$V_{0.3}Mo_{0.7}$	0.09	0.0	0.03	0.12
45	$V_{0.4}Mo_{0.6}$	0.12	0.0	0.0257	0.1028
46	$V_{0.5}Mo_{0.5}$	0.15	0.0	0.0214	0.0856
47	$V_{0.6}Mo_{0.4}$	0.18	0.0	0.0171	0.0684
48	$V_{0.7}Mo_{0.3}$	0.21	0.0	0.0129	0.0516

Table 1: Showing the different molar ratios of vanadium, niobium, molybdenum, and ascorbic acid used to create the different VNM materials.

Material	[Ti] / mol dm^{-3}	[Nb] / mol dm^{-3}	[KOH] / mol dm^{-3}

K1	0.10	0.20	3.00
K2	0.10	0.21	3.00
K3	0.10	0.22	3.00
K4	0.10	0.23	3.00
K5	0.10	0.24	3.00

Table 2: Showing the different molar ratios of titanium and niobium precursors to potassium hydroxide.

Material	Measured pH	[Ti] / mol dm^{-3}	[Nb] / mol dm^{-3}	[KOH] / mol dm^{-3}
K6	7	0.1	0.2	0.0000001
K7	8	0.1	0.2	0.0000010
K8	9	0.1	0.2	0.0000100
K9	10	0.1	0.2	0.0001000
K10	11	0.1	0.2	0.0010000
K11	12	0.1	0.2	0.01
K12	13	0.1	0.2	0.1
K13	14	0.1	0.2	1
K14	14	0.1	0.2	2
K15	14	0.1	0.2	3

Table 3: Showing the concentrations of the titanium and niobium precursors and the increasing concentrations of potassium hydroxide.

Material	Targeted pH	[Ti] / mol dm^{-3}	[Nb] / mol dm^{-3}	[NaOH] / mol dm^{-3}
N1	N/A	0.1	0.2	0.0
N2	7	0.1	0.2	0.0000001
N3	8	0.1	0.2	0.000001
N4	9	0.1	0.2	0.00001
N5	10	0.1	0.2	0.0001
N6	11	0.1	0.2	0.001
N7	12	0.1	0.2	0.01
N8	13	0.1	0.2	0.1
N9	14	0.1	0.2	1.0

Table 4: Showing the concentrations of titanium and niobium precursors and the different concentrations of sodium hydroxide used for each material.

Material	[Ti] / mol dm^{-1}	[Nb] / mol dm^{-3}	[sucrose] / mol dm^{-3}	[NaOH] / mol dm^{-3}

CTNO-1	0.1	0.2	0.1	1.0
CTNO-2	0.1	0.2	0.25	1.0
CTNO-3	0.1	0.2	0.5	1.0
CTNO-4	0.1	0.2	0.75	1.0
CTNO-5	0.1	0.2	1.0	1.0
CTNO-6	0.1	0.2	1.5	1.0
CTNO-7	0.1	0.2	1.75	1.0

Table 5: Showing the concentrations of titanium, niobium, sucrose, and sodium hydroxide used for the different CTNO materials.

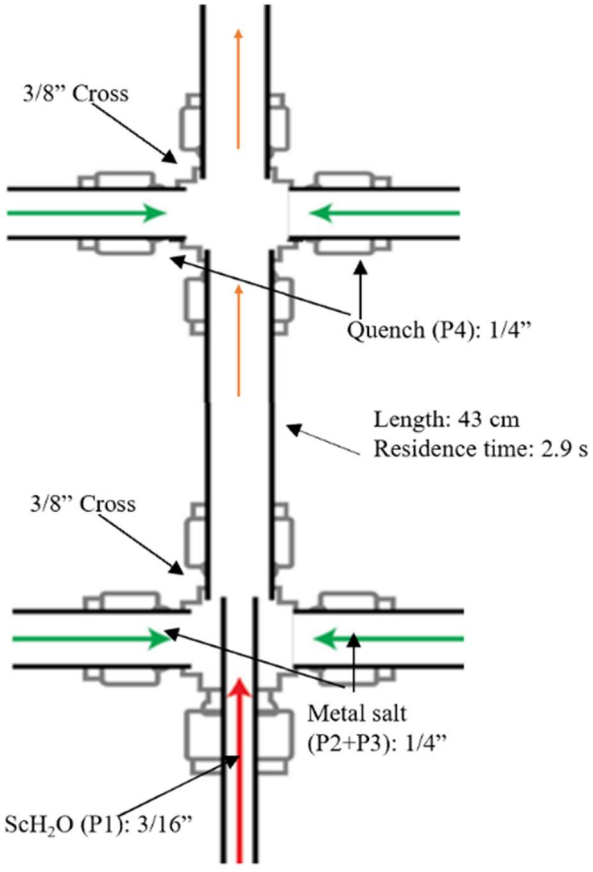

Figure 2: Diagram of the lab CHFS reactor mixer and quench used to synthesise the CVNM materials.

Material	Vanadium / mol cm^{-3}	Niobium / mol cm^{-3}	Molybdenum / mol cm^{-3}	Sucrose / mol cm^{-3}	Sucrose:VNM Molar ratio
CVNM-1	0.09	0.03	0.0257	0.2	0.67:1
CVNM-2	0.09	0.03	0.0257	0.25	0.83:1
CVNM-3	0.09	0.03	0.0257	0.3	1:1
CVNM-4	0.09	0.03	0.0257	0.35	1.17:1
CVNM-5	0.09	0.03	0.0257	0.4	1.33:1
CVNM-6	0.09	0.03	0.0257	0.45	1.5:1
CVNM-7	0.09	0.03	0.0257	0.5	1.67
CVNM-8	0.09	0.03	0.0257	0.6	2:1

Table 6: Showing the nominal ratios of the three metals and the forms of carbon in each material synthesised.

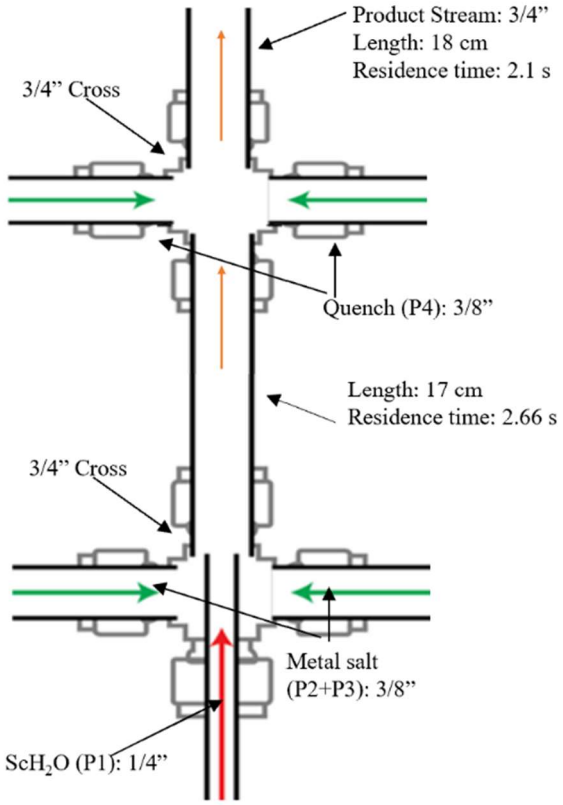

Figure 3: Diagram of the pilot scale CHFS double mixer and quench reactor used to synthesise the CVNM materials.

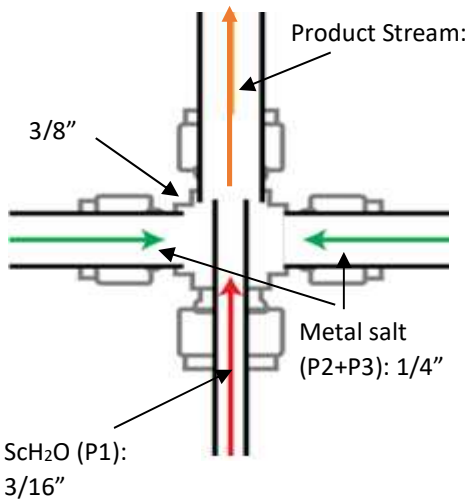

Figure 5: Diagram of the single mixer CJM used for the CHFS set for the synthesis of mixed Fe/Mn/Zn oxides.

Sample No.	Material	[Fe] / mol dm^{-3}	[Mn] / mol dm^{-3}	[Zn] / mol dm^{-3}	[KOH] / mol dm^{-3}	Colour of final powder
1	ZnO_x	0	0	0.1	1	White
2	FeO_x	0.1	0	0	1	Red
3	MnO_x	0	0.12	0	1	Pink/white
4	$Zn_{0.2}Fe_{0.8}O_x$	0.08	0	0.02	1	Orange
5	$Zn_{0.4}Fe_{0.6}O_x$	0.06	0	0.04	1	Orange
6	$Zn_{0.6}Fe_{0.4}O_x$	0.04	0	0.06	1	Orange
7	$Zn_{0.8}Fe_{0.2}O_x$	0.02	0	0.08	1	Orange
8	$Mn_{0.2}Fe_{0.8}O_x$	0.08	0.024	0	1	Brown/black
9	$Mn_{0.4}Fe_{0.6}O_x$	0.06	0.048	0	1	Brown/black
10	$Mn_{0.6}Fe_{0.4}O_x$	0.04	0.072	0	1	Brown/black
11	$Mn_{0.8}Fe_{0.2}O_x$	0.02	0.096	0	1	Brown/black
12	$Zn_{0.2}Mn_{0.8}O_x$	0	0.096	0.02	1	Yellow/pink
13	$Zn_{0.4}Mn_{0.6}O_x$	0	0.072	0.04	1	Yellow/pink
14	$Zn_{0.6}Mn_{0.4}O_x$	0	0.048	0.06	1	Orange/pink
15	$Zn_{0.8}Mn_{0.2}O_x$	0	0.024	0.08	1	Orange
16	$Zn_{0.6}Fe_{0.2}Mn_{0.2}O_x$	0.02	0.024	0.06	1	Brown
17	$Zn_{0.2}Fe_{0.6}Mn_{0.2}O_x$	0.06	0.024	0.06	1	Brown
18	$Zn_{0.2}Fe_{0.2}Mn_{0.6}O_x$	0.02	0.072	0.033	1	Brown
19	$Zn_{0.33}Fe_{0.33}Mn_{0.33}O_x$	0.033	0.04	0.033	1	Brown
20	$Zn_{0.4}Fe_{0.4}Mn_{0.2}O_x$	0.04	0.024	0.04	1	Brown
21	$Zn_{0.4}Fe_{0.2}Mn_{0.4}O_x$	0.02	0.048	0.04	1	Brown
22	$Zn_{0.2}Fe_{0.4}Mn_{0.4}O_x$	0.04	0.048	0.02	1	Brown

Table 7: Showing the different ratios of Fe/Mn/Zn salts and KOH used in CHFS to synthesise the mixed FMZ oxides, and the colours of the final collected powders.

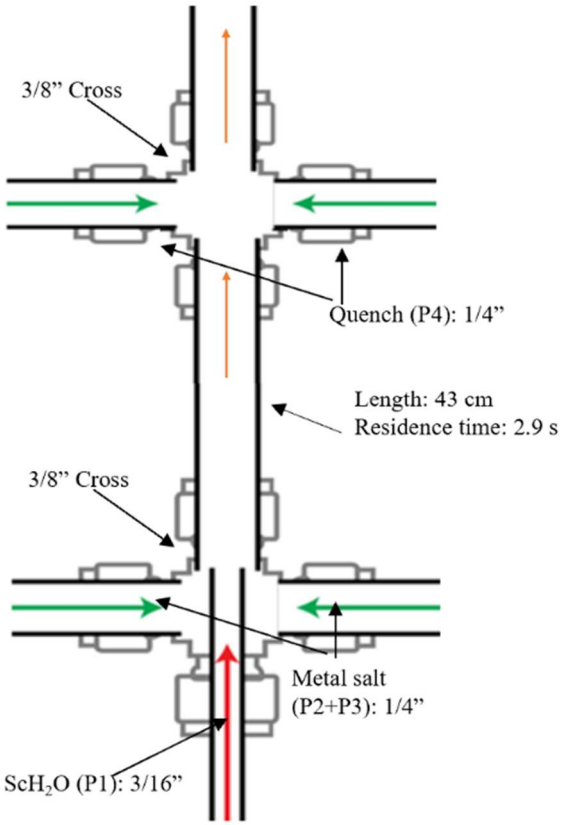

Figure 6: Diagram of the lab scale CHFS double mixer and quench set up used to synthesise carbon Fe/Mn/Zn composite materials.

Sample	Material	[Fe] / mol dm^{-3}	[Mn] / mol dm^{-3}	[Zn] / mol dm^{-3}	[KOH] / mol dm^{-3}	[Sucrose] / mol dm^{-3}
1	C(FeMn)-0.5	0.02	0.096	-	1	0.05
2	C(FeMn)-1	0.02	0.096	-	1	0.1
3	C(FeMn)-2	0.02	0.096	-	1	0.2
4	C(FeMn)-3	0.02	0.096	-	1	0.3
5	C(FeMn)-4	0.02	0.096	-	1	0.4
6	C(FeMn)-5	0.02	0.096	-	1	0.5
7	C(FeMnZn)-0.5	0.02	0.096	0.05	1	0.05
8	C(FeMnZn)-1	0.02	0.096	0.05	1	0.1
9	C(FeMnZn)-2	0.02	0.096	0.05	1	0.2
10	C(FeMnZn)-3	0.02	0.096	0.05	1	0.3
11	C(FeMnZn)-4	0.02	0.096	0.05	1	0.4
12	C(FeMnZn)-5	0.02	0.096	0.05	1	0.5

Table 8: Showing the different metal salt and sucrose molar ratios used to create the $C(Fe_aMn_b)$ and $C(Fe_aMn_bZn_c)$ materials.

9.2 Supplementary for Chapter 3

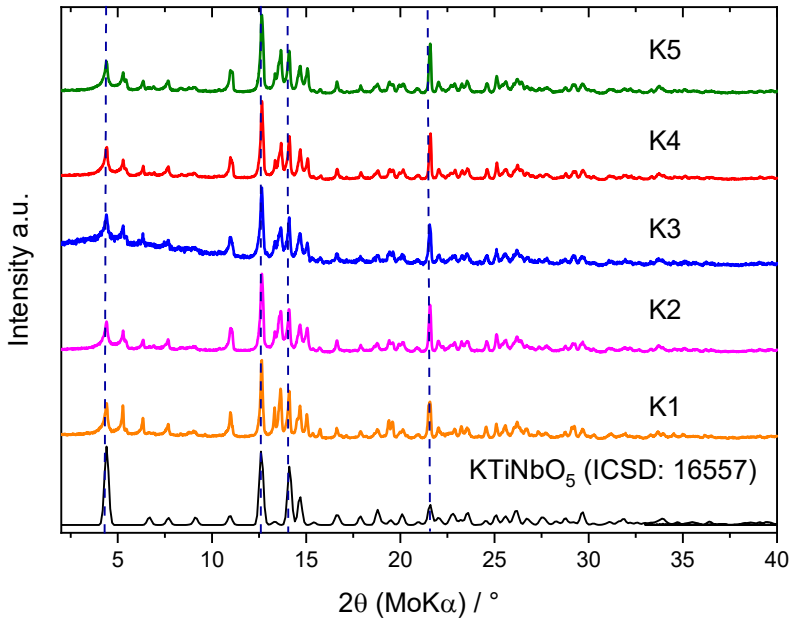

Figure 6: Graph showing the PXRD patterns for the TNO materials synthesised with KOH (K1-K5) and the $KTiNbO_5$ reference pattern (ICSD collection no. 16557.

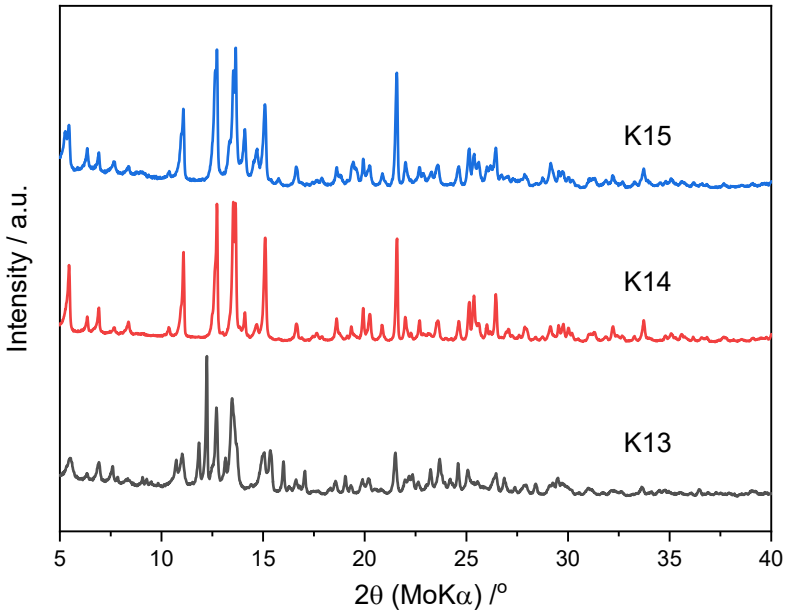

Figure 7: PXRD patterns for the materials K13 (black), K14 (red) and K15 (blue).

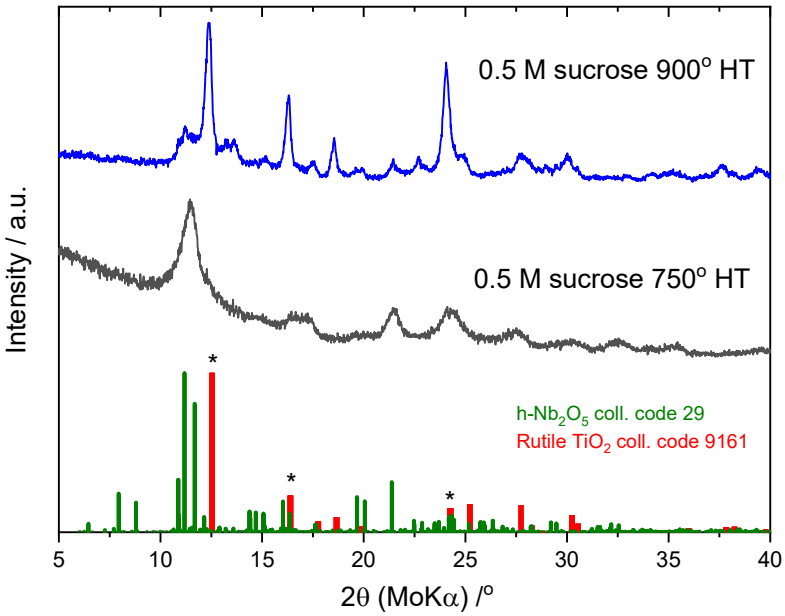

Figure 8: PXRD patterns of CTNO-3 after heat treatment at 750 (black) and 900 °C (blue) with the reference patterns of rutile TiO_2 (red and asterisked) and monoclinic Nb_2O_5 (green).

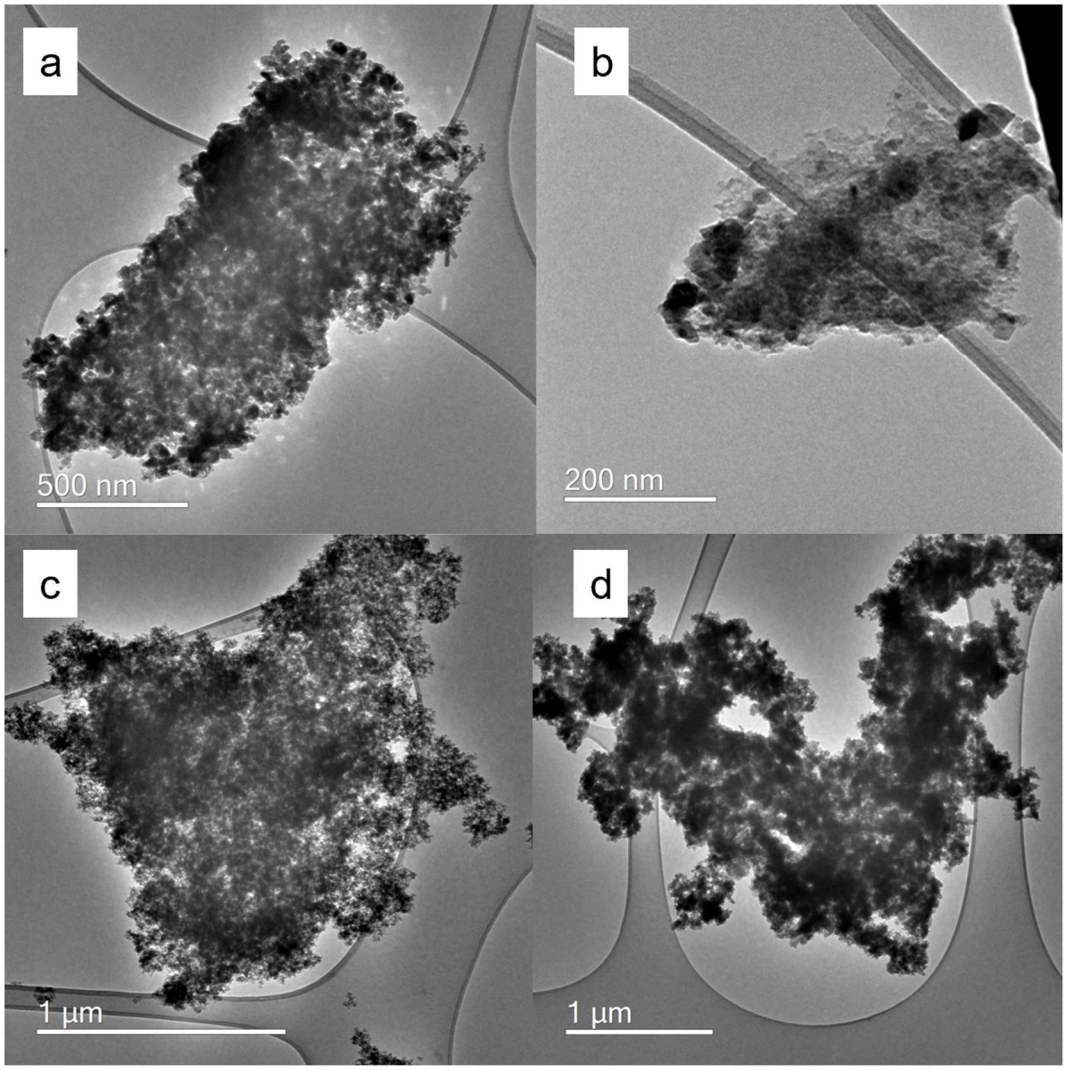

Figure 9: TEM images of (a) N13144HT (b) magnified image of N13144HT (c) N13146HT (d) N13149HT

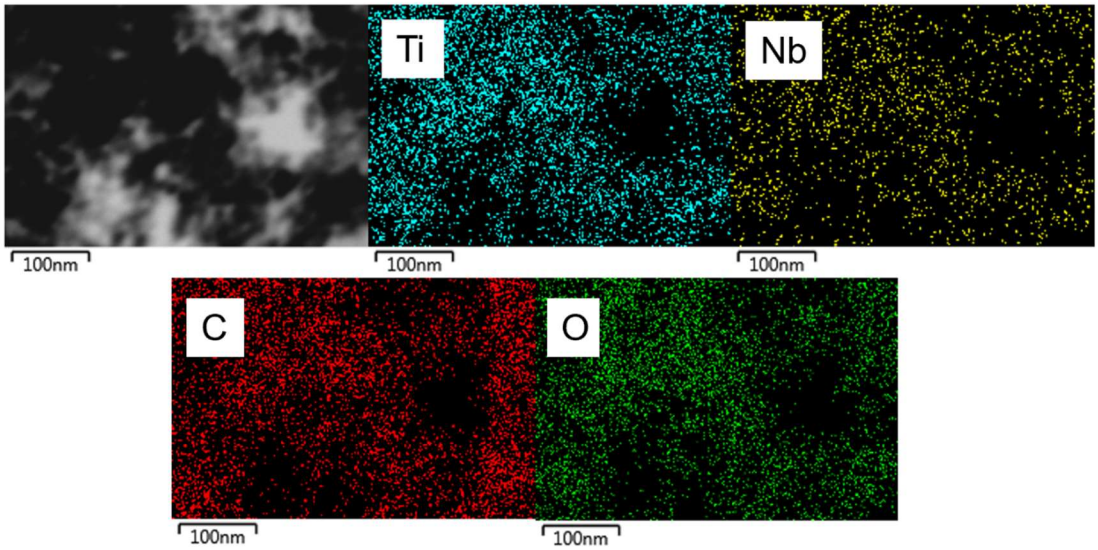

Figure 10: EDS scans of a TEM image of N13146HT for Ti (blue), Nb (yellow), C (red) and O (green).

Material	Titanium content / at. %	Niobium content / at. %
CTNO-1	51.6	48.3
CTNO-2	57.5	42.5
CTNO-3	66.3	33.7
CTNO-4	69.6	30.4
CTNO-5	63.9	36.1
CTNO-6	56.6	43.4

Table 9: Table showing the atomic percentages of Ti and Nb for all CTNO materials, determined by XRF.

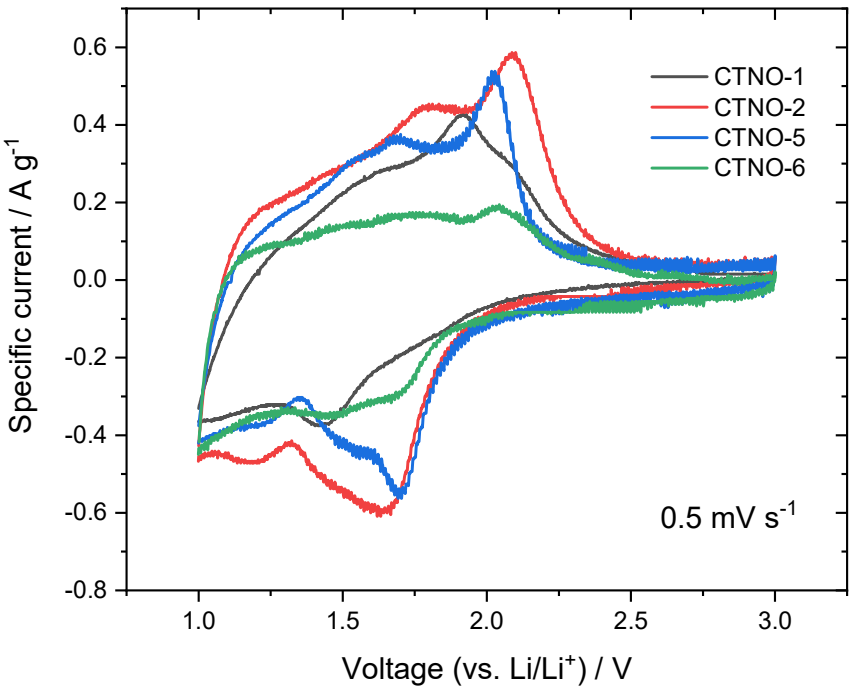

Figure 11: Graph showing the CV curves of CTNO materials 1, 2, 5 and 6 at a scan rate of 0.5 mV s^{-1}.

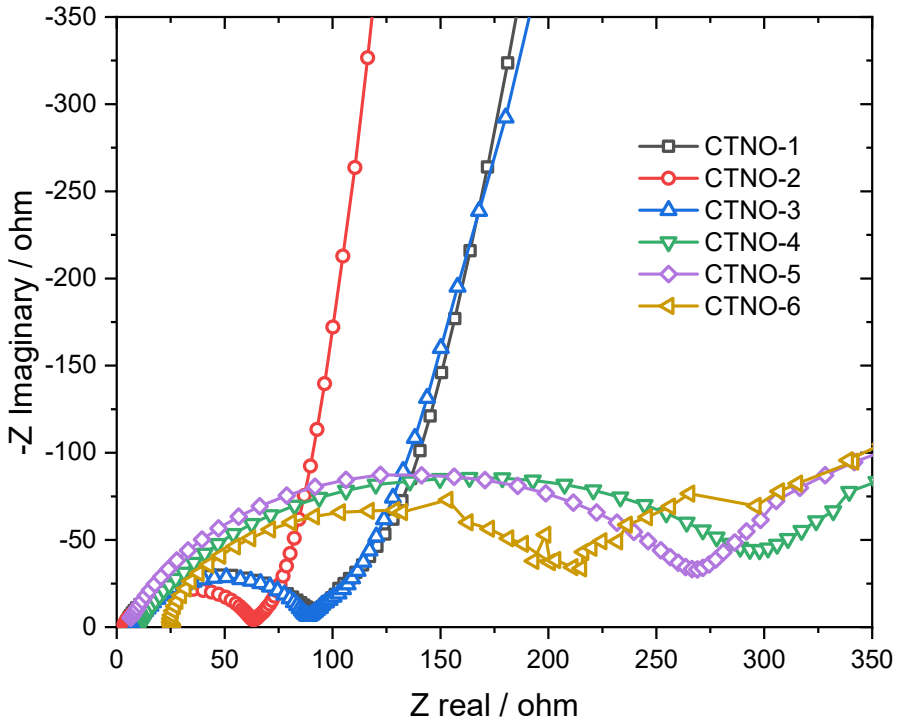

Figure 12: Graph showing the Nyquist plots for all the CTNO materials.

9.3 Supplementary for Chapter 4

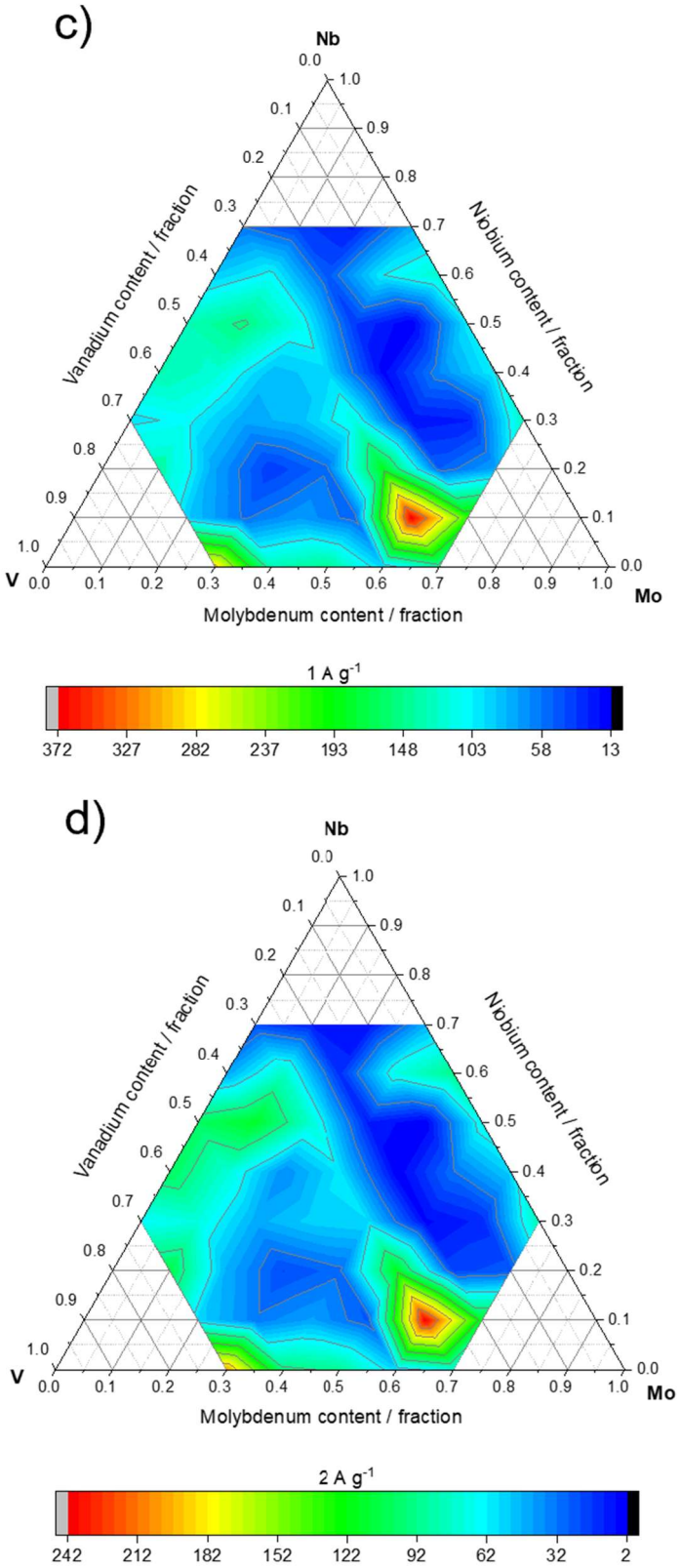

Figure 14 cont.: Ternary composition diagrams with specific capacity in lithium half-cells plotted as heat maps for the specific currents, (c) 1 A g^{-1} and (b) 2 A g^{-1}

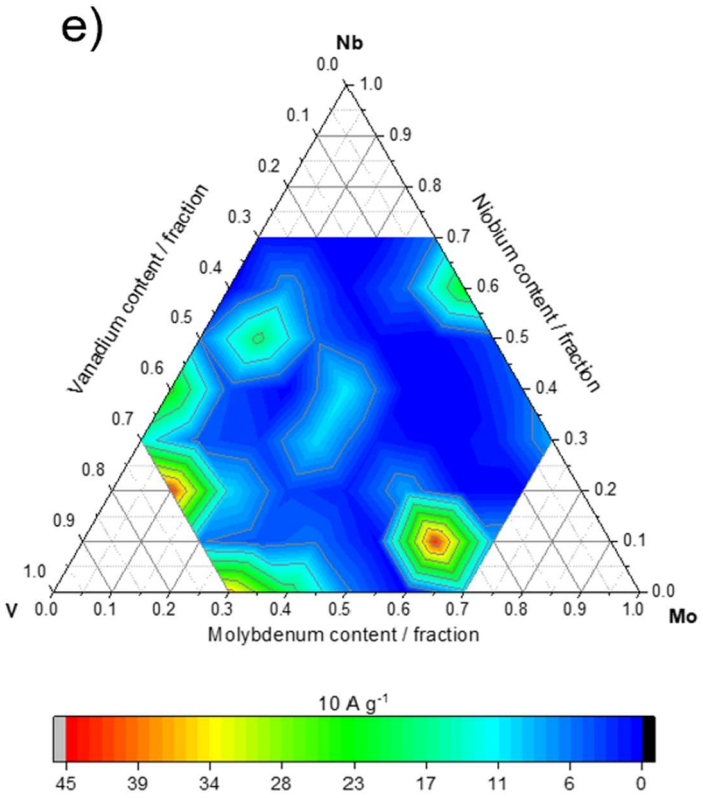

Figure 14 cont.: Ternary composition diagrams with specific capacity in lithium half-cells plotted as heat maps for the specific currents, (d) 10 A g^{-1}

	Specific capacity /mAh g^{-1}					
Material	**0.1 A g^{-1}**	**0.2 A g^{-1}**	**0.5 A g^{-1}**	**1 A g^{-1}**	**2 A g^{-1}**	**5 A g^{-1}**
V0.7Nb0.3	266.6	186.2	137.5	98.4	64.4	32.1
V0.7Nb0.1Mo0.2	291.1	222.3	140.7	89.6	54.9	24.3
V0.7Nb0.2Mo0.1	317.6	238.8	183.9	142.8	107.8	69.6
Mo0.7Nb0.3	314.8	236.8	175.7	129.4	83	35
V0.6Nb0.4	296	216.8	171.9	133.9	102.7	56
V0.6Nb0.1Mo0.3	379	240.4	115.1	56.3	33.8	15.7
V0.6Nb0.2Mo0.2	259.4	172.4	112.5	73.6	45.7	22.1
V0.6Nb0.3Mo0.1	270.2	192.2	142.7	106.7	71.9	30.7
Mo0.6Nb0.4	300.8	214.2	151.2	104	54	19.2
V0.5Nb0.5	305.4	200.1	171.4	132.3	102.2	43.3
V0.5Nb0.1Mo0.4	354.2	240.4	126.2	71.6	43	19.5
V0.5Nb0.2Mo0.3	265.1	152.1	73.9	36.8	21.6	11.2
V0.5Nb0.3Mo0.2	252.6	167.9	113.1	76	45	17.1
V0.5Nb0.4Mo0.1	293.2	213.1	163	121.8	74.1	25.7
Nb0.5Mo0.5	240.7	165.3	128.1	98.7	69.1	26.2
V0.4Nb0.6	248.6	175.9	127.5	89	43.3	5.7
V0.4Nb0.1Mo0.5	386.9	241.1	112.4	52.7	25.7	7
V0.4Nb0.2Mo0.4	279.3	202.6	111.1	55.7	29.9	10.6
V0.4Nb0.3Mo0.3	318.2	209.3	127.4	84.2	54.1	26
V0.4Nb0.4Mo0.2	343.6	230	148.8	83.9	37.5	6.01
V0.4Nb0.5Mo0.1	304.7	235	189.4	151.2	114.8	55.2
Nb0.6Mo0.4	311.1	213.7	160.4	124.6	91.7	51.3
V0.3Nb0.7	247.5	139.1	93.5	56.9	22.4	4.8
V0.3Nb0.1Mo0.6	661.3	650.3	505	371.2	241.3	120.3
V0.3Nb0.2Mo0.5	400.5	343.1	256.7	185.1	117.3	39.2
V0.3Nb0.3Mo0.4	411.3	296.1	195.4	115.8	56.9	11.7
V0.3Nb0.4Mo0.3	481.8	205.7	136.7	92.3	58.7	27.1
V0.3Nb0.5Mo0.2	323.7	220.5	157.3	113.6	74.4	28.2
V0.3Nb0.6Mo0.1	264.2	180.5	136.8	106.7	78.2	35.5
Nb0.7Mo0.3	239.2	159.9	110.5	75.4	45.5	18.3
V0.2Nb0.1Mo0.7	416.9	448.5	343.3	212.6	115	41.7

V0.2Nb0.2Mo0.6	269.2	184.1	101.7	50.8	20.6	3.6
V0.2Nb0.3Mo0.5	284.9	142.2	64.7	22.9	5.5	0.88
V0.2Nb0.4Mo0.4	174.8	108.6	57.6	17.6	3.2	0.5
V0.2Nb0.5Mo0.3	209	124.9	76.6	36.3	11	2.3
V0.2Nb0.6Mo0.2	222	133.8	86.7	46.8	14.8	2.7
V0.2Nb0.7Mo0.1	200	122.8	77.3	37.8	11.7	2.4
V0.1Nb0.2Mo0.7	370	253.9	148.4	74.7	24.3	3.6
V0.1Nb0.3Mo0.6	247.5	124	61.1	27.3	13.9	5.3
V0.1Nb0.4Mo0.5	209.8	133.7	99.6	65.3	31.4	4.9
V0.1Nb0.5Mo0.4	190	92.3	45.5	13.5	2.9	0.55
V0.1Nb0.6Mo0.3	262.7	177.4	134.3	102.4	71.2	28.7
V0.1Nb0.7Mo0.2	244.9	125.6	65.6	25.9	7.2	0.96
Mo0.7V0.3	390.6	327.1	233.7	138.7	72.4	31
Mo0.6V0.4	343.9	255.8	152.3	90.9	54.2	13.9
Mo0.5V0.5	365	298	210.5	144.1	89.7	31.1
Mo0.4V0.6	365.8	211.3	166.9	132.2	95	45.9
Mo0.3V0.7	402.5	417.4	375.7	289.6	201.3	101.4

Table 10: Table showing all the VNM materials and their specific capacity values used to plot the ternary heat maps.

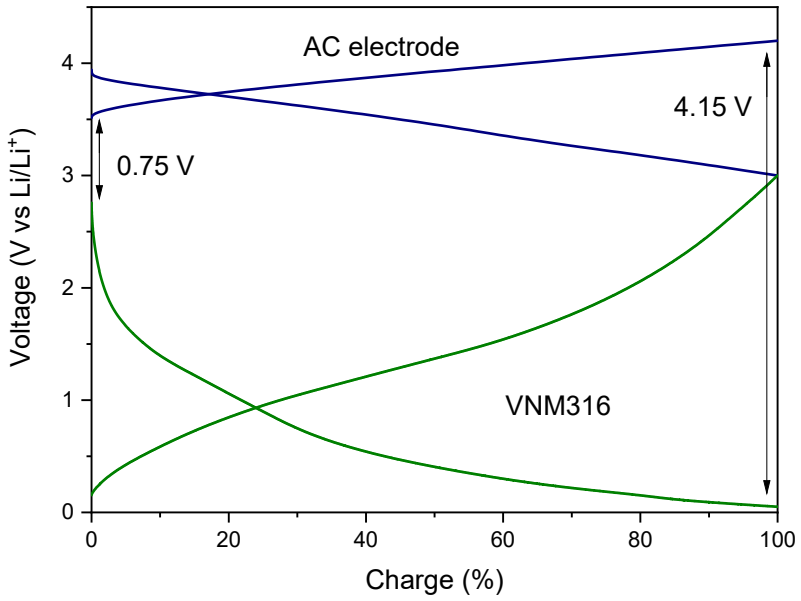

Figure 15: Graph of the GCD plots of VNM316 (green) and activated carbon (blue) with the voltage differences used to determine the potential window of operation for the HIC devices.

9.4 Supplementary for Chapter 5

There is no supplementary material for chapter 5.

9.5 Supplementary for Chapter 6

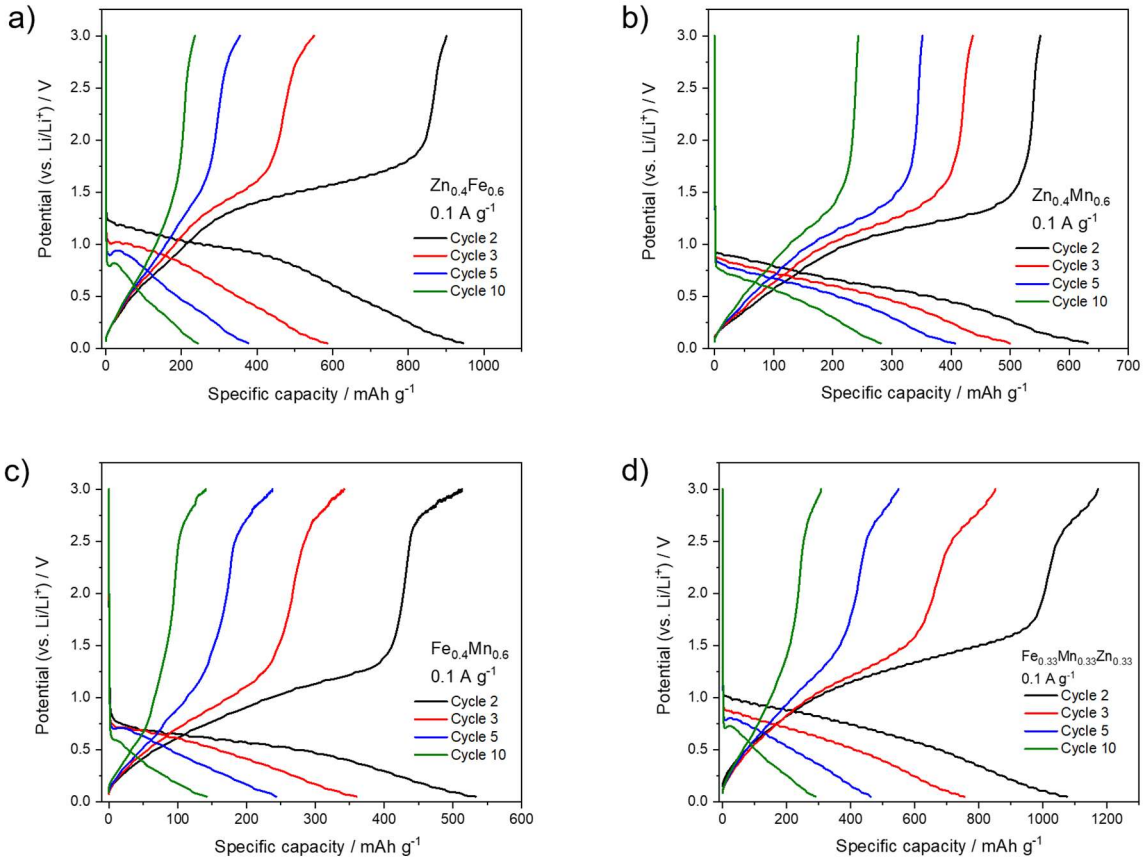

Figure 16: GCD plots of cycle 2 (black), cycle 3 (red), cycle 5 (blue) and cycle 10 (green) at 0.1 A g^{-1} for the materials (a) $Zn_{0.4}Fe_{0.6}$, (b) $Zn_{0.4}Mn_{0.6}$, (c) $Fe_{0.4}Mn_{0.6}$ and (d) $Fe_{0.33}Mn_{0.33}Zn_{0.33}$.

	Specific capacity (mAh g^{-1}) at different specific currents		
Material	**0.1 A g^{-1}**	**0.5 A g^{-1}**	**1 A g^{-1}**
ZnFe14	225.9	29	40.05
ZnFe23	349.65	80.25	55.6
ZnFe32	260.95	84.55	1.75
ZnFe41	270.8	14.95	20.55
MnFe14	531.75	79.55	11.15
MnFe23	358.75	47.3	4.15
MnFe32	245.65	20.35	105.4
MnFe41	383.9	172.05	24.85
ZnMn14	378.5	80.8	63.8
ZnMn23	278.55	104.2	34
ZnMn32	342.85	83.9	2.4
ZnMn41	224.25	8.45	14.4
ZnFeMn622	330.9	48.6	53.5
ZnFeMn262	491	98.9	54.15
ZnFeMn226	425.25	99.95	21.65
ZnFeMn111	479.35	71.05	35.9
ZnFeMn221	373.1	73.95	16.75
ZnFeMn212	301.45	60.4	47.65
ZnFeMn122	419.2	90.1	41.7
FeOx	288.3	87.7	42.9
MnOx	215.85	69.6	12.85
ZnOx	209.3	14.75	40.05

Table 11: Table showing the specific capacity values at set specific currents used to create the ternary heat maps.

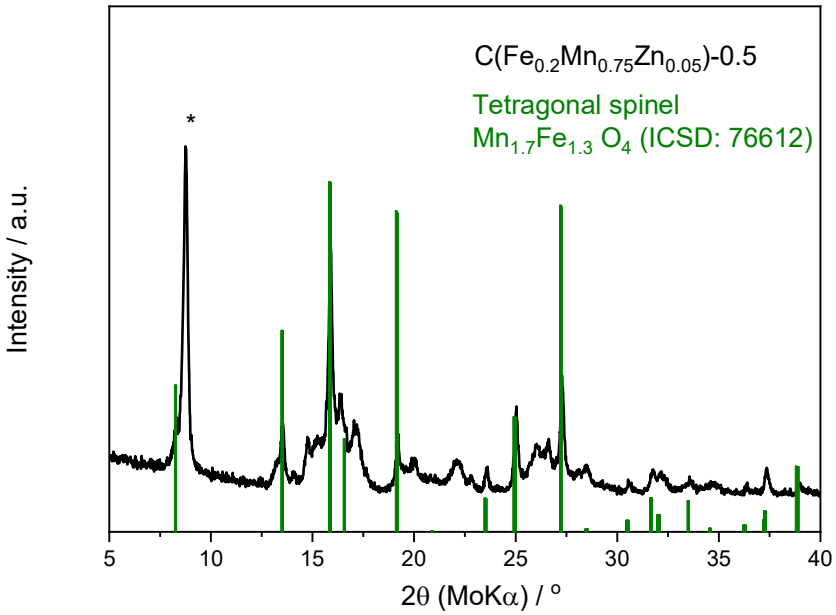

Figure 17: PXRD pattern of $C(Fe_{0.2}Mn_{0.75}Zn_{0.05})$-0.5 before heat treatment, with the reference pattern for mixed Mn and Fe tetragonal spinel (Green, ICSD collection code: 76612).

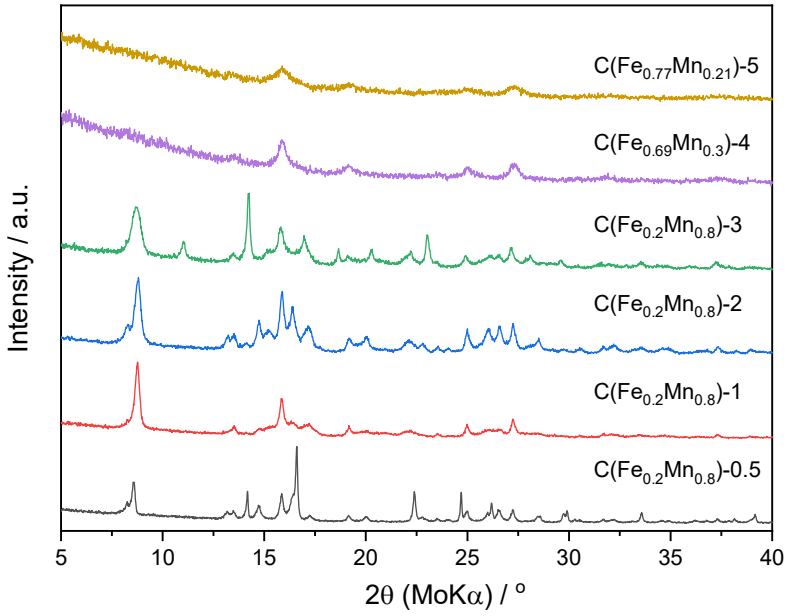

Figure 18: PXRD patterns of the $C(Fe_aMn_b)$-X materials prior to heat treatment.

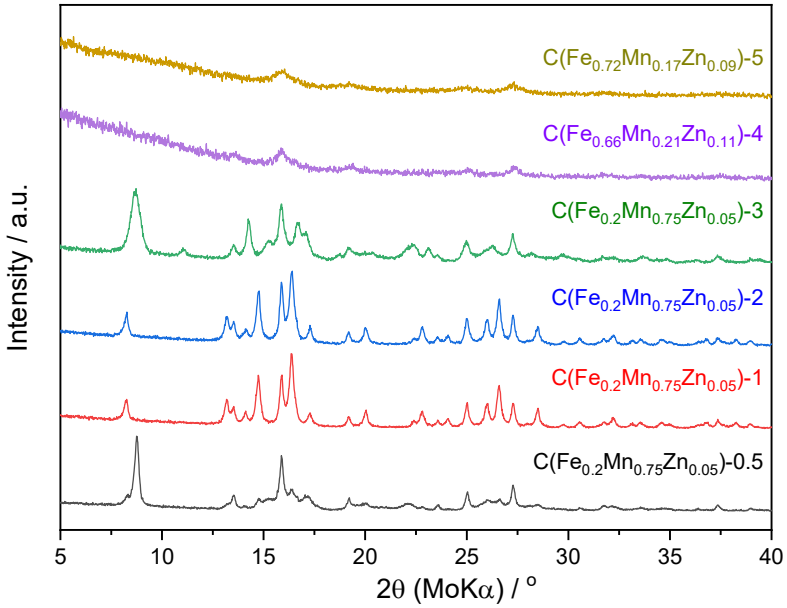

Figure 19: PXRD patterns of the C($Fe_aMn_bZn_c$)-X materials prior to heat treatment.

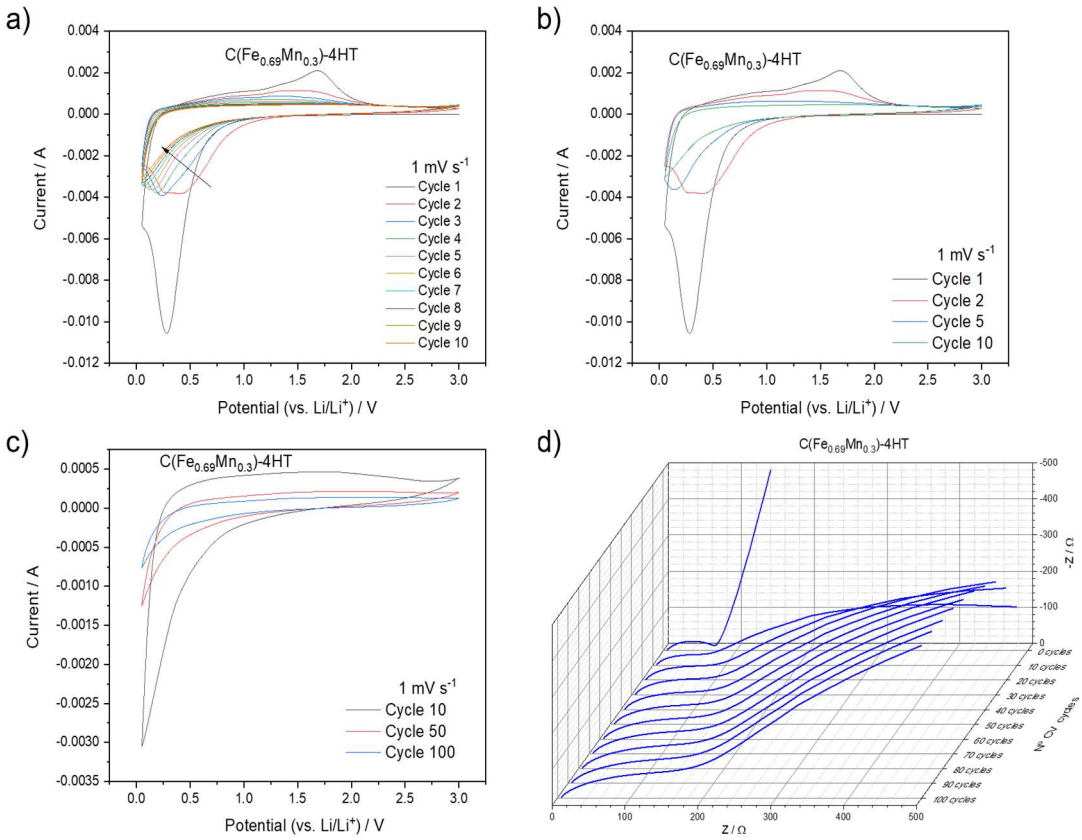

Figure 20: For the material $C(Fe_{0.69}Mn_{0.3})$-4HT (a) the first 10 CV cycles at a scan rate of 1 mV s^{-1}, (b) CV cycles 1, 2, 5 and 10, (c) CV curves 10, 50 and 100, (d) the Nyquist plots taken every 10 CV cycles.

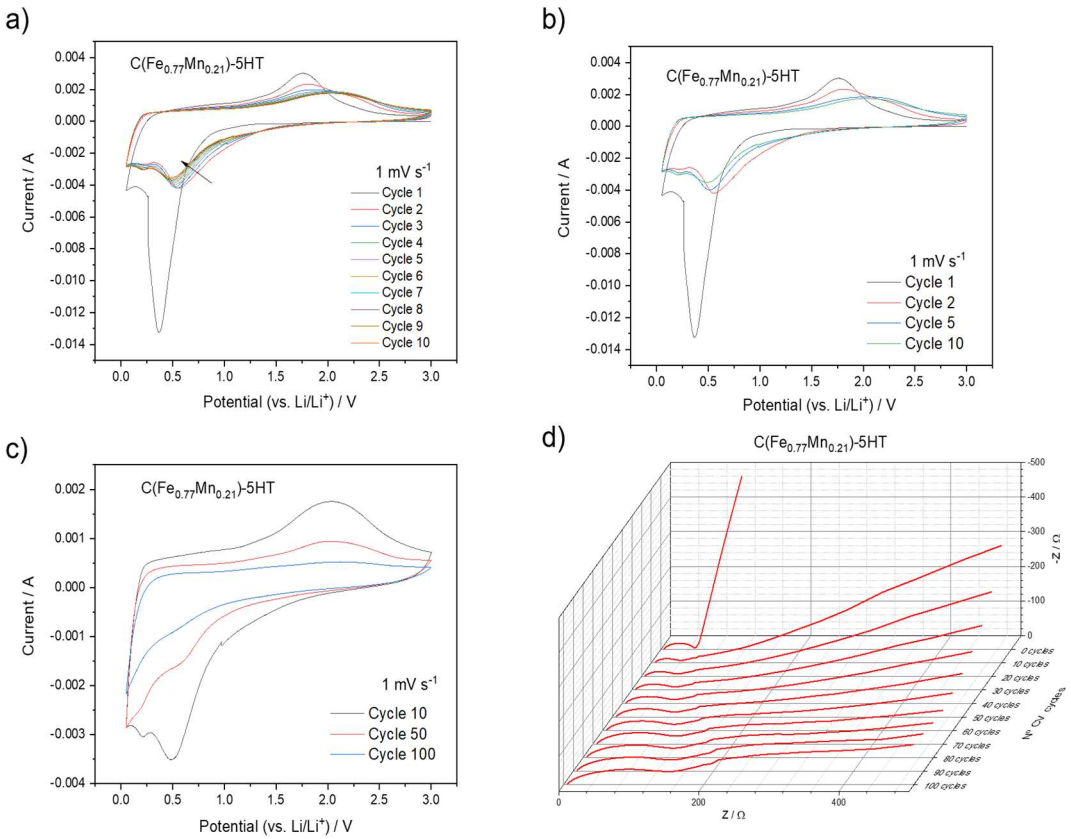

Figure 21: For the material $C(Fe_{0.77}Mn_{0.21})$-5HT (a) the first 10 CV cycles at a scan rate of 1 mV s^{-1}, (b) CV cycles 1, 2, 5 and 10, (c) CV curves 10, 50 and 100, (d) the Nyquist plots taken every 10 CV cycles.

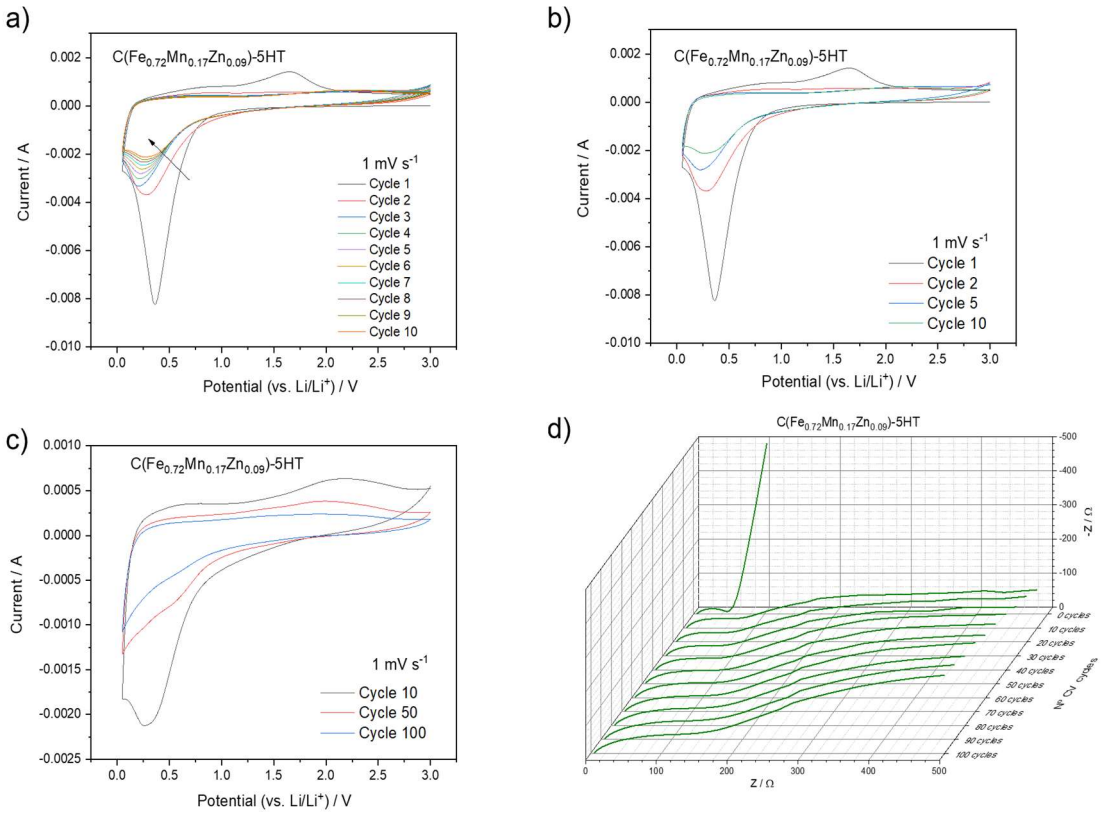

Figure 22: For the material C($Fe_{0.72}Mn_{0.17}Zn_{0.09}$)-5HT (a) the first 10 CV cycles at a scan rate of 1 mV s^{-1}, (b) CV cycles 1, 2, 5 and 10, (c) CV curves 10, 50 and 100, (d) the Nyquist plots taken every 10 CV cycles.